

# Structural Properties of Finite and Infinite Nuclear Systems and Related Phenomena

*By*

**Subrata Kumar Biswal**

**PHYS07201104002**

**Institute of Physics, Bhubaneswar  
INDIA**

A thesis submitted to the  
Board of studies in Physical Sciences  
In partial fulfillment of requirements

For the Degree of  
**DOCTOR OF PHILOSOPHY**

*of*

**HOMI BHABHA NATIONAL INSTITUTE**



**February, 2017**

## STATEMENT BY AUTHOR

This dissertation has been submitted in partial fulfillment of requirements for an advance degree at Homi Bhabha National Institute (HBNI) and deposited in the Library to be made available to borrowers under rules of the HBNI.

Brief quotations from this dissertation are allowed without special permission, provided that accurate acknowledgement of source is made. Requests for permission for extended quotation from or reproduction of this manuscript in whole or in part may be granted by the competent Authority of HBNI when in his or her judgment the proposed use of the material is in the interests of scholarship. In all other instances, however, permission must be obtained from the author.

Date:

(Subrata Kumar Biswal)

## DECLARATION

I, **Subrata Kumar Biswal**, hereby declare that the investigations presented in the thesis have been carried out by me. The matter embodied in the thesis is original and has not been submitted earlier as a whole or in part for a degree/diploma at this or any other Institution/University.

Signature

(Subrata Kumar Biswal)

Date :

## List of Publications arising from the thesis

### Journal

1. “The Effects of Self Interacting Isoscalar-Vector Meson on Finite Nuclei and Infinite Nuclear Matter”, **S. K. Biswal**, S. K. Singh, M. Bhuyan and S. K. Patra, *Braz. J. Phys*, **2014**, 45, 347-352.
2. “Isoscalar giant monopole resonance for drip-line and super heavy nuclei in the framework of relativistic mean field formalism with scaling calculation”, **S. K. Biswal** and S. K. Patra, *Cent. Eur. J. Phys.*, **2014**, 12, 582-596 .
3. “Search of double shell closure in the superheavy nuclei using a simple effective interaction”, **S. K. Biswal**, M. Bhuyan, S. K. Sing and S. K. Patra, *International Journal of Modern Physics E*, **2014**, 23, 1450017(1-14).
4. “Effects of N-N potentials on p Nuclides in the A~100-120 region”, C. lahiri, **S. K. Biswal** and S. K. Patra, *International Journal of Modern Physics E*, **2016**, 25, 1650015(1-15).
5. “Softness of Sn isotopes in relativistic semiclassical approximation”’ **S. K. Biswal**, S. K. Singh, and S. K. Patra, *Modern Physics Letters A*, **2015**, 30, 1550097(1-13).
6. “Effects of isovector scalar meson on neutron star both with and without hyperon”, **S. K. Biswal**, Bharat Kumar, and S. K. Patra, *International Journal of Modern Physics E*, **2016**, 25, 1650090(1-22).
7. “New constrained calculation of excitation energy of Isoscalar giant monopole resonance and Isovector giant dipole resonance in relativistic Thomas-Fermi formalism”, **S. K. Biswal**, X. Viñas, M. Centelles, and S. K. Patra.  
(Communicated to a Journal)

## Conferences

1. “Isovector giant dipole resonance in Relativistic Thomas-Fermi formalism”, **S. K Biswal**, S. K Patra and X. Viñas, *Proceedings of the DAE-BRNS Symp. on Nucl. Phys.*, **2015**, 60, 106-107.
2. “Effects of different NN potentials on  $^{120}\text{Te}$  nucleus”, C. Lahiri, **S.K. Biswal** and S.K. Patra, *Proceedings of the DAE-BRNS Symp. on Nucl. Phys.*, **2015**, 60, 214-215.
3. “Effects of the isovector-scalar meson on the softness of the Sn isotopes”, **S. K. Biswal**, S. K. Singh, S. K. Patra and B. K. Agrawal, *Proceedings of the DAE Symp. on Nucl. Phys.*, **2014**, 59, 84-85.
4. “Effect of Isospin on compressibility of drip line and superheavy nuclei”, **S. K. Biswal** and S. K. Patra, *Proceedings of the DAE Symp. on Nucl. Phys.*, (2013), **58**, 146-147.

(Subrata Kumar Biswal)

*To My Parents*

---

## ACKNOWLEDGMENTS

With my deep respect, I like to thank my supervisor Prof. S. K. Patra for his constant support and guidance during my research work. His experienced advice has helped me in many ways, without which it would not have been possible to complete this thesis. He has been always available for me, which helped me to accelerate my research work. Not only nuclear physics, he has also taught me the fact of life and philosophies, which will constantly guide me throughout my life. I take this opportunity to thanks, Prof. L. Satpathy, whose inspirational words made me more versatile during my Ph.D carrier. Prof. Satpathy is a man of physics and philosophies. His words make me to think beyond my capacity.

Special thanks to Prof. Xavier Viñas for his help. I will remain always greatfull to him for his kindness. I would like to express my sincere gratitude to Prof. Sudhakara Panda, Director, Institute of Physics. His helpful attitude has made my rigorous Ph.D. life more enjoyable and worth living. Thanks for his constant support.

Institute of Physics always provided us a good academic and friendly atmosphere. I would like to thank all the office and library staffs of the Institute. Special thanks to Rajesh Mohapatra, Ramchandra Hansda, Ravana and others. for their co-operation during my stay at IOP. I like to thank my junior Bharat Kumar and my senior S. K. Singh, M. Ikram and M. Bhuyan for their support.

After all, I thank, Department of Atomic Energy for giving me financial support to conduct my Ph.D. work.

I will always remain grateful to my parents and my friends for their patience and support.

**Date:**

**Subrat Kumar Biswal**

# Contents

<b>Synopsis</b>	<b>xi</b>
<b>List of Figures</b>	<b>xix</b>
<b>List of Tables</b>	<b>xxvi</b>
<b>1 Introduction</b>	<b>1</b>
1.1 Effective Theory . . . . .	2
1.2 Non relativistic self consistent theory . . . . .	3
1.3 Relativistic self consistent theory . . . . .	4
1.4 Drip-line and Super heavy nuclei . . . . .	5
1.5 Giant resonances . . . . .	8
1.6 Infinite Nuclear matter (INM) . . . . .	9
1.7 Neutron Star . . . . .	13
1.8 Hyperon Star . . . . .	14
1.9 Plan of the thesis . . . . .	15
1.9.1 In chapter 2 . . . . .	15
1.9.2 In chapter 3 . . . . .	15
1.9.3 In chapter 4 . . . . .	16
1.9.4 In chapter 5 . . . . .	16
1.9.5 In chapter 6 . . . . .	16
1.9.6 In chapter 7 . . . . .	16
<b>2 Double shell closure in the super-heavy region</b>	<b>17</b>
2.1 Introduction . . . . .	17
2.2 The Theoretical Framework . . . . .	19



2.2.1	Simple Effective Interaction . . . . .	19
2.2.2	Relativistic mean field (RMF) formalism . . . . .	19
2.2.3	Pairing Correlation . . . . .	21
2.3	Results and Discussions . . . . .	22
2.3.1	Ground state binding energy . . . . .	22
2.3.2	Density distribution of Neutrons and Protons . . . . .	25
2.3.3	Two neutron separation energy and location of closed shell . .	25
2.3.4	Pairing gaps and pairing energy . . . . .	27
2.3.5	Chemical energy and stability . . . . .	28
2.3.6	Single particle energy . . . . .	30
2.4	Summary and Conclusions . . . . .	31
<b>3</b>	<b>Monopole resonance in drip-line and super heavy region.</b>	<b>32</b>
3.1	Introduction . . . . .	33
3.2	The Formalism . . . . .	35
3.3	Results and Discussions . . . . .	44
3.3.1	Force parameters of relativistic mean field formalism . . . . .	44
3.3.2	Proton and neutron drip-lines . . . . .	49
3.3.3	Isoscalar giant monopole resonance . . . . .	49
3.3.4	Incompressibility of finite nuclei . . . . .	57
3.4	Application of scaling and constrained formalism to Sn isotopes . . .	61
3.5	Analysis of Sn results . . . . .	62
3.6	Summary and Conclusions . . . . .	70
<b>4</b>	<b>Perturbative constrained calculation of excitation energy of ISGMR and IVGDR in semiclassical RMF theory.</b>	<b>72</b>
4.1	Introduction . . . . .	73
4.2	Formalism . . . . .	75
4.3	Relativistic Thomas-Fermi approximation . . . . .	77
4.4	The constrained perturbative approach . . . . .	79
4.4.1	Isoscalar giant monopole resonance . . . . .	80
4.4.2	Isovector giant dipole resonance . . . . .	83
4.5	Results and Discussions . . . . .	85

4.6	Summary and outlook . . . . .	89
<b>5</b>	<b>Effects of self interacting <math>\omega</math>-meson on finite and infinite nuclear system.</b>	<b>91</b>
5.1	Introduction . . . . .	92
5.2	Theoretical frameworks . . . . .	93
5.2.1	Non-linear case . . . . .	94
5.3	Results and Discussions . . . . .	96
5.3.1	Energy density and Pressure density . . . . .	99
5.3.2	Binding energy, Excitation energy and Compressibility . . . . .	102
5.4	Summary and Conclusions . . . . .	103
<b>6</b>	<b>Effects of <math>NN</math> potentials on <math>p</math> nuclides in the <math>A \sim 100-120</math> region</b>	<b>104</b>
6.1	Introduction . . . . .	105
6.2	Procedure . . . . .	106
6.3	Results and discussions . . . . .	111
6.3.1	RMF calculations . . . . .	111
6.3.2	Astrophysical S factor and reaction rates . . . . .	112
6.3.3	Optical potentials and effects of non-linearity . . . . .	120
6.4	Summary . . . . .	122
<b>7</b>	<b>Effects of hyperon on both static and rotating neutron star</b>	<b>123</b>
7.1	Introduction . . . . .	123
7.2	Theoretical formalism . . . . .	126
7.3	Results and discussions . . . . .	128
7.3.1	Parametrization of $g_\rho$ and $g_\delta$ with constant symmetry energy . . . . .	129
7.3.2	Fields of $\sigma, \omega, \rho$ and $\delta$ mesons . . . . .	133
7.3.3	Energy per particle and pressure density . . . . .	134
7.3.4	Stellar properties of static and rotating neutron stars . . . . .	137
7.3.5	Effects of $\delta$ -meson on static and rotating stars . . . . .	140
7.3.6	Effects of $\delta$ -meson on baryon production . . . . .	144
7.3.7	Fitting of $g_\rho$ and $g_\delta$ with fixed binding energy and charge radius . . . . .	146
7.4	Summary and Conclusions . . . . .	147

<b>8 Summary and Conclusions</b>	<b>149</b>
<b>REFERENCES</b>	<b>153</b>

## Synopsis

The atomic nucleus is a strongly interacting many-body quantum mechanical system that exhibits a fascinating variety of shape and excitation modes, starting from spherical to super deformed and from single particle excitation to collective excitation like vibration and rotation of nucleus as a whole. The study of nuclear structure attempts to elucidate the unified mechanism by which these rich patterns of behavior emerge from a common underlying strong nuclear force between the nucleons. Nucleons are the building blocks of the nucleus. It is the nature of nucleon-nucleon interaction, that decides the each and every characteristic of a nucleus. Nuclear structure is a consequence of the nuclear interaction. A thorough study of the nuclear structure gives prerequisite information about the interaction of a nucleon with another nucleon. Not only the study of a finite nucleus but also the study of an infinite nuclear matter (INM) system like neutron star has attracted nuclear physicists and many information can be accumulated from the study of INM. A neutron star is a very complex and dense system. It also provides a well-riched laboratory to test the nuclear theory under extreme condition of density and asymmetry, which can not be created in a terrestrial laboratory. Our primary aim is to study nuclear structure for both finite and infinite nuclear matter. In the present thesis, we explore both finite nuclei and neutron star structure using relativistic mean field (RMF) formalism.

In finite nuclear structure physics, the magic number has a special place. The magic combinations of protons and neutrons give the extra stability to the nucleus in comparison with the neighboring one. We have searched a magic combination of protons and neutrons in the super heavy region. We found the proton number  $Z=120$  and corresponding neutron number  $N=182/184$  [1] can be a possible combination of the next magic numbers beyond  $^{208}Pb$  in the super heavy region. We have shown that our newly developed non-relativistic interaction, simple effective interaction (SEI) along relativistic RMF model with various parameter sets predict similar results. Our prediction of magic combination based on the various signature of the magic nuclei like the sharp decrease in the two-neutron separation energy  $S_{2n}$  and two-proton

separation energy  $S_{2p}$  - energy, zero pairing gaps  $\Delta_n$  and  $\Delta_p$  and the large gap in protons and neutrons single particle energy levels. All the evidences show a clear signature of the presence of magic number at  $Z=120$  and  $N=182$  or  $184$  [1].

In recent years with the advent of the radio active ion beam (RBI) facility drip-line and super-heavy nuclei are on the spot light. We have studied the collective excitation of drip-line and super-heavy nuclei. As we know that nucleus is a many-body quantum system, collective excitation happens quite often instead of single particle excitation. In collective excitation, nucleons are excited collectively ( all protons and neutrons excited together ) instead of single particle excitation. There are various types of collective excitation present like Isoscalar giant monopole resonance (ISGMR) , isovector giant dipole resonance (IVGDR), isovector giant monopole resonance (IVGMR) etc . ISGMR and IVGDR play very important role in nuclear structure physics. Both are known as the squeezing mode of vibration. In ISGMR the protons and neutrons vibrate in the same phase to each other. Either both the proton and neutron Fermi sphere expand or compress at the same time. It is related to the incompressibility of a nucleus [2]. From the finite nuclear incompressibility, we can calculate the infinite nuclear matter incompressibility ( $K_\infty$ ) by leptodermous expansion [2]. In the leptodermous expansion, the finite nuclear incompressibility ( $K_A$ ) can be expanded into various terms like volume, surface and asymmetry as :

$$K_A = K_\infty + K_s A^{-1/3} + K_{curv} A^{-2/3} + K_\tau \frac{(N-Z)^2}{A^2} + K_c Z^2 A^{-4/3}. \quad (0.1)$$

Volume term of the finite nuclear incompressibility gives the value of  $K_\infty$ , which has a very imperative role in deciding the nature of the equation of state (EOS). Softness and stiffness of an EOS are decided by its  $K_\infty$  value. Usually higher  $K_\infty$  corresponds to the stiff EOS, while low  $K_\infty$  gives soft EOS. In other words,  $K_\infty$  controls the curvature of EOS at saturation density. But incompressibility is not a directly measurable quantity. In experiment, we measured excitation energy of ISGMR, which can be related to the incompressibility of finite nucleus by the formula :

$$E_x = \hbar \sqrt{\frac{AK_A}{m \langle r^2 \rangle}}. \quad (0.2)$$

There is also another method to calculate  $K_\infty$  from  $K_A$ . Theoretical strength function distribution is calculated with the microscopic model like random phase approximation (RPA) with various parameter sets. The  $K_\infty$  of the parameter set which reproduces the experimental strength distribution exactly is considered as the right  $K_\infty$  value.

We have calculated the incompressibility ( $K_A$ ) and the excitation energy of the dripline and super heavy nuclei [3]. The collective excitation like ISGMR is a smooth function of the mass number ( $A$ ). So we can apply semiclassical approximation like relativistic Thomas-Fermi (RTF) and extended Thomas-Fermi (RETF) approximation [4] to study the excitation energy as well as the incompressibility of the finite nucleus. In the present thesis, we have applied RETF approximation along with the constrained and scaling approximation to calculate excitation energy ( $E_x$ ) of ISGMR. In order to compare the excitation energy of macroscopic model with the microscopic model, three average energy are defined : constrained energy ( $\sqrt{\frac{m_1}{m_{-1}}}$ ), centroid energy ( $\frac{m_1}{m_0}$ ) and scaling energy ( $\sqrt{\frac{m_3}{m_1}}$ ). We focused to calculate the constrained and scaling energy. The constrained energy is calculated by minimizing the constrained energy functional ( $\mathcal{H} - \lambda Q$ ), where  $Q$  is the excitation operator and  $\lambda$  is the parameter. In scaling approach, we scaled the density and solved the scaled equation of motion to calculate the restoring force :

$$C_M = \left[ \frac{\partial^2}{\partial \lambda^2} \int d(\lambda r) \frac{\mathcal{H}_\lambda(r)}{\lambda^3} \right]_{\lambda=1}. \quad (0.3)$$

The restoring force and incompressibility are connected by the formula

$$E_x = \sqrt{\frac{C_M}{B_M}}, \quad (0.4)$$

where  $C_m$  is the restoring force and  $B_M$  is the mass parameter. In relativistic case, mass parameter is defined like

$$B_M = \int \mathcal{H} r^2 dr \quad (0.5)$$

and in the non-relativistic case  $B_M^{nr} = mA < r^2 >$ .

Along with the constrained method developed in the recent past, we have developed also a different constrained technique, which is based on the Taylor series expansion around the equilibrium. As we know that the giant resonance can be

viewed as a small amplitude vibration of density or shape around the equilibrium, we can expand the constrained energy functional around the equilibrium in Taylor series. We have applied the new method to calculate the excitation energies of both ISGMR and IVGDR. We have compared our results with other theoretical models like random phase approximation (RPA). Our results well matched with other theoretical calculations as well as experimental data.

Apart from the drip-line and super-heavy region the medium-heavy nuclei ( $A \sim 100$ ) have also very crucial in the study of giant resonance. In recent years, softness of Sn isotopes have gained a lot of attention for nuclear theorists. The excitation energy of isoscalar giant monopole resonance of Sn series ( $Sn^{112-124}$ ) shows a low value with respect to the experimental excitation energy, whereas excitation energy of  $^{208}Pb$  and  $^{90}Zr$  well matched with the experimental data. Now the question arises why Sn is so floppy ? Lots of literature have been devoted to explain this softness of Sn isotopes. But still, it is an open problem. We have discussed this problem within our RETF formalism. We elaborately discussed the contribution of various terms of RMF Lagrangian [5]. A large number of nonlinear relativistic force parameters are used in these calculations. We find that a parameter set is capable of reproducing the experimental monopole energy of Sn isotopes when its nuclear matter compressibility lies within 210-230 MeV, however, it fails to reproduce the GMR energy of other nuclei. That means, simultaneously a parameter set cannot reproduce the GMR values of Sn and other nuclei.

The nuclear force is the central theme of the nuclear physics ever since from the starting point (1932: discovery of neutron). It is the aim of every nuclear physicist to understand the atomic nuclei on the basis of bare nucleon-nucleon interaction. The interaction between the nucleon is the strong interaction in nature, so in principle, one should use quantum chromo dynamics (QCD) to study the atomic nuclei. But it is not easy to use QCD starting from quark interaction to calculate various properties of nucleus. In fact, we can not use perturbative formalism like QCD approach in a case of nuclear physics due to the energy range involved. In this energy range, the QCD coupling constants become large so the perturbative approach is not valid. In nuclear physics, it is a tradition to use nucleons as the degrees of freedom and massive bosons are exchanged between the nucleon to generate the nuclear force.

Patra et al. have calculated nucleon-nucleon potential starting from the effective RMF Lagrangian. This is known as the R3Y interaction [6]. We have used this R3Y interaction to calculate various properties of finite nuclei. We have also introduced a new cross-coupling of omega meson into the interaction and analyzed its effects on the finite and infinite nuclear system. We found that self-interacting  $\omega$ -meson term has a significant influence on the finite as well as an infinite nuclear system. A strong but an attractive components of nuclear force is generated due to  $\omega^4$  term at very short distance ( $r < 0.2$  fm) [7]. We have applied R3Y as well as the M3Y interaction to obtain the folding potential to study the (p,  $\gamma$ ) and (p, n) types of reaction for proton-rich nuclei. These proton-rich nuclei are very less in number but has great astrophysical implication to study r- and p- processes. Effects of linear and non-linear interaction terms of RMF Lagrangian on s-factor calculation is discussed [8]. We have shown that the non-linear  $\sigma$  meson coupling has strong effect on the S-factor calculation on the p-nuclei.

After discussion of various aspects of finite nuclear structure, we shifted our attention to the infinite nuclear matter, which is a hypothetical system of an infinite number of nucleons interacting through nuclear force only (uncharged), having infinite volume (no surface). Due to the heavy mass, the contribution of  $\delta$ -meson has been neglected for many years in RMF theory. But in a neutron star, a highly asymmetric and dense system, we can not overlook the contribution of  $\delta$ -meson. It affects the transport properties of asymmetric nuclear matter in a significant way. Using the effective field theory approach, like RMF, we discussed the dominance of isovector-scalar  $\delta$ -meson on the neutron stars as well as hyperon star [9]. From simplification point of view, we started with an assumption that neutron star is a static and uncharged body, constituted with a maximum number of neutrons and little amount of proton and electrons, which are necessary for the  $\beta$ -equilibrium. Then extended our investigation to a more realistic situation, where a neutron can rotate with hyperon at the core of the star. Neutron star is a system of degenerate fermions, so simple energetic consideration implies the presence of hyperon in the high density (9-10 times of  $\rho_0$ ) environment of a neutron star. Further the time scale associated with the neutron star is much larger than the time scale associated with the weak interaction, which favors the production of hyperons inside the neutron star. However, in the standard



picture, the inclusion of hyperon degrees of freedom leads a considerable softening of EOS, which consequently leads a maximum allowed the mass of neutron star lower than the current observation. So there is no question of hesitance to re-investigate the EOS of neutron star with new degrees of freedom in different physical condition. We focused on the effects of  $\delta$ -meson on : (a) static proton-neutron and hyperon star. (b) rotating proton-neutron and hyperon star. All the calculation have done with RMF formalism with G2+ $\delta$  parameter set. G2 is considered as one of the efficient parameter set, where maximum number of interactions have been taken care. We have added an extra  $\delta$ -degrees of freedom with existing  $\sigma$ ,  $\omega$  and  $\rho$ -mesons. It is not conceptually right to vary the  $\delta$ -meson strength ( $g_\delta$ ) as a free parameter to see the effects of the  $\delta$ -meson on the nuclear system. Due to the isovector nature of both  $\rho$  and  $\delta$ -meson, they contribute to the isovector channel simultaneously. It is customary to take into account the contribution of  $\rho$ -meson, while discussing the effects of the  $\delta$ -meson [10]. There are various procedure to fit  $g_\rho$  and  $g_\delta$  to see the effects. We have adopted two of them. In one case, the  $g_\rho$  and  $g_\delta$  are fitted in such way a that the symmetry energy of the original G2 parameter (36.4 MeV) remain fixed and in another case the coupling constants are adjusted to fix the binding energy and charge radius of finite nucleus fixed. We calculated the maximum allowed mass of the neutron start with these pairs of  $g_\rho$  and  $g_\delta$ . With the inclusion of  $\delta$ -meson, the maximum allowed mass value of mass for proton-neutron star increases due to the stiff equation of state at higher density. Results are same for both rotating and static case. Quantitatively we get maximum mass of static and rotating proton-neutron star  $\sim 2 M_\odot$  and  $\sim 2.4 M_\odot$  respectively in G2 + $\delta$  parameter, which are close to the current observations. But in hyperon star, maximum mass decreases with the inclusion of  $\delta$ -meson, this is due to the increase of strangeness in the system. The  $\delta$ -meson interaction affects the production yield of hyperon and hyperon produced at a lower density than in non- $\delta$ -system. To see a consistent effects of  $\delta$ -meson on the nuclear system, the more appropriate way to form a parameter set by reshuffling all the parameters and readjusting with various finite and infinite nuclear matter properties. Work in this direction is in progress.

# Bibliography

- [1] S. K. Biswal, S. K. Singh, M. Bhuyan and S. K. Patra, Int. J. Mod. Phys. E **23**, 1450017 (2014).
- [2] J.P. Blaizot , J. E Berger, J. Decharg, M. Girod, Nucl. Phys. A **591**, 435-457 (1995).
- [3] S. K. Biswal and S. K. Patra, Cent. Eur. J. Phys. **12** 582-596 (2014).
- [4] S. K. Patra, X. Viñas, M. Centelles and M. Del Estal, Nucl. Phys. A **703**, 240 (2002).
- [5] S. K. Biswal, S. K. Singh and S. K. Patra, Mod. Phys. Lett. A **30** 1550097 (2015).
- [6] B. B. Sahu, S. K. Singh, M. Bhuyan, S. K. Biswal and S. K. Patra, Phys. Rev. C **89**, 034614 (2014).
- [7] S. K. Biswal and S. K. Singh, M. Bhuyan and S. K. Patra, Braz. J. Phys. **45**, 347 (2014).
- [8] C. Lahari, S. K. Biswal and S. K. Patra, Int. J. Mod. Phys. E **23** 1650015 (2016).
- [9] S. K. Biswal, Bharat Kumar and S. K. Patra, communicated to Journal (<http://arxiv.org/abs/1602.08888> ).
- [10] S. Kubis and M. Kutschera, Phys. Lett. B **399**, 191 (1997).

# List of Figures

1.1	Various electric and magnetic giant resonance, which classified on the basis of their multi polarity(L), spin (s)and isospin(T) quantum number.	10
2.1	The ground state densities with SEI for $^{208}\text{Pb}$ , $^{298}114$ , $^{304}120$ and $^{310}126$ are compared with the RMF(NL3) results. . . . .	24
2.2	The two neutron separation energy obtained from NL3 and SEI for $^{208}\text{Pb}$ , $^{298}114$ , $^{304}120$ and $^{310}126$ . . . . .	25
2.3	The calculated pairing gap of neutron $\Delta_n$ with SEI for the isotopic series $Z=82$ , 114, 120 and 126 are compared with the NL3 results. . .	26
2.4	(a)The pairing gap of proton $\Delta_p$ with SEI for the isotopic series $Z=82$ , 114, 120 and 126 compared with the NL3 results. . . . .	27
2.5	The pairing energy as a function of neutron number for $Z=82$ , 114, 120 and 126 with SEI and NL3 forces. . . . .	28
2.6	Systematic of chemical energy $\mu_n$ and $\mu_p$ as a function of neutron number for $Z=82$ , 114, 120 and 126 with SEI and NL3 sets. . . . .	29
2.7	The single particle energy levels for $^{304}120$ with NL3 and SEI parametrization. . . . .	30
3.1	The excitation energy isoscalar giant monopole resonance (ISGMR) for O, Ca, Ni, and Sn isotopes from proton to neutron drip-lines as a function of mass number. . . . .	50
3.2	The excitation energy isoscalar giant monopole resonance (ISGMR) for Pb, $Z=114$ , and $Z=120$ isotopes starting from proton to neutron drip-lines as a function of mass number. . . . .	51

3.3	The difference between the monopole excitation energies of scaling and constrained calculations $\Sigma = \frac{1}{2}\sqrt{E_3^2 - E_1^2}$ as a function of mass number $A$ for O, Ca, Ni, and Sn. . . . .	54
3.4	Same as Fig. 3.3, but for Pb, $Z=114$ , and $Z=120$ . . . . .	55
3.5	The incompressibility modulus obtained by both scaling and constrained approaches in the isotopic series of O, Ca, Ni, and Sn. . . . .	57
3.6	Same as Fig. 3.5, but for Pb, $Z=114$ , and $Z=120$ . . . . .	58
3.7	Compressibility for finite nuclei obtained by scaling calculation $K_A^s$ versus nuclear matter incompressibility $K_\infty$ . . . . .	60
3.8	The isoscalar giant monopole excitation energy obtained by scaling method with various parameter sets are compared with experimental data of $\sqrt{\frac{m_3}{m_1}}$ and $\sqrt{\frac{m_1}{m_{-1}}}$ for Cd and Sn isotopes [125,126]. The upper and lower panels are $\sqrt{\frac{m_3}{m_1}}$ and $\sqrt{\frac{m_1}{m_{-1}}}$ , respectively. . . . .	63
3.9	(a) The variation of giant monopole excitation energy $E_x$ with mass number $A$ for Sn isotopes, (b) the scaling monopole excitation energy within RETF and RTF formalisms compared with the experimental moments ratio $\sqrt{m_3/m_1}$ [119], (c) variation of the difference of giant monopole excitation energy obtained from RETF and RTF ( $\Delta E = RETF - RTF$ ) formalisms with various parameter sets for Sn isotopic chain, (d) moments ratio $\sqrt{m_3/m_1}$ for Sn isotopes obtained with NL3+ $\Lambda_V$ is compared with NL3, QRPA(T5) and experimental data. . . . .	64
5.1	The effective NN interaction potentials as a function of distance $r$ from Eq. 5.6- 5.12 for NL3 parameter set. . . . .	97
5.2	The contribution of $\sigma$ -potential from linear, non-linear and total as a function of distance $r$ for NL3 parameter set. . . . .	97
5.3	The contribution of $\omega$ -potential from linear, non-linear and total as a function of distance $r$ for for NL3 parameter set. . . . .	98
5.4	The energy per particle of symmetric nuclear matter as a function of baryon density for various values of $c_3$ . . . . .	99

5.5	The pressure density of symmetric nuclear matter as a function of baryon density for various values of $c_3$ . . . . .	100
5.6	The binding energy of $^{40}\text{Ca}$ and $^{208}\text{Pb}$ in their ground state for different values of $c_3$ . . . . .	101
5.7	The excitation energy as a function of $c_3$ for $^{40}\text{Ca}$ and $^{208}\text{Pb}$ . (b) The incompressibility of $^{40}\text{Ca}$ and $^{208}\text{Pb}$ as a function of $c_3$ . . . . .	101
6.1	Comparison of charge density from our calculation with Fourier- Bessel analysis of experimental electron scattering data [203] . . . . .	105
6.2	Experimental and calculated cross sections for elastic proton scattering at 9.7 MeV proton energy. . . . .	113
6.3	S factors from two different microscopic potentials are compared with experimental measurements for $^{102}\text{Pd}$ . Here “Exp-1”is the experimental data from reference [226], “Exp-2”from reference [227] and “DDM3Y”is for the DDM3Y-folded potential. . . . .	115
6.4	S factors extracted from theory compared with experimental measurements for $^{106,108}\text{Cd}$ . Here “Exp”is the experimental data from reference [228]. . . . .	116
6.5	S factors extracted from theory compared with experimental measurements for $^{112}\text{Sn}$ . . . . .	116
6.6	Astrophysical reaction rates for $(p, \gamma)$ reactions of some important $p$ nuclei compared with NONSMOKER rates [206]. Here Green Continuous line: Present calculation, Red Dotted line: NONSMOKER calculation. . . . .	118
6.7	Astrophysical reaction rates for $(p, n)$ reactions compared with NONSMOKER rates [206]. Here Green Continuous line: Present calculation, Red Dotted line: NONSMOKER calculation. . . . .	118
6.8	S factors extracted from our calculations compared with experimental measurements for $^{120}\text{Te}$ . Here “Exp”is the experimental data from reference [230]. For other details, see the text. . . . .	119
6.9	(Color online) Effective interaction potential for $^{120}\text{Te}$ . . . . .	120

6.10	(Color online) Real central part of folded potentials and Coulomb potential for 7 MeV proton(Lab) incident on $^{120}\text{Te}$ . . . . .	121
7.1	Variation of $g_\rho$ and $g_\delta$ at a constant value of symmetry energy $E_{sym} = 36.4$ MeV for both nuclear and neutron matter. . . . .	130
7.2	Various meson fields are obtained from the RMF theory with $G2 + g_\delta$ and NL3 parameter sets. The $\sigma$ - meson field $V_\sigma$ and $\omega$ -meson field $V_\omega$ from $G2 + g_\delta$ calculations are compared with the results of DBHF theory [264] and NL3 set. . . . .	133
7.3	(Color online) Variation of binding energy per particle with density at various $g_\rho$ and $g_\delta$ . . . . .	135
7.4	Variation of energy per particle (panel (a)) and pressure density (panel (b)) with $\rho_B/\rho_0$ at different values of $g_\rho$ and $g_\delta$ . The enlarged version of energy per particle for sub-saturation region is in panel (c). The results of other theoretical models like Baldo-Maieron [267], DDHF [268], Firedman [266] and AFDMC [269] are also given for comparison. . . . .	136
7.5	(Color online) The mass-radius profile for static star with different parametrization like G2 [251], NL3 [49], NL3* [93], NL-SH [241], FSU [90] and FSU2 [279]. (a) is for proton-neutron star and (b) is for the hyperon star. The maximum mass $M$ and the corresponding radius obtained by various parameter sets are given in the parenthesis. . . . .	139
7.6	(Color online) The mass-radius profile of the static and rotating proton-neutron and hyperon stars with various combination of $g_\delta$ and $g_\rho$ in $G2+\delta$ . (a,c) is for proton-neutron star and (b,d) is for the hyperon star. (a,b) for static and (c,d) for rotating cases. . . . .	141
7.7	(Color online) Keplerian frequency of the rotating proton-neutron and hyperon stars with various combination of $g_\delta$ and $g_\rho$ in $G2+\delta$ . (a) is for proton-neutron star and (b) is for the hyperon star. The results are obtained from RNS code [276]. . . . .	142
7.8	(Color online) Yield of strange particles as a function of density. The upper panel (a) is with G2 parameter set (without taking $\delta$ -meson coupling) and the lower panel (b) is with $\delta$ -meson coupling. . . . .	145

- 7.9 (Color online) Mass and radius profile of hyperon star with G2+ $\delta$  parameter set, but with different meson-hyperon coupling of Ref. [281]. 146

# List of Tables

2.1	The value of interaction parameters for simple effective interaction (SEI) and RMF (NL3) [33] sets and their nuclear matter properties at saturation. . . . .	20
2.2	The binding energy (BE) obtained from SEI calculation is compared with the RMF(NL3) [33], finite range droplet model (FRDM) [39] and with experimental data of some of the known super-heavy nuclei. The BE is in MeV. . . . .	23
3.1	The calculated binding BE and charge radius $r_{ch}$ obtained from relativistic extended Thomas-Fermi (RETF) approximation is compared with relativistic Hartree (with various parameter sets) and experimental results [108, 109]. The RETF results are given in the parentheses. The empirical values [19, 110] of nuclear matter saturation density $\rho_0$ , binding energy per nucleon BE/A, incompressibility modulus $K$ , asymmetry parameter $J$ , and ratio of effective mass to the nucleon mass $M^*/M$ are given in the lower part of the table. Energies are in MeV and radii are in fm. . . . .	45
3.2	The results of isoscalar giant monopole resonance with various parameter sets for some known nuclei are compared with recent experimental data [111]. The calculations are done with relativistic extended Thomas-Fermi (RETF) approximation using both scaling and constrained schemes. The values of $\Delta_1$ , $\Delta_2$ , and $\Delta_3$ are obtained by subtracting the results of (NL3, NL3*), (NL3*, FSUGold), and (NL3, FSUGold), respectively. The monopole excitation energies with scaling $E^s$ and constrained $E^c$ are in MeV. . . . .	47



3.3	The predicted proton and neutron drip-lines PDL and NDL for $O$ , $Ca$ , $Ni$ , $Sn$ , $Pb$ , $Z=114$ , and $Z=120$ in relativistic mean field formalism (RMF) with various parameter sets are compared with experimental (wherever available) and Finite Range Droplet Model (FRDM) predictions [112]. . . . .	48
3.4	The calculated excitation energies in the RETF formalism with FSUG-old parameter set are compared with other theoretical formalisms and experimental data [75, 115, 116]. . . . .	53
3.5	Moments ratio for Sn isotopes using RETF approximation with FSUG-old and NL1 sets are compared with QRPA(T6) predictions [140]. . .	65
3.6	Moments ratio $\sqrt{m_1/m_{-1}}$ for Pb isotopes within RETF is compared with pairing+ MEM results and experimental data. . . . .	66
3.7	Contribution of the $\rho$ -meson to the total binding energy in the RTF and RETF approximations with FSUGold, NL1 and NL3+ $\Lambda_V$ parameter set. RETF represent $\rho$ meson contribution to total energy from $R^2$ term and RETF $\Lambda_V$ represent contribution from the $\Lambda_v R^2 V^2$ . . .	69
3.8	$^S K_A$ and $^C K_A$ are incompressibility for finite nuclei obtained from scaling and constraint methods, respectively are compared with the values obtained from the equation of state (EOS). . . . .	69
4.1	Excitation energy of the ISGMR in MeV of some spherical nuclei calculated as $\sqrt{m_1/m_{-1}}$ using the NL3 model. $E_c(RTF - P)$ is the estimate of the present work, $E_c(RETF)$ is the RETF result computed as in Ref. [81], $E_c(RMF)$ and $E_c(RPA)$ are the constrained Hartree and RPA results, respectively, reported in [117]. . . . .	86
4.2	Excitation energy of the IVGDR in MeV of some spherical nuclei calculated as $\sqrt{m_1/m_{-1}}$ using the NL3 model. $E_c(RTF - P)$ is the estimate of the present work and $E(RPA)$ are the RPA results reported in [173]. . . . .	87

4.3	Semi-classical $m_{-1}$ sum rule in $\text{fm}^2 \text{MeV}^{-1}$ of some spherical nuclei computed as explained in this work ( $RTF - P$ ) and using the DM approach (4.44) ( $RTF - LDM$ ) input). All these calculation are performed with the NL3 parameter set. . . . .	87
5.1	The values of $m_\sigma$ , $m_\omega$ , $m_\rho$ (in MeV) and $g_\sigma$ , $g_\omega$ , $g_\rho$ for RMF (NL3) force, along with the self-interacting $\omega$ - field with coupling constant $c_3$ .	100
6.1	Model parameters for the Lagrangian FSUGold [90], NL3 [49] and TM1 [87]. . . . .	110
6.2	Calculated binding energy per nucleon (B.E/A) [219] and charge radii $r_{ch}$ [220] for some selected $p$ nuclei compared with experimental values. .	111
7.1	The parameters for G2 set are in the upper panel of the Table. The nuclear matter saturation properties are in the middle panel and various $g_\rho$ and $g_\delta$ combinations are in the lower panel, keeping symmetry energy $E_{sym} = 36.4 \text{ MeV}$ fixed. . . . .	131
7.2	Binding energy (MeV) and charge radius (fm) are calculated with various combination of $g_\rho$ and $g_\delta$ in G2+ $\delta$ . The results are compared with experimental data [263]. . . . .	131
7.3	Mass and radius of the neutron star are calculated at different values of $g_\rho$ and $g_\delta$ keeping binding energy of $^{208}\text{Pb}$ (1633.296 MeV) constant. The calculated results of $E_{sym}$ , $L_{sym}$ and $K_{sym}$ are for nuclear matter at different combinations of $(g_\rho, g_\delta)$ pairs. . . . .	132

# Chapter 1

## Introduction

Nuclear Physics has been providing a platform to test all four types of basic interactions unlike to any other branch of physics. It is not an easy task to deal with nuclear physics because it needs a sound knowledge in all four fundamental interactions starting from the electromagnetic interaction between protons of finite nuclei to gravitational interaction in the case of the neutron star, which can be viewed as a big nucleus. The most mysterious and puzzling thing in nuclear physics is the nucleon-nucleon (N-N) interaction, which has consumed maximum manpower to fix its nature, but still a debatable subject. In 1911, Rutherford [1] discovered nucleus from the famous  $\alpha$ -particle scattering experiment. Factual nature of a nucleus came to known after the discovery of neutron by James Chadwick in 1932. A nucleus consists of protons and neutrons, both the individuals are known as nucleon. Nucleons are the quanta of the nucleus. In 1935 Yukawa purposed the meson theory [2, 3] of nuclear force. According to this theory, nucleons interact with each other through the exchange of mesons. The nuclear force is similar to the Van der Waals force between atoms and molecules. Both Van der Waals and Nuclear forces are residual forces of fundamental interaction. The former one is the residual interaction of electromagnetic interaction, while later one is same as the strong interaction. In some sense, nuclear force is not a fundamental force rather it is the residual interaction of strong interaction between the quarks. In principle, we can study the interaction between two nucleons starting from the interaction between the quarks, which are the constituent particles of nucleons. But for practical purpose, it is very difficult

to deal with a theory starting from quark-quark interaction i.e. QCD (Quantum Chromo Dynamics). In the QCD level, things become very complicated to study the properties of finite and infinite nuclear systems. So in nuclear physics it is customary to use effective mean field theories, like SHF ( Skyrme Hartree-Fock ), RMF (Relativistic Mean Field), DBHF (Dirac- Bruckner Hartree Fock ). In effective theories, the total interaction is not the sum of all possible two-body interactions but each nucleon feels as if it moves in a common (mean) potential/ field generated by rest of the nucleons. Suppose in a nucleus there are  $A$  number of nucleons then every nucleon will feel a mean field generated by  $A-1$  number of nucleons. Basically, there are two types of effective theories mostly adopted in nuclear physics. In one case nucleons are treated like non-relativistic particles (SHF, Gogny) [4–6] and in other case nucleons are treated like relativistic particles (RMF) [7–9]. In the non-relativistic case nucleon's motion are governed by Schrodinger equation (SC), while in the case of relativistic one nucleons motion are governed by Dirac equation . There are some merits of relativistic formalism over the non-relativistic formalism. Relativistic formalism is one step ahead of non-relativistic formalism. In relativistic formalism, we deal with Dirac equations, so the spin-orbit interaction comes in a more natural way unlike to the non-relativistic model. No extra parameter is used to fit the spin-orbit interaction term. In relativistic mechanics, there is the presence of both positive and negative energy solution. We avoid the negative solution by assuming Dirac no sea approximation.

## 1.1 Effective Theory

Self-consistent models are efficacious tools for the investigation of the nuclear structure and low energy dynamics. Mean field models are based on the effective energy-density functional theory. Interaction between nucleons is formulated in terms of density dependent Lagrangian. Energy-density functional contains many free parameters whose values are fitted to reproduce empirical and experimental data. These parameters are fitted based on the constraints related with

- Experimental data on the static properties of the finite nucleus ( Binding energy and charge radius ).

- Characteristic properties of the nuclear matter ( saturation density, binding energy per nucleon at saturation density, symmetry energy).
- Excitation of giant monopole and dipole resonances.
- Observational information of the neutron star and supernovae ( mass and radius of the neutron star).

## 1.2 Non relativistic self consistent theory

Basically, there are two types of non-relativistic theories widely used , one is zero range Skryme Hartree-Fock (SHF) and other is finite range Gogny interaction. In both the cases, basic assumption is that nucleons are moving at a speed much less than the speed of light. This assumption is validated taking into account the average binding energy per nucleon in an nucleus is  $\sim 8$  MeV comparing with the mass of the nucleon  $\sim 938$  MeV. So no relativistic formalism is needed. In Skryme Hartree Fock approach the effective potential between the nucleons can be written as the sum of two bodies and three bodies interactions. That is

$$V_{eff} = \sum_{ij} V_{ij}^{(2)} + \sum_{ijk} V_{ijk}^{(3)}, \quad (1.1)$$

where  $V_{ij}$  and  $V_{ijk}$  are two body and three body interactions respectively. It is a tedious work to deal with 3-body and many-body interactions. Thus for the practical purpose, the leading order interaction i.e the 2-body and for very specific case the 3-body is sufficient. In short range expansion of two body interaction. The Skryme energy functional can be written as

$$\begin{aligned} \mathcal{E} = & \frac{1}{2}t_0 \left[ \left(1 + \frac{x_0}{2}\right)\rho^2 - \left(x_0 + \frac{1}{2}\right) \sum_q \rho_q^2 \right] + t_1 \left[ \left(1 + \frac{x_1}{2}\right) \left[ \rho\tau + \frac{3}{4}(\Delta\rho)^2 \right] \right. \\ & - \left. \left(x_1 + \frac{1}{2}\right) \sum_q \left[ \rho_q\tau_q + \frac{3}{4}(\Delta\rho_q)^2 \right] \right] + \frac{t_2}{4} \left(1 + \frac{x_2}{2}\right) \left[ \rho\tau - \frac{1}{4}(\Delta\rho)^2 \right] \\ & + \left(\frac{x_2}{2} + \frac{1}{2}\right) \sum_q \left[ \rho_q\tau_q - \frac{1}{4}(\Delta\rho)^2 \right] - \frac{1}{16}(t_1x_1 + t_2x_2)J^2 + \frac{1}{16}(t_1 - t_2) \sum_q J_q^2 \\ & + \frac{1}{12}t_3\rho^\gamma \left[ \left(1 + \frac{x_3}{2}\right)\rho^2 - \left(x_3 + \frac{1}{2}\right) \sum_q \rho_q^2 \right] + \frac{1}{2}W_0(J\Delta\rho + \sum_q J_q\Delta\rho_q). \quad (1.2) \end{aligned}$$

The terms proportional to  $\rho^2$  represent two body attractive potential. It is counter balanced by the terms proportional to the  $\rho^{\gamma+2}$ , which are the repulsive terms. These two terms counter balance each other and give saturation properties of nuclear force. The terms proportional to the  $\rho\tau$  give kinetic energy contribution. The surface term  $(\Delta\rho)^2$  is essential for finite nuclei. Spin-orbit interaction has also a vital role in finite nuclei, which is represented by  $J\Delta\rho$ .

- $\rho$  = Local baryon density
- $\tau$  = Kinetic energy density of the baryon
- $J$  = Spin-orbit density

In the Skyrme energy functional there are both  $T=0$  ( isoscalar ) and  $T=1$  (isovector) part. The densities without subscript represent isoscalar part and densities with subscript  $q$  represent isovector part.

### 1.3 Relativistic self consistent theory

Fundamentally RMF is different from SHF and Gogny, by including the relativistic effects in the formalism. In simple words, one can say RMF is nothing but the relativistic generalization of non-relativistic mean field formalism. Unlike SHF, the RMF is a finite range interaction. Nucleons are interact with each other through the exchange of various effective mesons-like  $\sigma$ -,  $\omega$ -,  $\rho$ - and  $\delta$ - mesons. In nature, there are so many effective mesons are present, but why few of them are taken into account ? This is due to the symmetry of nuclear potential. Except the symmetry, there are some meson's contribution are excluded due to their heavy masses and negligible contributions. They do not give any significant contribution neither qualitatively nor quantitatively for the improvement of the model, except the mathematical complexity. So it is wise to take the minimal set of mesons, which can describe the nucleon-nucleon interaction up to a desired level. In our work we have taken  $\sigma$ -,  $\omega$ - and  $\rho$ - mesons in most of cases.  $\delta$ -meson is also added in some cases. The starting point of the RMF theory is the nucleon-meson interacting Hamiltonian, which is given by

$$\begin{aligned}
\mathcal{H} = & \underbrace{\sum_i \varphi_i^\dagger \left[ -i\vec{\alpha} \cdot \vec{\nabla} \right] \varphi_i}_{\text{a}} + \underbrace{\sum_i \varphi_i^\dagger \beta m^* \varphi_i}_{\text{b}} + \underbrace{\sum_i \varphi_i^\dagger g_v V \varphi_i}_{\text{c}} + \underbrace{\sum_i \varphi_i^\dagger \frac{1}{2} g_\rho R \tau_3 \varphi_i}_{\text{d}} + \underbrace{\frac{1}{2} e \mathcal{A} (1 + \tau_3) \varphi_i}_{\text{e}} \\
& + \underbrace{\frac{1}{2} [(\vec{\nabla} \phi)^2 + m_s^2 \phi^2]}_{\text{f}} - \underbrace{\frac{1}{2} [(\vec{\nabla} V)^2 + m_v^2 V^2]}_{\text{g}} - \underbrace{\frac{1}{2} [(\vec{\nabla} R)^2 + m_\rho^2 R^2]}_{\text{h}} - \underbrace{\frac{1}{2} (\vec{\nabla} \mathcal{A})^2}_{\text{i}} - \underbrace{\frac{\zeta_0}{24} g_v^4 V^4}_{\text{j}} \\
& + \underbrace{\frac{1}{3} b \phi^3 + \frac{1}{4} c \phi^4}_{\text{k}} - \underbrace{\Lambda_V g_v^2 g_\rho^2 R^2 V^2}_{\text{l}}
\end{aligned} \tag{1.3}$$

The meaning of the terms in the Hamiltonian are as follow:

- a: The kinetic energy contribution of the nucleons.
- b: Rest energy of the nucleon plus interaction between the nucleons and sigma meson.
- c,d: Interaction between the omega and rho-mesons with nucleons respectively.
- e: Interaction of photon with the proton.
- f,g, h: Free meson contribution of  $\sigma$ ,  $\omega$ , and  $\rho$ -meson respectively. First term represents the kinetic part and second term is the rest energy part for each case.
- i: Kinetic energy contribution of the photon. Rest energy part is zero because of zero rest mass.
- j,k: Self coupling of the  $\omega$  and  $\sigma$ -mesons respectively.
- l: Cross coupling between the  $\omega$  and  $\rho$ -mesons.

## 1.4 Drip-line and Super heavy nuclei

Both drip-lines and super-heavy regions are most venerable areas of nuclear physics. Many exotic phenomena can be found in these areas of landscape. Physics inside light nuclei is not exactly same as in super-heavy nuclei. As the nuclear force is density depended, it changes with number of nucleons. There are lots of discrepancy in the drip-line and  $\beta$ - stable nuclei. The experimental and theoretical investigations of

nuclei far from the valley of  $\beta$ - stability is the main aim of modern nuclear structural research. Radio active ion beam (RIB) facilities have disclosed a wealth of structural phenomena in exotic nuclei having the extreme value of  $N/Z$  ratio. The super-heavy and drip-line nuclei regions involve many exotic and anomalous phenomena like

- Halo Nucleus
- Neutron skin
- Quenching of the shell effect in neutron-rich nuclei and the resulting deformation
- New magic number (N, Z)
- Shape co-existence
- Ground-state proton radioactive
- Synthesis of the heavy-element
- Onset of the exotic collective modes.

New upgraded experimental facilities will improve and extend our understanding of physics of nuclei up to drip-line and super-heavy region. With the modern technology, we can find out the exact location of proton and neutron drip-line and possible to synthesis of super heavy nuclei having a longer life time so that spectroscopy of the nuclei can also be studied. More new important information will be accumulated on masses, life times and reaction cross-sections, which are urgently needed in astrophysical calculations for better understanding of nuclear process occurring in the universe. Proton-rich nuclei play a vital role in understanding the astrophysical process like r- and p- process ( rapid neutron capture process and rapid proton capture process).

Unraveling of the physics of drip-line and super-heavy regions not only due to the lack of experimental up-gradation, but also the lack of the proper theoretical understanding. All most all theoretical models converge in the light nuclei and  $\beta$ - stable region with acceptable error. But if we start the journey towards the drip-line and super-heavy region they diverge with an unacceptable difference. In drip line region the exotic phenomena mainly due to (a) pronounced effects of the coupling between bound state and particle continuum (while in the  $\beta$  stable nuclei system



is mostly bound state ) (b) weak binding energy of outer most neutron (c) region of neutron halo with very diffuse neutron density (d ) major modification in shell structure. The vital problem of theoretical investigation in the drip-line region is the closeness of Fermi level to the particle continuum. Self-consistent theories (relativistic and non-relativistic ) can describe the coupling between the bound state and particle continuum. But both relativistic and non-relativistic lead to a huge discrepancy in the drip-line region, while they move in hand to hand in the  $\beta$ - stability line. Particularly in the way they describe spin-orbit are very different from each other and its iso-spin dependence also. This is due to the fitting of the parameter, which mostly belongs to the  $\beta$ - stability region.

In general,  $A > 210$  is considered as super-heavy region in the nuclear chart. The most challenged task in the super heavy nuclear physics is its production in the laboratory or available in nature. Its reaction cross-section goes inversely with atomic number in the super heavy region. Most of the super heavy elements have a half-life in the order of few  $\mu$ -seconds, which is too small to characterize its chemical and structural properties. This is the main reason of worried for a nuclear physicists to find a combination of  $Z$  and  $N$ , which gives element with an appreciable half-life in nuclear scale. Due to the lack of technical up-gradation, experimentalists always depend upon the theoretical confirmation. Theorists also face compulsion due to the diverge behavior of the various models. They always face problem to conclude with an unique combination of  $N$  and  $Z$ . Condition become more worst, when a model with different parameter sets lead different conclusion. Basic reason of this is the non-transparent nature of nuclear force, which is a fundamental problem in the nuclear physics for all time. Then the validity and applicability of the different nuclear force and the model becomes a debatable subject, which consumed maximum man power in the nuclear theory.

In the present thesis, we are particularly concerned about nuclear structure. Nuclear structure is the result of an interplay between the surface tension and elector-magnetic interaction between protons. Surface tension originates from nuclear force between the nucleons and tries to maintain a spherical shape, while Coulomb force provokes the nucleus to be deformed. Most of the heaviest elements were found in three " heavy elements factories ": Lawrence Berkely Laboratory in Berkely, Joint

Institute for Nuclear Research (JINR), Dubna (Russia) and GSI near Darmstadt, Germany. Probably the first theoretical prediction of the super heavy element was by Nilsson et.al [10] with the help of liquid drop model plus Strutinsky shell correction, and the prediction was  $Z=114$  and  $N=184$ . The magic number  $Z=118$  was predicted in earliest macro-microscopic calculation [11] and later confirmed in [7, 12]. The fully microscopic approaches predict the proton shell closure at  $Z=120$  [13],  $Z=126$ , or  $Z=114, 120, 126$  [14] depending upon the chosen nucleon-nucleon interaction in mean field theories. The neutron magic number  $N=184$  is almost firmly predicted by different theoretical models. With the advent of radioactive ion beam (RIB) facilities, last twenty years have remained as a golden era for heavy elements production. New super-heavy elements are now produced with both cold and hot combination of colliding nuclei. The heaviest yet discovered element is  $Z=118$ , synthesized in hot fusion reaction of  $^{48}\text{Ca}$  beam and  $^{248}\text{Cf}$  is the heaviest available target, which has been used in this  $Z=118$  [15]. Thus to get super heavy (SH) elements with  $Z > 118$  fusion reaction, one should be processed to heavier than  $^{48}\text{Ca}$  projectile ( $^{50}\text{Ti}$ ,  $^{54}\text{Cr}$ ). The corresponding cross-section for the production of elements  $Z=119$  and  $Z=120$  are predicted to be smaller by about two order of magnitude as compared  $^{48}\text{Ca}$ -induced fusion reaction. Another limitation of the fusion reaction (both hot and cold) for producing SH elements consists in the fact that they lead to neutron deficient isotopes having rather a short lifetime. In Chapter 2, we discuss the prediction of magic number at  $Z=120$  and  $N=182/184$  with our new non-relativistic SEI model and compared with other theoretical calculations.

## 1.5 Giant resonances

Giant resonance is a collective vibration in which the protons and neutrons vibrate in a collective manner instead of single particle vibration. In microscopic formalism, it can be viewed as a coherent superposition of particle-hole excitation. Macroscopic formalism describes it as a vibration of shape and density of nucleus around the equilibrium shape and density. On the basis of their quantum numbers like multipolarity (L), spin (S) and isospin (T), giant resonances can be divided like isoscalar giant monopole resonance (ISGMR), isovector giant monopole resonance (IVGMR),

isovector giant dipole resonance (IVGDR) etc. . . . Some of the resonances like ISGMR and IVGDR are crucial in the nuclear structure physics. ISGMR is also refereed as the breathing mode of oscillation. In ISGMR the proton and neutron vibrate in a phase to each other, either they are expanding or compressing. It is a density oscillation just like human breathing, expansion, and compression of the nucleus. In another word, it corresponds to the radial oscillation, in which the radius oscillates around the equilibrium radius. It has a small amplitude of vibration, only 1-2 % of the original radius. As it is related to breathing mode, the excitation energy of the ISGMR gives a way to calculate the incompressibility ( $K$ ) of the finite nucleus and consequently the incompressibility of infinite nuclear matter ( $K_\infty$ ). Infinite nuclear matter incompressibility is a key quantity in the calculation of equation of state (EOS) of a neutron star. In IVGDR, the protons and neutrons vibrate in opposite phase to each other. It related to the symmetry energy of a nuclear system, which is another most important quantity to calculate the EOS of a neutron star. In the present thesis, we have developed a slightly different formalism to calculate the excitation energy  $E_x$  of ISGMR and IVGDR. Our formalism is based on constrained method calculation. This constrained formalism is based on Taylor series expansion, which is different from the constrained Hartree-Fock formalism, where we have to minimize the constrained Hartree-Fock constrained Hamiltonian. Generally, we defined three mean energy like constrained energy ( $\sqrt{\frac{m_1}{m_{-1}}}$ ), centroid energy ( $\frac{m_1}{m_0}$ ) and scaling energy ( $\sqrt{\frac{m_3}{m_1}}$ ). We will discuss more the excitation energy and incompressibility in Chapter IV.

## 1.6 Infinite Nuclear matter (INM)

The universe contains a remarkable wide variety of atomic nuclei with the mass number up to  $A \sim 250$ . There are many interesting properties, which differentiate these nuclei from each other, while there is also a powerful set of systematic trend and general properties that provide an important and useful frame work for understanding the basic structure of nuclei. We can classified the properties of nucleus mainly into two categories: local and global properties. These global properties are well studied with the help of a hypothetical system i.e., infinite nuclear matter (INM). Properties of this system do not depends on the local parameters like a number of the nucleon

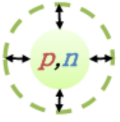
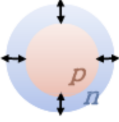
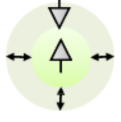
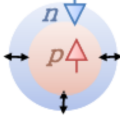
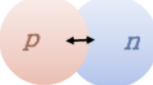
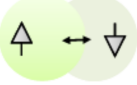

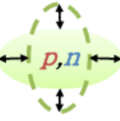
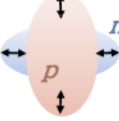
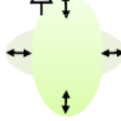
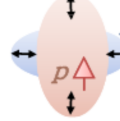
$\Delta L=0$	 ISGMR	 IVGMR	 ISSMR	 IVSMR
$\Delta L=1$		 IVGDR	 ISSDR	 IVSDR
$\Delta L=2$	 ISGQR	 IVGQR	 ISSQR	 IVSQR
	$\Delta S=0$ $\Delta T=0$	$\Delta S=0$ $\Delta T=1$	$\Delta S=1$ $\Delta T=0$	$\Delta S=1$ $\Delta T=1$

Figure 1.1: Various electric and magnetic giant resonance, which classified on the basis of their multi polarity(L), spin (s)and isospin(T) quantum number.

and structure of the nucleus. We can define the INM as " it is a hypothetical interacting system of infinite number of nucleons, with no surface effect and in an absence of Coulomb interaction". The nucleons interact through strong interaction only. As we are considering  $A \rightarrow \infty$ , so there must not be any boundary (zero surface effect). Then a common question arises "How can we address the infinite nuclear matter"? For that, we have to attribute some properties to the infinite nuclear matter. These are (a) saturation density ( $\rho_0$ ) (b) binding energy per particle at saturation density ( $E/A$ ) (c) symmetry energy ( $J$ ) (d) L-coefficient (e) incompressibility ( $K_\infty$ ). In semi-empirical mass formula, the binding energy per particle of a finite nucleus can be written as

$$E/A = \underbrace{a_V}_{\text{Global (bulk)}} - \underbrace{\frac{a_s}{A^{1/3}} - a_c \frac{Z(Z-1)}{A^{2/3}} - a_{sym} \frac{(N-Z)^2}{A^2}}_{\text{local}} \pm \delta \quad (1.4)$$

Here  $a_v$ ,  $a_s$ ,  $a_c$  and  $a_{sym}$  carry their usual meaning of volume, surface, Coulomb and symmetry coefficient respectively. In binding energy per particle expression, first term is independent of  $A$ , which represent the bulk properties and same for all nucleus. Second part differentiate nucleus from each other. The first term (volume) represents the INM properties with the condition of symmetric nuclear matter ( $N=Z$ ). Thus we will get rid of the asymmetry and Coulomb terms. The surface contribution goes on decreasing in comparison with the volume term with an increase of the mass number and Coulomb term is switched off by definition. The pairing term can be neglected, which is very small in comparison to the volume term. So finally binding energy expression of INM left with  $a_v$  term, which has value  $a_v \sim -16 \text{ MeV}$ .

Another characteristic property of the INM is the saturation density, which has a typical value of  $\rho_0 = 0.16 \text{ fm}^{-3}$ . It is the maximum density, which can be achieved inside the finite nuclei. In other words, one can say, it is not possible to go beyond this density under the nuclear force only. This property is the bi-product of the short range repulsive nature of the nucleon-nucleon interaction. We can not compress the nuclear system after certain limit due to its repulsive nature at short range. We need some other force to increase the density of a nuclear system. This is the gravity which helps the system of the neutron star to increase 9-10 time of the saturation density. INM is a homogeneous and isotropic infinite system, the position of the nucleons do not depend only the relative distance between the nucleon matter. Due to the

homogeneity nature, we can write the nucleon wave function as plane wave function  $e^{ikx}$ . The particle density is obtained by the sum over all the occupied state inside the phase space volume  $(2\pi)^3$ .

$$\rho = \frac{N}{V} = \sum_{K,\lambda} \psi_{k,\lambda}^*(\vec{r}) \psi_{k,\lambda}(\vec{r}) \rightarrow \frac{\gamma}{(2\pi)^3} \int d^3K n(\vec{k}) \quad (1.5)$$

Here  $\gamma$  is the degeneracy factor, which has value  $\gamma = 4$  for the symmetric nuclear matter (N=Z) and  $\gamma = 2$  for the pure neutron matter. The nuclear matter symmetry energy  $E_{sym}(\rho)$  is an essential tool to characterize the isospin dependent part of the equation of state (EOS) of the asymmetric nuclear matter. Knowledge about the symmetry energy is unavoidable in understanding many aspects of the nuclear physics and astrophysics [16–18]. The symmetry energy of the nuclear matter can be defined as the difference between the energies of pure neutron matter and symmetric nuclear matter as function of the density. Energy density can be function of density and asymmetry of the system  $E(\rho, \alpha = \frac{N-Z}{A})$ .

$$E(\rho, \alpha) = E(\rho, 0) + S(\rho)\alpha^2 + O(\alpha^4) + \dots \quad (1.6)$$

$$S(\rho) = \frac{1}{2} \frac{\partial^2 E(\rho, \alpha)}{\partial \alpha^2} \Big|_{\alpha=0} = S_v + \frac{P_0}{\rho_s^2}(\rho - \rho_s) + \frac{\Delta K}{18\rho_s^2}(\rho - \rho_s)^2 + \dots \quad (1.7)$$

$S_v$  is the infinite nuclear matter symmetry energy, whose empirical value lies  $30 \pm 5$  MeV.

Another most important quantity of the infinite nuclear matter is its incompressibility ( $K_\infty$ ). The nuclear matter incompressibility ( $K_\infty$ ) is the measure of the stiffness of the equation of state (EOS). It can be calculated from the curvature of the EOS at saturation density.  $K_\infty$  puts a stringent constraint on the theoretical description of effective nuclear interaction and density dependence of the nuclear interaction. The correct value of the infinite nuclear matter incompressibility ( $K_\infty$ ) is a debatable subject in the current scenario. It has been remained a long standing technique to constraint the  $K_\infty$  with the help of isoscalar giant monopole resonance [19]. There are two ways to calculate the infinite nuclear matter incompressibility ( $K_\infty$ ). One

is the direct way, in which the monopole excitation energy is calculated for heavy nucleus with different nucleon-nucleon interaction and the correct nucleon-nucleon interaction is pointed out which gives the exact excitation energy. With this nucleon-nucleon interaction, the incompressibility of infinite nuclear matter is calculated. The second method is little indirect, first, the monopole excitation energy of different nuclei is measured and the incompressibility of finite nuclei is calculated by the formula  $E_A = \sqrt{\left[\frac{\hbar^2 K_A}{m \langle r^2 \rangle}\right]}$ . Like the semi-empirical mass formula, the finite nuclear incompressibility can be expanded in terms of volume, surface, asymmetry and Coulomb expression.

$$K_A = K_V + K_s A^{-1/3} + K_c A^{-2/3} + [K_{\delta v} + K_{\delta s} A^{-1/3}] \delta^2 + K_{coul} \frac{Z^2}{A^{4/3}} + \dots \quad (1.8)$$

In the limit of infinite nuclear matter ( $A \rightarrow \infty$ ) all other terms go to zero except  $K_V$ . So  $K_V$  gives the infinite nuclear matter incompressibility ( $K_\infty$ ). The various coefficient in the expression (1.8) can be estimated from the chi-square fitting with the experimental data. But there is a huge uncertainty in the value of  $K_\infty$  due to very limited number of excitation energy data. It is also model sensitive quantity. In current scenario both the relativistic and non-relativistic formalism come to a conclusion with a value of  $240 \pm 20$  of  $K_\infty$ . There is various application of the concept of infinite nuclear matter in understanding nuclear physics and astrophysics, mainly the physics of the neutron star.

## 1.7 Neutron Star

A neutron star is probably the densest object found in the visible universe, which has the density around 9-10 times the density of the infinite nuclear matter (density of infinite nuclear matter  $\rho_0 \approx 0.16 \text{ fm}^{-3}$ ). Neutron star is the compact remnants of a massive star after it undergoes core collapse. During the lifetime of a star, a hydrodynamical equilibrium is maintained between the radiation pressure created from the fusion process, which is outward and the gravitational attraction towards the core of the star. Fusion process starts with the fusion of hydrogen to form Helium with a huge amount of energy production. This process continues till the production of  ${}^{56}\text{Fe}$ ,

after which it become an endothermic process and not favorable for further processed. With the absence of the outward pressure gravity, contract and core collapse starts. Fate of a star after core collapse usually decided by the mass of the star before the core collapse. The star whose mass below  $4M_{\odot}$  become the white dwarf after the core collapse. Neutron stars and black hole are believed to originate from a more massive star. However, the dividing line between those stars that from neutron star and those that form a black hole is very uncertain because the final stage of the evolution of massive star are poorly understood. The formation of neutron star from a massive star is in the mass range  $4 - 10M_{\odot}$  and assume that all star with masses greater than  $10M_{\odot}$  end up as a black hole. One should not misunderstood from the name "Neutron star", that is composed of the only neutron. Neutron star derive their name from the predominance of neutrons in their interior, following the mutual elimination of electron and proton by inverse  $\beta$ -process. Neutron star composed of neutrons, protons and electrons. One can simply shows that  $n_e : n_p : n_n = 1 : 1 : 8$  in the limit of very large density is a trivial consequence of charge neutrality,  $\beta$ - equilibrium and extremely relativistic degeneracy. Due to the high density, there is the probability of production of strange baryon (hyperon ). It is also assumed that quarks become unconfined due to extremely high density in the inner core of the neutron star.

## 1.8 Hyperon Star

As we know that neutron star is one of the most dense object of the universe. Neutron star has a core of density 9-10 times denser than the saturation density ( $0.16fm^{-3}$ ). This high density is the main cause of the many anomalous physics inside the neutron star. As the density increases, new hadronic degree of freedom may appear in addition to the neutron and proton. One such degree of freedom is hyperon, baryon with strangeness quantum number. We can not deny the presence of hyperon inside the core of neutron star. So we need to study the EOS and mass-radius profile of the hyperon star for complete knowledge of the neutron structure. In Chapter V we will discuss about the effect on EOS with inclusion of the baryon octet.



## 1.9 Plan of the thesis

In this thesis we have outlined the structural properties of finite and infinite nuclear matter. The thesis is organized as follows:

### 1.9.1 In chapter 2

We have discussed the magic number in the super heavy region. The familiar magic numbers  $Z= 2, 8, 20, 28, 50, 82$  and  $N= 2, 8, 20, 28, 50, 82, 126$  in the light and medium heavy region. However the magic number in super heavy region beyond  $^{208}Pb$  is not clear. Magic number has a great importance in the nuclear structure physics. It is a basic assumption that both proton and neutron double magic nuclei are spherical. In this chapter we will discuss the prediction of magic number with help two proton and neutron separation energy,  $\Delta_n$  and  $\Delta_p$  gaps, single particle energy levels and chemical potential. All the calculation have done with both relativistic (RMF) and non-relativistic (SEI) formalism.

### 1.9.2 In chapter 3

In this chapter, we will discuss about the excitation energy of the isoscalar giant monopole resonance (ISGMR) energy. Excitation energy of ISGMR provides a crucial tool to calculate infinite nuclear matter (INM) incompressibility ( $K_\infty$ ). This  $K_\infty$  has a major role in the EOS of infinite nuclear matter. So ( $K_\infty$ ) plays an imperative role in both structure of finite and neutron star. The study of nuclear structure physics will remain incomplete without the study of giant resonance excitation. In this chapter, we have discussed only one type of resonance i.e., ISGMR. Mostly we discussed the excitation energy of ISGMR in super-heavy region. In recent years the excitation energy measurement reveals the softness behavior of the Sn isotopes. Last part of this chapter is dedicated to explain the softness of Sn nuclei in our formalism, relativistic extended Thomas-Fermi the (RETF) formalism.

### **1.9.3 In chapter 4**

This chapter is fully dedicated to develop a new formalism to calculate the giant resonance excitation energy of nucleus. Here we have developed a new technique based on Taylor series expansion to calculate the constrained energy ( $E_1 = \sqrt{\frac{m_1}{m_1}}$ ) for isoscalar giant monopole resonance (ISGMR) and isovector giant dipole resonance (IVDGR). We have given a comprehensive analysis of our new model and compared with other theoretical model as well as with the experimental data.

### **1.9.4 In chapter 5**

In this chapter, the effects of nucleon-nucleon interaction on the finite and infinite nuclear system are discussed. All the results are obtained with R3Y interaction, which was purpose recently by our group. The effects of self-interaction of  $\omega$  meson on various properties of nuclear system is also extensively discussed.

### **1.9.5 In chapter 6**

We have investigated the cross-section and astrophysical S-factor for the proton rich nuclei in the mass range  $A \sim 100-120$ , using the R3Y and density dependent M3Y interaction. The effect of self-interaction of  $\sigma$  and  $\omega$  meson are also discussed extensively.

### **1.9.6 In chapter 7**

After the discussion of finite nuclear structure, we move forward to the infinite nuclear matter. The best example of INM is neutron star. We have calculated mass-radius profile of the neutron star using Tollmann-Volkoff- Oppenheimer (TOV) equation. The EOS for the TOV equation has taken from the RMF formalism with an extra degree of freedom  $\delta$  -meson, which generally never included in the most of the RMF interaction. We have analyzed the effect of  $\delta$ -meson on the EOS of both neutron and hyperon stars. Both static and rotating systems have been taken into consideration.

# Chapter 2

## Double shell closure in the super-heavy region

Magic number is one of the most important tool to study the nuclear structure. Magic numbers in the  $\beta$ -stability regions are well known but in the drip-line and super heavy area it is still a debatable subject. Various theoretical models proposed different combination of protons and neutrons as magic combinations. In this chapter, an attempt to search for spherical double shell closure nuclei beyond  $Z=82$ ,  $N=126$  is discussed. We have used the non-relativistic (SEI) and relativistic (RMF) calculations for our analysis. This will help us to reduce the theoretical uncertainty in the prediction of magic number. Here the calculations and results are based on a newly developed approach entitled simple effective interaction (SEI) and well known RMF formalism. Our results predict the combination of magic nucleus occurs at  $N=182$  and  $Z=114,120,126$ . All possible evidence for the occurrence of magic nuclei is discussed systematically.

### 2.1 Introduction

Starting from the discovery of nucleus, the formation of new element is an interesting topic in Nuclear Physics. So far the synthesis of heaviest element in laboratory is  $Z=118$  in the hot fusion reaction process at JINR Dubna [20,21]. The possibility of the existence (synthesis) of these super-heavy elements is mainly due to the attractive

shell corrections against the destructive Coulomb repulsion. Although atomic number  $Z=114$  was predicted to be the next magic number after  $Z=82$  and neutron number  $N=184$ , recently attention has shifted to the nucleus  $Z=120$  with  $N=182/184$  [14, 22, 23]. The experimental discovery of the super-heavy elements also support this prediction to some extent. Thus, the synthesis of  $Z=120$  is in full swing at the worlds' most laboratories like, Dubna (Russia), RIKEN (Japan), GSI (Germany).

Using cold fusion reaction, elements from  $Z = 107 - 112$  are synthesized at GSI [24–30]. At the production time of  $Z = 112$  nucleus at GSI, the fusion cross section was extremely small (1 pb) [28], which led to the conclusion that reaching still heavier elements will be very difficult by this process. The element  $Z=113$  was also synthesized in cold-fusion reaction at RIKEN with a very low cross section  $\sim 0.03$  pb [31] confirming the limitation of cold-fusion synthesis. To overcome this problem in hot fusion evaporation reaction with deformed actinide targets and neutron-rich doubly magic spherical projectile like  $^{48}\text{Ca}$  are used in the production of super-heavy nuclei  $Z = 112 - 118$  at Dubna [32–37].

It is thus a matter of challenge for every theoretical prediction in nuclear physics to find suitable combination of proton and neutron, which gives double closure shell nuclei beyond  $^{208}\text{Pb}$  and will be the next element of epicenter for experimental synthesis. Our aim is to look for a suitable combination of proton and neutron in such a way that the resultant combination will be the next magic nucleus after  $^{208}\text{Pb}$ . This work is not new, but a revisit of our earlier prediction with in a new simple effective interaction (SEI). The SEI interaction is recently developed in Ref. [38] and given a parameter set which is consistent with both nuclear matter and finite nuclei. Here, we have used this SEI interaction. A systematic investigation of the nuclear structure is done and reconfirmed the double closed nucleus as  $Z=120$  with  $N=182/184$ .

This chapter is organized as follows: In Sec. 2.2, the theoretical formalism of the SEI is presented. The procedures for numerical calculations to estimate the binding energy and root mean square radii are outlined. The results and discussions are given in Sec.2.3. The characteristics of magic structure of nucleus using two neutron separation energy, pairing gap of proton and neutron are analyzed for super-heavy region. In this section stability of such nuclei are also studied in terms of the chemical potentials. Finally summary and concluding remarks are given in Sec. 2.4.

## 2.2 The Theoretical Framework

### 2.2.1 Simple Effective Interaction

The present formalism is based on a simple way to make a consistent parametrization for both finite nucleus and infinite nuclear matter with a momentum dependence finite range term of conventional form, such as *Yukawa*, *Gaussian* or *exponential* to the standard Skyrme interaction [38–40]. We have used the technique of Refs. [38–40] considering a Gaussian term as the momentum dependence finite range interaction which simulate the effect of Gogny type interaction [6, 41]. Then it is applied to nuclear equation of state as well as to finite nuclei through out the periodic table [38]. The Hartree-Fock (HF) formalism is adopted to calculate the wave-function of the nuclear system which then used to evaluate the nuclear observable, such as binding energy, root mean square radii etc. The detail formalism and numerical procedure can be found in [38]. The form of the simple effective interaction (SEI) is given by [38]:

$$\begin{aligned} v_{eff}(\mathbf{r}) = & t_0(1 + x_0 P_\sigma) \delta(\mathbf{r}) + t_3(1 + x_3 P_\sigma) \left( \frac{\rho(\mathbf{R})}{1 + b\rho(\mathbf{R})} \right)^\gamma \delta(\mathbf{r}) \\ & + (W + B P_\sigma - H P_\tau - M P_\sigma P_\tau) f(\mathbf{r}) \\ & + i W_0 (\sigma_i + \sigma_j) (\mathbf{k}' \times \delta(\mathbf{r}_i + \mathbf{r}_j) \mathbf{k}). \end{aligned} \quad (2.1)$$

Where,  $f(\mathbf{r})$  is the functional form of the finite range interaction containing a single range parameter  $\alpha$ . The finite range Gaussian form is given as  $f(\mathbf{r}) = e^{-r^2/\alpha^2}$ . The other terms having their usual meaning [38]. To prevent the supra luminous behavior of the nuclear matter, the usual value of  $b$  [42–45] is taken. There are 11-parameters in the interaction, namely  $t_0$ ,  $x_0$ ,  $t_3$ ,  $x_3$ ,  $b$ ,  $W$ ,  $B$ ,  $H$ ,  $M$ ,  $\gamma$  and  $\alpha$ . The expression for energy density, single particle energy and other relevant quantities are obtained from Eq. (2.1) for Gaussian  $f(r)$  defined in Ref. [38]. The numerical values of the parameter set, SEI and RMF(NL3) are given in Table 2.1.

### 2.2.2 Relativistic mean field (RMF) formalism

The starting point of the RMF theory is the basic Lagrangian containing nucleons interacting with  $\sigma$ -,  $\omega$ - and  $\rho$ -meson fields. The photon field  $A_\mu$  is included to take care of the Coulomb interaction of protons. The relativistic mean field Lagrangian

Table 2.1: The value of interaction parameters for simple effective interaction (SEI) and RMF (NL3) [33] sets and their nuclear matter properties at saturation.

SEI		RMF (NL3)	
$\gamma$	$\frac{1}{2}$	$M$ (MeV)	939
$b$ ( $fm^3$ )	0.5914	$m_\sigma$ (MeV)	508.1941
$t_0$ ( $MeV fm^3$ )	437.0	$m_\omega$ (MeV)	782.6010
$x_0$	0.6	$m_\rho$ (MeV)	7630.0
$t_3$ ( $MeV fm^{3(\gamma+1)}$ )	9955.2	$g_\sigma$	10.2169
$x_3$	-0.1180	$g_\omega$	12.8675
$W$ (MeV)	-589.09	$g_\rho$	8.9488
$B$ (MeV)	130.36	$g_2$ ( $fm^{-1}$ )	-10.4307
$H$ (MeV)	-272.42	$g_3$	28.8851
$M$ (MeV)	-192.16		
$\alpha$ (fm)	0.7596		
$W_0$ (MeV)	115.0		
Nuclear matter			
$\rho_o$ ( $fm^{-3}$ )	0.157	$\rho_o$ ( $fm^{-3}$ )	0.148
$e(\rho_0)$ (MeV)	-16.0	$e(\rho_0)$ (MeV)	-16.24
$E_s$ (MeV)	35.0	$E_s$ (MeV)	37.4
$K_0$ (MeV)	245	$K_0$ (MeV)	271.5

density is expressed as [46, 47],

$$\begin{aligned}
L = & \bar{\psi}_i \{ i\gamma^\mu \partial_\mu - M \} \psi_i + \frac{1}{2} \partial^\mu \sigma \partial_\mu \sigma - \frac{1}{2} m_\sigma^2 \sigma^2 - g_\sigma \bar{\psi}_i \psi_i \sigma - \frac{1}{4} \Omega^{\mu\nu} \Omega_{\mu\nu} + \frac{1}{2} m_w^2 V^\mu V_\mu \\
& - g_w \bar{\psi}_i \gamma^\mu \psi_i V_\mu - \frac{1}{4} \vec{B}^{\mu\nu} \cdot \vec{B}_{\mu\nu} + \frac{1}{2} m_\rho^2 \vec{R}^\mu \cdot \vec{R}_\mu - g_\rho \bar{\psi}_i \gamma^\mu \vec{\tau} \psi_i \cdot \vec{R}_\mu - \frac{1}{2} m_\delta^2 \delta^2 + g_\delta \bar{\psi}_i \delta \vec{\tau} \psi_i.
\end{aligned} \tag{2.2}$$

Here  $M$ ,  $m_\sigma$ ,  $m_\omega$  and  $m_\rho$  are the masses for nucleon,  $\sigma$ -,  $\omega$ - and  $\rho$ -mesons and  $\psi$  is the Dirac spinor. The field for the  $\sigma$ -meson is denoted by  $\sigma$ ,  $\omega$ -meson by  $V_\mu$  and  $\rho$ -meson by  $R_\mu$ . The parameters  $g_s$ ,  $g_\omega$ ,  $g_\rho$  and  $e^2/4\pi=1/137$  are the coupling constants for the  $\sigma$ ,  $\omega$ ,  $\rho$ -mesons and photon respectively.  $g_2$  and  $g_3$  are the self-interaction coupling constants for  $\sigma$  mesons. By using the classical variational principle we obtain the field equations for the nucleons and mesons. A static solution is obtained from the equations of motion to describe the ground state properties of nuclei. The set of nonlinear coupled equations are solved self-consistently [48]. The total energy of the system is given by

$$E_{total} = E_{part} + E_\sigma + E_\omega + E_\rho + E_c + E_{pair} + E_{c.m.}, \tag{2.3}$$

where  $E_{part}$  is the sum of the single particle energies of the nucleons and  $E_\sigma$ ,  $E_\omega$ ,  $E_\rho$ ,  $E_c$ ,  $E_{pair}$ ,  $E_{cm}$  are the contributions of the meson fields, the Coulomb field, pairing energy and the center-of-mass motion correction energy, respectively. We have used the well known NL3 parameter set [49] in our calculations for RMF formalism.

### 2.2.3 Pairing Correlation

To take care of the pairing correlation for open shell nuclei the constant gap, BCS-approach is used in our calculations. The pairing energy expression is written as

$$E_{pair} = -G \left[ \sum_{i>0} u_i v_i \right]^2, \tag{2.4}$$

with  $G$  is the pairing force constant. The quantities  $v_i^2$  and  $u_i^2 = 1 - v_i^2$  are the occupation probabilities [50–52]. The variational approach with respect to  $v_i^2$  gives the BCS equation

$$2\epsilon_i u_i v_i - \Delta(u_i^2 - v_i^2) = 0, \tag{2.5}$$

using  $\Delta = G \sum_{i>0} u_i v_i$ . The occupation number is defined as

$$n_i = v_i^2 = \frac{1}{2} \left[ 1 - \frac{\epsilon_i - \lambda}{\sqrt{(\epsilon_i - \lambda)^2 + \Delta^2}} \right]. \quad (2.6)$$

The chemical potentials  $\lambda_n$  and  $\lambda_p$  are determined by the particle number for protons and neutrons. The pairing energy is computed as  $E_{pair} = -\Delta \sum_{i>0} u_i v_i$ . For a particular value of  $\Delta$  and  $G$ , the pairing energy  $E_{pair}$  diverges if it is extended to an infinite configuration space. In fact, in all realistic calculations with finite range forces,  $\Delta$  decreases with state for large momenta near the Fermi surface. In the present case, we assume equal pairing gap for all states  $|\alpha\rangle = |nljm\rangle$  near the Fermi surface. We use a pairing window, where the equations are extended up to the level  $\epsilon_i - \lambda \leq 2(41A^{1/3})$ . The factor 2 has been determined so as to reproduce the pairing correlation energy for neutrons in  $^{118}\text{Sn}$  using Gogny force [6, 50, 51].

## 2.3 Results and Discussions

The quasi local Density Functional Theory (DFT) is used in this work, which is similar to the one used by Hoffman and Lenske in Ref. [29]. The total energy is nothing but the sum of the energy density contribution from different components of the interaction along with spin-orbit and Coulomb term. The energy density  $\mathcal{H}_0$  for SEI set can be expressed as

$$\mathcal{H}_0 = \frac{\hbar^2}{2m} (\tau_n + \tau_p) + \mathcal{H}_d^{Nucl} + \mathcal{H}_{exch}^{Nucl} + \mathcal{H}^{SO} + \mathcal{H}^{Coul}. \quad (2.7)$$

From this effective Hamiltonian  $\tilde{H}$  we obtain the quasi local energy functional as:

$$\varepsilon_0 [\rho^{QL}] = \int \mathcal{H}_0 d^3 R. \quad (2.8)$$

The equations solved self-consistently to get the solution for nucleonic system. Here we have taken only spherical solution for both RMF and SEI.

### 2.3.1 Ground state binding energy

The main objective of the present study is to find the double shell closure in the superheavy valley. In this context, we have concentrated on few observable such as



Table 2.2: The binding energy (BE) obtained from SEI calculation is compared with the RMF(NL3) [33], finite range droplet model (FRDM) [39] and with experimental data of some of the known super-heavy nuclei. The BE is in MeV.

Element	BE			
	SEI	RMF(NL3)	FRDM	Expt.
$^{258}Md$	1896.19	1897.70	1911.53	1911.69
$^{258}Rf$	1884.95	1890.86	1905.25	1904.69
$^{261}Rf$	1906.38	1911.04	1924.28	1923.93
$^{259}Db$	1886.94	1894.58	1907.00	1906.33
$^{260}Db$	1894.31	1901.4	1913.34	1912.82#
$^{260}Sg$	1888.62	1897.9	1909.90	1909.07
$^{261}Sg$	1896.17	1905.02	1916.27	1915.68
$^{264}Hs$	1906.86	1915.5	1927.62	1926.77
$^{265}Hs$	1914.59	1922.9	1934.40	1933.50
$^{269}Ds$	1932.81	1941.21	1952.06	1950.290
$^{285}Fl$	2029.41	2039.19	2044.12	2040.03#
$^{286}Fl$	2036.74	2046.17	2051.59	2047.474#
$^{287}Fl$	2043.36	2052.50	2057.65	2053.19#
$^{288}Fl$	2050.14	2058.73	2065.01	2060.64#
$^{289}Fl$	2056.80	2064.87	2071.04	2066.06#

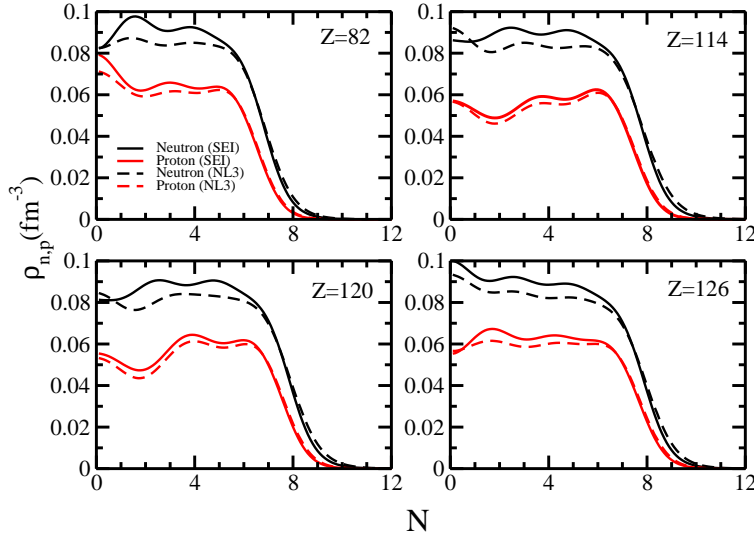


Figure 2.1: The ground state densities with SEI for  $^{208}\text{Pb}$ ,  $^{298}114$ ,  $^{304}120$  and  $^{310}126$  are compared with the RMF(NL3) results.

separation energy  $S_{2n}$ , chemical potential  $\mu_n$ , single-particle levels  $\mathcal{E}_{n,p}$  and pairing energy  $E_{pair}$ . Before going to this unknown region (super-heavy valley), it is important to test our model for known nuclei, which are experimentally and theoretically well established. We calculate the binding energy of few known super-heavy nuclei using SEI. The obtained results are compared with RMF, finite-Range-Droplet-Model (FRDM) [53] and experimental data [54] in Table 2.2. The # marks in the experimental column are for the extrapolated data from Ref [54]. From the table, we find that the SEI and NL3 results are slightly overestimated to the experimental values. A close observation of the table shows the superiority of FRDM over SEI or NL3 for lighter masses of the super-heavy nuclei. In contrast to the lighter region, the SEI predicts better results for heavier isotopes. For example, binding energy of  $^{289}\text{Fl}$  is 2056.80 MeV in SEI, whereas the values are 2064.87, 2071.04 and 2066.06 MeV in RMF(NL3), FRDM and experiment (or systematic), respectively. Based on this trend, one can expect that the prediction of SEI gives us better insight about the magic structures of super-heavy nuclei in heavier mass region, which is the main objective of this present investigation.

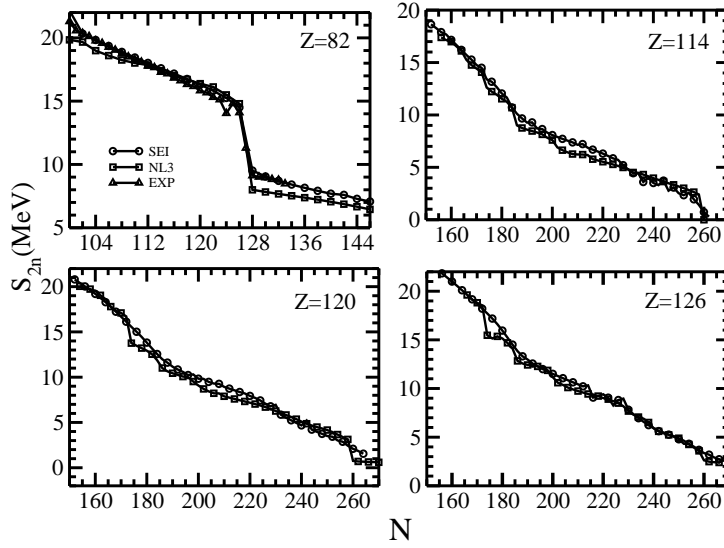


Figure 2.2: The two neutron separation energy obtained from NL3 and SEI for  $^{208}\text{Pb}$ ,  $^{298}_{114}$ ,  $^{304}_{120}$  and  $^{310}_{126}$ .

### 2.3.2 Density distribution of Neutrons and Protons

After convinced with the binding energy of the super-heavy nuclei, we present the density distribution of protons and neutrons in Fig. 2.1. The densities are compared with the RMF(NL3) calculations. In general, the RMF and SEI densities are almost similar with each other. However, a proper inspection reveals that the SEI densities slightly over estimate the RMF(NL3) densities. This overestimation is mostly at the middle region of the nucleus. The humps at the central region for both the densities show shell effect for all nuclei shown in the figure.

### 2.3.3 Two neutron separation energy and location of closed shell

From the binding energy, we have calculated the two neutron separation energy using the relation  $S_{2n}(N, Z) = BE(N, Z) - BE(N - 2, Z)$ . The  $S_{2n}$  for all the four isotopic chains are shown in Fig. 2.2 as a function of neutron numbers. In case of Pb isotopes, the sudden decrease of  $S_{2n}$  at neutron number  $N=126$ , is the well known neutron magic number for the largest known  $Z=82$  magic nucleus. The analysis is extended to the recently predicted proton magic numbers like  $Z=114$ , 120 and 126, which are

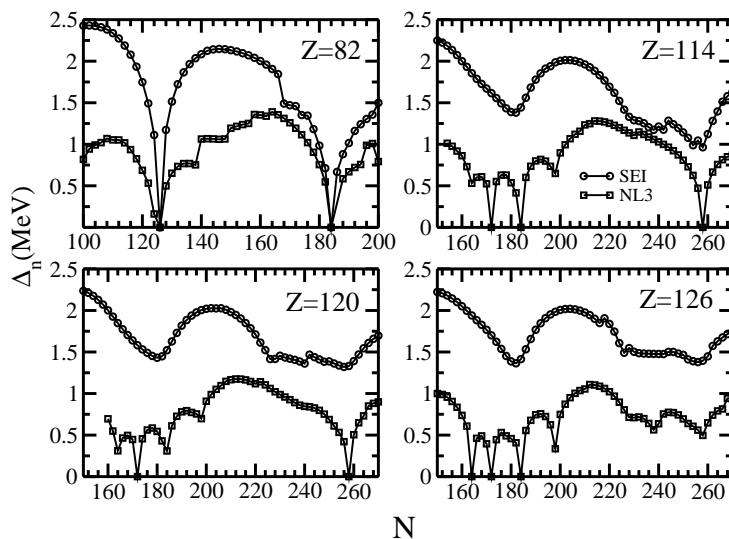


Figure 2.3: The calculated pairing gap of neutron  $\Delta_n$  with SEI for the isotopic series  $Z=82$ , 114, 120 and 126 are compared with the NL3 results.

currently under scrutiny for their confirmation.

It is important to mention that, the next proton magic number beyond  $Z=82$  would be  $Z=126$  considering the traditional proton and neutron magic numbers for known closed shell nuclei [55, 56]. However, several microscopic calculations [57–62] suggest a shift of this number to 114. One of the cause of the shift is the Coulomb effect on the spherical single particle levels. The use of shell correction by V. M. Strutinsky [63] to the liquid-drop calculation of binding energy (BE) opens a more satisfactory exploration towards the search of double closed nucleus beyond  $^{208}\text{Pb}$ . Using this approach,  $Z=114$  is supported to be the proton magic after 82 [64–67], which was regarded as the magic number in the super-heavy valley [68] with  $N=184$  as the corresponding neutron magic number. However, the recent relativistic mean field calculations using various force parameters [69], predict  $Z=120$  as the next magic number with  $N=172/182$  as the neutron closed shell. Contrary to all these predictions, some non-relativistic calculations reported  $Z=126$  as the next magic proton in the super-heavy valley. The microscopic calculations using Skyrme Hartree-Fock formalism predict  $N=182$  as the next neutron closed shell after  $N=126$ , which differs by 2 unit from other predictions [69].

Analyzing the  $S_{2n}$  energy for the isotopic chain of  $Z=82$ , 114, 120 and 126, the sharp fall of  $S_{2n}$  at  $N=126$  is a clear evidence of magic combination of  $Z=82$  and

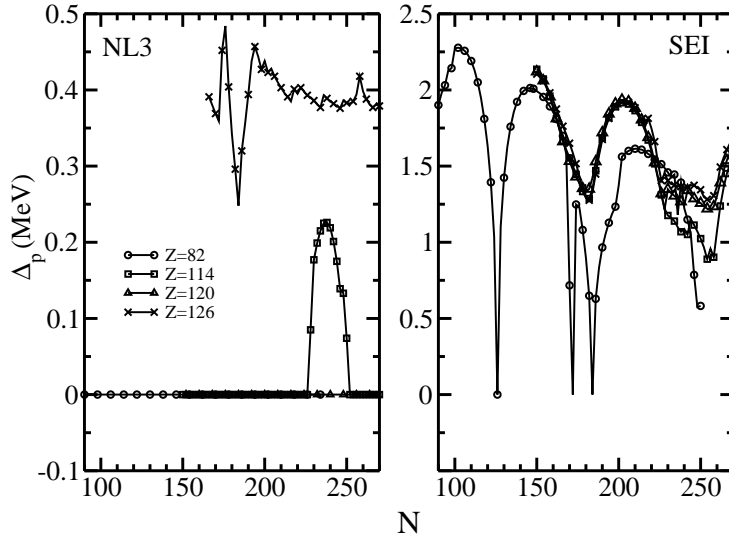


Figure 2.4: (a) The pairing gap of proton  $\Delta_p$  with SEI for the isotopic series  $Z=82$ , 114, 120 and 126 compared with the NL3 results.

$N=126$ . Our newly developed SEI model and previously existing NL3 follow the same trend as experiment. But whenever we analyzed the plots of  $Z=114$ , 120 and 126, we find a slight difference in these two models (SEI and RMF). In RMF(NL3), when we go from one magic neutron number to the next one, the  $S_{2n}$  energy suddenly decreases to a lower value, which reflect in Fig. 2.2. In SEI, the  $S_{2n}$  energy follows same pattern but the magnitude of decreases some how less.

### 2.3.4 Pairing gaps and pairing energy

Another important quantity, which helps us to locate the closed shell is the pairing gaps of proton and neutron in a constant force BCS calculation. Here, we calculate the pairing gap for the isotopic chain of  $Z=82$ , 114, 120 and 126 and locate the minimum values of  $\Delta_n$  and  $\Delta_p$ . The results are depicted in Figs. 2.3 and 2.4 and also compared with the RMF(NL3) force. It is well known that NL3 force satisfies this criteria for the location of magicity [23, 69]. Although, SEI overestimates the pairing gaps of  $\Delta_n$ ,  $\Delta_p$ , the trend for both NL3 and SEI are found to be similar. Consistence with NL3 results as well as with earlier calculations with a variety of force parameters, our present SEI reproduces minima at  $N=182/184$  and  $Z=120$  and to some extent at  $Z=114$ .

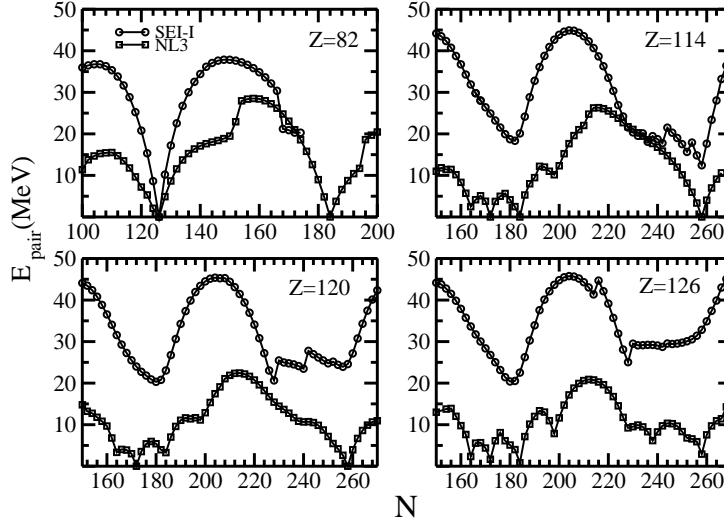


Figure 2.5: The pairing energy as a function of neutron number for  $Z=82$ , 114, 120 and 126 with SEI and NL3 forces.

To see the trend of pairing energy  $E_{pair}$  at the discussed neutron number  $N=184$ , we plot  $E_{pair}$  as a function of neutron number  $N$  in Fig. 2.5. Surprisingly, we get almost zero pairing energy at  $N=126$  for  $Z=82$  isotopic case. The formalism is extended to  $Z=114$ , 120 and 126 cases. We find minimum or zero  $E_{pair}$  at  $N=182/184$  confirming the earlier predictions of this neutron magic number at  $N=182/184$  [69]. Qualitatively, the SEI interaction follows the trend of RMF(NL3) as shown in Fig. 2.5, but fails when we have a quantitative estimation. For example, the  $\Delta_n$  or  $E_{pair}$  at  $N=182/184$  is minimum but has a finite value unlike to the NL3 prediction, which has zero value. As a matter of fact, the validity of pairing scheme to this region of nuclei may not be 100 % applicable. The improvement of pairing is needed to keep the value of  $\Delta_n$  and  $\Delta_p$  zero at the appropriate magic number.

### 2.3.5 Chemical energy and stability

The stability of an element not only depends on its binding energy and shell structure, but also very much affected by the chemical potential  $\mu$ . For a bound nucleus, both the chemical potentials of protons  $\mu_p$  and neutrons  $\mu_n$  must be negative. To realize the relative stability from chemical point of view, we have plotted  $\mu_p$  and  $\mu_n$  with

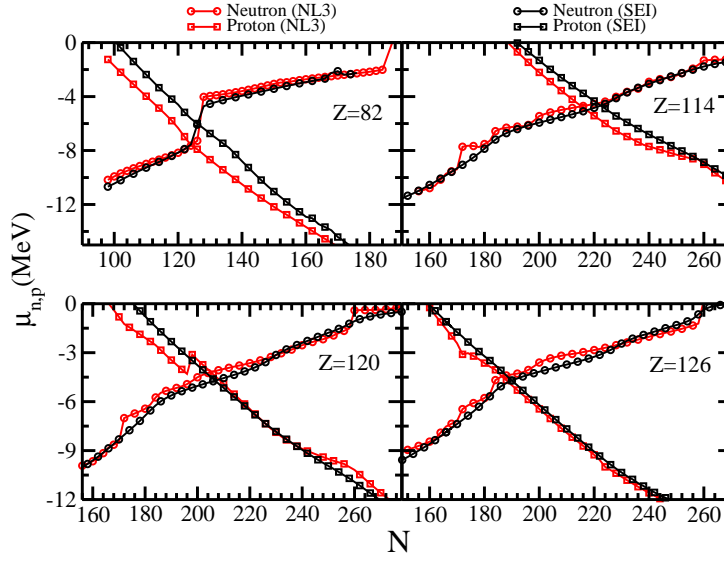


Figure 2.6: Systematic of chemical energy  $\mu_n$  and  $\mu_p$  as a function of neutron number for  $Z=82$ , 114, 120 and 126 with SEI and NL3 sets.

neutron number in Fig. 2.6. The results are also compared with the  $\mu$ -value of NL3 set. In both the cases, we find similar chemical potential. In some previous papers it is suggested that we can take  $N=172$  as magic number for neutron. But our SEI model shows that the combination  $Z=120$  and  $N=172$  is strictly not allowed. Because in this case  $\mu_p = 0.69$  MeV, which gives proton instability. However NL3 result shows this combination is a loosely bound system having  $\mu_n = -1.240$  MeV and  $\mu_p = -7.007$  MeV. Although the  $BE/A$  curve shows a local maximum at  $Z=114$  and  $N=172$  in SEI model, we can not take this as a stable system because of  $\Delta_n$  and  $\Delta_p$  value, which does not show any signature of stability. The SEI model gives a clear picture that the isotope  $^{302}120$  can be a suitable combination for the next double closed nucleus. One can justify it by analysis of  $BE/A$  data of  $^{302}120$ . For example  $BE/A = 7.007$  MeV which create a local maxima in its neighborhood for  $^{302}120$ . In the same time, the optimum negative value of chemical potential energies of  $\mu_n$  and  $\mu_p$  gives a sign of maximum stability. A similar analysis of numerical data for  $\mu_p$  of isotopes of  $Z=126$  shows that there is no reason of taking  $Z=126$  and  $N=182/184$  as a stable combination. This is because of the positive value of  $\mu_p$  (1.36) MeV.

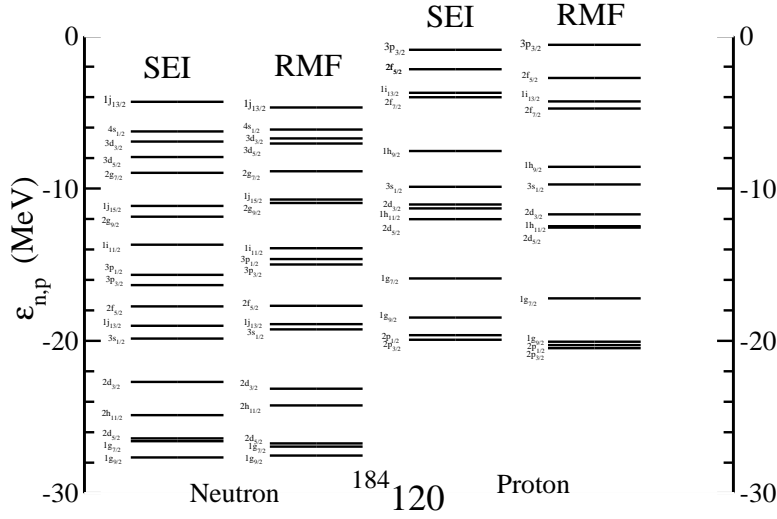


Figure 2.7: The single particle energy levels for  $^{304}120$  with NL3 and SEI parametrization.

### 2.3.6 Single particle energy

The single particle energies for  $^{304}120$  with NL3 and SEI for proton and neutron are shown in Fig. 2.7. The single particle solutions are obtained without including the pairing correlation into account to intact the degeneracy of the levels. The calculation of single particle energies of SEI with pairing shows that the degeneracy of the energy levels are not invariant. The basic cause of this discrepancy is the over estimation of our pairing strength in SEI model which may be an interesting analysis for pairing in future. The filling up single particle energy levels for neutrons in SEI with pairing is different from that of without pairing. The energy levels without pairing are given by [178]  $(3d_{3/2})^4$ ,  $(4s_{1/2})^2$  while the same with pairing are [178]  $(3d_{3/2})^3$ ,  $(4s_{1/2})^1$ ,  $(1j_{11/2})^2$ . That means an empty orbital is created at  $4s_{1/2}$  and occupied in  $1j_{11/2}$ . We have also analyzed the single particle levels for  $^{302}120$ , which is not given in the figure. From the anatomy of single particle energies for neutron and proton  $\epsilon_n$  and  $\epsilon_p$ , we find large gaps at neutron number  $N=184$  and proton number  $Z=120$ . The value of neutron gap at  $N=184$  is  $1.949 \text{ MeV}$  and that of proton is  $1.275 \text{ MeV}$  for the last occupied and first unoccupied nucleon. On the other hand the neutron and proton gap for  $^{302}120$  are respectively  $\sim 0.6$  and  $\sim 1.663 \text{ MeV}$ . The above data say the energy gaps for the neutron and proton in  $^{304}120$  are greater than the gap in  $^{302}120$ . This give us an indication to take the combination  $N=184$  and  $Z=120$  as the next



magic nucleus. From the analysis of single particle energy level of  $^{304}120$  with NL3 parameter set one can see the neutron and proton gaps are 1.4503 MeV and 2.1781 MeV respectively for the last occupied and first unoccupied nucleon. The RMF(NL3) and SEI data are comparable with each other.

## 2.4 Summary and Conclusions

In summery, we have calculated the binding energy,  $S_{2n}$  energy, single particle levels, pairing gaps and chemical potential, in the isotopic chain of  $Z=82, 114, 120$  and  $126$ . All our calculations are done in the frame work of SEI interaction. We have compared our results with standard RMF (NL3) parameter. Over all discussion and analysis of all possible evidences of shell closure property show that, one can take  $Z=120$  and  $N=182$  as the next magic combination beyond  $Z = 82$  and  $N = 126$ , which is different from Skyrme, Gogny and RMF(NL3) by two unit. However on the basis of single particle energy levels, the preferred gap is at  $N=184$  which is consistent with these (Skyrme, Gogny and RMF) force parameters. This happens due to the overestimation of pairing strength.

## Chapter 3

# Monopole resonance in drip-line and super heavy region.

In last chapter we discussed the magic properties of the super heavy and drip-line nuclei, which is prominently based on single particle nature of the nuclear system. Like the single particle state, the collective states are also equally responsible for the structure of the finite nucleus. Many information about the nuclear structure can be obtained from the collective excitation like the giant monopole, dipole, and quadrupole oscillations. Out of all collective excitation, isoscalar monopole and isovector dipole are most important for the nuclear structure physics. These are also known as the squeezing mode of oscillation. In isoscalar monopole resonance (ISGMR) the protons and neutrons vibrate in a phase to each other. It is also known as the breathing mode of oscillation. This collective mode is related to the incompressibility of finite nuclear system and using leptodermous expansion one can get the information about the infinite nuclear matter incompressibility ( $K_\infty$ ) from the finite one.  $K_\infty$  is one of the fundamental properties of the equation of state, which decides the mass and radius of the neutron star. The general assumption is that a heavy finite nuclear system has a great resembles with the infinite nuclear matter. So the study of the incompressibility and excitation energy of heavy and drip line nuclei become important. We study the isoscalar giant monopole resonance for drip-lines and super heavy nuclei in the framework of relativistic mean field theory with a scaling approach. The well-known extended Thomas-Fermi approximation in the nonlinear  $\sigma$ - the  $\omega$  model is used to

estimate the giant monopole excitation energy for some selected light spherical nuclei starting from the region of a proton to neutron drip-lines. The application is extended to the super heavy region for  $Z=114$  and  $120$ , which are predicted by several models as the next proton magic numbers beyond  $Z=82$ . We compared the excitation energy obtained by four successful force parameters NL1, NL3, NL3\*, and FSUGold.

### 3.1 Introduction

The study of nuclei far away from the drip-lines has a current research interest due to their very different properties from nuclei at the  $\beta$ -stability valley. New properties of these nuclei like the soft giant resonance, change of magic number, halo and skin structures, and new decay modes stimulate strongly research using radioactive ion beams (RIB) [70, 71]. On the other hand, super heavy nuclei which are on the stability line, but extremely unstable due to excessive Coulomb repulsion, attract much theoretical attention for their resemblance to the highly asymmetric nuclear matter limit [68, 72]. These nuclei possess a large amount of collective excitation and their study along an isotopic chain is more informative for the structural evaluation of astrophysical objects like neutron stars [73]. Also, the nuclear symmetry energy, and consequently the proton to neutron ratio, are crucial factors in constructing the equation of state (EOS) for asymmetric nuclear matter [74].

The incompressibility  $K_A$  of a nuclear system depends on its neutron-proton asymmetry. It is also well known that the EOS of a highly asymmetric and dense object like a neutron star is substantially influenced by its incompressibility. Although the incompressibility at various asymmetries is an important quantity, it is not a direct experimental observable. Thus, one has to determine the  $K_A$  from a linked experimental quantity (which is directly or indirectly related to  $K_A$ ) like isoscalar giant monopole resonance (ISGMR) [75, 76]. The ISGMR is a well-defined experimental observable, which can be measured precisely through various experimental techniques. The drip-lines and super heavy nuclei are vulnerable and unstable in nature, because of the presence of excess neutrons and large number of protons, respectively. Thus, it is instructive to know the giant monopole resonance, incompressibility modulus, and other related quantities for both drip-lines and super heavy nuclei. In this context,

our aim is to study the giant monopole excitation energy and the incompressibility of finite nuclei near the drip-line [71] as well as for recently discussed super heavy nuclei with proton numbers  $Z=114$  and  $120$ , which are predicted to be the next magic numbers beyond  $Z=82$  with various models [23, 77]. In addition, the calculations of Refs. [78, 79] suggest that these nuclei possess spherical ground state or low-lying spherical excited solutions. More specifically, we aimed to study the following within the frame-work of an extended relativistic Thomas-Fermi approximation:

- How the isoscalar excitation energy and the finite nuclear incompressibility vary in an isotopic chain in drip-lines and super heavy nuclei within a well-tested model like the relativistic extended Thomas-Fermi approximation using scaling and constrained approaches which were developed by some of us recently [80, 81].
- A comparative study of ISGMR obtained with various parameter sets, originated from several interactions, such as NL1, NL3, NL3\*, and FSUGold for the same drip-lines and super heavy nuclei. The large variation in nuclear matter incompressibility starting from  $K_\infty \sim 211.7 - 271.76$  MeV will give us an idea about the prediction of ISGMR with different values of  $K_\infty$ .
- The resonance widths  $\Sigma$ , which are mostly the difference between the scaling and constraint excitation energies are analyzed in the isotopic chains of light and super heavy nuclei.
- The relation between the finite nuclear incompressibility with the infinite nuclear matter values in various force parameter sets are looked for.
- Finally, We applied the scaling and constrained method for Cd and Sn isotopes and compared with the excitation energy with moments ratio  $\sqrt{\frac{m_3}{m_1}}$  and  $\sqrt{\frac{m_1}{m_{-1}}}$  obtained from multipole-decomposition analysis (MCA).

In relativistic mean field (RMF) formalism, the NL1 parameter set [82] has been considered for a long time to be one of the best interactions to predict the experimental observable. The excessively large value of the asymmetry coefficient  $J \sim 43.6$  MeV brings into question the accuracy of the prediction of neutron radius near the drip-line. As a result, the discovery of the NL3 parameter set [49] complements the

limitations of the NL1 force and evaluates the ground state properties of finite nuclei in excellent agreement with experiment [49,83–87]. It reproduces the proton or charge radius  $r_{ch}$  precisely along with the ground state binding energy. Unfortunately, the experimental data for neutron radius has a large error bar [88], which covers most of the prediction of all relativistic and non-relativistic models [89]. The FSUGold parameter set [90,91] reproduces the ISGMR pretty well with the experimental data for  $^{90}\text{Zr}$  and  $^{208}\text{Pb}$ . There is also a possibility to solve the problem of the uncertainty in neutron radius [92] using this interaction. The NL3\* force parametrization [93] is claimed to be an improved version of NL3 to reproduce the experimental observable. We used all these forces and made a comparison of their predictive power for various experimental data. Then we selected NL3 as a suitable parameter set for our further investigations for ISGMR and related quantities. This chapter is organized as follows: In section 3.2, we outline in brief the formalism used in the present work. In section 3.3, we discuss our results for the ground state properties and isoscalar giant monopole resonance (ISGMR) for drip-lines and super heavy nuclei. The isoscalar monopole excitation energy  $E_x$  and the incompressibility modulus of finite nuclei  $K_A$  are also analyzed. We give the summary and concluding remarks in section 3.6

## 3.2 The Formalism

We use the principle of scale invariant to obtain the virial theorem for the relativistic mean field theory in the relativistic Thomas–Fermi (RTF) and relativistic extended Thomas-Fermi (RETF) approximations [80, 94–98]. Although the scaling and constrained calculations are not new, the present technique was developed first by Patra et al [80] and not much has been explored for various regions of the periodic chart. Thus, it is interesting to apply the model specially for drip-lines and super heavy nuclei. The calculations will explore the region ranging from  $Z=8$  to  $Z=114, 120$ , where we can simulate the properties of neutron matter from the neutron-rich finite nuclei. For this purpose, we compute moments and average excitation energies of the isoscalar giant monopole resonance (ISGMR) through scaling and constrained self-consistent calculations for the ground state.

The detailed formalism of the scaling method is given in Refs. [80, 81]. For completeness, we have outlined briefly some of the essential expressions which are needed for the present purpose. We have worked with the non-linear Lagrangian of Boguta and Bodmer [99] to include the many-body correlation which arises from the non-linear terms of the  $\sigma$ -meson self-interaction [100] for a nuclear many-body system. The nuclear matter incompressibility  $K_\infty$  is also reduced dramatically by the introduction of these terms, which motivate us to work with this non-linear Lagrangian. We have also included the self-coupling of the vector  $\omega$ -meson ( $aV^4$ ) and the cross-coupling of the  $\omega$ - and  $\rho$ -mesons  $\Lambda R^2 V^2$  in the Lagrangian. The terms  $aV^4$  and  $\Lambda R^2 V^2$  are very important in the equations of state [87] and symmetry energy [90] for nuclear systems. The relativistic mean field Hamiltonian for a nucleon-meson interacting system is written as [80]:

$$\begin{aligned} \mathcal{H} = & \sum_i \varphi_i^\dagger \left[ -i\vec{\alpha} \cdot \vec{\nabla} + \beta m^* + g_v V + \frac{1}{2} g_\rho R \tau_3 + \frac{1}{2} e \mathcal{A} (1 + \tau_3) \right] \varphi_i + \frac{1}{2} \left[ (\vec{\nabla} \phi)^2 + m_s^2 \phi^2 \right] \\ & + \frac{1}{3} b \phi^3 + \frac{1}{4} c \phi^4 - \frac{1}{2} \left[ (\vec{\nabla} V)^2 + m_v^2 V^2 \right] - \frac{1}{2} \left[ (\vec{\nabla} R)^2 + m_\rho^2 R^2 \right] - \frac{1}{2} \left( \vec{\nabla} \mathcal{A} \right)^2 + a V^4 \\ & + \Lambda R^2 V^2. \end{aligned} \quad (3.1)$$

All the terms in the above Hamiltonian represent their usual meaning, which have already discussed in the chapter 2. Here we have added two new coupling constants, one is self-coupling of the vector meson  $\omega$  and other is the cross-coupling of the  $\omega$  and  $\rho$ -meson, which are represented by  $a = \frac{\zeta_0}{24} g_v^4$ , and  $\Lambda = \Lambda_V g_\rho^2 g_v^2$ , respectively. By using the classical variational principle we obtain the field equations for the nucleons and mesons. In semi-classical approximation all the terms containing single particle wave-function converted to their corresponding density form and the above Hamiltonian can be written in terms of density as:

$$\mathcal{H} = \mathcal{E} + g_v V \rho + g_\rho R \rho_3 + e \mathcal{A} \rho_p + \mathcal{H}_f, \quad (3.2)$$

where

$$\mathcal{E} = \sum_i \varphi_i^\dagger \left[ -i\vec{\alpha} \cdot \vec{\nabla} + \beta m^* \right] \varphi_i = \mathcal{E}_0 + \mathcal{E}_2, \quad (3.3)$$

$$\rho_s = \sum_i \varphi_i^\dagger \varphi = \rho_{s0} + \rho_{s2}, \quad (3.4)$$

$$\rho = \sum_i \bar{\varphi}_i \varphi_i, \quad (3.5)$$

$$\rho_3 = \frac{1}{2} \sum_i \varphi_i^\dagger \tau_3 \varphi_i, \quad (3.6)$$

and  $\mathcal{H}_f$  is the free part of the Hamiltonian, contains the free meson contribution.  $\mathcal{E}_2$  and  $\rho_{s2}$  correspond to the  $\hbar^2$  correction to the energy and scalar density, respectively. These terms are considered as the extension of Thomas-Fermi approximation and known as the extended Thomas-Fermi (ETF) approach. In Thomas-Fermi approach, the density is considered as locally constant (only depends on the position co-ordinate) but in extended Thoms-Fermi approach, the density contains the terms, which are function of position as well as the derivative at that point. This ETF is considered as one step forward to TF approach to explain the real nuclear system, where the variation of density takes place on the surface of a finite nucleus. The complete expression for these quantities is found in [80,81]. The total density  $\rho$  is the sum of the proton  $\rho_p$  and neutron  $\rho_n$  densities. The semi-classical ground-state meson fields are obtained by solving the Euler-Lagrange equations  $\delta\mathcal{H}/\delta\rho_q = \mu_q$  ( $q = n, p$ ).

$$(\Delta - m_s^2)\phi = -g_s\rho_s + b\phi^2 + c\phi^3, \quad (3.7)$$

$$(\Delta - m_v^2)V = -g_v\rho - 4aV^4 - 2\Lambda R^2V, \quad (3.8)$$

$$(\Delta - m_\rho^2)R = -g_\rho\rho_3 - 2\Lambda RV^2, \quad (3.9)$$

$$\Delta\mathcal{A} = -e\rho_p. \quad (3.10)$$

The above field equations are solved self-consistently in an iterative method. The pairing correlation is not included in the evaluation of the equilibrium properties including the monopole excitation energy. The Thomas-Fermi approach is a semi-classical approximation and pairing correlation has a minor role in giant resonance.

It is shown in [101, 102] that the pairing has a marginal effect on the ISGMR energy, and only for open-shell nuclei. As far as pairing correlation is concerned, it is a quantal effect and can be included in a semi-classical calculation as an average, as is adopted in semi-empirical mass formula. In Ref. [102], perturbative calculation on top of a semi-classical approach is done, and it suggests that pairing correlation is not important in such approaches like relativistic Thomas-Fermi (RTF) or relativistic extended Thomas-Fermi (RETF) approximations. In our present calculations, the scalar density ( $\rho_s$ ) and energy density ( $\mathcal{E}$ ) are calculated using RTF and RETF formalism. The RETF is the  $\hbar^2$  correction to the RTF, where the gradient of density is taken into account. This term of the density takes care of the variation of the density and involves more of the surface properties. Now transforming the term  $(\nabla V)^2 + m_v^2 V^2$  into  $V(-\Delta + m_v^2)V = -g_v V \rho$  (similarly for other fields), we can write the Hamiltonian as

$$\mathcal{H} = \mathcal{E} + \frac{1}{2}g_s\phi\rho_s^{eff} + \frac{1}{3}b\phi^3 + \frac{1}{4}c\phi^4 + \frac{1}{2}g_v V\rho + \frac{1}{2}g_\rho R\rho_3 + \frac{1}{2}e\mathcal{A}\rho_p - aV^4 - \Lambda R^2V^2, \quad (3.11)$$

with

$$\rho_s^{eff} = g_s\rho_s - b\phi^2 - c\phi^3. \quad (3.12)$$

In order to study the monopole vibration of the nucleus, we have scaled the baryon density [80]. The normalized form of the scaled baryon density is given by

$$\rho_\lambda(\mathbf{r}) = \lambda^3\rho(\lambda r), \quad (3.13)$$

where  $\lambda$  is the collective co-ordinate associated with the monopole vibration. The other quantities are scaled like

$$K_{Fq\lambda} = [3\pi^2\rho_{q\lambda}(\mathbf{r})]^{\frac{1}{3}} = \lambda K_{Fq}(\lambda r), \quad (3.14)$$

$$\tilde{m}_\lambda^*(r) = m - g_s\phi_\lambda(r)m_\lambda^*(r) \equiv \lambda\tilde{m}^*(\lambda r), \quad (3.15)$$

where  $\tilde{m}^{**}$  carries implicit dependence of  $\lambda$  apart from the parametric dependence of  $\lambda r$ .

$$\mathcal{E}_\lambda(\mathbf{r}) \equiv \lambda^4\tilde{\mathcal{E}}(\lambda\mathbf{r}) = \lambda^4[\tilde{\mathcal{E}}_0(\lambda\mathbf{r}) + \tilde{\mathcal{E}}_2(\lambda\mathbf{r})], \quad (3.16)$$



$$\rho_{s\lambda}(\mathbf{r}) \equiv \lambda^3 \tilde{\rho}_s(\lambda \mathbf{r}). \quad (3.17)$$

Similarly, the  $\phi$ ,  $V$ ,  $R$  and Coulomb fields are scaled due to the self-consistency Eq. 3.7-3.10. But the  $\phi$  field can not be scaled simply like the density and momentum, because its source term contains the  $\phi$  field itself. Putting in all of the scaled variables one can get the scaled Hamiltonian:

$$\begin{aligned} \frac{\mathcal{H}_\lambda}{\lambda^3} &= \lambda \tilde{\mathcal{E}} + \frac{1}{2} g_s \phi_\lambda \tilde{\rho}_s^{eff} + \frac{1}{3} \frac{b}{\lambda^3} \phi_\lambda^3 + \frac{1}{4} \frac{c}{\lambda^3} \phi_\lambda^4 + \frac{1}{2} g_v V_\lambda \rho + \frac{1}{2} g_\rho R_\lambda \rho_3 + \frac{1}{2} e A_\lambda \rho_p - a \frac{V_\lambda^4}{\lambda^3} \\ &- \frac{\Lambda}{\lambda^3} R_\lambda^2 V_\lambda^2. \end{aligned} \quad (3.18)$$

We know  $\tilde{\rho}_s = \frac{\partial \tilde{\mathcal{E}}}{\partial \tilde{m}^*}$ ,  $\frac{\partial \tilde{\mathcal{E}}}{\partial \lambda} = \frac{\partial \tilde{\mathcal{E}}}{\partial \tilde{m}^*} \frac{\partial \tilde{m}^*}{\partial \lambda} = \rho_s \frac{\partial \tilde{m}^*}{\partial \lambda}$ , and  $\frac{\partial m_\lambda^*}{\partial \lambda} = \lambda \frac{\partial \tilde{m}^*}{\partial \lambda} + \tilde{m}^* = -g_s \frac{\partial \phi_\lambda}{\partial \lambda}$ . Here we are interested in calculating the monopole excitation energy, which is defined as  $E^s = \sqrt{\frac{C_m}{B_m}}$ , where  $C_m$  is the restoring force and  $B_m$  is the mass parameter. In our calculations,  $C_m$  is obtained from the double derivative of the scaled energy with respect to the scaled co-ordinate  $\lambda$  at  $\lambda = 1$  [80]. The first derivative is given by

$$\begin{aligned} \left[ \frac{\partial}{\partial \lambda} \int d\lambda r \frac{\mathcal{H}_\lambda(r)}{\lambda^3} \right]_{\lambda=1} &= \int d\lambda r \left[ \tilde{\mathcal{E}} - \tilde{m}^* \tilde{\rho}_s - \frac{1}{2} g_s \tilde{\rho}_s^{eff} \frac{\partial \phi_\lambda}{\partial \lambda} + \frac{1}{2} g_s \phi_\lambda \frac{\partial \tilde{\rho}_s^{eff}}{\partial \lambda} - \frac{b}{\lambda^4} \phi_\lambda^3 \right. \\ &- \frac{3}{4} \frac{c}{\lambda^4} \phi_\lambda^4 + \frac{1}{2} g_\rho \rho_3 \frac{\partial R_\lambda}{\partial \lambda} + \frac{1}{2} g_v \rho \frac{\partial V_\lambda}{\partial \lambda} + \frac{1}{2} e \rho_p \frac{\partial A_\lambda}{\partial \lambda} - 4a \frac{v_\lambda^3}{\lambda^3} \frac{\partial V_\lambda}{\partial \lambda} + 3a \frac{V_\lambda^4}{\lambda^4} + \frac{3\Lambda}{\lambda^4} R_\lambda^2 V_\lambda^2 \\ &\left. - \frac{2\Lambda}{\lambda^3} R_\lambda^2 V_\lambda \frac{\partial V_\lambda}{\partial \lambda} - \frac{2\Lambda}{\lambda^3} R_\lambda V_\lambda^2 \frac{\partial R_\lambda}{\partial \lambda} \right]_{\lambda=1}. \end{aligned} \quad (3.19)$$

Now consider the field equation for the omega field

$$(\Delta - m_v^2) V = -g_v \rho - 4aV^3 - 2\Lambda R^2 V. \quad (3.20)$$

The scaled equation is

$$\left( \Delta_u - \frac{m_v^2}{\lambda^2} \right) V_\lambda = -\lambda g_v \rho - \frac{4aV_\lambda^3}{\lambda^2} - \frac{2\Lambda}{\lambda^2} R_\lambda^2 V_\lambda, \quad (3.21)$$

where  $u = \lambda r$ . Taking the first derivative with respect to  $\lambda$ , we have

$$\begin{aligned} \left( \Delta_u - \frac{m_v^2}{\lambda^2} \right) \frac{\partial V_\lambda}{\partial \lambda} &= -g_v \rho - \frac{12aV_\lambda^2}{\lambda^2} \frac{\partial V_\lambda}{\partial \lambda} + \frac{8aV_\lambda^3}{\lambda^3} - \frac{2m_v^2 V_\lambda}{\lambda^3} + 4 \frac{\Lambda}{\lambda^3} R_\lambda^2 V_\lambda \\ &- 4 \frac{\Lambda}{\lambda^2} R_\lambda V_\lambda \frac{\partial R_\lambda}{\partial \lambda} - 2 \frac{\Lambda}{\lambda^2} R_\lambda^2 \frac{\partial V_\lambda}{\partial \lambda}. \end{aligned} \quad (3.22)$$

Multiplying  $V_\lambda$  on both the sides and integrating, one can get

$$\begin{aligned} \int d(\lambda r) \frac{\partial V_\lambda}{\partial \lambda} \left( \Delta_u - \frac{m_v^2}{\lambda^2} \right) V_\lambda &= \int d\lambda r \left[ -g_v \rho V_\lambda - \frac{12aV_\lambda^3}{\lambda^2} \frac{\partial V_\lambda}{\partial \lambda} + \frac{8aV_\lambda^4}{\lambda^3} - \frac{2m_v^2 V_\lambda^2}{\lambda^3} \right. \\ &\quad \left. + 4\frac{\Lambda}{\lambda^3} R_\lambda^2 V_\lambda^2 - 4\frac{\Lambda}{\lambda^2} R_\lambda V_\lambda^2 \frac{\partial R_\lambda}{\partial \lambda} - 2\frac{\Lambda}{\lambda^2} R_\lambda^2 \frac{\partial V_\lambda}{\partial \lambda} V_\lambda \right]. \end{aligned} \quad (3.23)$$

Putting the field equation for omega field in the above equation, we get

$$\begin{aligned} \int dr \left[ \frac{1}{2} \rho g_v \frac{\partial V_\lambda}{\partial \lambda} - \frac{4aV_\lambda^3}{\lambda^3} \frac{\partial V_\lambda}{\partial \lambda} \right]_{\lambda=1} &= \int dr \left[ \frac{g_v V_\lambda \rho}{2\lambda} - \frac{4aV_\lambda^3}{\lambda^4} + \frac{m_v^2 V_\lambda^2}{\lambda^4} - 2\frac{\Lambda}{\lambda^4} R_\lambda^2 V_\lambda^2 \right. \\ &\quad \left. + 2\frac{\Lambda}{\lambda^3} R_\lambda V_\lambda^2 \frac{\partial R_\lambda}{\partial \lambda} \right]_{\lambda=1}. \end{aligned} \quad (3.24)$$

Now, consider the field equation for  $R$  field, where we have

$$(\Delta - m_\rho^2)R = -g_\rho \rho_3 - 2\Lambda R V^2. \quad (3.25)$$

By scaling the whole equation with the scaling parameter  $\lambda$ , we get the scaled equation as:

$$(\Delta_u - \frac{m_\rho^2}{\lambda^2})R_\lambda = -g_\rho \lambda \rho_3 - 2\frac{\Lambda R_\lambda V_\lambda^2}{\lambda^2}. \quad (3.26)$$

From the first and second derivative with respect to  $\lambda$  and using a similar procedure for  $\omega$ -field, one can get the following equation

$$(\Delta_u - \frac{m_\rho^2}{\lambda^2}) \frac{\partial R_\lambda}{\partial \lambda} = -g_\rho \rho_3 - 2R_\lambda \frac{m_\rho^2}{\lambda^3} + 4\frac{\Lambda}{\lambda^3} V_\lambda^2 R_\lambda - 4\frac{\Lambda}{\lambda^3} R_\lambda V_\lambda \frac{\partial V_\lambda}{\partial \lambda} - 2\frac{\Lambda}{\lambda^2} V_\lambda^2 \frac{\partial R_\lambda}{\partial \lambda}. \quad (3.27)$$

Substituting the relation of Eq.( 3.9) in ( 3.27) at  $\lambda = 1$ , we get,

$$\int dr g_\rho \frac{1}{2} \rho_3 \frac{\partial R_\lambda}{\partial \lambda} \Big|_{\lambda=1} = \int dr \left[ \frac{1}{2\lambda} g_\rho \rho_3 R_\lambda + \frac{R_\lambda^2 m_\rho^2}{\lambda^4} + 2\frac{\Lambda}{\lambda^4} R_\lambda^2 V_\lambda \frac{\partial V_\lambda}{\partial \lambda} - 2\frac{\Lambda}{\lambda^4} V_\lambda^2 R_\lambda^2 \right]_{\lambda=1}. \quad (3.28)$$

With the help of this expression, Eq.(3.19) becomes

$$\begin{aligned} \left[ \frac{\partial}{\partial \lambda} \int (d\lambda r) \frac{\mathcal{H}_\lambda(r)}{\lambda^3} \right]_{\lambda=1} &= \int d\lambda r \left[ \tilde{\mathcal{E}} - \tilde{m}^* \rho_s - \frac{1}{2} g_s \tilde{\rho}_s^{eff} \frac{\partial \phi_\lambda}{\partial \lambda} + \frac{1}{2} g_s \phi_\lambda \frac{\partial \tilde{\rho}_s^{eff}}{\partial \lambda} \right. \\ &\quad - \frac{b}{\lambda^4} \phi_\lambda^3 - \frac{3}{4} \frac{c}{\lambda^4} \phi_\lambda^4 + g_\rho \rho_3 \frac{1}{2\lambda} R_\lambda + g_v \rho \frac{1}{2\lambda} V_\lambda + e \rho_p \frac{1}{2} \frac{\partial A_\lambda}{\partial \lambda} - a \frac{v_\lambda^3}{\lambda^4} + \frac{m_v^2 V_\lambda^2}{\lambda^4} \\ &\quad \left. + \frac{m_\rho^2}{\lambda^4} R_\lambda^2 - \frac{\Lambda}{\lambda^4} R_\lambda^2 V_\lambda^2 \right]_{\lambda=1}. \end{aligned} \quad (3.29)$$

Again, differentiating w.r.t  $\lambda$  and substituting  $\lambda = 1$ , the restoring force  $C_m$  becomes:

$$\begin{aligned}
C_m = & \left[ \frac{\partial^2}{\partial \lambda^2} \int d\lambda r \frac{\mathcal{H}\lambda(r)}{\lambda^3} \right]_{\lambda=1} = \int d\lambda r \left[ -\tilde{m}^* \frac{\partial \tilde{\rho}_s}{\partial \lambda} - \frac{1}{2} g_s \tilde{\rho}_s^{eff} \frac{\partial^2 \phi_\lambda}{\partial \lambda^2} + \frac{1}{2} g_s \phi_\lambda \frac{\partial^2 \tilde{\rho}_s^{eff}}{\partial \lambda^2} \right. \\
& + 4 \frac{b}{\lambda^5} \phi_\lambda^3 + 3 \frac{c}{\lambda^5} \phi_\lambda^4 - \frac{3}{\lambda^4} (b \phi_\lambda^2 + c \phi_\lambda^3) \frac{\partial \phi_\lambda}{\partial \lambda} + \frac{1}{2\lambda} g_\rho \rho_3 \frac{\partial R_\lambda}{\partial \lambda} + \frac{2}{\lambda^4} m_\rho^2 R_\lambda \frac{\partial R_\lambda}{\partial \lambda} \\
& - \frac{2\Lambda}{\lambda^4} \left( R_\lambda V_\lambda^2 \frac{\partial R_\lambda}{\partial \lambda} \right) + R_\lambda^2 V_\lambda \frac{\partial V_\lambda}{\partial \lambda} + \frac{4\Lambda}{\lambda^5} R_\lambda^2 V_\lambda^2 + \frac{1}{2} e \rho_p \frac{\partial^2 \mathcal{A}_\lambda}{\partial \lambda^2} - \frac{g_v V_\lambda \rho}{2\lambda^2} \\
& \left. + \left[ \frac{g_v \rho}{2\lambda} - \frac{4a V_\lambda^3}{\lambda^4} + 2 \frac{m_v^2 V_\lambda}{\lambda^4} \right] \frac{\partial V_\lambda}{\partial \lambda} + \frac{4a V_\lambda^4}{\lambda^5} - 4 \frac{m_v^2 V_\lambda^2}{\lambda^5} - 4 \frac{m_\rho^2 R_\lambda^2}{\lambda^5} \right]_{\lambda=1}. \quad (3.30)
\end{aligned}$$

The  $\omega$ -meson field equation (3.24) at  $\lambda = 1$  can be written as

$$\int dr \left[ \frac{1}{2} g_v \rho - 4a V^3 \right] \frac{\partial V_\lambda}{\partial \lambda} \Big|_{\lambda=1} = \int dr \left[ \frac{g_v V \rho}{2} - 4a V^3 + m_v^2 V^2 - 2\Lambda R^2 V^2 + 2\Lambda R V^2 \frac{\partial R_\lambda}{\partial \lambda} \right]_{\lambda=1}. \quad (3.31)$$

Now consider the scaled equation for the sigma field,

$$\left( \Delta_u - \frac{m_s^2}{\lambda^2} \right) \phi_\lambda = -\lambda g_s \tilde{\rho}_s^{eff}. \quad (3.32)$$

The double derivative of Eq.(3.32) with respect to  $\lambda$  is given by:

$$\left( \Delta_u - \frac{m_s^2}{\lambda^2} \right) \frac{\partial^2 \phi_\lambda}{\partial \lambda^2} = -2g_s \frac{\partial \tilde{\rho}_s^{eff}}{\partial \lambda} - 2 \frac{m_s^2}{\lambda^3} \frac{\partial \phi_\lambda}{\partial \lambda} + \frac{6m_s^2}{\lambda^4} \phi_\lambda - g_s \lambda \frac{\partial^2 \tilde{\rho}_s^{eff}}{\partial \lambda^2}. \quad (3.33)$$

Multiplying by  $\phi_\lambda$  and then integrating both sides, we get

$$\int dr \left[ -\frac{1}{2} g_s \tilde{\rho}_s^{eff} \frac{\partial^2 \phi_\lambda}{\partial \lambda^2} \right] + \frac{1}{2} g_s \phi_\lambda \tilde{\rho}_s^{eff} \frac{\partial^2 \tilde{\rho}_s^{eff}}{\partial \lambda^2} = \int dr \left[ -g_s \phi \frac{\partial \tilde{\rho}_s^{eff}}{\partial \lambda} - 2m_s^2 \phi \frac{\partial \phi_\lambda}{\partial \lambda} + 3m_s^2 \phi^2 \right], \quad (3.34)$$

where

$$-g_s \frac{\partial \tilde{\rho}_s^{eff}}{\partial \lambda} \Big|_{\lambda=1} = -g_s \phi \frac{\partial \tilde{\rho}_s}{\partial \lambda} \Big|_{\lambda=1} - 3(b\phi^2 + c\phi^3) - 2(2b\phi + 3c\phi^2) \frac{\partial \phi_\lambda}{\partial \lambda} \Big|_{\lambda=1}. \quad (3.35)$$

Substituting the value of the scaled parameter  $\lambda = 1$ , the restoring force  $C_m$  can be written as:

$$\begin{aligned}
C_m &= \left[ \frac{\partial^2}{\partial \lambda^2} \int d\lambda r \frac{\mathcal{H}_\lambda(r)}{\lambda^3} \right]_{\lambda=1} \\
&= \int dr \left[ -\tilde{m}^* \frac{\partial \tilde{\rho}_s}{\partial \lambda} \Big|_{\lambda=1} - \frac{1}{2} g_s \tilde{\rho}_s^{eff} \frac{\partial^2 \phi_\lambda}{\partial \lambda^2} \Big|_{\lambda=1} + \frac{1}{2} g_s \phi \frac{\partial^2 \tilde{\rho}_s^{eff}}{\partial \lambda^2} \Big|_{\lambda=1} + 4b\phi^3 + 3c\phi^4 \right. \\
&\quad - 3(b\phi^2 + c\phi^3) \frac{\partial \phi_\lambda}{\partial \lambda} \Big|_{\lambda=1} + \frac{1}{2} g_\rho \rho_3 \frac{\partial R_\lambda}{\partial \lambda} \Big|_{\lambda=1} + 2m_\rho^2 R \frac{\partial R_\lambda}{\partial \lambda} \Big|_{\lambda=1} - \frac{2\Lambda}{\lambda^4} (RV^2 \frac{\partial V_\lambda}{\partial \lambda} \Big|_{\lambda=1} \\
&\quad + R^2 V \frac{\partial R_\lambda}{\partial \lambda} \Big|_{\lambda=1}) + 4\Lambda R^2 V^2 + \frac{1}{2} e \rho_p \frac{\partial^2 \mathcal{A}_\lambda}{\partial \lambda^2} \Big|_{\lambda=1} - \frac{g_v V \rho}{2} + \left( \frac{g_v \rho}{2} - 4aV^3 + 2m_v^2 V \right) \\
&\quad \left. \frac{\partial V_\lambda}{\partial \lambda} \Big|_{\lambda=1} + 4aV - 4m_v^2 V^2 - 4m_\rho^2 R^2 \right]. \tag{3.36}
\end{aligned}$$

We put  $\frac{\partial^2 \mathcal{A}}{\partial \lambda^2} = 0$ , as the photon has zero mass. Finally, substituting Eqs. (3.28), (3.31), (3.34), (3.35) into Eq. (3.36) and rearranging the terms, one can get the following expression for the restoring force

$$\begin{aligned}
C_m &= \int dr \left[ -m \frac{\partial \tilde{\rho}_s}{\partial \lambda} + 3 \left( m_s^2 \phi^2 + \frac{1}{3} b \phi^3 - m_v^2 V^2 - m_\rho^2 R^2 \right) - (2m_s^2 \phi + b\phi^2) \frac{\partial \phi_\lambda}{\partial \lambda} \right. \\
&\quad \left. + 2m_v^2 V \frac{\partial V_\lambda}{\partial \lambda} + 2m_\rho^2 R \frac{\partial R_\lambda}{\partial \lambda} \right]_{\lambda=1}. \tag{3.37}
\end{aligned}$$

The mass parameter  $B_m$  of the monopole vibration can be expressed as the double derivative of the scaled energy with the collective velocity  $\dot{\lambda}$  as

$$B_m = \int dr U(\mathbf{r})^2 \mathcal{H}, \tag{3.38}$$

where  $U(\mathbf{r})$  is the displacement field, which can be determined from the relation between collective velocity  $\dot{\lambda}$  and velocity of the moving frame,

$$U(\mathbf{r}) = \frac{1}{\rho(\mathbf{r}) \mathbf{r}^2} \int d\mathbf{r}' \rho_T(\mathbf{r}') \mathbf{r}'^2, \tag{3.39}$$

where  $\rho_T$  is the transition density defined as

$$\rho_T(\mathbf{r}) = \frac{\partial \rho_\lambda(\mathbf{r})}{\partial \lambda} \Big|_{\lambda=1} = 3\rho(\mathbf{r}) + \mathbf{r} \frac{\partial \rho(\mathbf{r})}{\partial \mathbf{r}}. \tag{3.40}$$

Taking  $U(\mathbf{r}) = \mathbf{r}$  the relativistic mass parameter can be written as:

$$B_m = \int dr r^2 \mathcal{H}. \tag{3.41}$$

Similarly in the non-relativistic limit, the mass parameter is defined as

$$B_m^{nr} = \int dr r^2 m \rho. \tag{3.42}$$

The scaled energy in terms of the moments of the strength function can be written as  $E_m^s = \sqrt{\frac{m_3}{m_1}}$ . The expressions for  $m_3$  and  $m_1$  can be found in [76]. In simple classical approximation the scaling excitation energy can be written  $E_x^s = \sqrt{\frac{C_m}{B_M}}$ .

Along with the scaling calculation, the monopole vibration can also be studied with a constrained approach [76, 103–106]. In the constrained method, one has to minimize the constrained energy functional:

$$\int dr [\mathcal{H} - \eta r^2 \rho] = E(\eta) - \eta \int dr r^2 \rho, \quad (3.43)$$

with respect to the variation of densities and meson fields. Here  $\eta$  is the constrained parameter. The densities, field and energy obtained from the solution of the above constrained equation ( Eq. 3.43 ) are the function of parameter  $\eta$ . The rms radius of the nucleus is given in terms of the parameter  $\eta$ :

$$R_\eta = \left[ \frac{1}{A} \int dr r^2 \rho \right]^{1/2}, \quad (3.44)$$

where  $A$  is the mass number of the nucleus. We are assuming that the parameter  $\eta$  is very small, so  $E(\eta)$  can be expanded around  $\eta=0$ , which corresponds to the ground state energy of the nucleus and  $R_0$  gives the rms radius of the nucleus in ground state. The expansion of  $E(\eta)$  around  $\eta = 0$  is given by:

$$E(\eta) = E(0) + R_0 \left. \frac{\partial E(\eta)}{\partial \eta} \right|_{\eta=0} + R_0 \left. \frac{\partial E(\eta)}{\partial \eta} \right|_{\eta=0}. \quad (3.45)$$

The second order derivative of the expansion gives the effective incompressibility of finite nucleus and it is defined as :

$$K_A^c = \frac{1}{A} R_0 \left. \frac{\partial^2 E(\eta)}{\partial \eta^2} \right|_{\eta=0}. \quad (3.46)$$

We can calculate the incompressibility using this simple formula. In classical approximation the average constraint excitation energy is given by :  $E_x^c = \sqrt{\frac{AK_A^c}{B_m^c}}$ , where  $B_m^c$  is the mass parameter. The expression for the mass parameter both in relativistic and non-relativistic are given in Eq. ( 3.41) and Eq. ( 3.42), respectively. Again, in the sum rule approach constrained excitation energy can be expressed as the ratio of moments of strength distribution. Constrained energy is defined as :  $E_x^c = \sqrt{\frac{m_1}{m_{-1}}}$ , where  $m_1$  and  $m_{-1}$  are the energy weighted and inverse energy weighted moments,

respectively.  $m_{-1}$  is interpreted as the polarizability of the system ie. nothing but the measure of energy changed due to excitation of the nucleus. Expression for the  $m_{-1}$  is given by :

$$m_{-1} = -\frac{A}{2} \frac{\partial R_\eta^2}{\partial \eta} \Big|_{\eta=0} = \frac{1}{2} \frac{\partial^2 E(\eta)}{\partial \eta^2} \Big|_{\eta=0}. \quad (3.47)$$

One can estimate  $m_{-1}$  by calculating first derivative of  $R_\eta^2$  with respect to  $\eta$  or second derivative of  $E(\eta)$  with respect to the  $\eta$ . We have calculated  $m_{-1}$  using both 5-point and 3-point formula.  $m_1$  is proportional to the mass parameter, which can expressed as :  $m_1 = \frac{2}{m} A < r^2 > = \frac{2}{m^2} B_M^{nr}$ . From the inequality relations satisfied by the moments of the strength distribution, we get  $\frac{m_1}{m_{-1}} \leq \frac{m_3}{m_1}$ . This implies that the scaling energy gives the upper limit of the resonance, while the constrained energy gives the lower limit of the resonance spectra. The resonance width [76, 107] is defined as:

$$\Sigma = \sqrt{(E_m^s)^2 - (E_m^c)^2} = \sqrt{\left(\frac{m_3}{m_1}\right)^2 - \left(\frac{m_1}{m_{-1}}\right)^2}. \quad (3.48)$$

## 3.3 Results and Discussions

### 3.3.1 Force parameters of relativistic mean field formalism

First of all, we examined the predictive power of various parameter sets. In this context we selected NL1 as a successful past set, and a few recently used forces like NL3, NL3\*, and FSUGold with varying incompressibilities as shown in Table 4.1 (lower part of the table). The ground state observable obtained by these forces are depicted in Table 4.1. Along with the relativistic extended Thomas-Fermi (RETF) results, the relativistic Hartree values are also compared with the experimental data [108, 109]. The calculated RMF results obtained by all the force parameters considered in the present thesis are very close to the experimental data [108, 109]. A detailed analysis of the binding energy and charge radius clearly show that NL1 and FSUGold have superior predictive power for  $^{16}\text{O}$  in RMF level. The advantage of FSUGold decreases with increased mass number of the nucleus. Although the predictive power of the relatively old NL1 set is very good for binding energy, it has a large asymmetry coefficient  $J$ , which may mislead the prediction in unknown territories, like the neutron drip-line or super heavy regions. The RETF prediction of binding energy and

Table 3.1: The calculated binding BE and charge radius  $r_{ch}$  obtained from relativistic extended Thomas-Fermi (RETF) approximation is compared with relativistic Hartree (with various parameter sets) and experimental results [108, 109]. The RETF results are given in the parentheses. The empirical values [19, 110] of nuclear matter saturation density  $\rho_0$ , binding energy per nucleon BE/A, incompressibility modulus  $K$ , asymmetry parameter  $J$ , and ratio of effective mass to the nucleon mass  $M^*/M$  are given in the lower part of the table. Energies are in MeV and radii are in fm.

Nucleus	Set	BE (calc.)	BE (Expt.)	$r_{ch}$ (calc.)	$r_{ch}$ (Expt.)
$^{16}\text{O}$	NL1	127.2(118.7)	127.6	2.772(2.636)	2.699
	NL3	128.7(120.8)		2.718(2.591)	
	NL3*	128.1(119.5)		2.724(2.603)	
	FSUGold	127.4(117.8)		2.674(2.572)	
$^{40}\text{Ca}$	NL1	342.3(344.783)	342.0	3.501(3.371)	3.478
	NL3	341.6(346.2)		3.470(3.343)	
	NL3*	341.5(344.2)		3.470(3.349)	
	FSUGold	340.8(342.2)		3.429(3.327)	
$^{48}\text{Ca}$	NL1	412.7(419.5)	416.0	3.501(3.445)	3.477
	NL3	414.6(422.6)		3.472(3.426)	
	NL3*	413.5(420.3)		3.469(3.429)	
	FSUGold	411.2(418.0)		3.456(3.418)	
$^{90}\text{Zr}$	NL1	784.3(801.1)	783.9	4.284(4.232)	4.269
	NL3	781.4(801.7)		4.273(4.219)	
	NL3*	781.6(798.7)		4.267(4.219)	
	FSUGold	778.8(797.3)		4.257(4.214)	
$^{116}\text{Sn}$	NL1	989.5(1013.7)	988.7	4.625(4.583)	4.625
	NL3	985.4(1014.6)		4.617(4.571)	
	NL3*	986.4(1011.0)		4.609(4.569)	
	FSUGold	984.4(1010.7)		4.611(4.569)	
$^{208}\text{Pb}$	NL1	1638.1(1653.7)	1636.4	5.536(5.564)	5.501
	NL3	1636.9(1661.2)		5.522(5.541)	
	NL3*	1636.5(1655.2)		5.512(5.538)	
	FSUGold	1636.2(1661.4)		5.532(5.541)	
Set	NL1	NL3	NL3*	FSUGold	empirical
$\rho_0$	0.154	0.150	0.148	0.148	0.17
$E/A$	16.43	16.31	16.30	16.30	15.68
$K$	211.7	271.76	258.27	230.0	$210 \pm 30$
$J$	43.6	38.68	37.4	32.597	$32 \pm 2$
$M^*/M$	0.57	0.594	0.60	0.61	0.6

charge radius (numbers in the parenthesis) is very poor with the experimental data as compared to the RMF calculations. However, for relatively heavy masses, the RETF results can be used within acceptable error. In general, taking into account the binding energy BE and root mean square charge radius  $r_{ch}$ , one may prefer to use either of the NL3 or NL3\* parametrization. Before accepting NL3 or NL3\* as the working parameter set for our further calculations, in Table 4.2, we have given the excitation energy of some selective nuclei both in light and super heavy regions with various parameter sets for some further verification. The isoscalar giant monopole energies  $E^s$  and  $E^c$  are evaluated using both scaling and constraint calculations, respectively. The forces like NL1, NL3, NL3\* and FSUGold have a wide range of incompressibility  $K_\infty$  starting from 211.7 to 271.7 MeV (see Table 4.1). Because of the large variation in  $K_\infty$  of these sets, we expect various values of  $E^s$  and  $E^c$  with different parametrization. From Table 4.2, it is noticed that the calculated results for  $^{16}\text{O}$  and  $^{40}\text{Ca}$  differ substantially from the data. Again this deviation of calculated results continues decreasing with increasing mass number, irrespective of the parameter set. This may be due to the use of semi-classical approximations like Thomas-Fermi and extended Thomas-Fermi. In these approaches, quantal corrections are averaged out. When we are going from light to the heavy and then super heavy nuclei, the surface correction decreases appreciably. Consequently, the contribution to monopole excitation energy decreases with mass number  $A$ . In column 11, 12 and 13 of Table 4.2, the differences in  $E_x$  obtained from various parameter sets are given, namely,  $\Delta_1$  is the difference in monopole excitation energy obtained by NL3 and NL3\*. Similarly,  $\Delta_2$  and  $\Delta_3$  are the ISGMR difference with (NL3\*, FSUGold) and (NL3, FSUGold), respectively. The values of  $\Delta_1$ ,  $\Delta_2$  or  $\Delta_3$  go on decreasing with increasing mass number of the nucleus without depending on the parameter used. In other words, we may reach the same conclusion in the super heavy region irrespective of the parameter set. However, it is always better to use a successful parameter set to explore an unknown territory. In this context, it is safer to choose the NL3 force for our further exploration. The second observation is also apparent from the Table. It is commonly believed that mostly the incompressibility of the force parameter affects the excitation energy of ISGMR of the nucleus. That means, forces having different  $K_\infty$  have different excitation energy for the same nucleus. For example,  $^{208}\text{Pb}$  has excitation energy 14.58 and



Table 3.2: The results of isoscalar giant monopole resonance with various parameter sets for some known nuclei are compared with recent experimental data [111]. The calculations are done with relativistic extended Thomas-Fermi (RETF) approximation using both scaling and constrained schemes. The values of  $\Delta_1$ ,  $\Delta_2$ , and  $\Delta_3$  are obtained by subtracting the results of (NL3, NL3\*), (NL3\*, FSUGold), and (NL3, FSUGold), respectively. The monopole excitation energies with scaling  $E^s$  and constrained  $E^c$  are in MeV.

Nucleus	NL1		NL3		NL3*		FSUGold		Expt.	$\Delta_1$	$\Delta_2$	$\Delta_3$
	$E^s$	$E^c$	$E^s$	$E^c$	$E^s$	$E^c$	$E^s$	$E^c$				
$^{16}\text{O}$	23.31	21.75	27.83	25.97	26.86	25.20	26.97	25.17	21.13 $\pm$ 0.49	0.97	0.11	0.86
$^{40}\text{Ca}$	20.61	19.77	24.01	23.16	23.32	22.48	22.98	22.30	19.20 $\pm$ 0.40	0.69	0.43	1.03
$^{48}\text{Ca}$	19.51	18.67	22.69	21.73	22.01	21.11	21.72	20.88	19.90 $\pm$ 0.20	0.68	0.29	0.97
$^{90}\text{Zr}$	16.91	16.41	19.53	19.03	18.97	18.50	18.60	18.21	17.89 $\pm$ 0.20	0.56	0.37	0.97
$^{110}\text{Sn}$	15.97	15.50	18.42	17.94	17.90	17.44	17.52	17.13		0.52	0.38	0.90
$^{112}\text{Sn}$	15.87	15.39	18.29	17.81	17.78	17.32	17.42	17.02	16.1 $\pm$ 0.10	0.51	0.36	0.86
$^{114}\text{Sn}$	15.76	15.28	18.16	17.67	17.65	17.18	17.31	16.90	15.9 $\pm$ 0.10	0.51	0.34	0.85
$^{116}\text{Sn}$	15.63	15.19	18.02	17.52	17.51	17.04	17.19	16.77	15.80 $\pm$ 0.10	0.51	0.32	0.83
$^{118}\text{Sn}$	15.51	15.03	17.87	17.36	17.37	16.89	17.07	16.63	15.6 $\pm$ 0.10	0.50	0.30	0.80
$^{120}\text{Sn}$	15.38	14.90	17.72	17.20	17.22	16.73	16.94	16.49	15.4 $\pm$ 0.20	0.50	0.28	0.78
$^{122}\text{Sn}$	15.24	14.76	17.56	17.03	17.07	16.57	16.81	16.34	15.0 $\pm$ 0.20	0.49	0.24	0.77
$^{124}\text{Sn}$	15.11	14.61	17.40	16.85	16.91	16.40	16.67	16.19	14.80 $\pm$ 0.20	0.48	0.24	0.72
$^{208}\text{Pb}$	12.69	12.11	14.58	13.91	14.18	13.55	14.04	13.44	14.17 $\pm$ 0.28	0.40	0.14	0.54
$^{286}_{114}$	11.32	10.60	13.00	12.14	12.64	11.83	12.55	11.79		0.36	0.09	0.45
$^{298}_{114}$	11.05	10.31	12.68	11.80	12.33	11.50	12.29	11.53		0.35	0.04	0.37
$^{292}_{120}$	11.28	10.53	12.96	12.07	12.60	11.76	12.48	11.69		0.36	0.12	0.27
$^{304}_{120}$	11.04	10.28	12.67	11.77	12.33	11.47	12.25	11.47		0.34	0.08	0.42

Table 3.3: The predicted proton and neutron drip-lines PDL and NDL for *O*, *Ca*, *Ni*, *Sn*, *Pb*, Z=114, and Z=120 in relativistic mean field formalism (RMF) with various parameter sets are compared with experimental (wherever available) and Finite Range Droplet Model (FRDM) predictions [112].

Nucleus	RMF								FRDM		Expt. [108]	
	NL1		NL3		NL3*		FSUGold					
	PDL	NDL	PDL	NDL	PDL	NDL	PDL	NDL	PDL	NDL	PDL	NDL
O	12	29	13	30	12	30	12	27	12	26	12	28#
Ca	34	69	33	71	34	71	34	66	30	73	35#	58 #
Ni	49	94	50	98	50	98	51	94	46	99	48	79
Sn	99	165	100	172	100	172	99	164	94	169	99#	138#
Pb	178	275	180	281	180	280	179	269	175	273	178	220#
114	267	375	271	392	274	390	271	376	269	339	285#	289#
120	285	376	288	414	288	410	289	396	287	339	-	-

14.04 MeV with NL3 and FSUGold, respectively. Although, the ground state binding energy of  $^{208}\text{Pb}$ , either with Hartree (RMF) or REFT approximation matches well with NL3 and FSUGold parameter sets (see Table 4.1), their ISGMR differ by 0.54 MeV, which is quite substantial. The reason behind this difference in  $E^s$  with various parameter sets is not yet clear. As we have stated, the incompressibility  $K_\infty$  is not the only controlling key to tune the monopole excitation energy. A lot of effort has been devoted to show that the ISGMR excitation energy can be altered by modifying other variables of the force parameter like effective mass  $M^*$  and the symmetry energy coefficient  $a_4$  [113]. Thus, the relation  $E^M = \sqrt{\frac{K_A}{M\langle r^2 \rangle}}$  needs modification with the inclusion of some other variables including the nuclear matter incompressibility, where  $\langle r^2 \rangle$  is the rms matter radius and  $M$  the mass of the nucleon. Actually, it is a long running debate and not yet clear, and the factors responsible for the ISGMR are invite more work in this direction.

### 3.3.2 Proton and neutron drip-lines

In Table 4.3 we have shown the proton and neutron drip-lines (PDL and NDL) for various parameter sets. The neutron (or proton) drip-line of an isotope is defined when the neutron (or proton) separation energy  $S_n$  (or  $S_p$ )  $\leq 0$ , where  $S_n = BE(N, Z) - BE(N-1, Z)$  or  $S_p = BE(N, Z) - BE(N, Z-1)$  with  $BE(N, Z)$  is the binding energy of a nucleus with  $N$  neutron and  $Z$  proton. From the table, it is seen that all the interactions predict almost similar proton and neutron drip-lines. If one compares the drip-lines of NL3 and NL3\*, then their predictions are almost identical, explicitly for lighter mass nuclei. Thus, the location of the drip-line with various forces does not depend on its nuclear matter incompressibility or asymmetry coefficient. For example, the asymmetry coefficient  $J = 43.6$  MeV and  $K_\infty = 211.7$  MeV for the NL1 set and these are 38.68 and 271.76 MeV in the NL3 parametrization. The corresponding proton drip-lines for O isotopes are 12 and 13, and the neutron drip-lines are 29 and 30, respectively. Similar effects are noticed for other isotopes of the considered nuclei (see Table 4.3).

### 3.3.3 Isoscalar giant monopole resonance

It is well understood that the ISGMR has a direct relation to the incompressibility of nuclear matter, which decides the softness or stiffness of an equation of state [19]. This EOS also estimates the structure of neutron stars, such as mass and radius. Thus, the ISGMR is an intrinsic property of finite nuclei as well as nuclear equations of state and needed to be determined to shine some light into nuclear properties. The excitation energies of ISGMR for O, Ca, Ni, Sn, Pb, Z=114, and Z=120 isotopic series are given in Figs. 3.1 and 3.2. The results are calculated by using both constrained and scaling approaches in the isotopic chain, starting from proton to neutron drip-lines. We use the relation  $E_m^s = \sqrt{\frac{AK_A^s}{B_m}}$  with the mass parameter  $B_m = \int d\mathbf{r} r^2 \mathcal{H}$ . The figure shows that excitation energy obtained from scaling calculation is always greater than the constrained value. The difference between the monopole excitation of scaling and constrained calculations, generally gives the resonance width  $\Sigma = \frac{1}{2}\sqrt{E_3^2 - E_1^2}$ , with  $E_3 = \sqrt{\frac{m_3}{m_1}}$  and  $E_1 = \sqrt{\frac{m_1}{m_1}}$  in terms of the ratios of the integral moments  $m_k = \int_0^\infty d\omega \omega^K S(\omega)$  of the random phase approximation (RPA) strength function

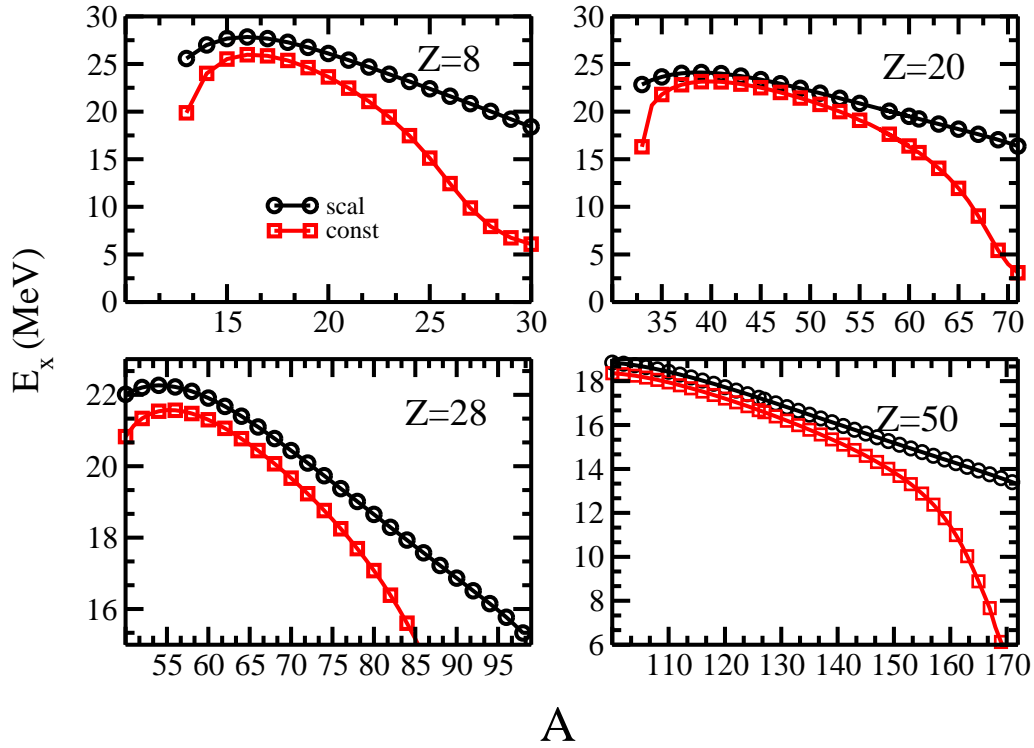


Figure 3.1: The excitation energy isoscalar giant monopole resonance (ISGMR) for O, Ca, Ni, and Sn isotopes from proton to neutron drip-lines as a function of mass number.

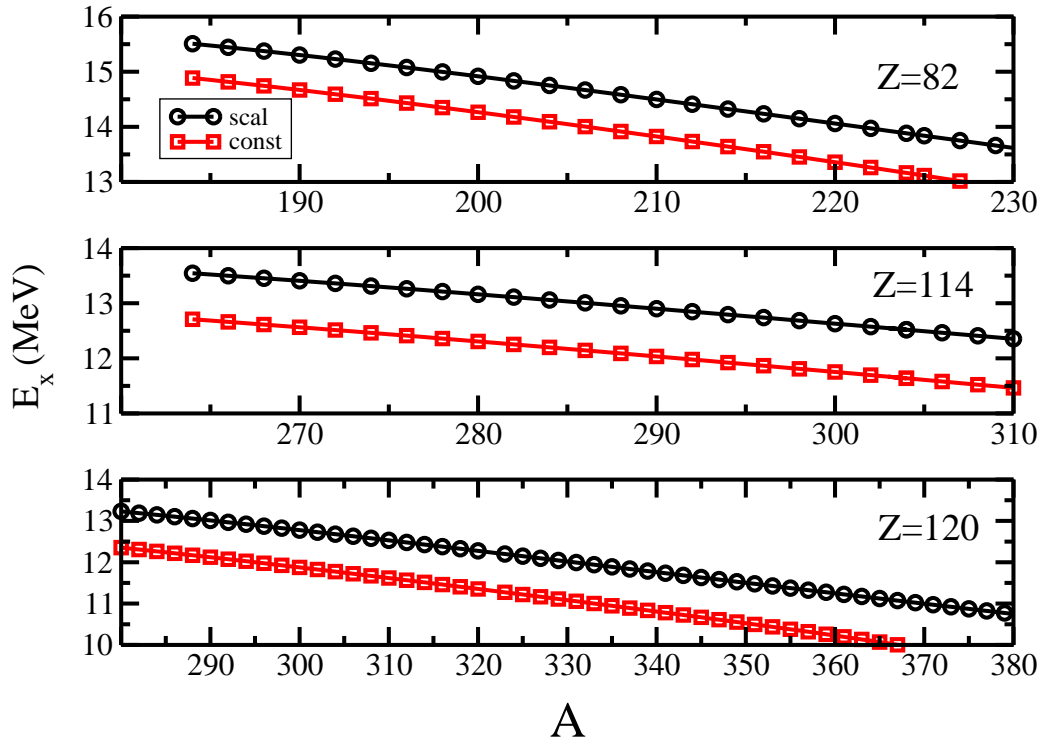


Figure 3.2: The excitation energy isoscalar giant monopole resonance (ISGMR) for Pb,  $Z=114$ , and  $Z=120$  isotopes starting from proton to neutron drip-lines as a function of mass number.

$S(\omega)$  [95]. It is also equivalent to  $m_1 = \frac{2}{m}A < r^2 >$  and from dielectric theorem, we have  $m_{-1} = -\frac{1}{2}A\left(\frac{\partial R_\eta^2}{\partial \eta}\right)\bigg|_{\eta=0}$ .

Now consider Fig. 3.1, where the excitation energies of giant isoscalar monopole resonance  $E_x$  for lighter mass nuclei are plotted. For  $Z=8$  the excitation energy decreases towards both the proton ( $A=12$ ,  $E_x^s = 22.51$  MeV) and neutron drip-lines ( $A=26$ ,  $E_x^s = 21.22$  MeV). Excitation energy has a maximum value near  $N=Z$  (here it is a double closed isotope with  $Z=8$ ,  $N=8$ ,  $E_x^s = 27.83$  MeV). Similar trend is followed in the isotopic chain of Ca with  $Z=20$ . We find the maximum excitation energy at  $^{40}\text{Ca}$  ( $E_x^s = 24.07$  MeV), whereas  $E_x^s$  is found to be smaller both in the proton ( $A=34$ ,  $E_x = 23.31$  MeV) and neutron drip-lines ( $A=71$ ,  $E_x^s = 16.80$  MeV). However, the trends are different for isotopic chains of higher  $Z$  like  $Z=50$ ,  $82$ ,  $114$ , and  $120$ . In these series of nuclei, the excitation energy monotonically decreases starting from proton drip-line to neutron drip-line. For example,  $^{180}\text{Pb}$  and  $^{280}\text{Pb}$  are the proton and neutron drip nuclei having excitation energy  $E_x = 15.63$  and  $E_x = 11.45$  MeV, respectively. Fig. 3.2 shows clearly the monotonic decrease of excitation energy for super heavy nuclei. This discrepancy between super heavy and light nuclei may be due to the Coulomb interaction and the large value of isospin difference. For lighter values of  $Z$ , the proton drip-line occurs at a combination of proton and neutron where the neutron number is less than or near to the proton number. But for higher  $Z$  nuclei, the proton drip-line is exhibited at a larger isospin. As the excitation energy of a nucleus is a collective property, it varies smoothly with its mass number, which is also reflected in the figures. Consider the isotopic chain of  $Z=50$ : the drip-line nucleus ( $A=100$ ) has excitation energy  $18.84$  MeV and the neutron drip nucleus  $A=171$  has  $E_x = 13.39$  MeV. The difference in excitation energy between these two isotopes is  $5.32$  MeV. This difference in proton and neutron drip nuclei is  $4.31$  MeV for  $Z=82$  and is  $2.37$  MeV in  $Z=114$ . In summary, for higher  $Z$  nuclei, the variation of excitation energy in an isotopic chain is less than for a lighter  $Z$  nucleus. Again, by comparing with the empirical formula of  $E_x = CA^{-1/3}$ , our predictions show similar variation throughout the isotopic chains. Empirically, the value of  $C$  is found to be  $80$  [114]. However, if we select  $C = 70 - 80$  for lighter mass isotopes and  $C = 80 - 86$  for the super heavy region, then that fits well with our results, which are slightly different than  $C=80$  obtained by fitting the data for stable nuclei [114].

Table 3.4: The calculated excitation energies in the RETF formalism with FSUGold parameter set are compared with other theoretical formalisms and experimental data [75, 115, 116].

Nucleus	Formalism (parameter)	Excitation energy
$^{16}\text{O}$	RPA(FSUGold)	23.09
	CRMF(FSUGold)	22.89
	RETF(FSUGold)	25.17
	Expt.	$21.13 \pm 0.49$
$^{40}\text{Ca}$	RPA(FSUGold)	20.67
	CRMF(FSUGold)	20.67
	RETF(FSUGold)	22.30
	Expt.	$19.18 \pm 0.37$
$^{90}\text{Zr}$	RPA(FSUGold)	17.44
	CRMF(FSUGold)	17.70
	RETF(FSUGold)	18.21
	Expt.	$17.89 \pm 0.20$
$^{208}\text{Pb}$	RPA(FSUGold)	13.76
	CRMF(FSUGold)	13.50
	RETF(FSUGold)	13.44
	Pairing+MEM	14.0
	Expt.	$13.5 \pm 0.1$
$^{204}\text{Pb}$	RETF(FSUGold)	13.6
	Pairing+MEM	13.4
	Expt.	$13.7 \pm 0.1$
$^{206}\text{Pb}$	RETF(FSUGold)	13.51
	Pairing+ MEM	13.4
	Expt.	$13.6 \pm 0.1$

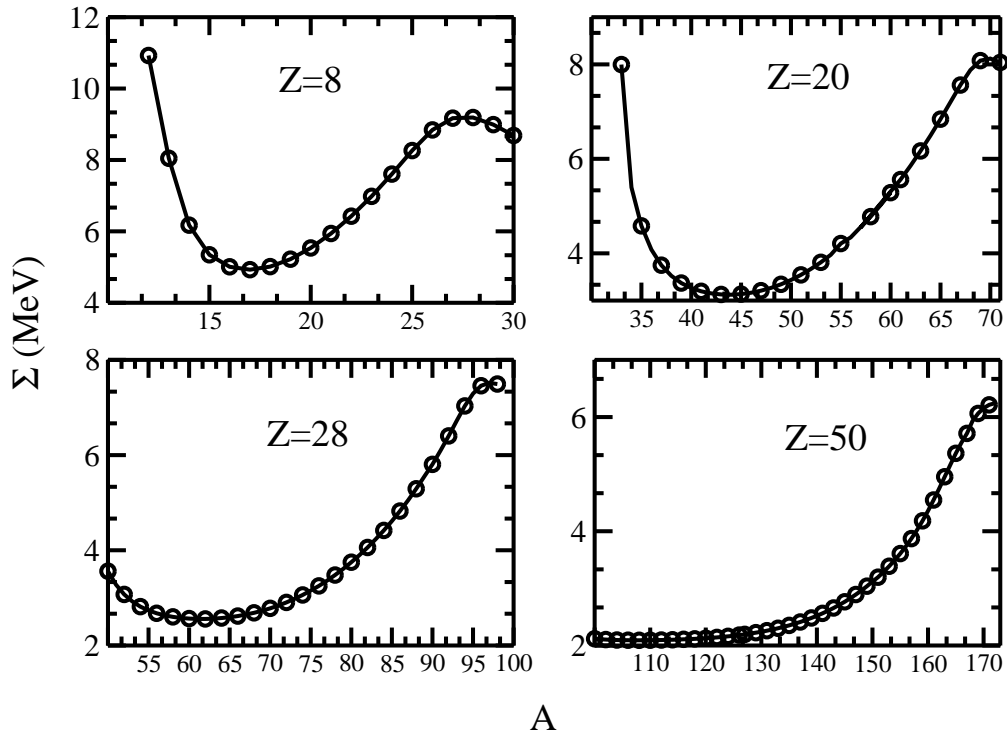


Figure 3.3: The difference between the monopole excitation energies of scaling and constrained calculations  $\Sigma = \frac{1}{2}\sqrt{E_3^2 - E_1^2}$  as a function of mass number  $A$  for O, Ca, Ni, and Sn.



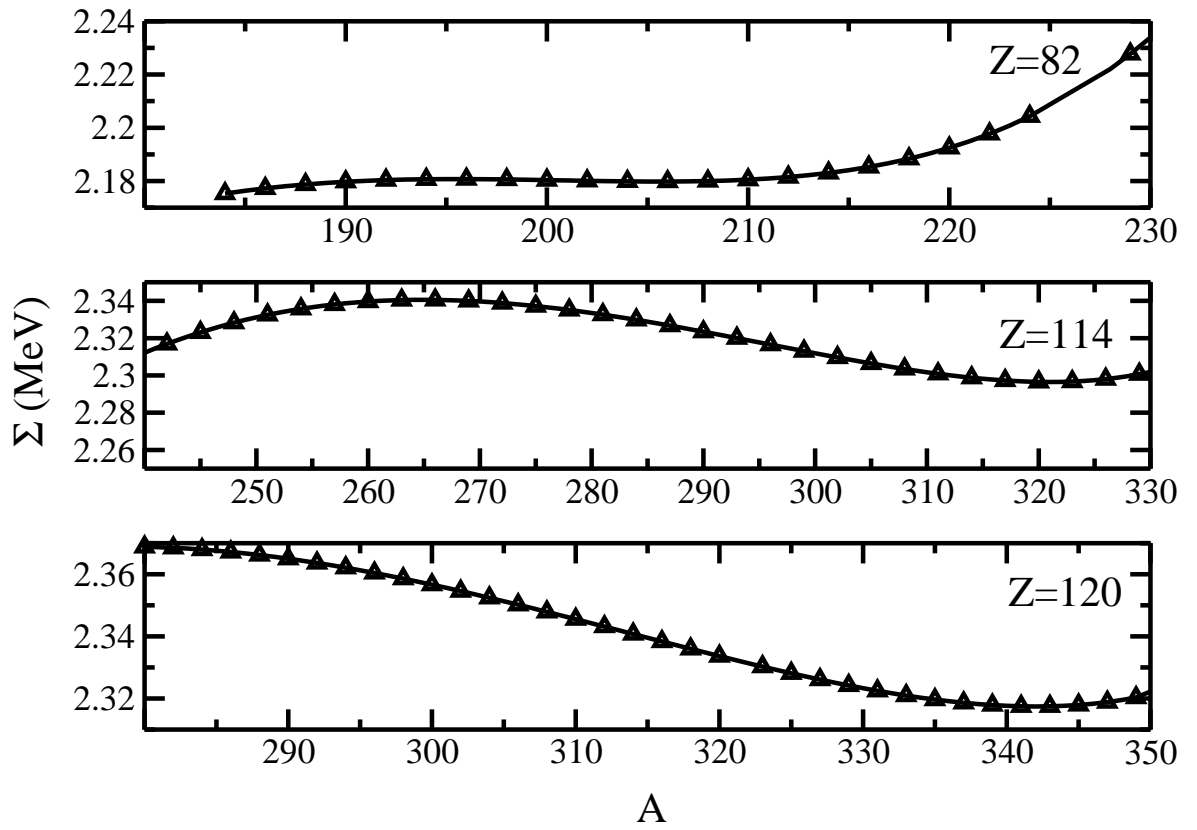


Figure 3.4: Same as Fig. 3.3, but for Pb,  $Z=114$ , and  $Z=120$ .

In table 3.4, we have shown the results obtained in the RETF formalism with the FSUGold parameter set and compared with other predictions like the random phase approximation (RPA) and constrained relativistic mean field (CRMf) [117]. The experimental data are also given, where ever available, for comparison. A comparative study of these results shows that for light nuclei such as  $^{16}\text{O}$ , the RPA and CRMf give better results than the semi-classical RETF approximation. For example, the difference between the excitation energies of  $^{16}\text{O}$  in the RPA and RETF formalism is  $\sim 2$  MeV and it is only 0.1 MeV for  $^{208}\text{Pb}$ . This implies, for heavy nuclei, that the RETF gives comparable results with RPA and CRMf. On the other hand, the RETF results obtained by constrained calculation are within the experimental error bar. In RETF, the quantal correction is averaged out. Thus, the RETF result of monopole excitation energy differs from the RPA prediction for light nuclei, where quantal correction has a significant role in structural properties. In heavy nuclei, the number of nucleons are larger, so the quantal and semi-classical approaches are almost similar. This could be a reason for the accuracy of application of semi-classical calculation to heavy mass nuclei. We have also compared our results with Pairing+MEM (mutually enhanced magicity) [118] and experimental data [119] for  $\text{Pb}$  isotopes. The Pairing+MEM theory says that a magic nucleus like  $^{208}\text{Pb}$  has a little higher excitation energy than its neighboring isotopes. But recent experimental data are not in favor of the manifestation of such an effect. Our theoretical results also come to the same conclusion.

There is no direct way to calculate  $\Sigma$  in the scaling or constrained method as in RPA. If we compare the excitation energy obtained from scaling calculations with the non-relativistic RPA result, then it is evident that the scaling gives the upper limit of the energy response function. On the other hand, the constrained calculation predicts the lower limit [76]. As a result, the resonance width  $\Sigma$  is obtained from the root mean square difference of  $E_x^s$  and  $E_x^c$ . We have plotted  $\Sigma$  for the light nuclei in Fig. 3.3 and for super heavy in Fig. 3.4. For lighter nuclei,  $\Sigma$  is larger both in the proton and neutron drip-lines. As one proceeds from proton to neutron drip-line, the value of  $\Sigma$  decreases up to a zero isospin combination ( $N=Z$  or double closed) and then increases. For example,  $\Sigma= 10.92, 5.0$  and  $8.9$  MeV for  $^{12}\text{O}$ ,  $^{16}\text{O}$ , and  $^{26}\text{O}$ , respectively. Similar trends are also followed by the medium nuclei  $Z=20, 28$ , and  $50$  isotopic chains. This

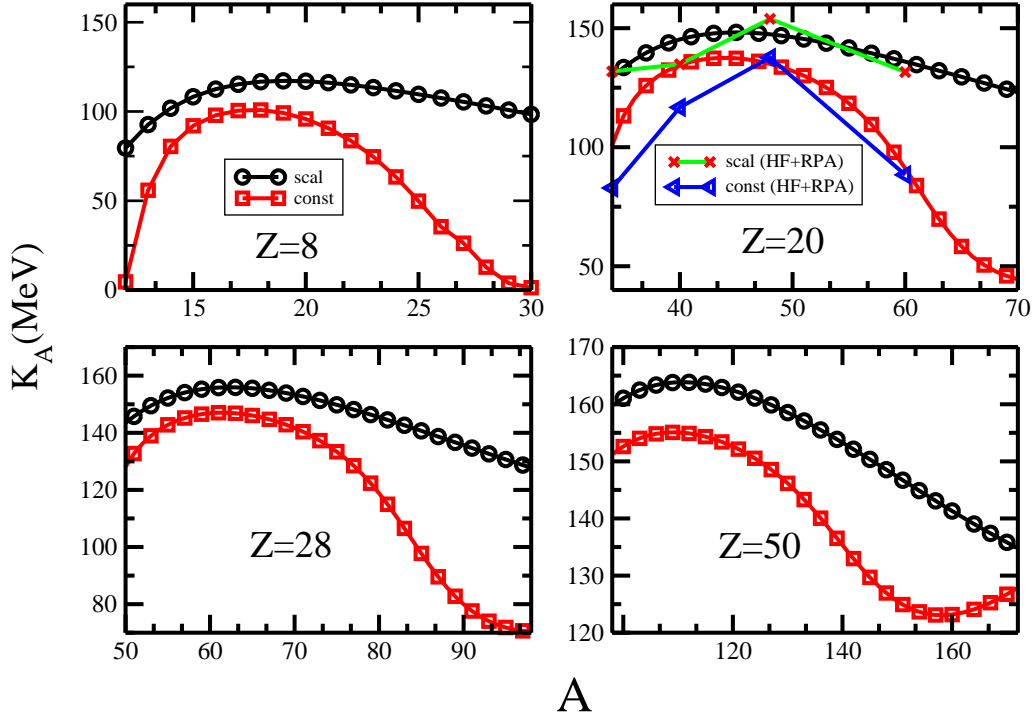


Figure 3.5: The incompressibility modulus obtained by both scaling and constrained approaches in the isotopic series of O, Ca, Ni, and Sn.

conclusion can be drawn from the results of the excitation energy also (see Figs. 3.1 and 3.2), i.e., the difference between the scaling and constrained excitation energies are more in proton and neutron drip-lines as compared to the  $Z=N$  region. The value of  $\Sigma$  in an isotopic chain depends very much on the proton number. It is clear from the isotopic chains of  $\Sigma$  for O, Ca, Ni, Sn, Pb, and  $Z=114, 120$ . All of the considered series have their own behavior and show various trends. Generally, for lighter elements, it decreases initially to some extent and again increases monotonically. On the other hand, for heavier nuclei like Pb,  $Z=114$ , or  $Z=120$  this characteristic of  $\Sigma$  differs with different mass number and can be seen in Fig. 3.4.

### 3.3.4 Incompressibility of finite nuclei

The nuclear matter incompressibility  $K_\infty$  is a key quantity in the study of the equation of state. It is the second derivative of the energy functional with respect to density at the saturation and is defined as  $K_\infty = 9\rho_0 \frac{\partial^2 \mathcal{E}}{\partial \rho^2} |_{\rho=\rho_0}$ , which has a fixed value for a particular force parametrization. It is well understood that a larger  $K_\infty$  of a parameter

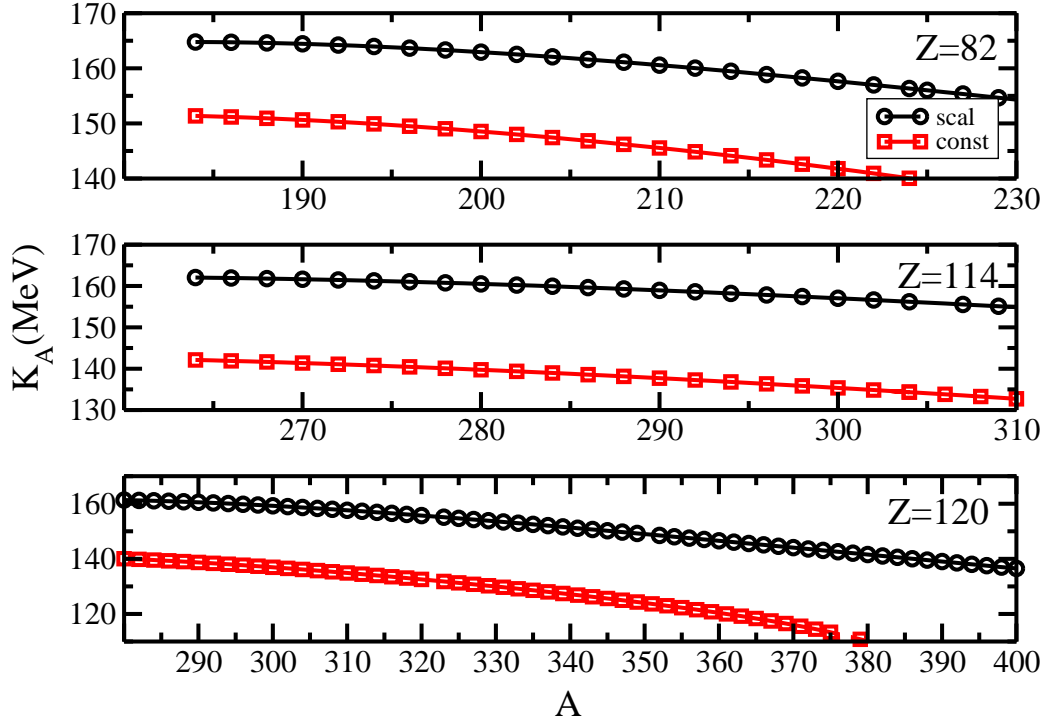


Figure 3.6: Same as Fig. 3.5, but for Pb,  $Z=114$ , and  $Z=120$ .

set gives a stiff EOS and produces a massive neutron star. It has also a direct relation to the asymmetry energy coefficient  $J$  of the parameter set [48]. In the limit  $A$  approaches infinitely large, the finite nucleus can be approximated to an infinite nuclear matter system ( $N=Z$  for symmetry and  $N \neq Z$  for asymmetry matter). Thus, it is instructive to study the nature of the incompressibility of a finite nucleus  $K_A$  in the isotopic chain of super heavy nuclei. Here, we calculate the  $K_A$  as a function of mass number for the light nuclei considered in the present study (O, Ca, Ni, Sn) and then extend the calculations to Pb,  $Z=114$  and  $Z=120$  in the super heavy region. Our calculated results are shown in Figs. 3.5 and 3.6. The incompressibility of finite nuclei follows the same trend as the excitation energy. For light nuclei, the incompressibility has a small value for the proton and neutron drip-lines, whereas it is maximum in the neighborhood of double closed combinations.

It can be easily understood from Fig. 3.5 that, at some particular proton to neutron combination, the  $K_A$  is high, i.e., at this combination of  $N$  and  $Z$ , the nucleus is more incompressible. In other words, the larger the incompressibility of a nucleus, the more compressible it will be. Here, it is worthy to mention that the nuclear

system becomes less compressible near both the neutron and proton drip-lines. This is because of the instability originating from the repulsive part of the nuclear force, revealing a large neutron-proton ratio, which progressively increases with the neutron/proton number in the isotope without much affecting the density [120]. Similar to the excitation energy, it is found that  $K_A$  obtained by the scaling method is always higher than the constrained calculation. The decrease in incompressibility near the drip-line regions is more prominent in constrained calculation than the scaling results. From leptodermous expansion [19], we can get some basic ideas about this decrease in the vicinity of drip-lines. The expression for finite nucleus incompressibility can be written as

$$K_A = K_\infty + K_{Sur}A^{-\frac{1}{3}} + K_\tau I^2 + K_{Coul}Z^2A^{-\frac{4}{3}}, \quad (3.49)$$

where  $I = \frac{N-Z}{A}$ . The coefficient  $K_\tau$  is negative, so incompressibility decreases with  $N - Z$ . For the Ca chain, the incompressibilities obtained by scaling and constrained calculations are compared with the Hartree-Fock plus RPA results [19] in Fig. 3.5. From Fig. 3.5, one can see that  $K_A$  evaluated by the semi-classical approximation deviates from RPA results for lighter isotopes, contrary to the excellent matching for the heavier Ca nuclei. This is because of the exclusion of the quantal correction in the semi-classical formalism. For higher mass nuclei, this correction becomes negligible and compares to the RPA predictions. This result is depicted in Fig. 3.6 for Pb and super heavy chain of nuclei. Here the results show completely different trends than for the lighter series. The incompressibility has a higher value in the vicinity of the proton drip-line and decreases monotonically towards the neutron drip-line. Because, for high Z-series, the proton drip-line appears at a greater value of N in contrast to the lighter mass region. Again, the incompressibility decreases with neutron number from the proton to neutron drip-lines. Finally, we would like to see the trend of  $K_A$  with nuclear matter incompressibility for various force parameters and also with the size of a nucleus which can reach the infinite nuclear matter limit. For this we choose  $^{286,298}_{114}$ ,  $^{292,304}_{120}$ , and  $^{40}\text{Ca}$  as the selected candidates as shown in Fig. 3.7. Although, the super heavy nuclei approach the nuclear matter limit, we can not reproduce the  $K_\infty$  from  $K_A$ . This may be due to the asymmetry needed to form a bound nucleus, which is the reason for the deviation. That means the asymmetry

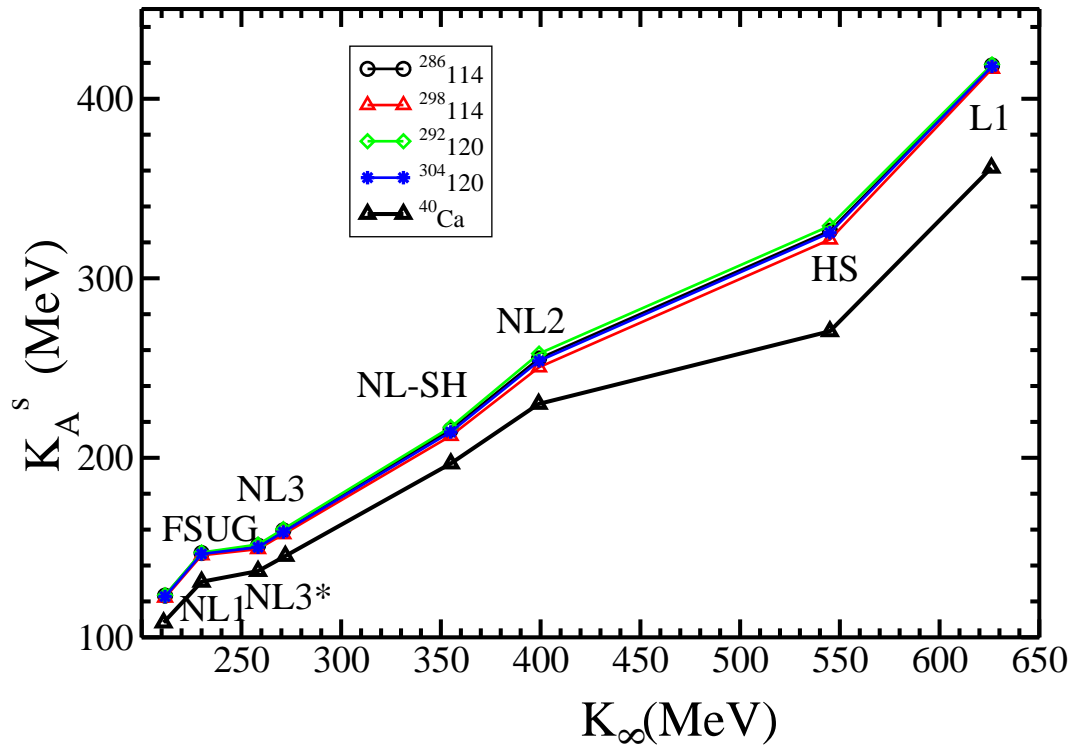


Figure 3.7: Compressibility for finite nuclei obtained by scaling calculation  $K_A^s$  versus nuclear matter incompressibility  $K_\infty$ .

$I$  of  $K_A$  and  $K_\infty$  differs significantly (where  $I = \frac{N-Z}{N+Z}$ ), which is the main source of deviation of  $K_A$  from  $K_\infty$ . Also, this deviation arises due to the surface contribution of the finite nuclei. For a quantitative estimation, we have calculated the  $K_A^s$  for different force parameters having various  $K_\infty$  at saturation. We find almost a linear variation of  $K_A^s$  with  $K_\infty$  for the considered nuclei as shown in Fig. 3.7. For Ca isotopes also we find variation similar in nature, but with smaller  $K_A$  than the super heavy nuclei.

### 3.4 Application of scaling and constrained formalism to Sn isotopes

In this part of the chapter, we applied the scaling and constrained formalism to analyse the anomalous nature of Sn Isotopes. In the previous section, we have discussed the excitation energy and incompressibility of super heavy and drip line nuclei. The recent experiment on the isotopic chain of Sn isotopes indicates the mismatch between the theoretical prediction and the experimental data of the excitation energy of isoscalar giant monopole resonance energy. This problem is addressed in the name of " why the tin nucleus is so floppy ?". So theoretical physicists are now more interested in the medium heavy region ( $A \sim 100$ ). In this section the excitation energy and the incompressibility isotopes of Cd and Sn nuclei are discussed, within the framework of relativistic Thomas-Fermi and relativistic extended Thomas-Fermi approximations. A large number of non-linear relativistic force parameters are used in the calculations that a parameter set is capable of reproducing the experimental monopole energy of Sn isotopes, when its nuclear matter incompressibility lies within 210 – 230 MeV, however, it fails to reproduce the GMR energy of other nuclei. That means, simultaneously a parameter set can not reproduce the GMR values of Sn and other nuclei.

Incompressibility of nuclear matter, also known as compression modulus  $K_\infty$  has a special interest in nuclear and astro-nuclear physics, because of its fundamental role in guiding the equation of state (EOS) of nuclear matter. The  $K_\infty$  can not be measured by any experimental technique directly, rather it depends indirectly on the

experimental measurement of isoscalar giant monopole resonance (ISGMR) for its confirmation [19]. This fact enriches the demand of correct measurement of excitation energy of ISGMR. The relativistic parameter with random phase approximation (RPA) constraints the range of the incompressibility  $270 \pm 10$  MeV [49, 121] for nuclear matter. Similarly, the non-relativistic formalism with Hartree-Fock (HF) plus RPA allows the acceptable range of incompressibility  $210 - 220$  MeV, which is less than the relativistic one. It is believed that the part of this discrepancy in the acceptable range of compressional modulus comes from the diverse behavior of the density dependence of symmetry energy in relativistic and non-relativistic formalism [122]. Recently, both the formalism come to a general agreement on the value of nuclear matter incompressibility i.e.,  $K_\infty = 240 \pm 10$  MeV [90, 123, 124]. But the new experiment on Sn isotopic series i.e.,  $^{112}\text{Sn}-^{124}\text{Sn}$  rises the question "why Tin is so fluffy?" [125–127]. This question indicates toward the correct theoretical investigation of incompressibility. Thus, it is worthy to investigate the incompressibility in various theoretical formalisms. Most of the relativistic and non-relativistic models reproduce the strength distribution very well for medium and heavy nuclei, like  $^{90}\text{Zr}$  and  $^{208}\text{Pb}$ , respectively. But at the same time it overestimates the excitation energy of Sn around 1 MeV. This low value of excitation energy demands lower value of nuclear matter incompressibility. Till date, lots of effort have been devoted to solve this problem like inclusion of pairing effect [128–134], mutually enhanced magicity (MEM) etc. [118]. But the pairing effect reduces the theoretical excitation energy only by 150 KeV in Sn isotopic series, which may not be sufficient to overcome the puzzle. Similarly, new experimental data are not in favor of MEM effect [119]. Measurement on excitation energy of  $^{204,206,208}\text{Pb}$  shows that the MEM effect should rule out in manifestation of stiffness of the Sn isotopes. Here, we use the relativistic Thomas-Fermi (RTF) and relativistic extended Thomas-Fermi (RETF) [135–139] with scaling and constraint approaches in the frame-work of non-linear  $\sigma - \omega$  model [99].

### 3.5 Analysis of Sn results

We calculate the GMR energy using both the scaling and constraint methods in the frame-work of relativistic extended Thomas-Fermi approximation using various



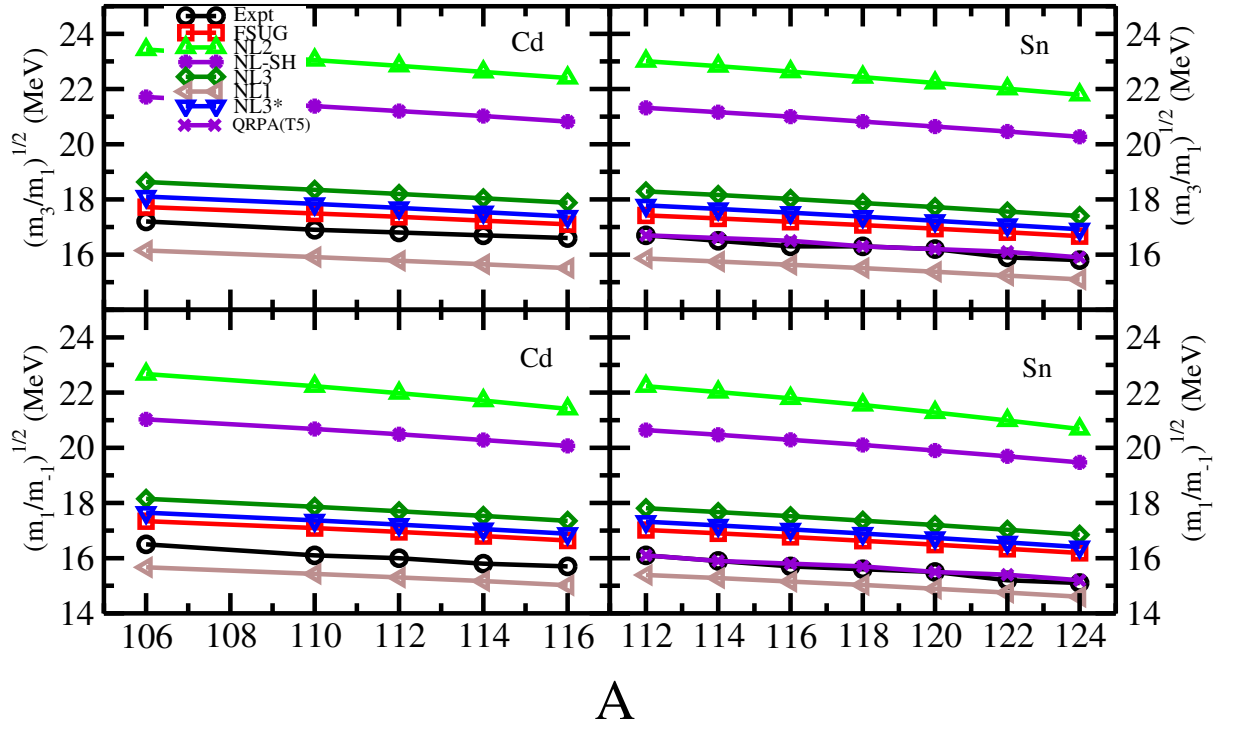


Figure 3.8: The isoscalar giant monopole excitation energy obtained by scaling method with various parameter sets are compared with experimental data of  $\sqrt{\frac{m_3}{m_1}}$  and  $\sqrt{\frac{m_1}{m_{-1}}}$  for Cd and Sn isotopes [125,126]. The upper and lower panels are  $\sqrt{\frac{m_3}{m_1}}$  and  $\sqrt{\frac{m_1}{m_{-1}}}$ , respectively.

parameter sets for Cd and Sn nuclei and compared with the excitation energy with moments ratio  $(m_3/m_1)^{1/2}$  and  $(m_1/m_{-1})^{1/2}$  obtained from multipole-decomposition analysis (MDA).

The basic reason to take a number of parameter sets is that the infinite nuclear matter incompressibility of these forces cover a wide range of values. For example, NL-SH has incompressibility 399 MeV, while that of NL1 is 210 MeV. From MDA analysis, we get different moments ratio, such as  $m_3/m_1$ ,  $m_0/m_1$  and  $m_1/m_{-1}$ . These ratios are connected to scaling, centroid and constraint energies, respectively. In Fig. 3.8, we have shown the  $(m_3/m_1)^{1/2}$  and  $(m_1/m_{-1})^{1/2}$  ratio for isotopic chains of Cd and Sn. The results are also compared with experimental data obtained from Research Center for Nuclear Physics (RCNP) [125,126]. From the figures, it is cleared that the experimental values lie between the results obtained from FSUG (FSUGold) and NL1

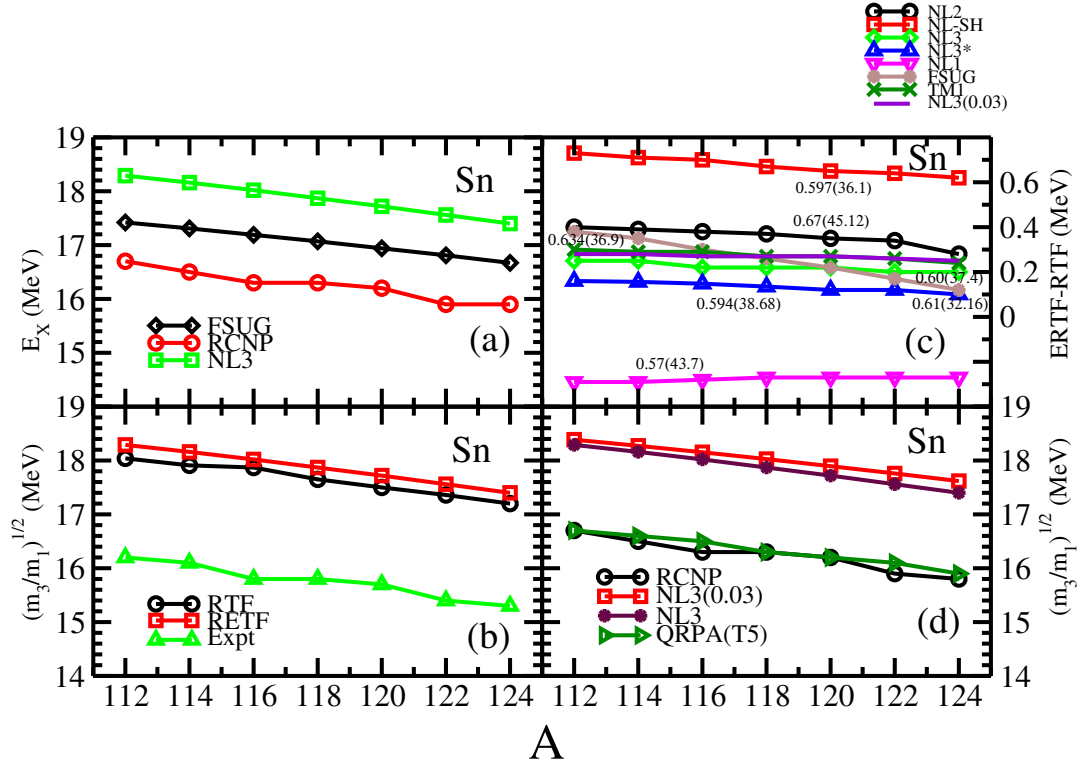


Figure 3.9: (a) The variation of giant monopole excitation energy  $E_x$  with mass number  $A$  for Sn isotopes, (b) the scaling monopole excitation energy within RETF and RTF formalisms compared with the experimental moments ratio  $\sqrt{m_3/m_1}$  [119], (c) variation of the difference of giant monopole excitation energy obtained from RETF and RTF ( $\Delta E = RETF - RTF$ ) formalisms with various parameter sets for Sn isotopic chain, (d) moments ratio  $\sqrt{m_3/m_1}$  for Sn isotopes obtained with NL3+ $\Lambda_V$  is compared with NL3, QRPA(T5) and experimental data.

Table 3.5: Moments ratio for Sn isotopes using RETF approximation with FSUGold and NL1 sets are compared with QRPA(T6) predictions [140].

Nucleus	$(m_3/m_1)^{1/2}(\text{MeV})$				$(m_1/m_{-1})^{1/2}(\text{MeV})$			
	QRPA (T6)	RETF (FSUG)	RETF (NL1)	Expt.	QRPA (T6)	RETF (FSUG)	RETF (NL1)	Expt.
$^{112}\text{Sn}$	17.3	17.42	15.86	16.7	17.0	17.2	15.39	16.1
$^{114}\text{Sn}$	17.2	17.32	15.75	16.5	16.9	16.9	15.28	15.9
$^{116}\text{Sn}$	17.1	17.19	15.63	16.3	16.8	16.77	15.15	15.7
$^{118}\text{Sn}$	17.0	17.07	15.51	16.3	16.6	16.63	15.03	15.6
$^{120}\text{Sn}$	16.9	16.94	15.38	16.2	16.5	16.44	14.89	15.5
$^{122}\text{Sn}$	16.8	16.81	15.24	15.9	16.4	16.34	14.75	15.2
$^{124}\text{Sn}$	16.7	16.67	15.1	15.8	16.2	16.19	14.6	15.1

force parameters. If one compares the experimental and theoretical results for  $^{208}\text{Pb}$ , the FSUG set gives better results among all. For example, the experimental data and theoretical result for monopole energies are  $14.17 \pm 0.1$  and 14.04 MeV, respectively. From this, one could conclude that the infinite nuclear matter incompressibility lies nearer to that of FSUG (230.28 MeV) parametrization. But experimental result on ISGMR in RCNP shows that the predictive power of FUSG is not good enough for the excitation energy of Sn isotopes. This observation is not only confined to RCNP data, but also persists in the more sophisticated RPA. In Table 3.5, we have given the results for QRPA(T6), RETF(FSUG) and RETF(NL1). The experimental data are also given to compare all these theoretical results.

The infinite nuclear matter incompressibility  $K_\infty$  with T6 parameter set [140] is 236 MeV and that of FSUG is 230.28 MeV. The similarity in incompressibility (small difference of 6 MeV in  $K_\infty$ ) may be a reason for their prediction in equal value of GMR. The table shows that, there is only 0.1 MeV difference in QRPA(T6) and RETF(FSUG) results in the GMR values for  $^{112}\text{Sn}$ – $^{116}\text{Sn}$  isotopes, but the results exactly match for the  $^{118}\text{Sn}$ – $^{124}\text{Sn}$  isotopes. This implies that for relatively higher mass nuclei, both the QRPA(T6) and RETF(FSUG) results are almost similar. If some one consider the experimental values of Sn isotopic series, then QRPA(T5) gives

Table 3.6: Moments ratio  $\sqrt{m_1/m_{-1}}$  for Pb isotopes within RETF is compared with pairing+ MEM results and experimental data.

Nuclear Mass	$(m_1/m_{-1})^{1/2}$ (MeV)			$\Sigma$ (MeV)	
	pairing+MEM	our work	Expt.	our work	Expt.
$^{204}\text{Pb}$	13.4	13.6	$13.7 \pm 0.1$	2.02	$3.3 \pm 0.2$
$^{206}\text{Pb}$	13.4	13.51	$13.6 \pm 0.1$	2.03	$2.8 \pm 0.2$
$^{208}\text{Pb}$	14.0	13.44	$13.5 \pm 0.1$	2.03	$3.3 \pm 0.2$

better result. For example, experimental value of  $(m_3/m_1)^{1/2}$  for  $^{112}\text{Sn}$  is  $16.7 \pm 0.2$  MeV and that for QRPA(T5) is 16.6 MeV. It is shown by V. Tselyaev et al. [140] that the T5 parameter set with  $K_\infty = 202$  MeV, better explains the excitation energy of Sn isotopes, but fails to predict the excitation energy of  $^{208}\text{Pb}$ . The experimental data of ISGMR energies for  $^{90}\text{Zr}$  and  $^{114}\text{Sn}$  lies in between the calculated values of T5 and T6 forces. In brief, we can say that the RPA analysis predicts the symmetric nuclear matter incompressibility within  $K_\infty = 202 - 236$  MeV and our semi-classical calculation gives it in the range 210 – 230 MeV. These two predictions almost agree with each other in the acceptable limit.

In Table 3.6, we have displayed the data obtained from a recent experiment [119] and compared our results. Column two of the table is also devoted to the result obtained from pairing plus MEM effect [118]. The data show clearly that our formalism (RETF) predicts the excitation energy more accurately than the result obtained by Pairing+ MEM prediction for Pb isotopes. For example, the difference between the pairing+MEM result and experimental observation is 0.3 MeV for  $^{204}\text{Pb}$ , which is away from the experimental error. It is only 0.1 MeV (within the error bar) in RETF calculation. This trend also follows for  $^{206}\text{Pb}$  and  $^{208}\text{Pb}$ . As it is mentioned earlier, we have not included the pairing correlation externally, yet the result is good enough in comparison with MEM+pairing as pairing has a marginal role for the calculation of collective excitation. Fig. 3.5(a) shows the variation of excitation energy with mass number A for Sn isotopes. This results can also be treated as the monopole excitation energy  $E_x$  with proton-neutron asymmetry ( $I = \frac{N-Z}{N+Z}$ ). The graph shows that the variation of monopole excitation energy  $E_x$  with both NL3 and FSUGold are following similar pattern as experimental one with a different magnitude. In Fig. 3.5(b),

we have compared our results obtained from RETF(NL3) and RTF(NL3) with the experimental data for Sn isotopes. The graph shows that there is only a small difference ( $\sim 0.2$  MeV) in scaling monopole energies obtained with RETF and RTF calculations. Interestingly, the RETF correction is additive to the RTF result instead of softening the excitation energy of Sn isotopes. To see the behavior of different parametrization, we have plotted Fig. 3.5(c), where it has shown the difference of  $\sqrt{m_3/m_1}$  obtained with RETF and RTF results ( $\Delta E = RETF - RTF$ ) for various parameter sets. For all sets, except NL1, we find  $\Delta E$  as positive. Thus, it is a challenging task to entangle the term which is the responsible factor to determine the sign of RETF-RTF. Surprisingly, for most of the parameter sets, RTF is more towards experimental data. In spite of this, one cannot say anything about the qualitative behavior of RETF. Because, the variation of the density at the surface taken care by the RETF formalism, which is essential. One more interesting observation is that, when one investigate the variation of  $\Delta E$  in the isotopic chain of Sn, it remains almost constant for all the parameter sets, except FSUGold. In this context, FSUGold behaves differently.

Variation of RETF-RTF with neutron-proton asymmetry for FSUGold set shows some possible correlation of RETF with the symmetry energy, which is absent in all other parameter sets. Now it is essential to know, in which respect the FSUGold parameter set is different from other. The one-to-one interaction terms for NL3, NL2, NL1 and NL-SH have similar couplings. However, the FSUGold is different from the above parameters in two aspects, i.e., two new coupling constants are added. One corresponds to the self-interaction of  $\omega$  and other one corresponds to the isoscalar-isovector meson coupling. It is known that self-interaction of  $\omega$  is responsible for softening the EOS [87, 141] and the isoscalar-isovector coupling takes care the softening of symmetric nuclear matter [142]. The unique behavior shown by the FSUGold parametrization may be due to the following three reasons:

1. introduction of isoscalar-isovector meson coupling  $\Lambda_V$ ,
2. introduction of self-coupling of  $\omega$ -meson,
3. or simultaneous introduction of both these two terms with refitting of parameter set with new constraint.

In order to discuss the first possibility, we plotted NL3+ $\Lambda_V(0.03)$  in Fig. 3.5(d). The graph shows that there is no difference between NL3 and NL3+ $\Lambda_V$ , except the later set predicts a more positive RETF-RTF. It is well known that, the addition of  $\Lambda_V$  coupling, i.e., NL3+ $\Lambda_V(0.03)$  gives a softer symmetry energy [143]. This implies that, models with softer energy have greater difference in RETF and RTF. At a particular proton-neutron asymmetry, RETF-RTF has a larger value for a model with softer symmetry energy. This observation is not conclusive, because all the parameter sets do not follow this type of behavior. Quantitatively, the change of RETF-RTF in the Sn isotopic series is about 70% with FSUGold force, while this is only 20 – 30% in NL3 and other parameter sets.

In Table 3.7, we have listed the  $\rho$ -meson contribution to the total binding energy. From the analysis of our results, we find that only  $\rho$ -contribution to the total binding energy change much more than other quantity, when one goes from RTF to RETF. But this change is more prominent in FSUGold parameter set than other sets like NL1, NL2, NL3 and NL-SH. Simple assumption says that the absent of  $\Lambda_V$  coupling may be the reason for this behavior in rest of the parameter sets. But we have checked for the parameter NL3+ $\Lambda_V$ , which does not follow the assumption. This also shows similar behavior like other sets. In Table 3.8, we have given the results for FSUGold, NL3+ $\Lambda_V$  and NL1. The data show a huge difference of monopole excitation energy in RETF and RTF with FSUGold parameter set. For example, the  $\rho$ -meson contribution to the GMR in RETF for  $^{112}\text{Sn}$  is 21.85 MeV, while in RTF it is only 0.00467 MeV. However, this difference is nominal in NL3+ $\Lambda_V$  parameter set, i.e., it is only 0.48 MeV. Similarly, this value is 1.18 MeV in NL1 set. The contribution of  $\rho$ -meson to total energy comes from two terms: (i) one from  $\Lambda_V R^2 V^2$  and other (ii) from  $\rho^2$ . We have explicitly shown that contribution comes from  $\Lambda_V R^2 V^2$  makes a huge difference between the GMR obtained from RETF and RTF formalisms. This type of contribution does not appear from NL3+ $\Lambda_V$ . For example, in  $^{112}\text{Sn}$  the contribution of  $\Lambda_V R^2 V^2$  with RETF formalism is -6.0878 MeV, while with RTF formalism is -5.055 MeV.

The above discussion gives us significant signature that the contribution of  $\Lambda_V$  may be responsible for this anomalous behavior. But an immediate question arises, why NL3+ $\Lambda_V$  parameter set does not show such type of effects, inspite of having

Table 3.7: Contribution of the  $\rho$ -meson to the total binding energy in the RTF and RETF approximations with FSUGold, NL1 and NL3+ $\Lambda_V$  parameter set. RETF represent  $\rho$  meson contribution to total energy from  $R^2$  term and RETF $\Lambda_V$  represent contribution from the  $\Lambda_V R^2 V^2$ .

Nucleus	FSUGold				NL3(0.03)		NL1	
	RETF	RETF $\Lambda_V$	RTF $\Lambda_V$	RTF	RETF	RTF	RETF	RTF
$^{112}\text{Sn}$	21.85	-6.66	-0.00130	0.00467	20.60	20.12	17.91	16.73
$^{114}\text{Sn}$	28.72	-8.64	-0.00202	0.00664	27.11	26.48	23.51	22.00
$^{116}\text{Sn}$	36.42	-10.83	-0.00248	0.00829	34.40	33.62	29.73	27.90
$^{118}\text{Sn}$	44.87	-13.23	-0.00298	0.01013	42.42	41.499	36.52	34.37
$^{120}\text{Sn}$	54.04	-15.82	-0.00353	0.01213	51.13	50.05	43.84	41.37
$^{122}\text{Sn}$	63.88	-18.58	-0.00411	0.01429	60.48	59.24	51.63	48.85
$^{124}\text{Sn}$	74.33	-21.49	-0.00473	0.01660	70.43	69.03	59.84	56.76

$\Lambda_V R^2 V^2$  term. This may be due to the procedure in which  $\Lambda_V R^2 V^2$  term is interpreted in these two parameter sets. In NL3+ $\Lambda_V(0.03)$ , the  $\Lambda_V R^2 V^2$  term is not added independently. The  $\Lambda_V$  and  $g_\rho$  are interdependent to each other to fix the binding energy and difference in neutron and proton rms radii  $R_n$ - $R_p$ . But in FSUGold,  $\Lambda_V$  coupling constant is incorporate independently to reproduce the nuclear observable.

In Table 3.8, we have listed the incompressibility of some of the selected nuclei in scaling  $^S K_A$  and constraint  $^C K_A$  calculations. This results are compared with

Table 3.8:  $^S K_A$  and  $^C K_A$  are incompressibility for finite nuclei obtained from scaling and constraint methods, respectively are compared with the values obtained from the equation of state (EOS).

Nucleus	NL3			FSUGold		
	$^S K$	$^C k$	$^{EOS} K$	$^S K$	$^C K$	$^{EOS} K$
$^{208}\text{Pb}$	164.11	149.96	145	147.37	134.57	138.42
$^{116}\text{Sn}$	164.64	155.39	131.57	147.11	139.71	127.64
$^{40}\text{P}$	136.70	110.43	105	123.40	100.36	102.53
$^{40}\text{Ca}$	145.32	134.47	105	130.93	123.15	102.53

the computed values obtained from the equation of state (EOS) model. To evaluate the incompressibility from the EOS, we have followed the procedure as discussed in Refs. [144,145]. M. Centelles et al. [144], parametrized the density for finite nucleus as  $\rho_A = \rho_0 - \rho_0/(1 + c * A^{1/3})$  and obtained the asymmetry coefficient  $a_{sym}$  of the nucleus with mass A from the EOS at this particular density. Here also, we have used the same parametric form of the density and obtained the incompressibility for finite nucleus from the EOS. For example,  $\rho_A = 0.099$  for  $A = 208$  in FSUGold parameter set, and the calculated incompressibility is  $\sim 145$  MeV at this particular density. We have also calculated the incompressibility independently in Thomas-Fermi and extended Thomas-Fermi using scaling and constraint calculations, which are 161 MeV and 146.1 MeV, respectively.

### 3.6 Summary and Conclusions

In summary, we have calculated the isoscalar giant monopole resonance for O, Ca, Ni, Sn, Pb, Z=114, and Z=120 isotopic series starting from the proton to the neutron drip-lines. We used four successful parameter sets, NL1, NL3, NL3\*, and FSUGold, with a wide range of incompressibility starting from 211.7 MeV to 271.76 MeV to see the dependency of the ISGMR on  $K_\infty$ . Also, we have analyzed the predictions of ISGMR with these forces, which originate from various interactions and found that whatever may be their origin, the differences in ISGMR predicted by them are found to be marginal in the super heavy region. A recently developed scaling approach in a relativistic mean field theory is used. A simple, but accurate constrained approximation is also performed to evaluate the isoscalar giant monopole excitation energy. From the scaling and constrained ISGMR excitation energies, we have evaluated the resonance width  $\Sigma$  for the whole isotopic series. This is obtained by taking the root mean square difference of  $E_x^s$  and  $E_x^c$ . The value of  $E_x^s$  is always higher than the constrained result  $E_x^c$ . In a sum rule approach, the  $E_x^s$  can be compared with the higher and  $E_x^c$  as the lower limit of the resonance width. In general, we found an increasing trend of  $\Sigma$  for both the light and super heavy regions near the proton and neutron drip-lines. The magnitude of  $\Sigma$  is predicted to be a minimum in the vicinity of N=Z or in the neighborhood of a double closed nucleus and it is a maximum for



highly asymmetric systems. We have also estimated the incompressibility of finite nuclei. For some specific cases, the incompressibility modulus is compared with the nuclear matter incompressibility and found a linear variation among them. It is also concluded that the nucleus becomes less compressible with the increase of neutron or proton number in an isotopic chain. Thus neutron-rich matter, like neutron stars as well as drip-line nuclei, are less compressible than normal nuclei. In case of finite drip-line nuclei, the nucleus is incompressible, although it possess a normal density. In brief, we analyzed the predictive power of various force parameters, like NL1, NL2, NL3, NI-SH and FSUGold in the frame-work of relativistic Thomas-Fermi and relativistic extended Thomas-Fermi approaches for giant monopole excitation energy of Sn-isotopes. Then the calculation is extended to some other relevant nuclei. The analysis shows that Thomas-Fermi approximation gives comparable results with pairing+MEM data. It exactly reproduces the experimental data for Sn isotopes, when the incompressibility of the force parameter is within 210 – 230 MeV, however, fails to reproduce the GMR data for other nuclei within the same accuracy.

We have qualitatively analyzed the difference in GMR energies RETF-RTF using RETF and RTF formalisms in various force parameters. The FSUGold parameter set shows different behavior from all other forces. Also, extended our calculations of monopole excitation energy for Sn isotopes with a force parametrization having softer symmetry energy (NL3+  $\Lambda_V$ ). The excitation energy decreases with the increase of proton-neutron asymmetry agreeing with the experimental trend. In conclusion, after all these thorough analysis, it seems that the softening of Sn isotopes is an open problem for nuclear theory and more work in this direction are needed.

## Chapter 4

# Perturbative constrained calculation of excitation energy of ISGMR and IVGDR in semiclassical RMF theory.

In last two chapter, we have extensively discussed the isoscalar giant monopole resonances in super heavy and medium-heavy nuclei. Semi-classical approximation like RTF and RETF are used, which are proved very successful to calculate the collective excitation. We have used constrained and scaling calculations for the excitation energy of ISGMR. In this chapter, we discuss a new constrained calculation, which we have developed to calculate the excitation energy of both ISGMR and IVGDR. From the theoretical point of view both the old and new constrained calculations are different from each other, but gives similar results. In old constrained calculation, we minimize the constrained energy functional with a constrained parameter  $\lambda$ . We get a different value of constrained energy with a different value of  $\lambda$  and double derivative of constrained energy with respect to  $\lambda$  gives the constrained excitation energy. The new constrained calculation based on the perturbative approaches, in which we expand the energy functional in Taylor series around equilibrium state. We calculated the excitation energy for some spherical (or double closed ) nuclei, where the experimental data are available.

## 4.1 Introduction

The nuclear matter incompressibility ( $K_\infty$ ) is a measure of stiffness of the equation of state (EOS). It can be calculated from the curvature of the EOS around the saturation density ( $\rho_0$ ). This quantity is important in nuclear physics because it is related to many properties of finite nuclei (such as radii, masses and giant resonances), the dynamics of heavy-ion collisions, neutron stars and supernovae collapses [19, 146]. As  $K_\infty$  is not an observable, its value must be deduced from a measurable quantity. In this respect, an important source of information on  $K_\infty$  is provided by the measurements of compression modes, such as the isoscalar giant monopole resonance (ISGMR), in finite nuclei, in particular in  $^{208}\text{Pb}$ . An accepted value  $K_\infty = 240 \pm 20$  MeV, predicted by the majority of mean field models, extracted from different analysis of experimental data and theoretical calculation [147].

On the other hand, the existence of strong resonances in the photo-absorption cross sections was established almost seventy years ago [148] and theoretically explained few years later [149, 150]. These resonances, identified with the isovector giant dipole resonance (IVGDR), are correlated via the electrical polarizability with the neutron skin thickness of neutron rich nuclei and with the properties of the nuclear symmetry energy around saturation [151, 152].

The ISGMR and IVGMR can be understood as small amplitude oscillations, which are the responses of the nucleus to an external field generated by electromagnetic or hadronic probes. The standard theory to deal with these oscillations is the random-phase approximation (RPA), which allows to study microscopically giant resonances. The key output provided by the RPA calculations is the strength distribution  $S_Q(E)$  associated to a given excitation operator  $\mathbf{Q}$ . If  $S_Q(E)$  is concentrated in a narrow region of the energy spectrum, which is usually the case of the ISGMR and IVGMR at least for heavy stable nuclei, the knowledge of few low energy weighted moments of  $S_Q(E)$  (sum rules) allows to estimate the average excitation energy of the resonances. In some particular cases it is possible to express some odd sum rules in a compact form involving only ground-state properties, which avoids the calculation of the strength distribution [76]. However, the full quantal calculation of these sum rules is still complicated because the exact ground-state is, in general, unknown. Introducing

additional approximations, some sum rules can be calculated in a rather simple way, as for instance the cubic energy weighted sum rule, which can be computed by using the scaling method [19, 76, 153] or the inverse energy weighed sum rule, which can be obtained through constrained Hartree-Fock (HF) calculations [19, 153–155].

The theoretical study of giant resonances in the relativistic domain has been usually done through relativistic RPA (RRPA) calculations. The RRPA approximation corresponds to the small amplitude limit of the time-dependent relativistic mean field (RMF) theory [156–158]. On the other hand the time-dependent theory has also been directly used to study the isovector dipole [159] as well as the isoscalar and isovector quadrupole [159] and monopole [160] oscillations. As difference with the non-relativistic case, the sum rule theorems, which relate different moments of the RRPA strength with ground-state properties computed at RMF level, have not been proved in the relativistic domain [117]. There are few relativistic constrained calculations available in the literature [103–105, 117, 158]. In Ref. [158] the results of constrained RMF calculations of the  $m_{-1}$  sum rule were compared with the corresponding RRPA values and it was suggested that the RRPA  $m_{-1}$  moment could be estimated from a RMF calculation. More recently, in Ref. [117], this suggestion was carefully analyzed for several nuclei along the periodic table using two different RMF parameter sets. It was found an excellent agreement between the average energies of ISGMR obtained through RMF constrained calculation and extracted from RRPA results. In Ref. [81] the scaling approach to the isoscalar giant monopole and quadrupole resonances in relativistic Thomas-Fermi (RTF) theory [161, 162] was discussed in detail. It was found that the semi-classical average excitation energies reproduced well the RRPA results. In the same reference the excitation energies of the ISGMR were also calculated performing RTF constrained calculations finding good agreement with the constrained RMF results of Ref. [105]. As a conclusion, these results together with the conjecture of Ref. [158] points out that the scaling method and constrained calculations using the semi-classical RTF energy density functional may be a very efficient and simplified way to estimate the average excitation energy of some giant resonances. Although the constrained RTF approach has been used in [81] to compute the average excitation energy of the ISGMR, in this chapter we want to use a new constrained method applied together with the RTF approach, which is able

to study not only the ISGMR but also the IVGDR. This new constrained calculation is based on a Taylor series expansion of the constrained energy density functional around the equilibrium. In Section 4.2 we outline the general formalism to calculate excitation energy of ISGMR and ISVGDR. In Section 4.3 we discussed the application of relativistic Thomas-Fermi approximation to calculate the energy and particle density. Section 4.4 is dedicated to the explanation of perturbative approaches to calculate the excitation energy of ISGMR and ISVGDR. Results of our new method with old one are given in section 4.5 and concluded in section 4.6.

## 4.2 Formalism

The strength distribution associated to an excitation operator  $\mathbf{Q}$  is defined as

$$S_Q(E) = \sum_{n \neq 0} |\langle n | \mathbf{Q} | 0 \rangle|^2 \delta(E - E_n), \quad (4.1)$$

where  $|0\rangle$  and  $|n\rangle$  are the ground and excited eigenstates, respectively, of the exact Hamiltonian  $H = T + V$  and  $E_n$  is the excitation energy.

The energy weighted moments, also known as sum rules, are defined as

$$m_k = \int_0^\infty E^k S_Q(E) dE = \sum_{n \neq 0} E_n^k |\langle n | \mathbf{Q} | 0 \rangle|^2, \quad (4.2)$$

which allow to estimate the average excitation energy as

$$\tilde{E}_K = \sqrt{\frac{m_k}{m_{k-2}}}. \quad (4.3)$$

In this work we concentrate in the study of the  $\tilde{E}_1$  average energy to estimate the excitation of the ISGMR and the IVGDR. A very useful approximation arises when the exact energy eigenstates of the Hamiltonian  $H$  in (4.1) is replaced by the one-hole-one particle (1p1h) RPA ones. In this case it is possible to show that some sum rules, in particular  $m_1$  and  $m_{-1}$ , can be exactly obtained by replacing the RPA ground-state by the uncorrelated Hartree-Fock (HF) or by performing constrained HF calculations (see [76] for more details). In the monopole case, the energy weighted sum rule  $m_1$  is almost a model independent quantity and according to the Thouless theorem it is given by

$$m_1 = \sum_n E_n |\langle n | \sum_{i=1}^A |0\rangle|^2 = 2A \frac{\hbar^2}{m} \langle r^2 \rangle. \quad (4.4)$$

For the isovector dipole, the previous simple approach provided in Eq.(4.4) does not hold good because the excitation operator  $\mathbf{Q}$  does not commute, in general, with the potential part  $V$  of the Hamiltonian. In the isovector case the full calculation of the  $m_1$  sum rule is complicated and usually this moment is factorized as

$$m_1 = m_1^0(1 + \kappa), \quad (4.5)$$

where  $m_1^0$  is the sum rule computed assuming  $[Q, V] = 0$  and  $\kappa$  is the so-called enhancement factor. In the dipole case, the  $m_1^0$  is given by the kinetic Thomas-Reiche-Kuhn (TRK) term and therefore, the full energy weighted sum rule reads as

$$m_1 = \frac{\hbar^2}{2m} \frac{NZ}{A} (1 + \kappa). \quad (4.6)$$

For relativistic model the TRK enhancement factor in nuclear matter is given by [163]

$$\kappa(k_F) = \frac{m}{\sqrt{m^{*2} + k_F^2}} - 1, \quad (4.7)$$

where  $k_F$  the Fermi momentum. Notice that in nuclear matter  $\kappa$  is a function of  $k_F$ . In order to estimate the average enhancement factor in finite nuclei, we use (4.7) together with a local density approximation:

$$\kappa = \frac{1}{A} \int \kappa(k_F) \rho(r) \mathbf{d}\mathbf{r}, \quad (4.8)$$

where the local Fermi momentum  $k_F$  is related to the finite nucleus density by  $k_F(r) = (3\pi^2 \rho(r))^{1/3}$ .

To obtain the inverse energy-weighted sum rule, we take into account the fact that this sum rule computed at 1p1h RPA level, according to the dielectric theorem, can also be obtained from a constrained HF calculation performed with the Hamiltonian  $H + \lambda Q$ , where  $H$  is the Hamiltonian that describe the nucleus and  $Q$  the one-body excitation operator as

$$m_{-1} = \sum_n \frac{|\langle n|Q|0\rangle|^2}{E_n} = \frac{1}{2} \frac{\partial \langle \lambda|Q|\lambda\rangle}{\partial \lambda} \Big|_{\lambda=0} = \frac{1}{2} \frac{\partial^2 \langle \lambda|H|\lambda\rangle}{\partial \lambda^2} \Big|_{\lambda=0}, \quad (4.9)$$

where  $|\lambda\rangle$  is the HF ground state of the constrained Hamiltonian  $H + \lambda Q$ .

### 4.3 Relativistic Thomas-Fermi approximation

In this work we describe the average excitation energy of ISGMR and IVGDR by using Thomas-Fermi approximation to the RMF theory discussed in early literature [80, 81, 161, 162]. A reason for using semi-classical technique is to study giant resonances is the fact that these oscillations are strong collective motion where shell effects have only a marginal impact [81, 164]. In the linear RMF model nucleons interact via the exchange of the effective  $\sigma$ ,  $\omega$  and  $\rho$  mesons [8]. However, due to the high incompressibility  $K_\infty$  predicted by this model, self-interactions of the  $\sigma$  meson, through non-linear terms, have been introduced in the formalism to reduce  $K_\infty$  to a more realistic value [99]. The starting point of the semi-classical RMF theory is the nucleon-nucleon interacting effective Lagrangian density, which can be written as

$$\mathcal{H} = \mathcal{E} + g_v V \rho + g_\rho R \rho_3 + e \mathcal{A} \rho_p + \mathcal{H}_f, \quad (4.10)$$

where  $\rho = \rho_n + \rho_p$  is the baryon density,  $\rho_3 = (\rho_p - \rho_n)/2$  is the isovector density and  $\mathcal{E}$  the nucleon energy density, which at RTF level can be written as [80, 81, 161, 162]

$$\mathcal{E} = \sum_q \frac{1}{8\pi^2} [k_{F_q}^3 \epsilon_{F_q} + k_{F_q}^3 \epsilon_{F_q} - m^{*4} \frac{k_{F_q} + \epsilon_{F_q}}{m^*}]. \quad (4.11)$$

For each kind of nucleon ( $q = n, p$ ), the local Fermi momentum  $k_{F_q}$  and energy  $\epsilon_{F_q}$  are defined as

$$k_{F_q} = (3\pi^2 \rho_q)^{1/3} \quad ; \quad \epsilon_{F_q} = \sqrt{k_{F_q}^2 + m^{*2}}. \quad (4.12)$$

In Eq. (4.10),  $\mathcal{H}_f$  stands for the free contribution of the meson fields  $\phi$ ,  $V$  and  $R$ , associated to the  $\sigma$ ,  $\omega$  and  $\rho$  mesons, and for the Coulomb field  $\mathcal{A}$ . This contribution reads

$$\begin{aligned} \mathcal{H}_f = & \frac{1}{2} [(\vec{\nabla}\phi)^2 + m_s^2 \phi^2] + \frac{1}{3} b \phi^3 + \frac{1}{4} c \phi^4 - \frac{1}{2} [(\vec{\nabla}V)^2 + m_v^2 V^2] \\ & - \frac{1}{2} [(\vec{\nabla}R)^2 + m_\rho^2 R^2] - \frac{1}{2} (\vec{\nabla}\mathcal{A})^2, \end{aligned} \quad (4.13)$$

where  $m_s$ ,  $m_v$  and  $m_\rho$  are the masses of the mesons and  $m^*$ , entering in Eqs.(4.11) and (4.12), is the nucleon effective mass defined by  $m^* = m - g_s \phi$ . In these equations  $g_s$ ,  $g_v$ ,  $g_\rho$  and  $e$  are the coupling constants for the  $\sigma$ ,  $\omega$  and  $\rho$  mesons and for the photon, respectively. In Eq.(4.13)  $b$  and  $c$  stand for the coupling constants associated

to the  $\sigma$  meson non-linear terms. These self-interactions of the  $\sigma$ - meson generates analogous effect of three body interaction due to its *off-shell* meson couplings. These self-interactions are also essential for the saturation properties of infinite nuclear matter [165–167].

The semi-classical ground-state densities and meson fields are obtained by solving the variational equations derived from the energy density (4.10) constrained by the condition of fixed neutron ( $N$ ) and proton ( $Z$ ) numbers, which read

$$\epsilon_{F_n} + g_v V - \frac{1}{2}g_\rho R - \mu_n = 0, \quad (4.14)$$

$$\epsilon_{F_p} + g_v V + \frac{1}{2}g_\rho R + e\mathcal{A} - \mu_p = 0, \quad (4.15)$$

$$\Delta V - m_v^2 V + g_v \rho = 0, \quad (4.16)$$

$$\Delta R - m_\rho^2 R + g_\rho \rho_3 = 0, \quad (4.17)$$

$$\Delta \phi - m_s^2 \phi + g_s \rho_s - b\phi^2 - c\phi^3 = 0, \quad (4.18)$$

and

$$\Delta \mathcal{A} + e\rho_p = 0. \quad (4.19)$$

In Eqs.(4.14) and (4.15)  $\mu_n$  and  $\mu_p$  are the neutron and proton chemical potentials, respectively, introduced to ensure the right  $N$  and  $Z$  values. In Eq.(4.18)  $\rho_s$  is the semi-classical scalar density given by

$$\rho_s = \frac{\partial \mathcal{E}}{\partial m^*} = \sum_q \frac{m^*}{2\pi^2} [k_{F_q} \epsilon_{F_q} - m^{*2} \frac{k_{F_q} + \epsilon_{F_q}}{m^*}]. \quad (4.20)$$



## 4.4 The constrained perturbative approach

We apply now the constrained method to estimate the excitation energy of the ISGMR and IVGDR. In the semi-classical context one has to minimize the constrained energy density functional [81]

$$\int [\mathcal{H} - \mu_n \rho_n - \mu_p \rho_p - \lambda Q] d\mathbf{r} = E(\lambda) - \lambda \langle Q \rangle. \quad (4.21)$$

In previous studies of the ISGMR using the constrained method [81, 117, 164] one minimizes Eq. (4.21) for several values of  $\lambda$  and then computes numerically the derivatives respect to  $\lambda$ , which define the  $m_{-1}$  sum rule (see Eq.(4.9)) , using three- or five-point formulas. This technique may also be applied, in principle, to estimate the excitation energy of the IVGDR using a deformed code. We present here an alternative route which avoids the explicit use of deformation. Keeping in mind that the derivatives respect to the parameter  $\lambda$  in Eq.(4.9) are computed at  $\lambda = 0$ , we expand the constrained energy density functional (4.21) around equilibrium in powers of  $\lambda$  up to quadratic terms, which according to Eq.(4.9), is needed to compute the  $m_{-1}$  sum rule. To this end, we write the nuclear densities and meson fields as the sum of the unperturbed solutions, obtained by solving self-consistently Eqs.(4.14)-(4.20), plus a perturbative contribution, which is linear in  $\lambda$  and has the same angular dependence as the excitation operator  $Q$ . Notice that, as far as the right number of particles is obtained by the unperturbed density, the additional constraint  $\int \delta \rho_n(\mathbf{r}) d\mathbf{r} = \int \delta \rho_p(\mathbf{r}) d\mathbf{r} = 0$  must be imposed. This can be achieved by introducing additional contributions to the neutron and proton chemical potentials,  $\delta \mu_n$  and  $\delta \mu_p$ , respectively, which are also linear in the parameter  $\lambda$ .

The independent term of the constrained energy functional (4.21) in powers of  $\lambda$  is just the unperturbed energy  $E_0$  of the ground-state of the nucleus. The linear term in  $\lambda$  are proportional to the equation of motion of the unperturbed problem Eqs.(4.14)-(4.20), while the quadratic contribution provides the set of equations of motion corresponding to the perturbative part to the nuclear densities and meson fields by applying the variations principle. According to Eq. 4.9,  $m_{-1}$  sum rule is given by one half of the second derivative of the constrained energy with respect to the parameter  $\lambda$ . At this point two important comments are in order. First, the equations of motion of the perturbative part of the nuclear densities and fields can

also be obtained by performing a second order variation with respect to the densities and fields in the equations of motion of the unperturbed problem, Eqs. (4.14)-(4.20). Second, by replacing the solutions of the perturbative contribution to densities and fields in the second derivative of the energy density functional respect to the parameter  $\lambda$ , one can recast this expression as one half of the first derivative of the excitation operator  $Q$  respect to  $\lambda$ , in agreement with Eq.(4.9). These two comments point out that this perturbative approach to the calculation of the  $m_{-1}$  sum rule is properly formulated. We will now apply this perturbative constrained method to estimate the excitation energies of the ISGMR and IVGDR.

#### 4.4.1 Isoscalar giant monopole resonance

The ISGMR is a collective excitation in which proton and neutron vibrate in a phase to each other. It corresponds to the radial oscillation of nucleus around its equilibrium radius. In order to calculate excitation energy we write the excitation operator as  $Q = r^2 - \langle r^2 \rangle_0$ , where  $\langle r^2 \rangle_0^{1/2}$  is the rms radius computed using the unperturbed equilibrium density  $\rho_0$ . We apply the constrained perturbative method by writing the perturbative nuclear densities and fields as  $\lambda\delta\rho_n$ ,  $\lambda\delta\rho_p$ ,  $\lambda\delta V_0$ ,  $\lambda\delta\phi$ ,  $\lambda\delta R$  and  $\lambda\delta\mathcal{A}$ . Due to the spherical symmetry of the problem, we shall also introduce the corrections  $\lambda\delta\mu_n$  and  $\lambda\delta\mu_p$  to the neutron and proton chemical potentials. With all these ingredients

we expand Eq. (4.21) up to order  $\lambda^2$  obtaining

$$\begin{aligned}
\tilde{E} = & \int dr \left[ \mathcal{H}^0 + \lambda \left[ \left( \epsilon_{F_n}^0 + g_v V^0 - \frac{1}{2} g_\rho R^0 \right) \delta \rho_n \right. \right. \\
& + \left( \epsilon_{F_p}^0 + g_v V^0 + \frac{1}{2} g_\rho R^0 + e \mathcal{A}^0 \right) \delta \rho_p + (\Delta \mathcal{A}^0 + e \rho_p^0) \delta \mathcal{A} \\
& + \left( \Delta V^0 - m_v^2 V^0 + g_v \rho^0 \right) \delta V + \left( \Delta R^0 - m_\rho^2 R^0 + g_\rho \rho_3^0 \right) \delta R \\
& - \left( \Delta \phi - m_s^2 \phi^0 + g_s \rho_s^0 - b \phi^{02} - c \phi^{03} \right) \delta \phi \left. \right] \\
& + \frac{\lambda^2}{2} \left[ \left( \frac{\partial \epsilon_{F_n}^0}{\partial \rho_n^0} \delta \rho_n - g_s \frac{\partial \epsilon_{F_n}^0}{\partial m_0^*} \delta \phi + g_v \delta V - \frac{1}{2} g_\rho \delta R \right) \delta \rho_n \right. \\
& + \left( \frac{\partial \epsilon_{F_p}^0}{\partial \rho_p^0} \delta \rho_p - g_s \frac{\partial \epsilon_{F_p}^0}{\partial m_0^*} \delta \phi + e \delta \mathcal{A} + g_v \delta V + \frac{1}{2} g_\rho \delta R \right) \delta \rho_p \\
& + \left( g_v \delta \rho + \Delta \delta V - m_v^2 \delta V \right) \delta V + \left( g_\rho \delta \rho_3 + \Delta \delta R - m_\rho^2 \delta R \right) \delta R \\
& + \left( e \delta \rho_p + \Delta \delta \mathcal{A} \right) \delta \mathcal{A} + \left( \left( g_s^2 \frac{\partial \rho_s^0}{\partial m^{*0}} + 2b \phi^0 + 3c \phi^{02} \right) \delta \phi \right. \\
& - \left. g_s \frac{\partial \epsilon_{F_n}^0}{\partial m^{*0}} \delta \rho_n - g_s \frac{\partial \epsilon_{F_p}^0}{\partial m^{*0}} \delta \rho_p - \Delta \delta \phi + m_s^2 \delta \phi \right) \delta \phi \left. \right] \\
& - \mu_n^0 \rho_n^0 - \mu_p^0 \rho_p^0 - \left( \mu_n^0 + \lambda \delta \mu_n \right) \lambda \delta \rho_n - \left( \mu_p^0 + \lambda \delta \mu_p \right) \lambda \delta \rho_p \\
& - \lambda (r^2 - \langle r^2 \rangle^0) (\delta \rho_n + \delta \rho_p) \left. \right]. \tag{4.22}
\end{aligned}$$

In the above equation the superscript 0 indicates quantities which are calculated using the unperturbed densities and fields. The linear contributions of the perturbative components of densities and fields in Eq.(4.22) vanish, because their prefactors are just the motion equations of the unperturbed densities and fields Eqs.(4.14)-(4.20), which are zero for the self-consistent solutions. Therefore, the constrained energy Eq.(4.21) becomes a quadratic function of the perturbative corrections to the nuclear densities and meson fields, from where the motion equations for  $\delta \rho_n$ ,  $\delta \rho_p$ ,  $\delta V$ ,  $\delta R$ ,  $\delta \mathcal{A}$  and  $\delta \phi$  are easily obtained:

$$\frac{\partial \epsilon_{F_n}^0}{\partial \rho_n^0} \delta \rho_n - g_s \frac{\partial \epsilon_{F_n}^0}{\partial m_0^*} \delta \phi + g_v \delta V - \frac{1}{2} g_\rho \delta R - \delta \tilde{\mu}_n - r^2 = 0, \tag{4.23}$$

$$\frac{\partial \epsilon_{F_p}^0}{\partial \rho_p^0} \delta \rho_p - g_s \frac{\partial \epsilon_{F_p}^0}{\partial m_0^*} \delta \phi + e \delta \mathcal{A} + g_v \delta V + \frac{1}{2} g_\rho \delta R - \delta \tilde{\mu}_p - r^2 = 0, \tag{4.24}$$

$$g_v \delta \rho + \Delta \delta V - m_v^2 \delta V = 0, \quad (4.25)$$

$$g_\rho \delta \rho_3 + \Delta \delta R - m_\rho^2 \delta R = 0, \quad (4.26)$$

$$(e \delta \rho_p + \Delta \delta \mathcal{A} = 0, \quad (4.27)$$

and

$$\left( g_s^2 \frac{\partial \rho_s^0}{\partial m^{*0}} + 2b\phi^0 + 3c\phi^{02} \right) \delta \phi - g_s \frac{\partial \epsilon_{F_n}^0}{\partial m^{*0}} \delta \rho_n - g_s \frac{\partial \epsilon_{F_p}^0}{\partial m^{*0}} \delta \rho_p - \Delta \delta \phi + m_s^2 \delta \phi = 0. \quad (4.28)$$

In Eqs.(4.23) and (4.24)  $\delta \tilde{\mu}_q = \delta \mu_q - < r^2 >^0$  ( $q = n, p$ ). The self-consistent solution of the set of equations Eqs.(4.23)-(4.24) gives the perturbed neutron and proton densities,  $\delta \rho_n$  and  $\delta \rho_p$ , respectively, as well as the corrections to the fields  $\delta V$ ,  $\delta \phi$ ,  $\delta R$  and  $\delta \mathcal{A}$ , where  $\delta_n$  and  $\delta_p$  are the transition densities. The  $m_{-1}$  sum rule is given by the second order derivative of the semi-classical energy  $E(\lambda)$  (see Eq.(4.21)) with respect to the parameter  $\lambda$ . Combining Eq.(4.22) with the motion equations (4.23)-(4.24) for the perturbative nuclear densities and meson and photon fields are easily obtained

$$m_{-1} = \int \left( \delta \tilde{\mu}_n \delta \rho_n + \delta \tilde{\mu}_p \delta \rho_p + r^2 \delta \rho \right) d\mathbf{r}, \quad (4.29)$$

where  $\delta \rho = \delta \rho_n + \delta \rho_p$ . Taking into account the constraint  $\int \delta \rho_q d\mathbf{r} = 0$ , we get the final form of the  $m_{-1}$ ,

$$m_{-1} = \int r^2 \delta \rho d\mathbf{r}. \quad (4.30)$$

In order to solve the motion equations (4.23)-(4.24) for the perturbative corrections to the nuclear densities and meson fields we need to know, in the ISGMR case, the corrections to the neutron and proton chemical potentials. To this end we

first isolate these in equations  $\delta\rho_n$  and  $\delta\rho_p$  and next, using explicitly the constraints  $\int \delta\rho_n d\mathbf{r} = \int \delta\rho_p d\mathbf{r} = 0$ , we obtain after little algebra the corrections  $\delta\tilde{\mu}_n$  and  $\delta\tilde{\mu}_p$  as

$$\delta\tilde{\mu}_n = \frac{\int k_{F_n}^0 \left[ \epsilon_{F_n}^0 \left( g_v \delta V - \frac{1}{2} g_\rho \delta R - r^2 \right) - m^{0*} g_s \delta \phi \right] d\mathbf{r}}{\int k_{F_n}^0 \epsilon_{F_n}^0 d\mathbf{r}}, \quad (4.31)$$

and

$$\delta\tilde{\mu}_p = \frac{\int k_{F_p}^0 \left[ \epsilon_{F_p}^0 \left( g_v \delta V + \frac{1}{2} g_\rho \delta R + e \delta A - r^2 \right) - m^{0*} g_s \delta \phi \right] d\mathbf{r}}{\int k_{F_p}^0 \epsilon_{F_p}^0 d\mathbf{r}}. \quad (4.32)$$

The self-consistent solution of the coupled equations (4.23)-(4.24) allows to obtain the perturbative contribution to the nuclear densities and fields. From Eq.(4.30) one can obtain the inverse energy weighted sum rule  $m_{-1}$ , which combined with the  $m_1$  sum rule given by Eq.(4.4) provides an estimate of the excitation energy of the ISGMR given by  $E_1 = \sqrt{m_1/m_{-1}}$ .

#### 4.4.2 Isovector giant dipole resonance

In case of IVGDR protons and neutrons vibrate in opposite phase to each other in such a way that the center of mass of the whole system remains unchange. This constraint is introduced through the excitation operator  $Q = z - \langle z \rangle = r Y_{10}(\Omega)$ , where  $\langle z \rangle$  is the z-coordinate of the center of mass of the nucleus. As in the case of ISGMR, we write the neutron and proton densities as the sum of unperturbed solution plus a perturbative term, which follows the geometry of the excitation operator, i.e.  $\rho_n(\mathbf{r}) = \rho_n^0(r) + \lambda \delta\rho_n(r) Y_{10}(\Omega)$  and  $\rho_p(\mathbf{r}) = \rho_p^0(r) + \lambda \delta\rho_p(r) Y_{10}(\Omega)$ . With this choice of the nuclear densities the right normalization of neutrons and protons is ensured and, consequently, the corrections  $\delta\mu_n$  and  $\delta\mu_p$  to the corresponding chemical potentials is not needed in the case of the IVGDR. Using this parametrization of the nuclear densities we compute now the expectation values of the dipole operator  $Q$  defined before. It is easy to show that

$$\begin{aligned} \langle z \rangle &= \int (\rho_n(\mathbf{r}) + \rho_p(\mathbf{r})) r Y_{10}(\Omega) d\mathbf{r} \\ &= \frac{1}{A} \int r^3 (\delta\rho_n(r) + \delta\rho_p(r)) dr = \frac{N}{A} \langle z \rangle_n + \frac{Z}{A} \langle z \rangle_p, \end{aligned} \quad (4.33)$$

and

$$\begin{aligned}
\langle Q \rangle &= \int (\rho_p(\mathbf{r}) - \rho_n(\mathbf{r})) (rY_{10}(\Omega) - \langle z \rangle) d\mathbf{r} \\
&= 2 \left[ \frac{N}{A} \int r^3 \delta\rho_p(r) dr - \frac{Z}{A} \int r^3 \delta\rho_n(r) dr \right] \\
&= \frac{2NZ}{A} (\langle z \rangle_p - \langle z \rangle_n).
\end{aligned} \tag{4.34}$$

We assume, as in the ISGMR case, that the fields also split into an unperturbed part plus a corrective contribution that follows the excitation field, i.e.  $V = V^0 + \lambda\delta V Y_{10}$ ,  $R = R^0 + \lambda\delta R Y_{10}$ ,  $\mathcal{A} = \mathcal{A}^0 + \lambda\delta\mathcal{A} Y_{10}$  and  $\phi = \phi^0 + \lambda\delta\phi Y_{10}$ . Therefore, one can write the energy density functional (4.21) in powers of  $\lambda$  and derive from this expansion the motion equations of the nuclear densities and fields, as we have done in the case of ISGMR starting from Eq.(4.22). However, as we have pointed out before, it is also possible derive the variational equations for  $\delta\rho_n$ ,  $\delta\rho_p$ ,  $\delta V$ ,  $\delta R$ ,  $\delta\phi$  and  $\delta\mathcal{A}$  expanding the motion equations associated to the constrained energy density functional (4.21). In case of the IVGDR, these equations for the meson and photon fields are formally given by Eqs.(4.16)-(4.19), keeping in mind, however, that in this case densities and fields are, the ones associated to the constrained problem. The variations equations for neutron and proton are

$$\epsilon_{F_n} + g_v V - \frac{1}{2} g_\rho R - \mu_n + \lambda r Y_{10} \frac{N}{A} = 0, \tag{4.35}$$

and

$$\epsilon_{F_p} + g_v V + \frac{1}{2} g_\rho R + e\mathcal{A} - \mu_p - \lambda r Y_{10} \frac{N}{A} = 0, \tag{4.36}$$

which correspond to Eqs.(4.14) and (4.15) modified by the contribution of the excitation field. Expanding the densities and fields in these variations equations in powers of  $\lambda$ , the independent term gives the motion equations of unperturbed densities and fields and the linear terms in  $\lambda Y_{10}$  correspond to the variations equations for the perturbations of densities and fields, which read

$$\frac{\partial \epsilon_{F_n}^0}{\partial \rho_n^0} \delta\rho_n - g_s \frac{\partial \epsilon_{F_n}^0}{\partial m_0^*} \delta\phi + g_v \delta V - \frac{1}{2} g_\rho \delta R + \frac{Z}{A} r = 0, \tag{4.37}$$

$$\frac{\partial \epsilon_{F_p}^0}{\partial \rho_p^0} \delta\rho_p - g_s \frac{\partial \epsilon_{F_p}^0}{\partial m_0^*} \delta\phi + e\delta\mathcal{A} + g_v \delta V + \frac{1}{2} g_\rho \delta R - \frac{N}{A} r = 0, \tag{4.38}$$

$$g_v \delta \rho Y_{10} + \Delta(\delta V Y_{10}) - m_v^2 \delta V Y_{10} = 0, \quad (4.39)$$

$$g_\rho \delta \rho_3 Y_{10} + \Delta(\delta R Y_{10}) - m_\rho^2 \delta R Y_{10} = 0, \quad (4.40)$$

$$(e \delta \rho_p Y_{10} + \Delta(\delta \mathcal{A} Y_{10})) = 0, \quad (4.41)$$

and

$$\begin{aligned} & \left( g_s^2 \frac{\partial \rho_s^0}{\partial m^{*0}} + 2b\phi^0 + 3c\phi^{02} \right) \delta \phi Y_{10} - g_s \frac{\partial \epsilon_{F_n}^0}{\partial m^{*0}} \delta \rho_n Y_{10} \\ & - g_s \frac{\partial \epsilon_{F_p}^0}{\partial m^{*0}} \delta \rho_p Y_{10} - \Delta(\delta \phi Y_{10}) + m_s^2 \delta \phi Y_{10} = 0. \end{aligned} \quad (4.42)$$

As in the case of ISGMR, we can also calculate the  $m_{-1}$  sum rule for the IVGDR from the second order derivative of the constrained energy with respect to the  $\lambda$ , which after little algebra and taking into account Eqs.(4.37)-(4.42) become

$$m_{-1} = \frac{\partial^2 E}{\partial \lambda^2} \cdot \int r^3 dr \left[ \frac{N}{A} \delta \rho_p - \frac{Z}{A} \delta \rho_n \right]. \quad (4.43)$$

## 4.5 Results and Discussions

Before going to discussions of the predictions of our model and compare with the results obtained applying another theoretical models as well as with the experimental data, we outline briefly our numerical procedure to estimate semi-classically the ISGMR and IVGDR excitation energies in finite nuclei. First, and assuming spherical symmetry, we compute for each nucleus the unperturbed densities and fields by solving self-consistently the set of equations (4.14)-(4.20). using the so-called imaginary time-step method [168–170]. and these unperturbed values we can be use to compute the  $m_1$  sum rules given by Eqs.(4.4) and (4.6), for the ISGMR and IVGDR, respectively. Next, we solve iteratively the sets of coupled linear equations (4.23)-(4.27) for the ISGMR and (4.37)-(4.42) for the IVGDR, which allow to obtain the perturbative

Table 4.1: Excitation energy of the ISGMR in MeV of some spherical nuclei calculated as  $\sqrt{m_1/m_{-1}}$  using the NL3 model.  $E_c(RTF - P)$  is the estimate of the present work,  $E_c(RETf)$  is the RETF result computed as in Ref. [81],  $E_c(RMF)$  and  $E_c(RPA)$  are the constrained Hartree and RPA results, respectively, reported in [117].

Nucleus	$E_c(RTF - P)$	$E_c(RETf)$	$E_c(RMF)$	$E_c(RPA)$	Expt.
$^{16}\text{O}$	26.26	25.98	23.34	23.35	$21.13 \pm 0.49$
$^{40}\text{Ca}$	22.89	23.20	21.55	21.57	$19.18 \pm 0.37$
$^{90}\text{Zr}$	18.74	19.08	18.58	18.55	$17.89 \pm 0.20$
$^{116}\text{Sn}$	17.29	17.57	16.98	17.06	$16.07 \pm 0.12$
$^{144}\text{Sm}$	16.05	16.33	16.08	16.16	$15.39 \pm 0.28$
$^{208}\text{Pb}$	13.84	13.91	14.07	14.10	$14.17 \pm 0.28$

corrections to the nuclear densities and meson and photon fields. Finally the  $m_{-1}$  sum rules can be obtained through Eqs.(4.30) and (4.43) for the ISGMR and IVGDR, respectively. All these calculations are performed at RTF level paying special attention to the convergence of the  $m_{-1}$  sum rule. The convergence of this quantity actually depends on the size of the box where the calculations are performed as well as on the number of iterations used in the unperturbed calculation.

Experimental information about the excitation energy of the ISGMR in medium and heavy nuclei is obtained from inelastic scattering of  $\alpha$  particles measured at forward angles [75,115,171,172]. As a first application of our perturbative constrained approach developed in previous sections, we compute the excitation energy of the ISGMR for several nuclei which value is experimentally known [75,115,171,172] using the RMF NL3 parametrization [49]. Although the sum rule approach, which assumes a well defined peak, for light nuclei may be questionable, we display in table 4.1 our semi-classical RTF estimate of the excitation energy of ISGMR of the nuclei  $^{16}\text{O}$ ,  $^{40}\text{Ca}$ ,  $^{90}\text{Zr}$ ,  $^{116}\text{Sn}$ ,  $^{144}\text{Sm}$  and  $^{208}\text{Pb}$  calculated with our perturbative constrained approach. In the same table we also show the constrained values obtained using the Relativistic Extended Thomas-Fermi Approach (RETf), which includes  $\hbar^2$  corrections, computed as described in Ref. [81] together with the corresponding experimental values. For



Table 4.2: Excitation energy of the IVGDR in MeV of some spherical nuclei calculated as  $\sqrt{m_1/m_{-1}}$  using the NL3 model.  $E_c(RTF - P)$  is the estimate of the present work and  $E(RPA)$  are the RPA results reported in [173].

Nucleus	$E_c(RTF - P)$	$E_c(RPA)$	Expt. [174]
$^{16}\text{O}$	22.05	21.1	22.3-24
$^{40}\text{Ca}$	19.90	19.57	$19.8 \pm 0.5$
$^{90}\text{Zr}$	17.18	17.19	$16.5 \pm 0.2$
$^{116}\text{Sn}$	16.25	15.77	$15.7 \pm 0.2$
$^{208}\text{Pb}$	13.54	13.16	$13.3 \pm 0.1$

Table 4.3: Semi-classical  $m_{-1}$  sum rule in  $\text{fm}^2 \text{ MeV}^{-1}$  of some spherical nuclei computed as explained in this work ( $RTF - P$ ) and using the DM approach (4.44) ( $(RTF - LDM)$  input). All these calculation are performed with the NL3 parameter set.

Nucleus	$m_{-1}(RTF - P)$	$m_{-1}(RTF - DM)$
$^{16}\text{O}$	0.219	0.192
$^{40}\text{Ca}$	0.699	0.657
$^{68}\text{Ni}$	1.499	1.403
$^{90}\text{Zr}$	2.130	2.076
$^{116}\text{Sn}$	3.061	3.012
$^{120}\text{Sn}$	3.250	3.173
$^{208}\text{Pb}$	7.685	7.256

a sake of completeness, we also display in the same table the constrained Hartree and RPA values of these excitation energies reported in Ref. [117]. From this table some comments are in order. First, as we mentioned previously, the constrained Hartree predictions of the excitation energy of the ISGMR practically concides with the values extracted from RRPA calculations, which numerically proves the conjecture of Ref. [158]. Second, as it was pointed out in [81], the importance of the  $\hbar^2$  corrections in the excitation energy of the ISGMR is actually small as it can be seen from the comparison between the RTF and RETF results. Third, the excitation energies of the ISGMR decreases with increasing mass number, as expected, in both semi-classical and quantal (constrained Hartree and RRPA) predictions. However, the slope is larger for the semi-classical than for the quantal estimates. For light and medium nuclei the semi-classical values overestimate the quantal ones while the opposite is true for  $^{208}\text{Pb}$ , which is the heaviest nucleus considered in this work.

The experimental values of the excitation energies of the IVGDR basically come from the analysis of the measured photo-absorption cross sections as mentioned before [175]. From a theoretical point of view there are many studies of the IVGDR at RPA and RRPA levels using different mean field models in both non-relativistic and relativistic frames [176]. However, from long ago the IVGDR has also been analyzed from a semi-classical point of view. Let us mention in this respect the estimate of the  $m_{-1}$  sum rule on the basis of the Droplet Model (DM) [177] reported more than thirty years ago. More recently, the excitation energies of the IVGDR has been estimated using the scaling method [178, 179] and performing constrained calculations [179]. In table 4.2 we display our constrained perturbative estimate of the excitation energy of some selected spherical even-even nuclei computed with the NL3 parameter set [49] as well as the RRPA predictions obtained with the same NL3 model [180] and the experimental values extracted from Ref. [174]. From this table it can be seen that our semi-classical RTF estimate reproduce remarkably well the RRPA values and the experimental data. This result point out, as discussed in earlier literature [177–179], that semi-classical approaches, as the constrained perturbative RTF method discussed in this work, are well suited for describing also the average excitation energy of the IVGDR due to the fact that shell corrections in this collective oscillation are, actually, small [177].

As mentioned before, the  $m_{-1}$  sum rule can also be estimated in the framework of the LDM as [177]

$$m_{-1} = \frac{A \langle r^2 \rangle}{48J} \left( 1 + \frac{15}{4A^{1/3}} \frac{J}{Q} \right), \quad (4.44)$$

where  $\sqrt{\langle r^2 \rangle}$  stands for the mass rms radius,  $J$  for the symmetry energy and  $Q$  is the so-called surface stiffness coefficient. This coefficient  $Q$  is obtained from a semi-classical RTF calculation in semi-infinite nuclear matter as explained in Ref. [97] and its corresponding value is  $J/Q=1.46$ . The DM estimates of the  $m_{-1}$  sum rule at RTF level for several nuclei are reported in table 4.3. To obtain these values, in addition to the  $J/Q$  ratio and the symmetry energy of the NL3 model ( $J=37.40$  MeV), we also use in Eq.(4.44) the  $\langle r^2 \rangle$  value obtained from a self-consistent RTF calculation for each considered nucleus. From table 4.3 we see that the semi-classical DM and the perturbative constrained RTF estimates of the  $m_{-1}$  sum rule are in a good agreement. Our RTF predictions of  $m_{-1}$  are also in good agreement with the values, computed semi-classically with the Skyrme Skm\* force, displayed in Table V of [179]. For example,  $m_{-1}$  values of 0.215, 0.682, 2.054 and 7.047 fm<sup>2</sup> MeV<sup>-1</sup> are reported in this reference for the nuclei <sup>16</sup>O, <sup>40</sup>Ca, <sup>90</sup>Zr and <sup>208</sup>Pb, respectively. In the same reference the experimental values of the  $m_{-1}$  sum rule, obtained as the integral up to the pion threshold of the measured total nuclear photoabsorption cross section [177], are also reported in the same Table V. These experimental values, 0.215±0.004, 0.682±0.016 and 7.35±0.51 fm<sup>2</sup>MeV<sup>-1</sup> for <sup>16</sup>O, <sup>40</sup>Ca and <sup>208</sup>Pb, respectively, are in harmony with our semi-classical predictions reported in table 4.3. However, I should be pointed out that recent measurements of the electric polarizability in <sup>208</sup>Pb, <sup>120</sup>Sn and <sup>68</sup>Ni give a smaller experimental value for the  $m_{-1}$  sum rule [152].

## 4.6 Summary and outlook

We have estimated the average excitation energy of the isoscalar monopole and isovector dipole giant resonances for several nuclei within a semiclassical sum rule approach in the relativistic mean field framework with the NL3 parameter set. We are aware that a sum rule approach only gives information about some selected moments of the RRPA strength function and that in this approach a precise prediction of the

excitation energy of the resonance is only possible if the strength is concentrated in a single peak, which is the usual scenario for medium and heavy nuclei but not for light nuclei where the resonance broadens and fragments. The  $m_1$  sum rules are evaluated at RPA level using the semi-classical expectation values calculated with the relativistic Thomas-Fermi approximation. The  $m_{-1}$  sum rule is obtained through a new constrained perturbative calculation also within the relativistic Thomas-Fermi theory. In this calculation the nuclear densities and meson and photon fields are splitted into a part corresponding to the unperturbed solution plus a perturbative correction, chosen in such a way that it follows the excitation field. The energy density corresponding to the constrained problem is expanded up to quadratic terms in these perturbations. The application of the variational principle to this energy density allows to obtain the equations of motion of the perturbative corrections to nuclear densities and fields. With this simple semi-classical method the average excitation energies of the isoscalar monopole and isovector dipole giant resonances is estimated reasonably well as compared with the more fundamental but also more cumbersome relativistic RPA calculations. The differences between both calculations are basically due to shell effects and are less than 5% in medium and heavy nuclei where the sum rule can be considered more confidently. This result is in agreement with previous findings in earlier literature pointing out that shell effects have little impact on the average excitation energies of the giant resonances studied in this chapter. Our constrained perturbative approach has been obtained at relativistic Thomas-Fermi level, therefore, it seems reasonable, to improve it by including the  $\hbar^2$  corrections which give a more realistic calculation at the nuclear surface. As far as our method is able to describe collective oscillations with excitation operators without spherical symmetry, as the isovector dipole, it seems also appealing to apply our method to another isoscalar and isovector oscillations of higher multipolarities.

## Chapter 5

# Effects of self interacting $\omega$ -meson on finite and infinite nuclear system.

The most mysterious and the debatable subject in nuclear physics is the nucleon-nucleon interaction. A lots of theories have been proposed for the nucleon-nucleon interaction but still it is not clear. The nucleon-nucleon interaction affects the nuclear structure in a more prominent way. So without the study of the nucleon -nucleon interaction nuclear structure will remain incomplete. In this chapter, a detailed study is made for the nucleon-nucleon interaction based on relativistic mean field theory in which the potential is explicitly expressed in terms of masses and the coupling constants of the meson fields. An unified treatment for self-coupling of isoscalar-scalar  $\sigma$ -, isoscalar-vector  $\omega$ -mesons and their coupling constants are given in an analytic form. The present investigation is focused on the effects of self-interacting higher order  $\sigma$  and  $\omega$  fields on nuclear properties. An attempt is made to explain the many-body effects by higher order couplings  $\sigma$ - and  $\omega$ -fields, which generally occurs in the high-density region. Both infinite nuclear matter and the finite nuclear properties are included in the present study to observe the behavior and sensitivity of this self-interacting terms.

## 5.1 Introduction

The Nucleon-Nucleon (NN) interaction has been investigated for over half a century [2]. Probably this is a long standing question in history of nuclear physics. In fact, describing the nuclear properties in terms of the interactions between the nucleon pair is indeed the main goal for nuclear physicists. The NN-interaction in terms of mediated mesons was put forwarded by Yukawa [2] in 1935. Although the meson theory is not fundamental from the QCD point of view, it has improved our understanding of the nuclear forces as well as highlighted some good quantitative results [181,182]. The modern theory of NN potential in term of particle exchanges was made possible by the development of quantum field theory [182]. However, at low-energy, one can assume that the interactions are instantaneous and therefore the concept of interaction potential becomes useful. The derivation of a potential through particle exchange is important to understand the nuclear force as well as structural properties.

Now-a-days, there are number of developments in the nuclear theory by introducing quark and gluon in connection with the NN-potential [183,184]. These models give the fundamental understanding of NN interaction at present. Here, we are not addressing all these rich and long standing problems about NN-potential. Our aim is to highlight some basic features of the NN-interactions arising from relativistic mean field (RMF) Lagrangian [185–188]. The behavior of this potential gives an idea about the saturation properties of nuclear force at high density limit.

This chapter is organized as follows. In Section 5.2, we briefly discuss the theoretical formalism of NN-interaction based on relativistic mean field (RMF) theory. The general forms of the NN potentials are expressed in the coordinate space (*r-space*) in term of masses and coupling constants of the force parameters. In Section 5.3, we review the effects of modified term in the Lagrangian and their effects on the finite nuclei and in infinite nuclear matter. In Section 5.4, we make few comments about the current form of the NN-interaction to saturation condition of nuclear systems.

## 5.2 Theoretical frameworks

The nuclear potential in relativistic mean field (RMF) is possible via various mesons interaction with nucleons. The linear relativistic mean field (RMF) Lagrangian density for a nucleon-meson many-body system [7, 8, 189, 190] is given as:

$$\begin{aligned}
\mathcal{L} = & \bar{\psi}_i \{ i\gamma^\mu \partial_\mu - M \} \psi_i + \frac{1}{2} \partial^\mu \sigma \partial_\mu \sigma - \frac{1}{2} m_\sigma^2 \sigma^2 - g_s \bar{\psi}_i \psi_i \sigma \\
& - \frac{1}{4} \Omega^{\mu\nu} \Omega_{\mu\nu} + \frac{1}{2} m_w^2 V^\mu V_\mu - g_w \bar{\psi}_i \gamma^\mu \psi_i V_\mu - \frac{1}{4} \vec{B}^{\mu\nu} \cdot \vec{B}_{\mu\nu} \\
& + \frac{1}{2} m_\rho^2 \vec{R}^\mu \cdot \vec{R}_\mu - g_\rho \bar{\psi}_i \gamma^\mu \vec{\tau} \psi_i \cdot \vec{R}_\mu - \frac{1}{4} F^{\mu\nu} F_{\mu\nu} \\
& - e \bar{\psi}_i \gamma^\mu \frac{(1 - \tau_{3i})}{2} \psi_i A_\mu.
\end{aligned} \tag{5.1}$$

If, we neglect the  $\rho$ - meson, it corresponds to the Walecka model in its original form [8, 189]. From the above relativistic Lagrangian, we obtain the field equations for the nucleons and mesons as,

$$\left( -i\alpha \cdot \nabla + \beta(M + g_\sigma \sigma) + g_\omega \omega + g_\rho \tau_3 \rho_3 \right) \psi_i = \epsilon_i \psi_i, \tag{5.2}$$

$$(-\nabla^2 + m_\sigma^2) \sigma(r) = -g_\sigma \rho_s(r), \tag{5.3}$$

$$(-\nabla^2 + m_\omega^2) V(r) = g_\omega \rho(r), \tag{5.4}$$

$$(-\nabla^2 + m_\rho^2) \rho(r) = g_\rho \rho_3(r). \tag{5.5}$$

In the limit of one-meson exchange and mean-field (the fields are replaced by their expectation values or c-number), for a heavy and static baryonic medium, the solution of single nucleon-nucleon potential for scalar ( $\sigma$ ) and vector ( $\omega$ ,  $\rho$ ) fields are given by [190, 191],

$$V_\sigma(r) = -\frac{g_\sigma^2}{4\pi} \frac{e^{-m_\sigma r}}{r}, \tag{5.6}$$

and

$$V_\omega(r) = +\frac{g_\omega^2}{4\pi} \frac{e^{-m_\omega r}}{r}, \quad V_\rho(r) = +\frac{g_\rho^2}{4\pi} \frac{e^{-m_\rho r}}{r}. \tag{5.7}$$

The total effective nucleon-nucleon potential is obtained from the scalar and vector parts of the meson fields. This can be expressed as [185],

$$v_{eff}(r) = V_\omega + V_\rho + V_\sigma = \frac{g_\omega^2}{4\pi} \frac{e^{-m_\omega r}}{r} + \frac{g_\rho^2}{4\pi} \frac{e^{-m_\rho r}}{r} - \frac{g_\sigma^2}{4\pi} \frac{e^{-m_\sigma r}}{r}. \quad (5.8)$$

### 5.2.1 Non-linear case

The Lagrangian density in the above Eq. 5.1 contains only linear coupling terms, which is able to give a qualitative description of the nuclear system [190,191]. The essential nuclear matter properties like incompressibility and the surface properties of finite nuclei cannot be reproduced quantitatively within this linear model. The suppression of the two-body interactions within a nucleus in favor of the interaction of each nucleon with the average nucleon density, means that the non-linearity acts as a smoothing mechanism and hence leads in the direction of the one-body potential and shell structure [99,141,192,193]. The replacement of mass term  $\frac{1}{2}m_\sigma^2\sigma^2$  of  $\sigma$  field by  $U(\sigma)$  and  $\frac{1}{2}m_\omega^2V^\mu V_\mu$  of  $\omega$  field by  $U(\omega)$ . This can be expressed as

$$U(\sigma) = \frac{1}{2}m_\sigma^2\sigma^2 + \frac{1}{3}g_2\sigma^3 + \frac{1}{4}g_3\sigma^4, \quad (5.9)$$

$$U(\omega) = \frac{1}{2}m_\omega^2V^\mu V_\mu + \frac{1}{4}c_3(V^\mu V_\mu)^2. \quad (5.10)$$

The terms on the right hand side of Eqs.( 5.9)- (5.10), except the first term, from the non-linear self coupling of the  $\sigma$  and  $\omega$  mesons, respectively [99,141]. Here, the non-linear parameter  $g_2$  and  $g_3$  due to  $\sigma$ - fields are adjusted to the surface properties of finite nuclei [194,195]. In general most of the successful fits like NL1 and NL3 sets yield, the  $+ve$  and  $-ve$  signs for  $g_2$  and  $g_3$ , respectively. The negative value of  $g_3$  is a serious problem in quantum field theory and responsible for the divergence of a solution in the lighter mass region of periodic table i.e. for higher density region. As, we are dealing within the mean field level and with normal nuclear matter density, the corresponding  $\sigma$  field is very small and the  $-ve$  value of  $g_3$  is still allowed [194,196]. Again,  $c_3 = \frac{1}{6}\zeta_0$  is the non-linear coupling constant for self-interacting  $\omega$ -mesons. With the addition of the non-linear terms in the Eqs. ( 5.9)- (5.10) to the Lagrangian,



the field equations for  $\sigma$  and  $\omega$ - fields (in Eq.5.6-5.7 ) are modified as:

$$(-\nabla^2 + m_\sigma^2)\sigma(r) = -g_\sigma \rho_s(r) - g_2 r \sigma^2(r) - g_3 \sigma^3(r),$$

$$(-\nabla^2 + m_\omega^2)V(r) = g_\omega \rho(r) - c_3 W^3(r). \quad (5.11)$$

Here,  $W(r) = g_\omega V_0(r)$  is the non-linear self-interacting  $\omega$ -fields. Because of the great difficulty in solving the above nonlinear differential equations, it is essential to have a variational principle for the estimation of the energies [194,195]. In the static case, the negative sign of the third term in the Lagrangian is computed with the correct source function and an arbitrary trial wave function. The limit on the energy has a stationary value equal to the proper energy when the trial wave-function is in the infinitesimal neighborhood of the correct one. Now, the solution for the modified  $\sigma$  and  $\omega$  fields are given as [194]

$$V_\sigma = -\frac{g_\sigma^2}{4\pi} \frac{e^{-m_\sigma r}}{r} + \frac{g_2^2}{4\pi} r \frac{e^{-2m_\sigma r}}{r} + \frac{g_3^2}{4\pi} \frac{e^{-3m_\sigma r}}{r},$$

$$V_\omega = \frac{g_\omega^2}{4\pi} \frac{e^{-m_\omega r}}{r} - \frac{c_3^2}{4\pi} \frac{e^{-3m_\omega r}}{r^2}. \quad (5.12)$$

The new NN-interaction analogous to  $M3Y$  form and is able to improve the incompressibility and deformation of the finite nuclei results [196]. In addition to this, the non-linear self coupling of the  $\sigma$  and  $\omega$ -mesons help to generate the repulsive and attractive part of the NN potential at *long* and at *short* distance, respectively to satisfy the saturation properties (Coester-band problem) [197]. We are dealing with two type of mesons, one is scalar ( $\sigma$ ) and other is vector ( $\omega$ ). The range of their interactions are also different due to their different masses. Consider the case of  $\sigma$ -meson, where the range of interaction is  $\sim \frac{\hbar}{m_\sigma c}$  fm. In this range the attractive part of the potential comes from the exchange of the  $\sigma$ -meson. The density dependent many-body effect demands a repulsive part in this region. This is given by the self interacting terms like  $\sigma^3$  and  $\sigma^4$  [165]. A suitable adjustment of the parameter able to reproduces the proper potential satisfying the Coester band problem. Generally, the exchange of  $\omega$ -meson gives the repulsive potential in the short-range part of the hard core region. Diametrically, opposite phenomenon is also occurs in case of  $\omega$ -meson coupling. Contrary to the non-linearity of  $\sigma$ -meson nature, the self-coupling of  $\omega$ -meson gives

an attractive component at very short distance ( $\sim 0.2$  fm) of the nuclear potential. The non-linear terms also generate the most discussed 3-body interaction [165]. The modified effective nucleon-nucleon interaction is defined as [185]:

$$\begin{aligned}
v_{eff}(r) &= V_\omega + V_\rho + V_\sigma \\
&= \frac{g_\omega^2}{4\pi} \frac{e^{-m_\omega r}}{r} + \frac{g_\rho^2}{4\pi} \frac{e^{-m_\rho r}}{r} - \frac{g_\sigma^2}{4\pi} \frac{e^{-m_\sigma r}}{r} \\
&\quad + \frac{g_2^2}{4\pi} r \frac{e^{-2m_\sigma r}}{r} + \frac{g_3^2}{4\pi} \frac{e^{-3m_\sigma r}}{r} - \frac{c_3^2}{4\pi} \frac{e^{-3m_\omega r}}{r}.
\end{aligned} \tag{5.13}$$

### 5.3 Results and Discussions

The Eq. ( 5.13) shows that the effective NN-potential in terms of the well known inbuilt RMF theory parameters of  $\sigma$ ,  $\omega$  and  $\rho$  meson fields. Here, we have used RMF (NL3) force parameter along with varying  $c_3$  for  $\omega$ -self interactions to determine the nuclear properties. The values of the parameters for NL3-force are listed in Table 5.1. Although, the  $\omega^4$  term is already there in the FSU-Gold parameter [90, 198], here we are interested to see the effect of non-linear self coupling of  $\omega$  meson. Thus, we have added the self-interaction of  $\omega$  with coupling constant  $c_3$  on top of NL3 set and observed the possible effects.

First of all, we have calculated the NN-potential for linear and non-linear cases using Eq. 5.8 and 5.13, respectively. The obtained results for each cases are shown in Fig. 5.1. From the figure, it is clear that without taking the non-linear coupling for RMF (NL3), one cannot reproduce a better NN-potential. In other word, the depth of the potential for linear and non-linear are  $\sim 150$  MeV and 50 MeV, respectively. Thus, the magnitude of the depth for linear case is not reasonable to fit the NN-data. Again, considering the values of  $c_3$ , there is no significant change in the total *nucleon-nucleon* potential. For example, the NN-potential does not change at all for  $c_3 \simeq \pm 0.6$ , which can be seen from Fig. 5.1.

Further, we have calculated the individual contribution of meson fields to the NN-potential in particular case of  $\sigma$  and  $\omega$ -mesons. In case of  $\sigma$ -field, we have calculated the linear and non-linear contributions separately, and combined to get the total  $\sigma$ -potential as shown in Fig. 5.2. From the figure, one can find the non-linear self-interacting terms in the  $\sigma$ -field play an important role (contributing a repulsive

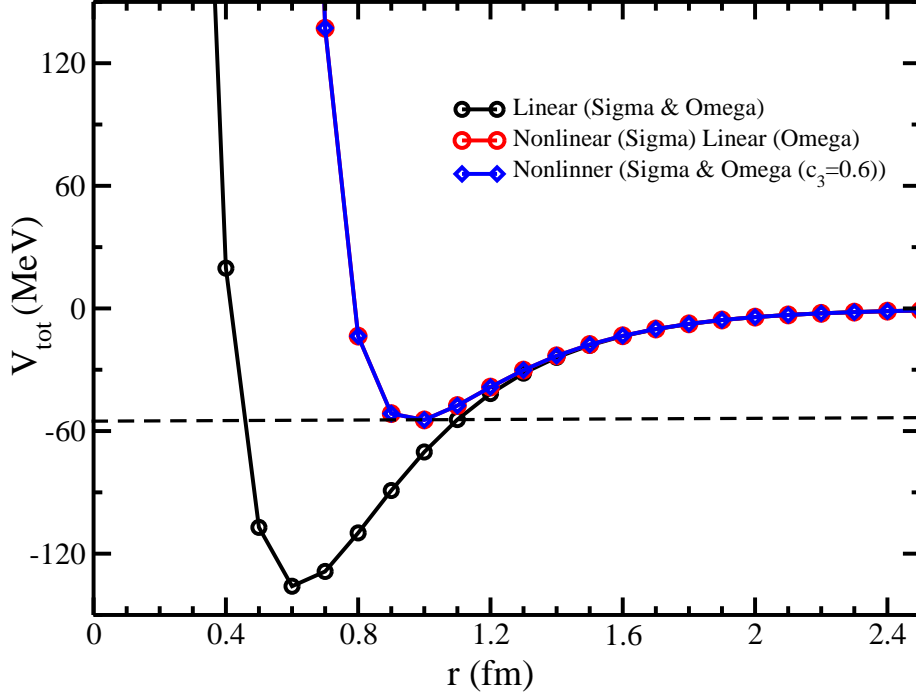


Figure 5.1: The effective NN interaction potentials as a function of distance  $r$  from Eq. 5.6- 5.12 for NL3 parameter set.

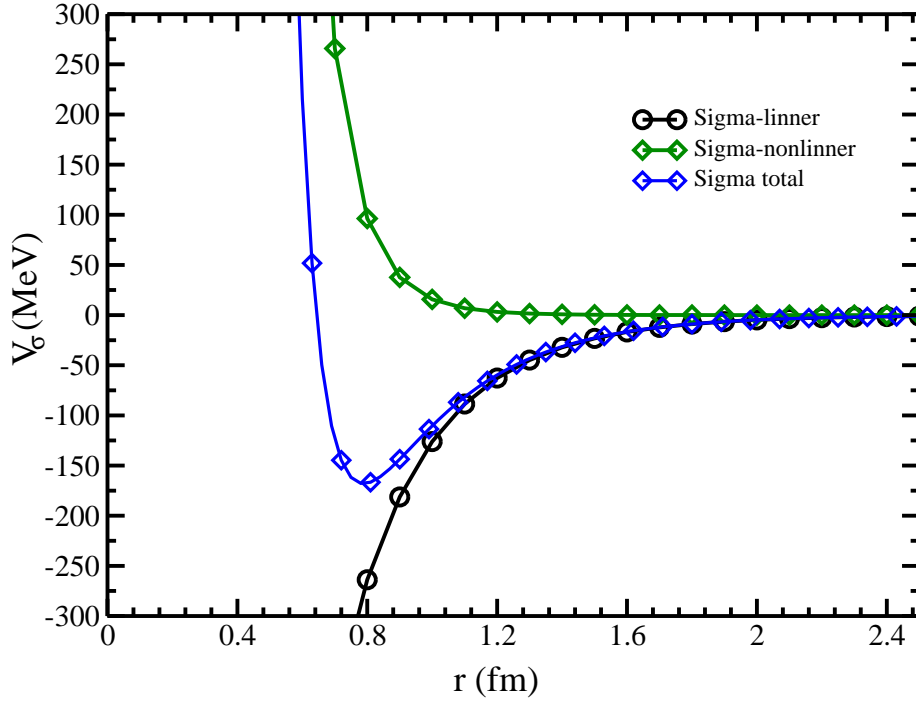


Figure 5.2: The contribution of  $\sigma$ -potential from linear, non-linear and total as a function of distance  $r$  for NL3 parameter set.

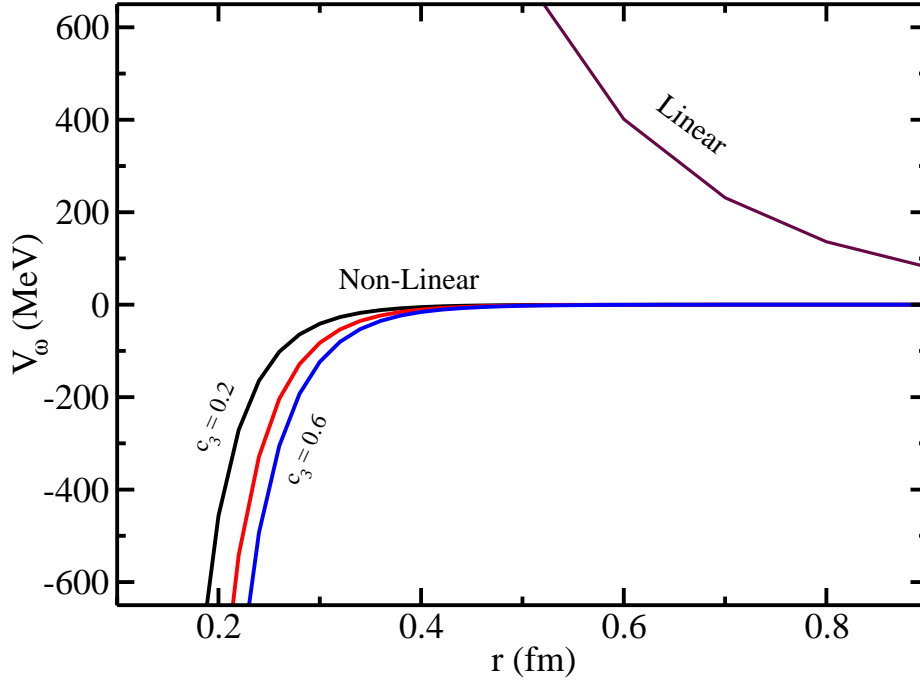


Figure 5.3: The contribution of  $\omega$ -potential from linear, non-linear and total as a function of distance  $r$  for for NL3 parameter set.

interaction) in the attractive part of the  $\sigma$ -meson domain, giving rise to a repulsive potential complementing the 3-body effect of the nuclear force in the total NN-potential [194]. The linear and non-linear contribution of the  $\omega$ -field at various  $c_3$  are shown in Fig. 5.3. The important feature in this figure is that the linear term give an infinitely large repulsive barrier at  $\sim 0.5$  fm, in which range, the influence of the non-linear term of the  $\omega$ -meson is zero. However, this non-linear terms is extremely active at very short distance ( $\sim 0.2$  fm), which can be seen from the figure.

That means, mostly the (i) linear term of the  $\sigma$ - meson is responsible for the attractive part of the nuclear force (nuclear binding energy) (ii) the non-linear terms are responsible for the repulsive part of the nuclear force at long distance, which simulate the 3-body interaction of the nuclear force [194], which also help to explain the Coester band problem. (iii) similarly, the linear term of the  $\omega$ - meson is restraint for the repulsive part of the nuclear force (*known as hard core*) and (iv) the non-linear self-coupling of the  $\omega$ - meson ( $\frac{1}{4}c_3V_\mu V^\mu$ ) is responsible for the attractive part in the very shortest ( $\sim 0.2$  fm) region of the NN-potential. It is worthy to mention that the values of these constants are different for different forces of RMF theory. Hence, the

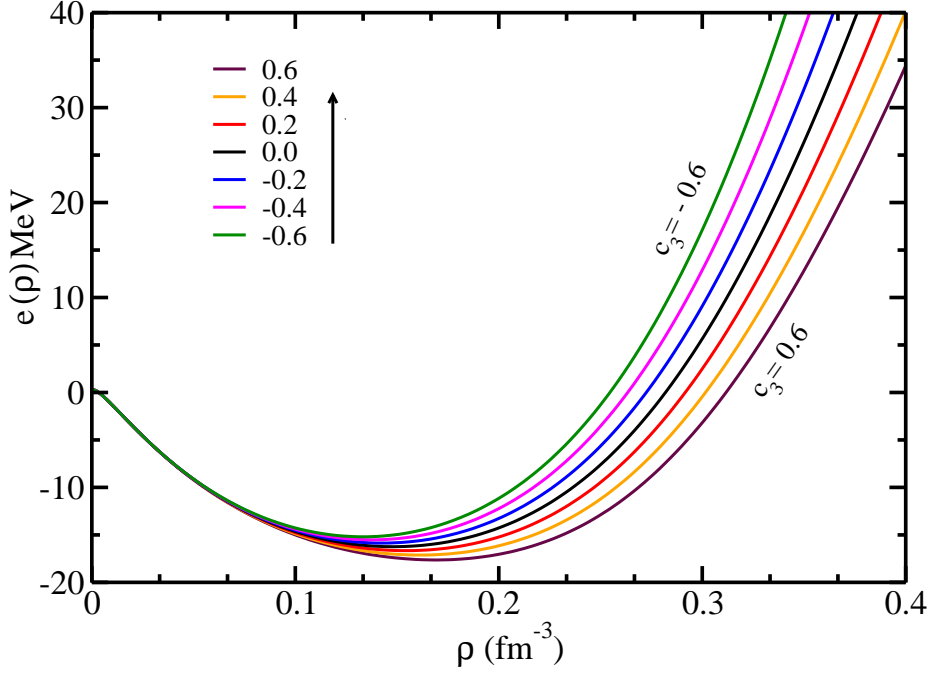


Figure 5.4: The energy per particle of symmetric nuclear matter as a function of baryon density for various values of  $c_3$ .

NN-potential somewhat change a little bit in magnitude by taking different forces, but the nature of the potential remains unchanged.

### 5.3.1 Energy density and Pressure density

In the present work, we study the effect of the additional term on top of the  $NL3$  force parameter to the Lagrangian [49], which comes from the self-interaction of the vector fields with  $c_3$  as it is done in the Refs. [90, 198–200]. The inclusion of this term is not new, it is already taken into account for different forces of RMF and effective field theory motivated relativistic mean field theory (E-RMF). Here, our aim is to see the effect of  $c_3$  to the nuclear system and the contribution to the attractive part of the hard core of NN-potential. We have solved the mean field equations self-consistently and estimated the energy and pressure density as a function of baryon density. The  $NL3$  parameter set along with the additional  $c_3$  is used in the calculations [199, 200]. The obtained results for different values of  $c_3$  are shown in Figs. 5.4 and 5.5, respectively. From the figure, it is clearly identified that the  $-ve$  value of  $c_3$  gives the *stiff* equation of state (EOS), meanwhile the  $+ve$  value shows the *soft* EOS. It is to be noted that mass

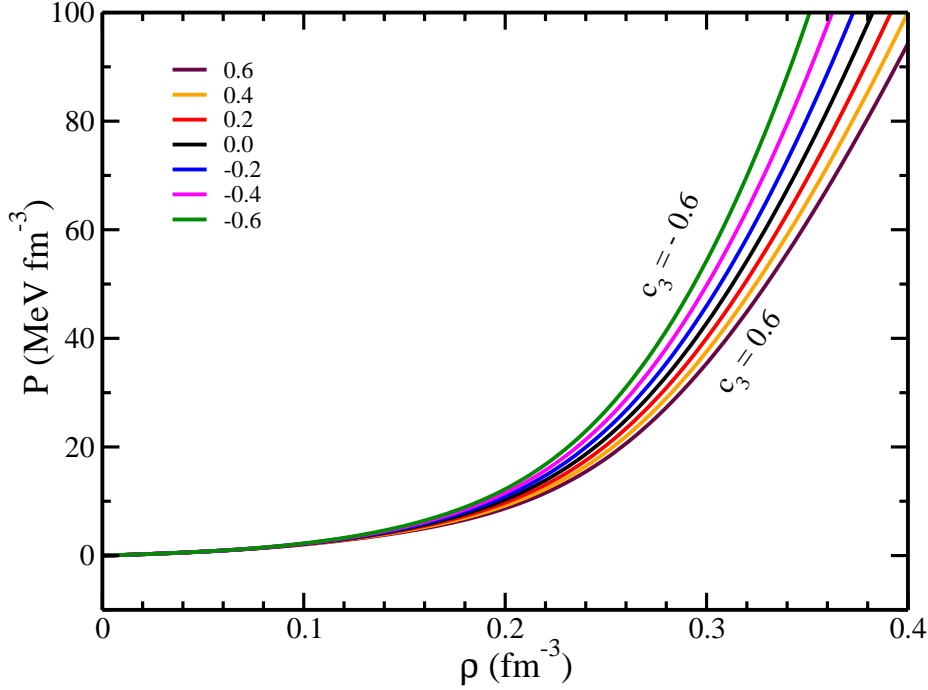


Figure 5.5: The pressure density of symmetric nuclear matter as a function of baryon density for various values of  $c_3$ .

Table 5.1: The values of  $m_\sigma$ ,  $m_\omega$ ,  $m_\rho$  (in MeV) and  $g_\sigma$ ,  $g_\omega$ ,  $g_\rho$  for RMF (NL3) force, along with the self-interacting  $\omega$ - field with coupling constant  $c_3$  .

set	$m_\sigma$	$m_\omega$	$m_\rho$	$g_\sigma$	$g_\omega$	$g_\rho$	$g_2(fm^{-1})$	$g_3$	$c_3$
NL3	508.194	782.5	763.0	08.31	13.18	6.37	-10.4307	-28.8851	$0.0 \pm 0.6$

and radius of the neutron star depends on the softness and stiffness of EOS. Here, in our investigation, we observed that the softening of the EOS depends on the non-linear coupling of the  $\omega$ - meson [90, 193]. The recent measurement of Demorest *et al.* [201] put a new direction that the NL3 force needs slightly softer EOS. However, when we deals with G2 (E-RMF) model, the results of Ref. [202] demands a slightly stiffer EOS. This implies that, the value of  $c_3$  should be fixed according to solve the above discussed problem.

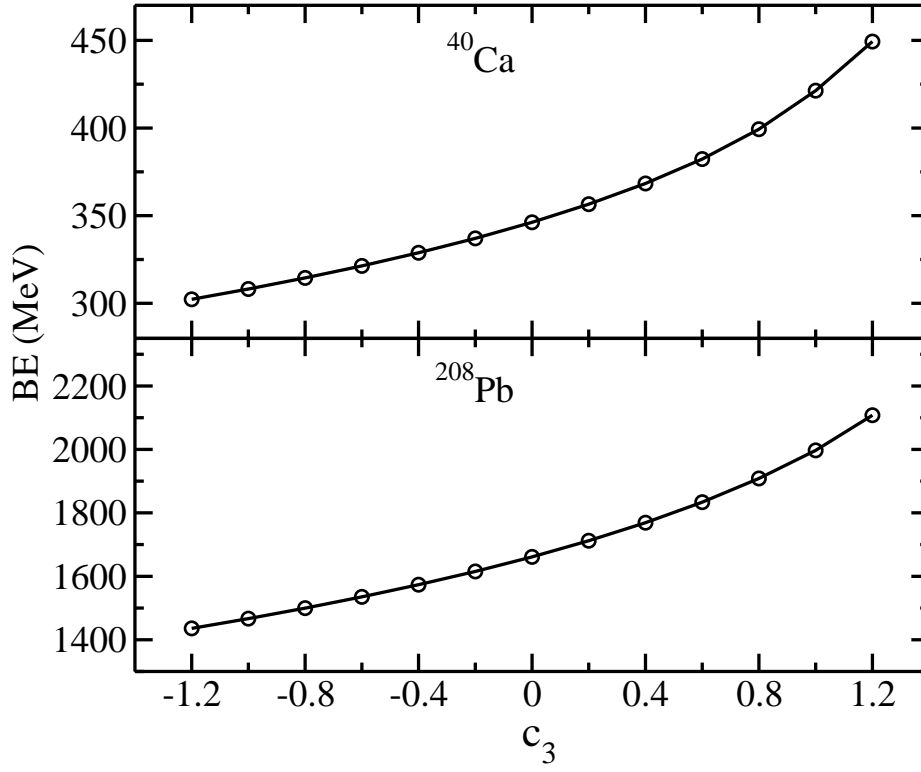


Figure 5.6: The binding energy of  $^{40}\text{Ca}$  and  $^{208}\text{Pb}$  in their ground state for different values of  $c_3$ .

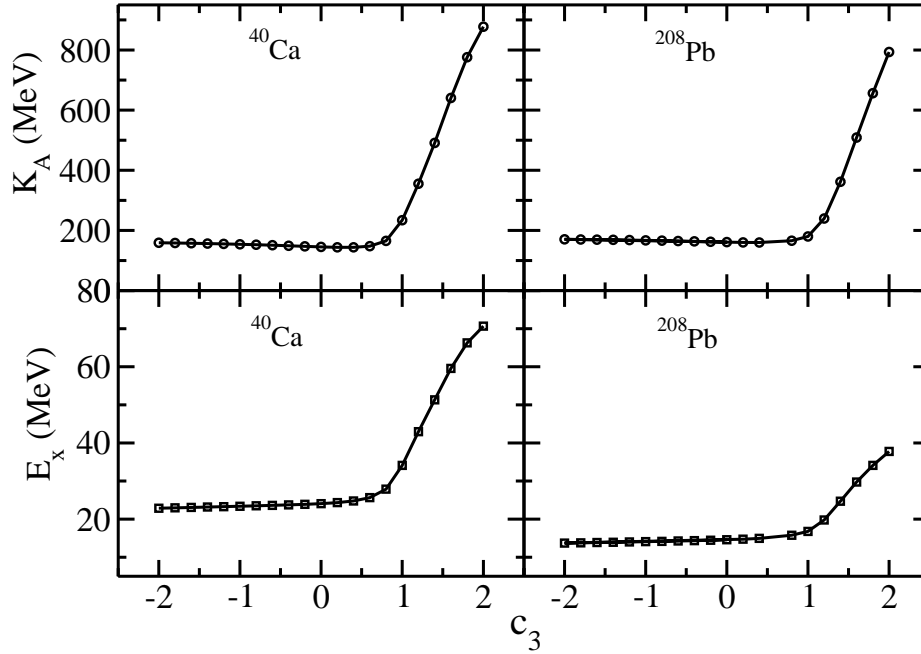


Figure 5.7: The excitation energy as a function of  $c_3$  for  $^{40}\text{Ca}$  and  $^{208}\text{Pb}$ . (b) The incompressibility of  $^{40}\text{Ca}$  and  $^{208}\text{Pb}$  as a function of  $c_3$ .

### 5.3.2 Binding energy, Excitation energy and Compressibility

To see the sensitivity of  $c_3$  on the finite nuclei, we calculated the binding energy (BE), giant monopole excitation energy ( $E_x$ ) for  $^{40}\text{Ca}$  and  $^{208}\text{Pb}$  nuclei as representative cases as a function of  $c_3$ . The excitation energy and incompressibility are calculated by scaling method within the framework of extended Thomas-Fermi approximation. The obtained results are shown in upper and lower panel of the Fig. 5.6 and 5.7. The experimental and empirical data are also displaced for comparison.

From the figure, one observes a systematic variation of binding energy by employing the isoscalar-vector selfcoupling parameter  $c_3$ . For example, the binding energy monotonically changes for all values of  $c_3$ . When  $c_3 = 0$ , the NL3 set reproduces the original binding energies for both  $^{40}\text{Ca}$  and  $^{208}\text{Pb}$ , which are fitted with the data while constructing the force parameters. As soon as the self-coupling constant is non-zero, the calculated BE deviates from the data, because of the influence of  $c_3$ . Again, analyzing the excitation energy, we find reasonable match of  $E_x$  with the observation (lower panel of Fig. 5.7). These values of  $E_x$  remain almost constant for a wide range of  $c_3$  ( $\sim 2$  to  $\sim 1$ ), beyond which  $E_x$  increases drastically for positive value only. Further, we analyze the variation of compressibility modulus with  $c_3$  for  $^{40}\text{Ca}$  and  $^{208}\text{Pb}$  (upper panel of Fig. 5.7). We include both positive and negative values of  $c_3$  ( $-2$  to  $+2$ ) to know the effects on the sign of  $c_3$ . Similar to the monopole excitation energy, we find that the compressibility modulus does not change with the increase of  $c_3$  up to some optimum value. The empirical (nuclear matter compressibility modulus  $K_\infty$ ) data of  $K_\infty^{emp} = 210 \pm 30$  MeV and the nuclear matter incompressibility for NL3 set (271.76 MeV) are given in the figure to have an idea about the bridge between the nuclear matter limit for finite nuclei. In general, these two values along with the finite nuclei compressibility modulus gives an overall estimation about a possible link among them in finite nuclei and nuclear matter limit. It is interesting to notice that although we get a stiff equation of state with negative value of  $c_3$  for infinite nuclear matter system, this behavior does not appear in finite nuclei, i.e. the  $K_A$  and  $E_x$  do not change with sign of  $c_3$ . May be the density with which we deal in the finite nucleus is responsible for this discrepancy. However,  $K_A$  and  $E_x$  increase substantially after certain value of  $c_3$ , i.e. the finite nucleus becomes too much softer at about  $c_3 \sim 1.0$  resulting a larger incompressibility.



## 5.4 Summary and Conclusions

In summary, we analyzed the effects of the non-linear self-coupling of the  $\sigma$ -scalar and  $\omega$ -vector mesons. At long range, i.e., more than 0.5 fm, the self coupling of the  $\sigma$ -meson gives a repulsive component contrary to the attractive part of the linear term. This repulsive nature of the nuclear potential originated from the nonlinear terms of the  $\sigma$ -meson couplings simulate the 3-body force. This 3-body force is mostly responsible to solve the Coester band problem in RMF formalism. On the other hand, at extremely short distance, the nonlinear term of the  $\omega$ -meson coupling gives a strongly attractive potential for both *positive* and *negative* value of  $c_3$ . This short range distance is about  $0.2fm$ , beyond (more than 0.2 fm) which the *vector*-meson interaction itself shows a strong repulsion due to its linear interaction of the  $\omega$ -meson and responsible for the saturation of nuclear force. Thus, one conclude that the effects of the vector self-coupling is crucial for the attractive nature of the nuclear force at the extremely short range region and should be taken in equal footing while constructing the force parameter in relativistic field theory.

## Chapter 6

# Effects of $NN$ potentials on $p$ nuclides in the $A \sim 100-120$ region

In the previous chapter, we discussed the effects of self-interacting  $\omega$  -meson ( $\omega^4$ ) coupling on various properties starting from the binding energy of finite nucleus to equation of state of the infinite nuclear matter. A special attention was given on the effect of  $\omega^4$  coupling on newly proposed R3Y nucleon-nucleon potential. In this chapter, we will discuss some more applications of our proposed nucleon-nucleon interaction, R3Y in the calculation of astrophysical S-factor. Microscopic optical potentials for low energy proton reactions have been obtained by folding density dependent M3Y and R3Y interaction derived from nuclear matter calculation with densities from mean field approach to study astrophysically important proton-rich nuclei in mass 100-120 region. We compare S factors for low-energy  $(p, \gamma)$  reactions with available experimental data and further calculate astrophysical reaction rates for  $(p, \gamma)$  and  $(p, n)$  reactions using both R3Y and M3Y interaction. Along with the linear R3Y interaction, we choose some nonlinear R3Y (NR3Y) interactions from RMF calculation and folded them with corresponding RMF densities to reproduce experimental S factor values in this mass region. Impact of the non-linearity of NR3Y interaction on S-factor of proton rich nuclei is discussed in detail.

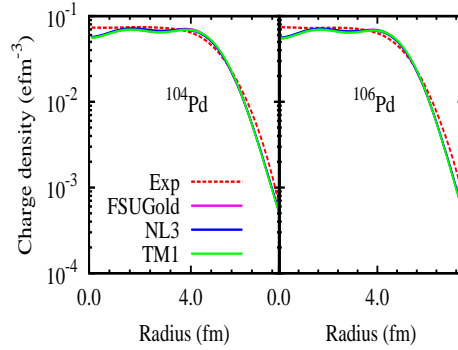


Figure 6.1: Comparison of charge density from our calculation with Fourier- Bessel analysis of experimental electron scattering data [203]

## 6.1 Introduction

In nature 35 nuclei, commonly termed as  $p$  nuclei, can be found on the proton-rich side of the nuclear landscape ranging between  $^{74}\text{Se}$  to  $^{196}\text{Hg}$ . As they are neutron deficit, the astrophysical reactions involved in the synthesis of these elements do not correspond to the slow( $s$ ) or fast( $r$ ) neutron capture processes. It mainly includes reactions such as proton capture, charge exchange and photo-disintegration. One can find a detailed study related to the  $p$  process in standard text books [for example, Illiadis [204]] and reviews [205].

The natural abundances for  $p$  nuclei are very low in the order of 0.01% to 1%. In general, the calculation of isotopic abundances require a network calculation typically involving 2000 nuclei and approximately 20000 reaction and decay channels and one major problem with this  $p$  network is that most of the nuclei involved in the reaction network are very shortly lived. As a consequence, it is very difficult to track the  $p$  process nucleosynthesis network experimentally. However, recent radioactive ion beam facilities are giving new prospects, still we are far away from measuring astrophysical reaction rates for the main reactions involved in the  $p$  process. Thus, one often has to depend on theoretical models to study these reactions. These type of calculations

acutely exploit the Hauser-Feshbach formalism where the optical model potential, in a local or a global form, is a key ingredient. Rauscher et.al. substantially calculated astrophysical reaction rates and cross sections in a global approach [206]. They further made a comment that the statistical model calculations may be improved by using locally tuned parameterization.

Here, we perform a fully microscopic calculation. The framework is based on microscopic optical model utilizing the theoretical density profile of a nucleus. In presence of a stable target, electron scattering experiment can be performed to avail nuclear charge density distribution data. However, in absence of a stable target, theory remains a sole guide to describe the density. Therefore, in this work we employ relativistic mean field (RMF) approach to extract the density information of a nucleus. This has the advantage of extending it to unknown mass regions. In some earlier works [207–211], this method has been used to study low energy proton reactions in the  $A \sim 55$ -100 region. Therefore we use this method in  $A \sim 100$ -120 region as an extension of previous works.

The non-linearity in the scalar field [186, 212] in a RMF theory has been proved very successful in reproducing various observable like nuclear ground state including nuclear matter properties and the surface phenomena like proton radioactivity etc. In this chapter, we intend to study the effects of microscopic optical potentials obtained from nonlinear  $NN$  interactions also in addition to the conventional linear  $NN$  interactions in the  $A \sim 100$ -120 region. We concentrate mainly on the region relevant to the  $p$  network and therefore mainly proton rich and stability region of the nuclear landscape is our main concern.

## 6.2 Procedure

The RMF approach has successfully explained various features of stable and exotic nuclei like ground state binding energy, radius, deformation, spin-orbit splitting, neutron halo etc. [7, 8, 163, 213, 214]. The RMF theory is nothing but the relativistic generalization of the non-relativistic effective theory like Skyrme and Gogny. This theory does the same job, what the non-relativistic theory can do, with an additional guarantee that it works in a better way in high density region [215]. We have used

the RMF formalism in both direct and indirect way. Directly we have calculated the nuclear density, which is an essential quantity to calculate the optical potential. Indirectly we used RMF Lagrangian to derive  $NN$  interactions also along with the phenomenologically availed  $NN$  interaction model. Here we have used different types of  $NN$  interactions, namely the density dependent M3Y interaction (DDM3Y) and nonlinear R3Y interactions(NR3Y). The concept of the NR3Y was originally developed from basic idea of the RMF formalism [216] and will be discussed later in this section.

In order to calculate the nuclear density, different forms of Lagrangian densities can be used from RMF approach. The chosen form of the interaction Lagrangian density is given by

$$\begin{aligned}\mathcal{L}_{int} = & \bar{\psi} \left[ g_{\sigma} \phi - \left( g_{\omega} V_{\mu} + \frac{g_{\rho}}{2} \tau \cdot \mathbf{b}_{\mu} + \frac{e}{2} (1 + \tau_3) A_{\mu} \right) \gamma_{\mu} \right] \psi - \frac{g_2}{3} \phi^3 - \frac{g_3}{4} \phi^4 + \frac{\xi}{4} (V_{\mu} V^{\mu})^2 \\ & + \Lambda (\mathbf{R}_{\mu} \cdot \mathbf{R}^{\mu}) (V_{\mu} V^{\mu}).\end{aligned}\tag{6.1}$$

The values of  $g_{\sigma}$ ,  $g_{\rho}$  and  $g_{\omega}$  are the coupling constants for sigma, rho, and omega mesons respectively, given in Table 6.1. The coupling constants for nonlinear terms of sigma are  $g_2$  and  $g_3$ , that for omega meson is given by  $\xi$  and  $\Lambda$  denotes the cross coupling strength between rho and omega meson.

For example, in case of FSUGold parameter set [90], one can see that, apart from the usual nucleon-meson interaction terms, it contains two additional nonlinear meson-meson self interaction terms including isoscalar ( $\omega$ ) meson self interactions, and mixed isoscalar-isovector ( $\omega^2 R^2$ ) coupling, whose main aim is to softening the equation of state (EOS) of symmetric nuclear matter. As a result, the new parameterization becomes more effective in reproducing quite a few nuclear collective modes, namely the breathing modes in  $^{90}\text{Zr}$  and  $^{208}\text{Pb}$ , and the isovector giant dipole resonance in  $^{208}\text{Pb}$  [90].

Again there are many other parameter sets in RMF which are different from each other in various ways like inclusion of new interaction or different value of masses and coupling constants of the mesons etc. For the comparison and better analysis we have included different parameter sets (NL3, TM1) as it is a matter of great concern to check their credibility in astrophysical prediction. Therefore, for the astrophysical calculations we have used nuclear densities from different sets of parameters like

NL3 and TM1 and folded them with corresponding  $NN$  interactions respectively. In case of DDM3Y interaction, which is not obtained from the RMF theory, we folded it with RMF density obtained from FSUGold. This FSUGold folded DDM3Y interaction have been used in earlier works [207–211] and successfully reproduced some astrophysically important cross sections and reaction rates in  $A \sim 55$ -100 region. Therefore, it will be interesting to see the behavior of such potential in  $A \sim 100$ -120 region.

Typically, a microscopic optical model potential is obtained by folding an effective interaction, derived either from the nuclear matter calculation, in the local density approximation, *i.e.* by substituting the nuclear matter density with the density distribution of the finite nucleus (for example DDM3Y), or directly by folding different R3Y interactions using different sets of parameters from RMF with corresponding density distributions. The folded potential therefore takes the form

$$V(E, \vec{R}) = \int \rho(\vec{r}') v_{eff}(r, \rho, E) d\vec{r}', \quad (6.2)$$

with  $\vec{r} = \vec{r}' - \vec{R}$  in fm. These effective interactions ( $v_{eff}(r, \rho, E)$ ) are described below in more details.

The density dependent M3Y (DDM3Y) interaction [217] is obtained from a finite range energy independent G-matrix elements of the Reid potential by adding a zero range energy dependent pseudo-potential and introducing a density dependent factor. The interaction is given by

$$v_{eff}(r) = t^{M3Y}(r, E)g(\rho). \quad (6.3)$$

Here  $v_{eff}(r)$  is a function of  $r$ ,  $\rho$  and  $E$ , where  $E$  is the incident energy and  $\rho$ , the nuclear density. The  $t^{M3Y}$  interaction is defines as

$$t^{M3Y} = 7999 \frac{e^{-4r}}{4r} - 2134 \frac{e^{-2.5r}}{2.5r} + J_{00}(E)\delta(r) \quad (6.4)$$

with the zero range pseudo potential  $J_{00}(E)$  given by,

$$J_{00}(E) = -276 \left( 1 - 0.005 \frac{E}{A} \right) \text{MeV} fm^3 \quad (6.5)$$

and  $g(\rho)$  is the density dependent factor expressed as,

$$g(\rho) = C(1 - b\rho^{2/3}), \quad (6.6)$$

with  $C = 2.07$  and  $b = 1.624 \text{ fm}^2$  [217].

In 2014, Sahu et.al. [186] introduced a simple form of nonlinear self-coupling of the scalar meson field and suggested a new  $NN$  potential from relativistic mean field theory (RMFT) analogous to the M3Y interaction. Rather than using usual phenomenological prescriptions, the authors derived the microscopic  $NN$  interaction from the RMF Lagrangian. Starting with the nonlinear relativistic mean field Lagrangian density for a nucleon-meson many-body system they solved the nuclear system under the mean-field approximation using the Lagrangian and obtained the field equations for the nucleons and mesons. It is necessary here to mention that the authors [186] had taken the nonlinear part of the scalar meson  $\sigma$  proportional to  $\sigma^3$  and  $\sigma^4$  in account. Finally for a normal nuclear medium the resultant effective nucleon-nucleon interaction, obtained from the summation of the scalar and vector meson fields takes the form.<sup>1</sup>

$$\begin{aligned} v_{eff}(r) = & \frac{g_\omega^2}{4\pi} \frac{e^{-m_\omega r}}{r} + \frac{g_\rho^2}{4\pi} \frac{e^{-m_\rho r}}{r} - \frac{g_\sigma^2}{4\pi} \frac{e^{-m_\sigma r}}{r} \\ & + \frac{g_2^2}{4\pi} r e^{-2m_\sigma r} + \frac{g_3^2}{4\pi} \frac{e^{-3m_\sigma r}}{r} - \frac{\xi^2}{4\pi} \frac{e^{-3m_\omega r}}{r} \\ & + J_{00}(E)\delta(r). \end{aligned} \quad (6.7)$$

Here  $m_\sigma$ ,  $m_\rho$ ,  $m_\omega$  are the masses of sigma, rho, and omega mesons respectively, whereas the zero range pseudo potential  $J_{00}(E)$  is given in Eqs.(6.5).

Using NL3 parameters from Table 6.1, Eqs. (6.7) becomes [186]

$$\begin{aligned} v_{eff}(r) = & 10395 \frac{e^{-3.97r}}{4r} + 1257 \frac{e^{-3.87r}}{4r} - 6554 \frac{e^{-2.58r}}{4r} \\ & + 6830r \frac{e^{-5.15r}}{4} + 52384 \frac{e^{-7.73r}}{4r} + J_{00}(E)\delta(r). \end{aligned} \quad (6.8)$$

---

<sup>1</sup>There is a typographical error in the expression of  $v_{eff}$  in Sahu et.al [186] and the corrected form is given in this thesis.

Table 6.1: Model parameters for the Lagrangian FSUGold [90], NL3 [49] and TM1 [87].

	FSUGold	NL3	TM1
$M$ (MeV)	939	939	938
$m_\sigma$ (MeV)	491.500	508.194	511.198
$m_\omega$ (MeV)	782.500	782.501	783.000
$m_\rho$ (MeV)	763.000	763.000	770.000
$g_\sigma$	10.592	10.2170	10.0290
$g_\omega$	14.298	12.8680	12.6140
$g_\rho$	11.767	4.4740	4.6320
$g_2$ (fm $^{-1}$ )	-4.2380	-10.4310	-7.2330
$g_3$	-49.8050	-28.8850	0.6180
$\xi$	2.0460	-	71.3070
$\Lambda$	0.0300	-	-

The authors of Ref. [186] denoted this  $NN$  interaction potential as NR3Y(NL3). Further, putting parameter sets from TM1 (Table 6.1), one can obtain  $v_{eff}$  for NR3Y(TM1).

Since the DDM3Y folded potential described above do not include any spin-orbit term, the spin-orbit potential from the Scheerbaum prescription [218] has been coupled with the phenomenological complex potential depths  $\lambda_{vso}$  and  $\lambda_{wso}$ . The spin-orbit potential is given by

$$U_{n(p)}^{so}(r) = (\lambda_{vso} + i\lambda_{wso}) \frac{1}{r} \frac{d}{dr} \left( \frac{2}{3} \rho_{p(n)} + \frac{1}{3} \rho_{n(p)} \right). \quad (6.9)$$

The depths are functions of energy, given by

$$\lambda_{vso} = 130 \exp(-0.013E) + 40,$$

and

$$\lambda_{wso} = -0.2(E - 20),$$

where  $E$  is in MeV. These standard values have been used in the present work. However, in case of nonlinear  $NN$  folded potentials from RMF (NR3Y(NL3), NR3Y(TM1)),



Table 6.2: Calculated binding energy per nucleon (B.E./A) [219] and charge radii  $r_{ch}$  [220] for some selected  $p$  nuclei compared with experimental values.

	B.E./A(MeV)				$r_{ch}$ (fm)			
	FSUGold	TM1	NL3	Exp	FSUGold	TM1	NL3	Exp
$^{102}\text{Pd}$	8.480	8.537	8.572	8.580	4.460	4.476	4.483	4.483
$^{106}\text{Cd}$	8.494	8.518	8.532	8.539	4.525	4.535	4.535	4.538
$^{108}\text{Cd}$	8.498	8.529	8.537	8.550	4.537	4.549	4.552	4.558
$^{113}\text{In}$	8.507	8.461	8.523	8.523	4.480	4.575	4.588	4.601
$^{112}\text{Sn}$	8.514	8.520	8.502	8.514	4.595	4.598	4.594	4.594
$^{114}\text{Sn}$	8.534	8.526	8.490	8.523	4.636	4.611	4.662	4.610
$^{115}\text{Sn}$	8.530	8.527	8.494	8.514	4.607	4.611	4.617	4.615
$^{120}\text{Te}$	8.461	8.461	8.460	8.477	4.682	4.688	4.735	4.704

one need not require to add spin-orbit term from outside, as it is contained within the RMF [186].

Finally reaction cross-sections and astrophysical reaction rates are calculated in the Hauser-Feshbach formalism using the computer package TALYS1.2 [221].

## 6.3 Results and discussions

For simplicity, this section is divided in three subsections. In the Sec. 6.3.1, results from RMF calculations are given. We will concentrate on the reaction cross-sections and astrophysical S factors in the Sec. 6.3.2. Furthermore, results for reaction rates for astrophysically important nuclei are provided. Sec. 6.3.3 is devoted to the effects of different  $NN$  potentials in this mass region.

### 6.3.1 RMF calculations

In some earlier works [207–211], FSUGold has been proved to be successful in reproducing experimentally obtained binding energy, charge radius and charge density data in the  $A \sim 55$ -100 region. Again in 1997, NL3 parameter set had been introduced by

Lalazissis et.al [49] with a aim to provide a better description not only for the properties of stable nuclei but also for those far from the  $\beta$  stability line and during last two decades, this parameter set successfully reproduces binding energy, charge radius etc. for various elements throughout the periodic table [49, 222]. In order to confirm the applicability of RMF calculations in  $A \sim 100$ -120 region, in Table 6.2, we compare nuclear binding energy per nucleon and charge radii of  $p$  nuclei in the concerned mass region with different sets of parameters of RMF formalism with existing experimental data [219, 220]. We find that, in most cases, our calculations with different sets of parameters match quite well with the experimental data. In Fig. 6.1 charge density from our calculations are compared with existing electron scattering data [203] for Pd isotopes and here also, the agreement is well enough to confirm the credibility of RMF models in this mass region.

### 6.3.2 Astrophysical S factor and reaction rates

In the present case, our calculations, being more microscopic, are more restricting. In general, phenomenological models are usually fine-tuned for nuclei near the stability valley, but not very successful in describing elements near the proton and neutron rich regions. Microscopic models, in contrary, can be extended to the drip line regions and therefore, this method can be used to study the reaction rates of nuclei involved in  $p$  process nucleosynthesis network ( $\sim 2000$  nuclei are present in the total  $p$  network). However, only a few number of stable  $p$  nuclides are available in nature that can be accessed by the experiment and therefore we are restricted to those nuclei for the purpose of comparison.

Let us first take the case of DDM3Y folded potential. As a first test of the optical model potential, we have calculated elastic proton scattering at low energies where experimental data are available. As the elastic scattering process involves the same incoming and outgoing channel for the optical model, it is expected to provide the easiest way to constrain various parameters involved in the calculation. Here we are mainly interested in the energy region between 2-8 MeV as the astrophysical important Gamow window lies within this energy range in the concerned mass region. However, scattering experiments are very difficult at such low energies, because the cross sections are extremely small, and hence no experimental data are available.

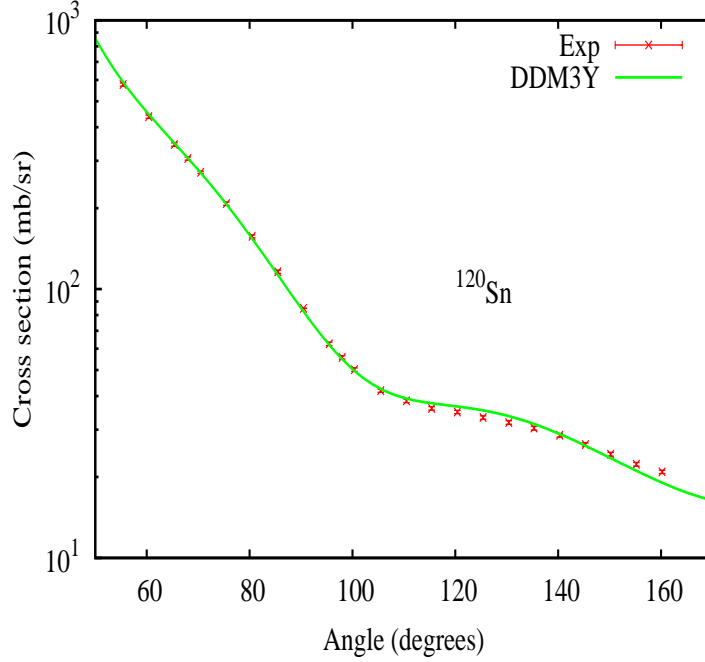


Figure 6.2: Experimental and calculated cross sections for elastic proton scattering at 9.7 MeV proton energy.

Therefore we have compared the cross sections from our calculations with the lowest energy experimental data available in the literature.

In Fig. 6.2, we present the result of our calculation with DDM3Y folded potential for  $^{120}\text{Sn}$  with available experimental data [223]. To fit the experimental data, at first, the folded DDM3Y potential is multiplied by factors 0.3 and 0.7 to obtain the real and imaginary parts of the optical potential, respectively. However better fits for individual reactions can be possible by varying different parameters. But if the present calculation has to be extended to an unknown mass region, this approach is clearly inadequate. Therefore, we have refrained from fitting individual reactions. A detailed description of these normalizing constants are available in references [207–211].

Yet, the astrophysical reaction rates depend on the proper choice of the level density and the E1 gamma strength. Therefore, we have calculated all of our results with microscopic level densities in Hartree-Fock (HF) and Hartree-Fock-Bogoliubov (HFB) methods, calculated for TALYS database by Goriley and Hilaire [221, 224] on the basis of Hartree-Fock calculations [225]. We have also compared our results using phenomenological level densities from a constant-temperature Fermi gas model,

a back-shifted Fermi gas model, and a generalized super-fluid model from TALYS. All these model parameters can be availed from TALYS database. We find that the cross sections are very sensitive to the level density parameters. We therefore analyzed, in most of the cases, the HF level densities fit the experimental data better in this mass region. Again, for E1 gamma strength functions, results derived from HF + BCS and HFB calculations, available in the TALYS database, are employed. In this case also, the results for HF+BCS calculations describe the experimental data reasonably well and we present our results for that approach only.

We now calculate some  $(p, \gamma)$  cross sections relevant to  $p$  nuclei in  $A \sim 100-120$  region, where experimental data are available. At such low energies, reaction cross-section varies rapidly making comparison between theory and experiment rather difficult. Therefore the usual practice in low-energy nuclear reaction is to compare another key observable, viz. the S factor. It can be expressed as [208]

$$S(E) = E\sigma(E)e^{2\pi\eta}, \quad (6.10)$$

where  $E$  is the energy in center of mass frame in keV, which factorises out the pre-exponential low energy dependence of reaction cross-section  $\sigma(E)$ , and  $\eta$  indicates the Sommerfeld parameter with

$$2\pi\eta = 31.29Z_pZ_t\sqrt{\frac{\mu}{E}}. \quad (6.11)$$

The factor  $\exp(2\pi\eta)$  is inversely proportional to the transmission probability through the Coulomb barrier with zero angular momentum(s-wave) and therefore removes exponential low energy dependence of  $\sigma(E)$ . Here  $\sigma(E)$  is in barn,  $Z_p$  and  $Z_t$  are the charge numbers of the projectile and the target, respectively and  $\mu$  is the reduced mass (in amu) of the composite system. This S factor varies much slowly than reaction cross-sections and for this reason, we calculate this quantity and compare it with experimentally obtained values.

In Figs. 6.3-6.5 we present the results of some of our calculations with folded DDM3Y potential for Pd, Cd and Sn isotopes, respectively, along with the corresponding experimental results. The experimental values for  $^{102}\text{Pd}$  are from Ref. [226](red point) and [227](blue cross),  $^{106,108}\text{Cd}$  from Gy. Gyürky et.al [228] and  $^{112}\text{Sn}$  from

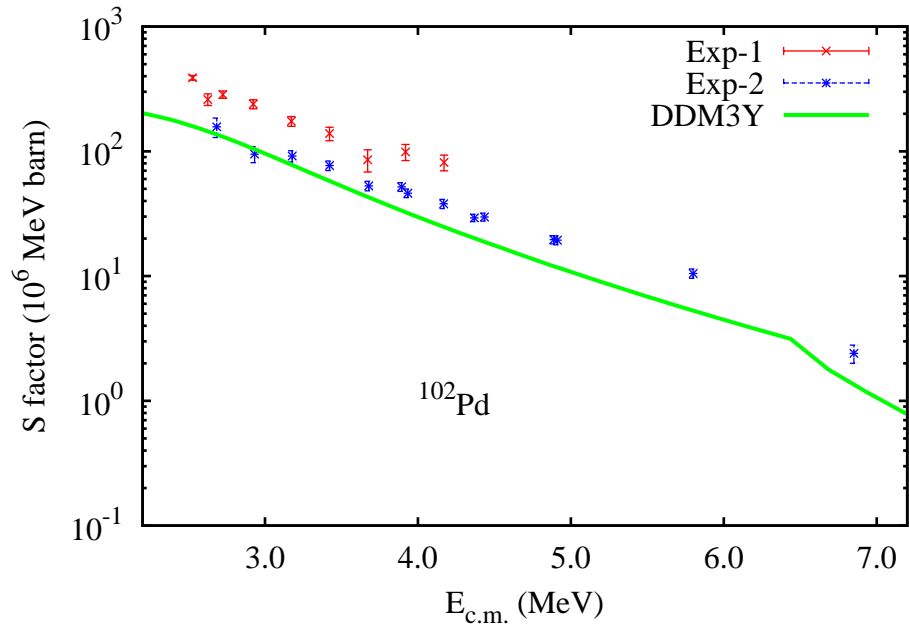


Figure 6.3: S factors from two different microscopic potentials are compared with experimental measurements for  $^{102}\text{Pd}$ . Here “Exp-1” is the experimental data from reference [226], “Exp-2” from reference [227] and “DDM3Y” is for the DDM3Y-folded potential.

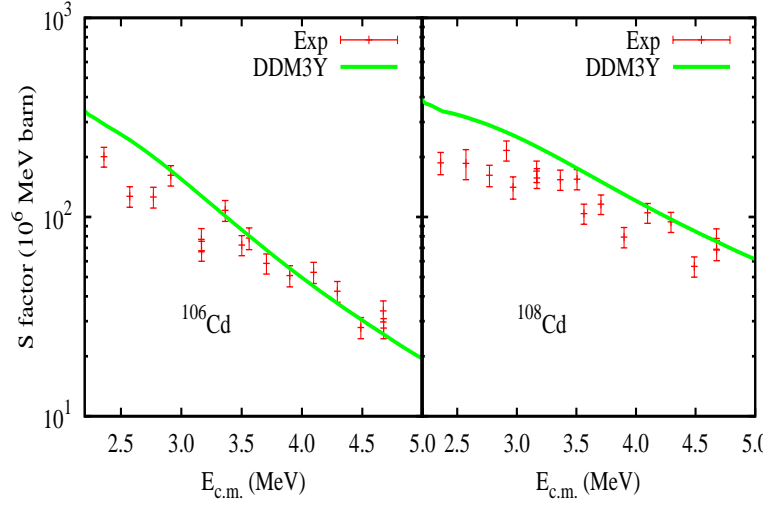


Figure 6.4: S factors extracted from theory compared with experimental measurements for  $^{106,108}\text{Cd}$ . Here “Exp” is the experimental data from reference [228].

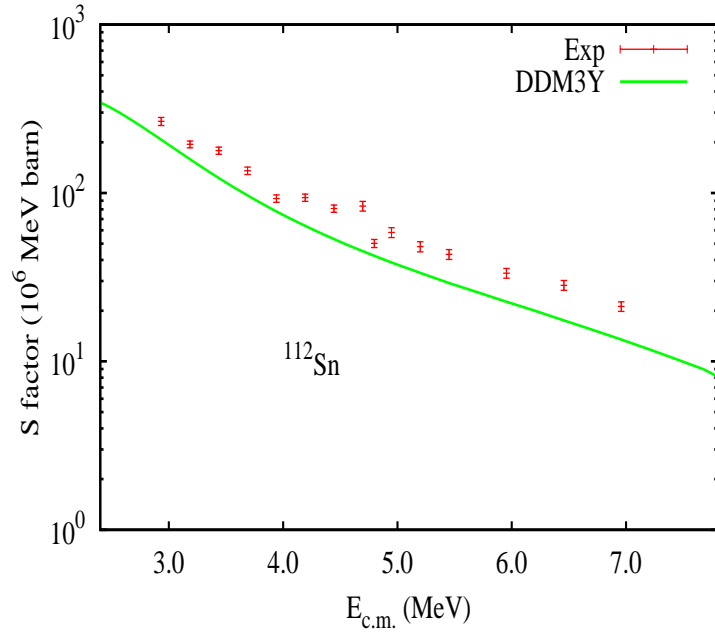


Figure 6.5: S factors extracted from theory compared with experimental measurements for  $^{112}\text{Sn}$ .

Ref. [229]. In case of  $^{102}\text{Pd}$  in Fig. 6.3, theoretical prediction is in a good agreement, mainly in the low energy regime, with the experimental data from Ref. [227] but under estimates the data obtained from the Ref. [226]. In Ref. [226], an activation technique was used in which gamma rays from decays of the reaction products were detected off-line by two hyper-pure germanium detectors in a low background environment, whereas in Ref. [227], cross-section measurements have been carried out at the cyclotron and Van de Graaff accelerator by irradiation of thin sample layers and subsequent counting of the induced activity. However, we can not comment on the individual merits of these experiments.

In case of  $^{106,108}\text{Cd}$  (in Fig. 6.4), one can find that the agreement of theory with experimental values are good enough, however there is a slight over estimation for  $^{108}\text{Cd}$  in the low energy regime. In case of  $^{112}\text{Sn}$  in Fig. 6.5, our calculation follows the experiment in a fairly good fashion.

The success of this microscopic optical potential (DDM3Y interaction folded with FSUGold density) in reproducing S-factor data for the above  $p$  nuclei leads us to calculate reaction rates of some astrophysically important reactions. In Fig. 6.6, we compare  $(p, \gamma)$  reaction rates for some important  $p$  nuclei with NONSMOKER rates [206] obtained from statistical model calculation with a global approach. Again in Fig. 6.7, reaction rates for charge exchange reactions  $(p, n)$  for some nuclei, however not astrophysically significant enough, in this mass region are compared with existing NONSMOKER calculations. One can see that the present calculation is very similar to the NONSMOKER values in almost all cases. Therefore, it is expected that all the results can also be reproduced with commonly used NONSMOKER rates.

In the remaining part, we mainly concentrate on the effects of optical potentials obtained by folding nonlinear interactions from RMF (NR3Y). In Fig. 6.8, S factors for  $^{120}\text{Te}$  obtained from NR3Y(NL3) and NR3Y(TM1) potentials are compared with the experimental data taken from Ref. [230]. The S- factor with DDM3Y interaction folded with FSUGold density is also given for comparison.

One can see that our calculation with folded DDM3Y potential shows a very nice agreement with experimental values throughout the energy range. In contrary, in case of NR3Y(NL3) folded potential, there is a wide deviation of the theory with experimental data after 6 MeV whereas the TM1 folded potential NR3Y(TM1) shows

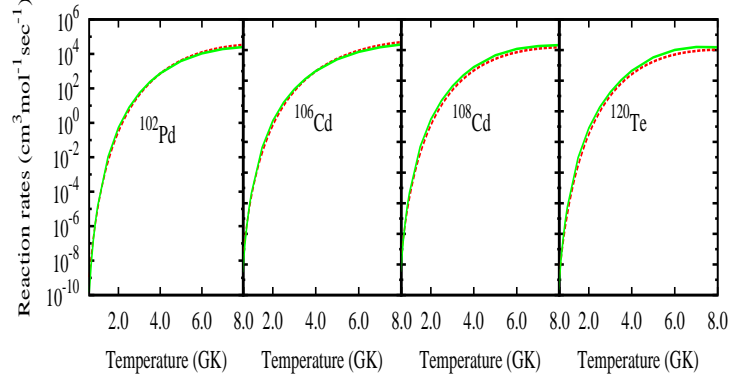


Figure 6.6: Astrophysical reaction rates for  $(p, \gamma)$  reactions of some important  $p$  nuclei compared with NONSMOKER rates [206]. Here Green Continuous line: Present calculation, Red Dotted line: NONSMOKER calculation.

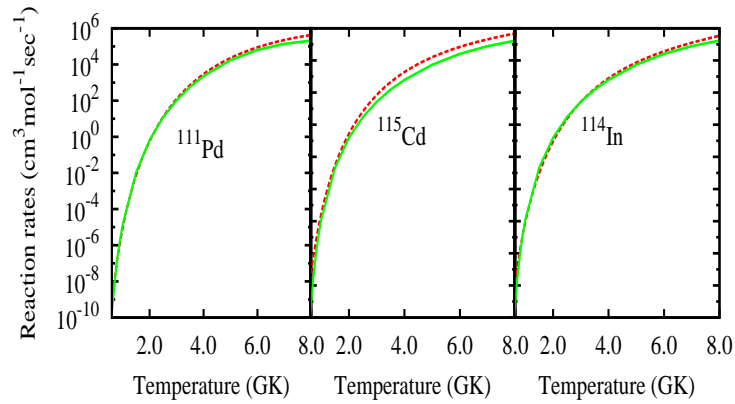


Figure 6.7: Astrophysical reaction rates for  $(p, n)$  reactions compared with NONSMOKER rates [206]. Here Green Continuous line: Present calculation, Red Dotted line: NONSMOKER calculation.



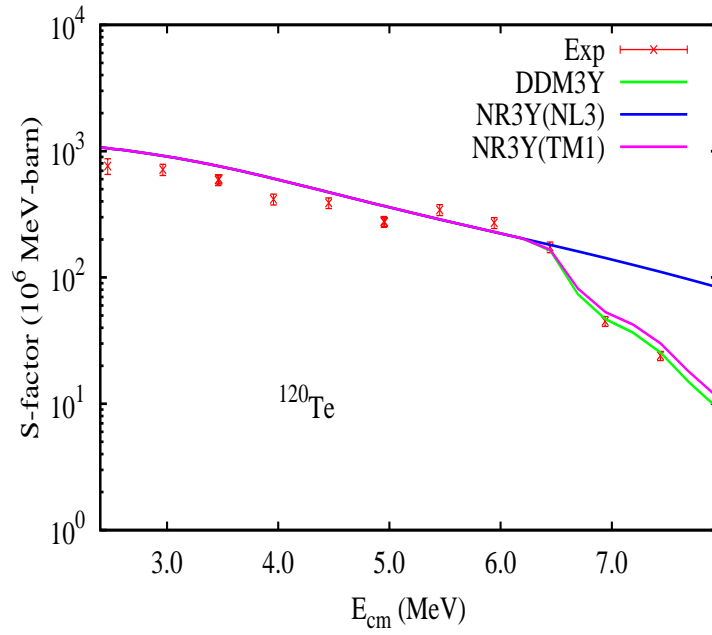


Figure 6.8: S factors extracted from our calculations compared with experimental measurements for  $^{120}\text{Te}$ . Here “Exp” is the experimental data from reference [230]. For other details, see the text.

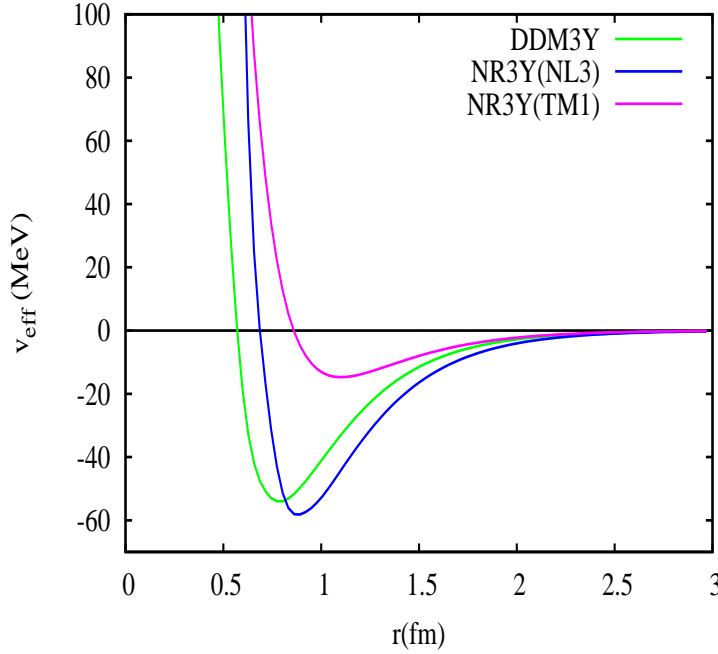


Figure 6.9: (Color online) Effective interaction potential for  $^{120}\text{Te}$ .

a decrease in S factor value around 6 MeV energy unlike the NR3Y(NL3) case.

The rapid drop of S factor values with increasing energy actually takes place due to the increasing contribution of higher angular momentum channels ( $l > 0$ ). Therefore, if the center of mass energy  $E_{c.m.}$  becomes larger than the Coulomb barrier for a specific set of nucleon-nucleus reaction ( $E_{c.m.} > E_c$ ), as a result the S factor will decrease rapidly with the growth of energy ( $E_{c.m.}$ ) [231]. In the next subsection, we illustrate this physics in detail and show how this phenomenon is associated with different form of potentials.

### 6.3.3 Optical potentials and effects of non-linearity

We now interpret the above results (for example, see Figs. 6.8) with help of the microscopic potentials obtained from different  $N - N$  interactions. In Fig. 6.9, the effective  $NN$  interaction potentials (in MeV) are plotted with the radius  $r$  (fm) for  $^{120}\text{Te}$ . The DDM3Y interaction, being dependent on the density, is different for different elements of the periodic table, whereas in contrary, other interactions remain unaltered for different elements. In Fig. 6.9 different forms of  $NN$  interactions are

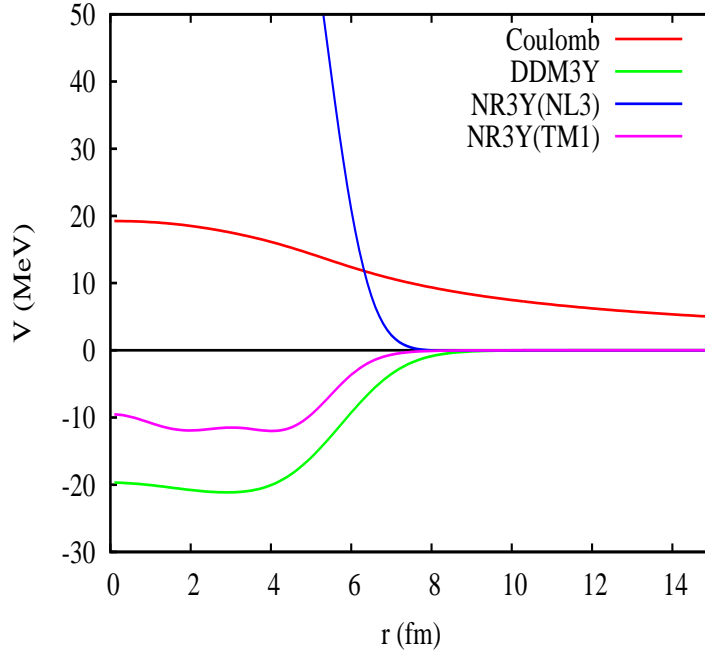


Figure 6.10: (Color online) Real central part of folded potentials and Coulomb potential for 7 MeV proton(Lab) incident on  $^{120}\text{Te}$

given. We find that the curves from DDM3Y and NR3Y(NL3) interactions generated from two different formalisms show almost similar trend.

A graphical representation of microscopic potentials for  $^{120}\text{Te}$  after folding the interactions is represented in Fig. 6.10. Here the real central part of the optical potential is plotted with the radius. In the figure, one can see that the DDM3Y folded potential provides an attractive potential whereas in case of NR3Y(NL3) folded potential, the repulsive part overpowers the attractive part, as well as the Coulomb part of the potential. As a result, the resultant repulsive barrier becomes greater than the Coulomb barrier almost upto a range for a nuclear reaction to occur. Therefore the penetrability of the higher angular momentum channels get reduced and as a obvious consequence, the desirable sharp drop in S factor (Fig. 6.8) has not been achieved. In case of TM1 folded potential, we can see that the effective contribution of the optical potential is attractive in nature similar to the DDM3Y potential and therefore, the Coulomb energy serves as the only repulsive barrier. As a result the penetration probability for higher angular momentum channels becomes higher than that of the NR3Y(NL3) case. This reason is replicated as a drop of S factor

values at higher energies in Fig. 6.8. In case of the imaginary part of the potential, the curves follow exactly the similar trend as that of the real part, i.e., apart from NR3Y(NL3) potential, rest of them gives attractive contribution. One can explain the above scenario from the numerical value of the nonlinear coupling constant  $g_3$  of TM1 parameter set, as given in Table 6.1, which is much less than that of the NL3 parameter set. Therefore it can be understood that with decreasing values of the nonlinear coupling constants  $g_2$  and  $g_3$ , the repulsive component of the optical potential also gets reduced and one point is attained when only the effect of Coulomb barrier remains as a dominating repulsive contributor and we will get patterns like TM1, DDM3Y as shown in Fig. 6.10 and we can find the expected drop of S factor at higher energies due to the opening of higher angular momentum channels. So from the above observations we can comment that there should be an upper cut-off for the coupling constants values of the nonlinear components.

## 6.4 Summary

To summarize, cross section for low energy ( $p, \gamma$ ) reactions for a number of  $p$  nuclei in  $A \sim 100$ -120 region have been calculated using microscopic optical model potential with the Hauser Feshbach reaction code TALYS. Mainly, microscopic potential is obtained by folding DDM3Y interaction with densities from RMF approach. Astrophysical reaction rates for ( $p, \gamma$ ) and ( $p, n$ ) reactions are compared with standard NONSMOKER results. Finally, the effect of microscopic optical potential obtained by folding nonlinear NR3Y(NL3) and NR3Y(TM1) interactions with corresponding RMF densities are employed to fit the experimental S factor data for  $^{120}\text{Te}$ . The reason of the deviation of theoretical prediction with nonlinear NR3Y(NL3) potential from experiment at higher energies has been discussed and finally we made a comment on magnitude of the coupling terms of the nonlinear components that an upper cut-off for  $g_2$  and  $g_3$  should be fixed to get proper repulsive component of the  $NN$  interaction.

# Chapter 7

## Effects of hyperon on both static and rotating neutron star

In last few chapters, we discussed the structure of finite nuclei by using relativistic as well as non-relativistic formalisms. Along with the finite nuclear system, an infinite nuclear system also plays very crucial role in understanding the nucleon-nucleon interaction and hence the nuclear structure. In this chapter, we have discussed the structure of the neutron star, which is a perfect example of the infinite nuclear matter system. Particularly, we study the effects of isovector-scalar ( $\delta$ )-meson on neutron and hyperon stars. Influence of  $\delta$ -meson on both static and rotating stars are discussed. The  $\delta$ -meson in a neutron star consisting of protons, neutrons, and electrons makes the equations of state stiffer at a higher density and consequently increases the maximum mass of the star. But induction of  $\delta$ -meson in the hyperon star decreases the maximum mass. This is due to the early evolution of hyperons in the presence of  $\delta$ -meson.

### 7.1 Introduction

Neutron star is a venerable candidate to discuss the physics at high density. We can not create such a high density in a terrestrial laboratory, so a neutron star is and the only object, which can provide much information on high-density nature of the matter [232, 233]. But it is not an easy task to deal with the neutron star for it's

complex nature, as all the four fundamental forces (strong, weak, gravitational and electromagnetic) are active. High gravitational field makes mandatory to use general theory of relativity for the study of neutron star structure. Equations of states (EOS) are the sole ingredient that must be supplied to the equation of stellar structure, Tolman-Oppenheimer-Volkoff (TOV) equation, whose output is the mass-radius profile of the dense neutron star. In this case, the nuclear EOS plays an intimate role in deciding the mass-radius of a neutron star. Its indispensable importance attracts the attention of physicists to have an anatomy of the interactions Lagrangian. As the name suggests, a neutron star is not completely made up neutrons, a small fraction of protons and electrons are also present, which is the consequence of the  $\beta$ -equilibrium and charge neutrality condition [234]. Also, the presence of exotic degrees of freedom like hyperons and kaons can not be ignored in such high dense matter. It is one among the most asymmetric and dense nuclear object in nature.

From last three decades [235, 236], the relativistic mean field (RMF) approximation, generalized by Walecka [8] and later on developed by Boguta and Bodmer [99] is one amongst the most reliable theory to deal with the infinite nuclear matter and finite nuclei. The original RMF formalism starts with an effective Lagrangian, whose degrees of freedom are nucleons,  $\sigma$ -,  $\omega$ -,  $\rho$ - and  $\pi$ -mesons. To reproduce proper experimental observable, it is extended to the self-interaction of  $\sigma$ -meson. Recently, all other self- and crossed interactions including the baryon octet are also introduced keeping in view the extra-ordinary condition of the system, such as highly asymmetric system or extremely high- density medium [237]. Since the RMF formalism is an effective nucleons-mesons model, the coupling constants for both nucleon-meson and hyperon-meson are fitted to reproduce the properties of selected nuclei and infinite nuclear matter properties [8, 99, 238, 239]. In this case, it is improper to use the parameters obtained from the free nucleon-nucleon scattering data. The parameters, with proper relativistic kinematics and with the mesons and their properties are already known or fixed from the properties of a small number of finite nuclei, the method gives excellent results not only for spherical nuclei but also well-known deformed cases. The same force parametrization can be used both for  $\beta$ -stable and  $\beta$ -unstable nuclei through-out the periodic table [49, 193, 240, 241].

The importance of the self- and crossed- interactions are significant for some specific properties of nuclei/nuclear-matter in certain conditions. For example, self-interaction of  $\sigma$ -meson takes care the reduction of nuclear matter incompressibility  $K_\infty$  from an unacceptable high value of  $K_\infty \sim 600$  MeV to a reasonable number of  $\sim 270$  MeV [99, 141], while the self-interaction of vector meson  $\omega$  soften the equations of states [90, 193]. Thus, it is imperative to include all the mesons and their possible interactions with nucleons and hyperons, self- and crossed terms in the effective Lagrangian density. However, it is not necessary to do so, because of the symmetry reason and their heavy masses [242]. For example, to keep the spin-isospin and parity symmetry in the ground state, the contribution of  $\pi$ -meson is ignored [243] and also the effect of heavier mesons are neglected for their negligible contribution. Taking into this argument, in many versions of the RMF formalism, the inclusion of isovector-scalar ( $\delta$ ) meson is neglected due to its small contribution. But recently it is seen [244–249] that the endowment of the  $\delta$ -meson goes on increasing with density and asymmetry of the nuclear system. Thus, it will be impossible for us to justify the abandon of  $\delta$ -meson both conceptually and practically, while considering the high asymmetry and dense nuclear systems, like the neutron star and relativistic heavy ion collision. Recent observation of neutron star like PSR J1614-2230 with mass of  $(1.97 \pm 0.04)M_\odot$  [201] and the PSR J0348+0432 with mass of  $(2.01 \pm 0.04)M_\odot$  [250] reopen the challenge in the dense matter physics. The heavy mass of PSR J0348+0432 ( $M=2.01 \pm 0.04M_\odot$ ) forces the nuclear theorists to re-think the composition and interaction inside the neutron star. Therefore, it is important to establish the effects of the  $\delta$ -meson and all possible interactions of other mesons for such compact and asymmetry system.

The paper is organized as follows: In Sec. 7.2, we have outlined a brief theoretical formalism. The necessary steps of the RMF model and the inclusion of  $\delta$ -meson is explained. The results and discussions are devoted in Sec. 7.3. Here, we have attempted to explain the effects of  $\delta$ -meson on the nuclear matter system like hyperon and proton-neutron stars. This analysis is done for both static and rotating neutron and neutron-hyperon stars. In this calculations, the E-RMF Lagrangian (G2 parameter set) is used to take care of all possible self- and crossed interactions [251]. On top of the G2 Lagrangian, the  $\delta$ -meson interaction is added to take care of the isovector

channel. The concluding remarks are given in section 7.4.

## 7.2 Theoretical formalism

From last one decade a lot of work have been done to emphasize the role of  $\delta$ -meson on both finite and infinite nuclear matter [252–255]. It is seen that the contribution of  $\delta$ -meson to the symmetry energy is negative [256]. To fix the symmetry energy around the empirical value ( $\sim 30$  MeV ) we need a large coupling constant of the  $\rho$ -meson ( $g_\rho$ ) value in the absence of the  $g_\delta$ . The proton and neutron effective masses split due to inclusion of  $\delta$ -meson and consequently it affects the transport properties of neutron star [246]. The addition of  $\delta$ -meson not only modify the property of infinite nuclear matter, but also enhances the spin-orbit splitting in the finite nuclei [252]. A lot of mysteries are present in the effects of  $\delta$ -meson till date. The motivation of the present chapter is to study such information. It is to be noted that both the  $\rho$ - and  $\delta$ -mesons correspond to the isospin asymmetry, and a careful precaution is essential while fixing the  $\delta$ -meson coupling in the interaction.

The effective field theory and naturalness of the parameter are described in [251, 257–260]. The Lagrangian is consistent with underlying symmetries of the QCD. The G2 parameter is motivated by E-RMF theory. The terms of the Lagrangian are taken into account up to 4<sup>th</sup> order in meson-baryon coupling. For the study of isovector channel, we have introduced the isovector-scalar  $\delta$ -meson. The baryon-meson interaction is given by [237]:

$$\begin{aligned}
\mathcal{L} = & \sum_B \bar{\psi}_B (i\gamma^\mu D_\mu - m_B + g_{\sigma B}\sigma + g_{\delta B}\delta \cdot \tau) \psi_B + \frac{1}{2}\partial_\mu \sigma \partial_\mu \sigma \\
& - m_\sigma^2 \sigma^2 \left( \frac{1}{2} + \frac{\kappa_3}{3!} \frac{g_\sigma \sigma}{m_B} + \frac{\kappa_4}{4!} \frac{g_\sigma^2 \sigma^2}{m_B^2} \right) - \frac{1}{4} \Omega_{\mu\nu} \Omega^{\mu\nu} \\
& + \frac{1}{2} m_\omega^2 \omega_\mu \omega^\mu \left( 1 + \eta_1 \frac{g_\sigma \sigma}{m_B} + \frac{\eta_2}{2} \frac{g_\sigma^2 \sigma^2}{m_B^2} \right) - \frac{1}{4} R_{\mu\nu}^a R^{\mu\nu a} \\
& + \frac{1}{2} m_\rho^2 \rho_\mu^a \rho^{a\mu} \left( 1 + \eta_\rho \frac{g_\sigma \sigma}{m_B} \right) + \frac{1}{2} \partial_\mu \delta \cdot \partial_\mu \delta - m_\delta^2 \delta^2 + \frac{1}{4!} \zeta_0 (g_\omega \omega_\mu \omega^\mu)^2 \\
& + \sum_l \bar{\psi}_l (i\gamma^\mu \partial_\mu - m_l) \psi_l.
\end{aligned} \tag{7.1}$$



The co-variant derivative  $D_\mu$  is defined as:

$$D_\mu = \partial_\mu + ig_\omega \omega_\mu + ig_\rho I_3 \tau^a \rho_\mu^a, \quad (7.2)$$

where  $R_{\mu\nu}^a$  and  $\Omega_{\mu\nu}$  are field tensors and defined as follow

$$R_{\mu\nu}^a = \partial_\mu \rho_\nu^a - \partial_\nu \rho_\mu^a + g_\rho \epsilon_{abc} \rho_\mu^b \rho_\nu^c, \quad (7.3)$$

$$\Omega_{\mu\nu} = \partial_\mu \omega_\nu - \partial_\nu \omega_\mu. \quad (7.4)$$

Here,  $\sigma$ ,  $\omega$ ,  $\rho$  and  $\delta$  are the sigma, omega, rho and delta meson fields, respectively and in real calculation, we ignore the non-abelian term from the  $\rho$ -field. All symbols are carrying their own usual meaning [237, 244].

The Lagrangian equation for different mesons are given by [237]:

$$\begin{aligned} m_\sigma^2 \left( \sigma_0 + \frac{g_\sigma \kappa_3 \sigma_0}{2m_B} + \frac{\kappa_4 g_\sigma^2 \sigma_0^2}{6m_B^2} \right) \sigma_0 - \frac{1}{2} m_\rho^2 \eta_\rho \frac{g_\sigma \rho_{03}^2}{m_B} \\ - \frac{1}{2} m_\omega^2 \left( \eta_1 \frac{g_\sigma}{m_B} + \eta_2 \frac{g_\sigma^2 \sigma_0}{m_B^2} \right) \omega_0^2 = \sum g_\sigma \rho_B^s, \end{aligned} \quad (7.5)$$

$$m_\omega^2 \left( 1 + \eta_1 \frac{g_\sigma \sigma_0}{m_B} + \frac{\eta_2 g_\sigma^2 \sigma_0^2}{2 m_B^2} \right) \omega_0 + \frac{1}{6} \zeta_0 g_\omega^2 \omega_0^3 = \sum g_\omega \rho_B, \quad (7.6)$$

$$m_\rho^2 \left( 1 + \eta_\rho \frac{g_\sigma \sigma_0}{m_B} \right) = \frac{1}{2} \sum g_\rho \rho_{B3}, \quad (7.7)$$

$$m_\delta^2 \delta^3 = g_\delta^2 \rho_{3B}^s, \quad (7.8)$$

with  $\rho_{3B}^s = \rho_p^s - \rho_n^s$ ,  $\rho_p^s$  and  $\rho_n^s$  are scalar densities for the proton and neutron, respectively. The total scalar density is expressed as the sum of the proton and neutron densities  $\rho_B^s = \rho_p^s + \rho_n^s$ , which is given by

$$\rho_i^s = \frac{2}{(2\pi)^3} \int_0^{k_i} \frac{M_i^* d^3 k}{E_i^*}, i = p, n \quad (7.9)$$

and the vector (baryon) density

$$\rho_B = \frac{2}{(2\pi)^3} \int_0^{k_i} d^3 k, \quad (7.10)$$

where,  $E_i^* = (k_i^2 + M_i^{*2})^{1/2}$  is the effective energy,  $k_i$  is the Fermi momentum of the baryons.  $M_p^*$  and  $M_n^*$  are the proton and neutron effective masses written as

$$M_p^* = M_p - g_\sigma \sigma_0 - g_\delta \delta^3 \quad (7.11)$$

$$M_n^* = M_n - g_\sigma \sigma_0 + g_\delta \delta^3, \quad (7.12)$$

which are solved self-consistently.  $I_3$  is the third component of isospin projection and  $B$  stands for baryon octet. The energy and pressure density depends on the effective mass  $M_B^*$  of the system, which first needed to solve these self-consistent equations and obtained the fields for mesons. Using the Einstein's energy-momentum tensor, the total energy and pressure density are given as [237]:

$$\begin{aligned} \mathcal{E} = & \sum_B \frac{2}{(2\pi)^3} \int_0^{k_B} d^3k E_B^*(k) + \frac{1}{8} \zeta_0 g_\omega^2 \omega_0^4 + m_\sigma^2 \sigma_0^2 \left( \frac{1}{2} + \frac{\kappa_3}{3!} \frac{g_\sigma \sigma_0}{m_B} + \frac{\kappa_4}{4!} \frac{g_\sigma^2 \sigma_0^2}{m_B^2} \right) \\ & + \frac{1}{2} m_\omega^2 \omega_0^2 \left( 1 + \eta_1 \frac{g_\sigma \sigma_0}{m_B} + \frac{\eta_2}{2} \frac{g_\sigma^2 \sigma_0^2}{m_B^2} \right) + \frac{1}{2} m_\rho^2 \rho_{03}^2 \left( 1 + \eta_\rho \frac{g_\sigma \sigma_0}{m_B} \right) \\ & + \frac{1}{2} \frac{m_\delta^2}{g_\delta^2} (\delta^3)^2 + \sum_l \varepsilon_l, \end{aligned} \quad (7.13)$$

and

$$\begin{aligned} \mathcal{P} = & \sum_B \frac{2}{3(2\pi)^3} \int_0^{k_B} d^3k E_B^*(k) + \frac{1}{8} \zeta_0 g_\omega^2 \omega_0^4 - m_\sigma^2 \sigma_0^2 \left( \frac{1}{2} + \frac{\kappa_3}{3!} \frac{g_\sigma \sigma_0}{m_B} + \frac{\kappa_4}{4!} \frac{g_\sigma^2 \sigma_0^2}{m_B^2} \right) \\ & + \frac{1}{2} m_\omega^2 \omega_0^2 \left( 1 + \eta_1 \frac{g_\sigma \sigma_0}{m_B} + \frac{\eta_2}{2} \frac{g_\sigma^2 \sigma_0^2}{m_B^2} \right) + \frac{1}{2} m_\rho^2 \rho_{03}^2 \left( 1 + \eta_\rho \frac{g_\sigma \sigma_0}{m_B} \right) \\ & - \frac{1}{2} \frac{m_\delta^2}{g_\delta^2} (\delta^3)^2 + \sum_l P_l, \end{aligned} \quad (7.14)$$

where  $P_l$  and  $\varepsilon_l$  are lepton's pressure and energy density, respectively.

### 7.3 Results and discussions

Before going to the discussions of our results, we give a brief description of the parameter fitting procedure for  $g_\rho$  and  $g_\delta$ . As it is commonly known, the symmetric energy  $E_{sym}$ , is an important quantity to select the equation of states. This value

of  $E_{sym}$  determines the structure of both static and rotating neutron stars. On the other hand, an arbitrary combination of  $g_\rho$  and  $g_\delta$  with a fixed value of  $E_s$  can affect the ground state properties of finite nuclei. Thus, to have a clear picture on the effect of  $g_\delta$  on hyperon star structure, we have chosen two different prescriptions for the selection of  $g_\delta$  in our present calculations. (1) In the first method, we have constructed various sets of  $g_\rho$  and  $g_\delta$  keeping  $E_s$  fixed. Here, all the other parameters of G2 set are remained unchanged. The G2 set and the combination of  $g_\rho$  and  $g_\delta$  are displayed in Table 7.1. (2) In the second procedure, we have chosen the  $g_\rho$ ,  $g_\delta$  pairs keeping the binding energy constant (experimental binding energy) for finite nuclei. The values of these  $g_\rho$  and  $g_\delta$  are given in Table 7.3 with other properties of infinite nuclear matter. It is worthy to re-emphasized here that we are not looking for a full-fledged parameter set including the  $\delta$ -meson coupling, but our aim in this paper is to study the effects of  $\delta$ -meson coupling on hyperon star and the production of baryon octet. Therefore, after splitting the  $g_\rho$  coupling constant into two parts ( $g_\rho$ ,  $g_\delta$ ) using the first prescription, the results on hyperon star along with the neutron star structures both for static and rotating cases under  $\beta$ -equilibrium condition are discussed in the subsequent subsections 7.3.2, 7.3.3, 7.3.4, 7.3.5 and 7.3.6. In Sec. IV, we follow the second procedure to get the ( $g_\rho$ ,  $g_\delta$ ) pairs and applied these to some selective cases.

### 7.3.1 Parametrization of $g_\rho$ and $g_\delta$ with constant symmetry energy

It is important to fix  $g_\delta$  value to see the effects of the  $\delta$ -meson. The isovector channels in RMF theory come to exist through both the  $\rho$ - and  $\delta$ -mesons couplings. While considering the effects of the  $\delta$ -meson, we have to take the  $\rho$ -meson into account. Since both the isovector channels are related to isospin, one can not optimize the  $g_\delta$  coupling independently. Here, we have followed a more reliable procedure by fixing the symmetry energy  $E_{sym}$  with adjusting simultaneously different values of  $g_\rho$  and  $g_\delta$  [246]. In general, for most of the non-relativistic formalism, the symmetry energy  $E_{sym}$  is around 30-33 MeV. However, in some specific parametrization like GS4,  $E_{sym} = 12.83$  MeV and for PRC45 set it is 51.01 MeV [261, 262]. On the other hand, in non-linear, density-dependent and point-coupling relativistic mean

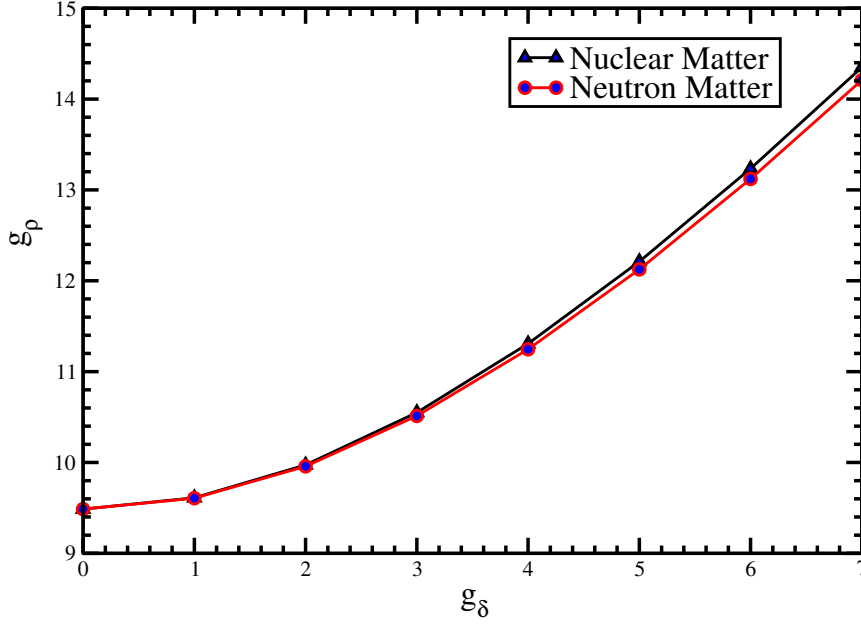


Figure 7.1: Variation of  $g_\rho$  and  $g_\delta$  at a constant value of symmetry energy  $E_{sym} = 36.4$  MeV for both nuclear and neutron matter.

field forces, the  $E_{sym}$  varies from 26.1 to 44.0 MeV. Here we have used the well known G2 parametrization, which has a moderate symmetry energy  $E_{sym} = 36.4$  MeV. It is to be noted that the symmetry energy plays a crucial role both in finite nuclei and in the equation of state, which include the neutron distribution radius in the nucleus and the mass and radius of a neutron star, respectively. For a smaller value of  $E_{sym}$ , both the relativistic and non-relativistic forces predict a smaller neutron star mass contrary to the recent observation of about  $2M_\odot$ . A detail variation of symmetry energies for Skyrme effective interaction and non-linear relativistic mean field formalism is available in Refs. [261, 262]. Recently, a large number of papers have been devoted to  $E_{sym}$  for a definite value, but till it is under active discussions.

As it is mentioned earlier, we have added  $g_\delta$  on top of the G2 parameter set. Thus, the symmetry energy of G2 parameter  $E_{sym} = 36.4$  MeV is kept constant at the time of re-shuffling  $g_\rho$  and  $g_\delta$ . It is to be noted that, we do not want to change the value of  $E_{sym}$  of the original G2 parameter set with the addition of  $\delta$ -meson. The G2 parameters and the  $g_\delta$  and  $g_\delta$  combinations are displayed in Table 7.1. The nuclear matter properties are also listed in the table (middle panel). For a particular value of  $E_{sym} = 36.4$  MeV, the variation of  $g_\rho$  and  $g_\delta$  are plotted in Fig. 7.1. From

Table 7.1: The parameters for G2 set are in the upper panel of the Table. The nuclear matter saturation properties are in the middle panel and various  $g_\rho$  and  $g_\delta$  combinations are in the lower panel, keeping symmetry energy  $E_{sym} = 36.4$  MeV fixed.

$m_n = 939.0$ MeV	$m_\sigma = 520.206$ MeV	$m_\omega = 782.0$ MeV	$m_\rho = 770.0$ MeV	$m_\delta = 980.0$ MeV	$\Lambda = 0.0$	$\zeta_0 = 2.642$	$\eta_\rho = 0.39$	
$g_\sigma = 10.5088$	$g_\omega = 12.7864$	$g_\rho = 9.5108$	$g_\delta = 0.0$	$k_3 = 3.2376$	$k_4 = 0.6939$	$\eta_1 = 0.65$	$\eta_2 = 0.11$	
$\rho_0 = 0.153 fm^{-3}$	$E/A = -16.07$ MeV	$K_\infty = 215$ MeV	$E_{sym} = 36.4$ MeV	$m_n^*/m_n = 0.664$				
$(g_\rho, g_\delta)$	(9.510, 0.0)	(9.612, 1.0)	(9.973, 2.0)	(10.550, 3.0)	(11.307, 4.0)	(12.212, 5.0)	(13.234, 6.0)	(14.349, 7.0)

Table 7.2: Binding energy (MeV) and charge radius (fm) are calculated with various combination of  $g_\rho$  and  $g_\delta$  in G2+ $\delta$ . The results are compared with experimental data [263].

$(g_\rho, g_\delta)$	(9.510, 0.0)	(9.612, 1.0)	(9.973, 2.0)	(10.550, 3.0)	(11.307, 4.0)	(12.212, 5.0)	(13.234, 6.0)	(14.349, 7.0)	
Nucleus	Theory								Expt.
<sup>16</sup> O (BE)	127.2	127.2	127.2	127.2	127.2	127.2	127.2	127.2	127.6
$r_{ch}$	2.718	2.718	2.718	2.718	2.718	2.717	2.717	2.716	2.699
<sup>40</sup> Ca (BE)	341.1	341.1	341.1	341.1	341.1	341.1	341.1	341.1	342.0
$r_{ch}$	3.453	3.453	3.453	3.453	3.452	3.451	3.450	3.449	3.4776
<sup>48</sup> Ca (BE)	416.0	415.8	415.2	414.1	412.6	410.7	408.4	405.7	416.0
$r_{ch}$	3.440	3.439	3.438	3.437	3.435	3.432	3.430	3.427	3.477
<sup>56</sup> Ni (BE)	480.4	480.3	480.3	480.3	480.3	480.3	480.3	480.2	484.0
$r_{ch}$	3.730	3.730	3.730	3.730	3.730	3.730	3.730	3.724	
<sup>58</sup> Ni (BE)	497.2	497.2	497.1	497.0	496.9	496.7	496.5	496.3	506.5
$r_{ch}$	3.765	3.765	3.763	3.762	3.761	3.758	3.756	3.753	3.775
<sup>90</sup> Zr (BE)	781.6	781.2	780.6	779.4	777.9	775.9	773.6	770.8	783.9
$r_{ch}$	4.238	4.238	4.237	4.235	4.233	4.230	4.228	4.225	4.269
<sup>116</sup> Sn (BE)	981.2	980.7	979.4	977.2	974.1	970.2	965.6	960.3	988.7
$r_{ch}$	4.604	4.603	4.601	4.598	4.594	4.589	4.584	4.579	4.625
<sup>118</sup> Sn (BE)	997.6	997.1	995.4	992.7	989.0	984.3	978.7	972.2	1004.9
$r_{ch}$	4.620	4.619	4.617	4.613	4.610	4.604	4.599	4.594	4.639
<sup>120</sup> Sn (BE)	1013.9	1013.2	1011.2	1008.0	1003.5	998.0	991.3	983.8	1020.5
$r_{ch}$	4.627	4.626	4.624	4.620	4.616	4.610	4.605	4.600	4.652
<sup>208</sup> Pb (BE)	1633.3	1631.4	1625.7	1616.2	1603.0	1586.4	1566.4	1543.5	1636.4
$r_{ch}$	5.499	5.498	5.497	5.494	5.492	5.489	5.487	5.485	5.501

Table 7.3: Mass and radius of the neutron star are calculated at different values of  $g_\rho$  and  $g_\delta$  keeping binding energy of  $^{208}\text{Pb}$  (1633.296 MeV) constant. The calculated results of  $E_{sym}$ ,  $L_{sym}$  and  $K_{sym}$  are for nuclear matter at different combinations of  $(g_\rho, g_\delta)$  pairs.

$(g_\rho, g_\delta)$	$\frac{M}{M_\odot}$	Radius (Km)	$E_{sym}$ (MeV)	$L_{sym}$ (MeV)	$K_{sym}$ (MeV)
(9.510, 0.0)	1.980	11.230	36.4	101.0	-7.58
(9.588, 1.746)	1.993	11.246	35.3	98.3	-0.60
(9.896, 3.543)	1.997	11.262	31.7	90.2	20.90
(10.518, 5.742)	2.004	11.294	23.8	72.5	67.07
(11.774, 8.834)	2.018	11.510	6.35	30.6	169.03

Fig. 7.1, it is clear that as the  $g_\delta$  increases the  $g_\rho$  value also increases, almost linearly, to fix the symmetry energy unchanged. This implies that  $\rho$ - and  $\delta$ -mesons have opposite effect on  $E_{sym}$  contribution, i.e., the  $\delta$ -meson has negative contribution of the symmetry energy contrary to the positive contribution of  $\rho$ -meson.

We feel that it is instructive to check the finite nuclear properties with these combinations of  $g_\rho$  and  $g_\delta$ . We have tabulated the binding energy and charge radius of some spherical nucleus in Table 7.2. From the table, it is clear that binding energy for asymmetric nucleus goes on decreasing with increasing  $\delta$ -meson and decreasing  $\rho$ -meson couplings. However, it is well understood that the scalar  $\delta$ -meson gives a positive contribution to the binding energy. Thus, the binding energy of asymmetric nuclei should go on increasing with  $g_\delta$  contrary to the observation seen in Table 7.2. This happens, because of the simultaneous change of  $(g_\rho, g_\delta)$  pair to keep the constant symmetry energy, i.e.,  $g_\rho$  is decreasing and  $g_\delta$  is increasing. As a result, the contribution of  $\rho$ - meson, which is negative to the binding energy dominates over the  $\delta$ -meson effect on binding energy. But in case of symmetric nucleus, like  $^{16}\text{O}$  etc. the effects of both  $\rho$ - and  $\delta$ -mesons are absent due to iso-spin symmetry. A further inspection of Table 7.2 reveals a slight change in binding energy and charge radius even for symmetric nuclei because of the slight different in density distribution of protons and neutrons, although it is small.

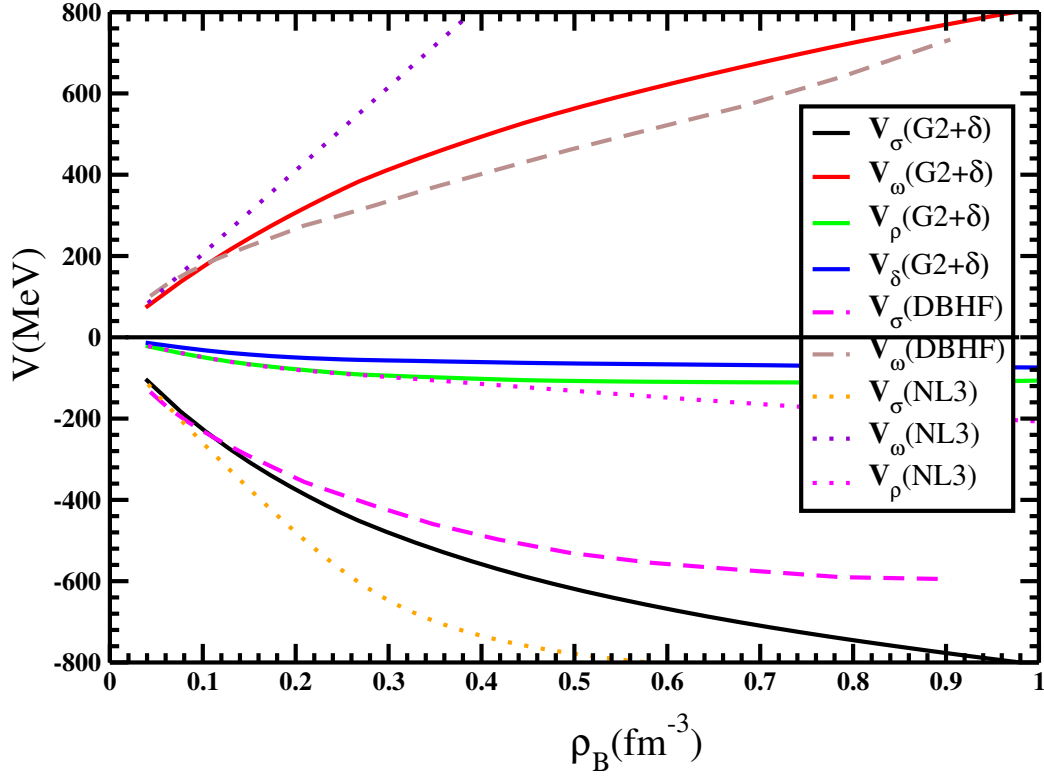


Figure 7.2: Various meson fields are obtained from the RMF theory with  $G2 + g_\delta$  and NL3 parameter sets. The  $\sigma$ -meson field  $V_\sigma$  and  $\omega$ -meson field  $V_\omega$  from  $G2 + g_\delta$  calculations are compared with the results of DBHF theory [264] and NL3 set.

### 7.3.2 Fields of $\sigma, \omega, \rho$ and $\delta$ mesons

The fields of the meson play a crucial role to construct the nuclear potential, which is the deciding factor for all type of calculations in the relativistic mean field model. In Fig. 7.2, we have plotted various meson fields included in the present calculations, such as  $\sigma$ ,  $\omega$ ,  $\rho$  and  $\delta$  with  $g_\delta$  on top of G2 parameter set ( $G2 + g_\delta$ ). It is obvious that  $V_\sigma$  and  $V_\omega$  are opposite to each other, which is also reflected in the figure. This means, the positive value of  $V_\omega$  gives a strong repulsion, which is compensated by the strongly attractive potential of the  $\sigma$ -meson field  $V_\sigma$ . The nature of the curves for  $V_\sigma$  and  $V_\omega$  are almost similar except the sign. The magnitude of  $V_\sigma$  and  $V_\omega$  looks almost equal. However, in real (it is not clearly visible in the curve, because of the scale), the value of  $V_\sigma$  is slightly larger than  $V_\omega$ , which keeps the overall nuclear potential strongly attractive. The attractive  $V_\sigma$  and repulsive  $V_\omega$  potentials combinely give the saturation properties of the nuclear force. It is worthy to mention that the

contributions of self-interaction terms are taken care both in  $V_\sigma$  and  $V_\omega$ , which are the key quantities to solve the Coester band problem [186] and the explanation of quark-gluon-plasma (QGP) formation within the relativistic mean field formalism [265]. The self-interaction of the  $\sigma$ -meson gives a repulsive force at long range part of the nuclear potential, which is equivalent to the 3-body interaction and responsible for the saturation properties of nuclear force. The calculated results of  $V_\sigma$  and  $V_\omega$  are compared with the results obtained from DBHF theory with Bonn-A potential [264] and NL3 [49] force.

Fig. 7.2 clearly shows that in the low density region (density  $\rho_B \sim 2\rho_0$ ) both RMF and DBHF theories well matched. But as it increases beyond density  $\rho_B \sim 2\rho_0$  ( $\rho_0$  is the nuclear saturation density) both the calculations deviate from each other. The possible reason may be the fitting procedure of parameters in Bonn-A potential is up to 2 – 3 times of saturation density  $\rho_0$ , beyond that the DBHF data are simple extrapolation of the DBHF theory. Again, the  $V_\omega$  and  $V_\sigma$  fields of NL3 are very different from  $G2 + \delta$  results. The  $V_\omega$  for NL3 follows a linear path contrary to the results of  $G2 + \delta$  and Bonn-A. This could be due to the absence of self- and crossed couplings in NL3 set. The contribution of both  $\rho$ - and  $\delta$ - mesons correspond to the isovector channel. The  $\delta$ -meson gives different effective masses for proton and neutron, because of their opposite iso-spin of the third component. The nuclear potential generated by the  $\rho$ - and  $\delta$ -mesons are also shown in Fig 7.2. We noticed that although their contributions are small, but non-negligible. These non-zero values of  $V_\rho$  and  $V_\delta$  to the nuclear potential has a significant consequence, mostly in compact dense object like neutron or hyperon stars, which will be discussed later in this paper.

### 7.3.3 Energy per particle and pressure density

The energy and pressure densities as a function of baryonic density  $\rho_B$  are known as equations of states (EOS). These quantities are the key ingredients to describe the structure of neutron/hyperon stars. To see the sensitivity of the EOS, we have plotted energy per particle ( $E/\rho_B - M$ ) as a function of density for pure neutron matter in Fig 7.3. Each curve corresponds to a particular combination of  $g_\delta$  and  $g_\rho$  (taken from Table 7.1), which reproduce the symmetry energy  $E_{sym} = 36.4$  MeV without destabilizing other parameters of G2 set. The green line represents for  $g_\delta = 0$ , i.e.,



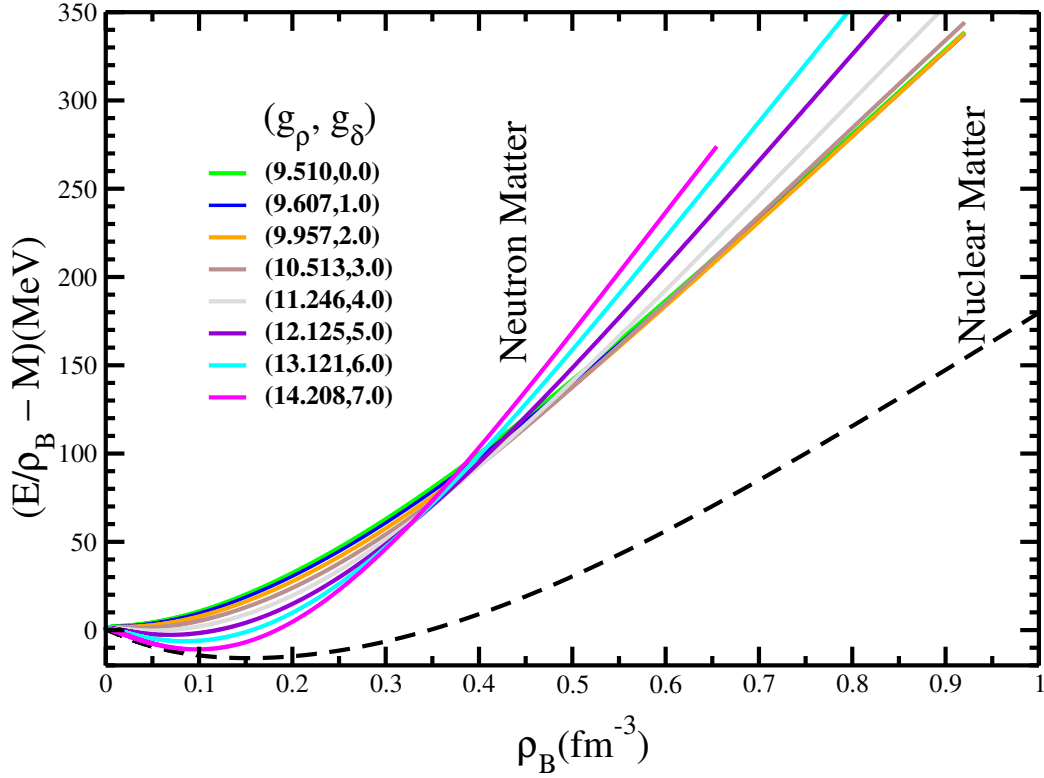


Figure 7.3: (Color online) Variation of binding energy per particle with density at various  $g_\rho$  and  $g_\delta$ .

with pure G2 parameter set. Both the binding energy per particle as well as the pressure density increase with the value of  $g_\delta$ . This process continues till the value of  $g_\delta$  reaches, at which  $E/\rho_B - M$  equals the nuclear matter binding energy per particle. An unphysical situation arises beyond this value of  $g_\delta$  because the binding energy of the neutron matter will be greater than  $E/\rho_B - M$  for the symmetric nuclear matter. In the case of G2+ $\delta$  parametrization, this limiting value of  $g_\delta$  reaches at  $g_\delta = 0.7$ , after which we do not get a convergence solution in our calculations.

In Fig 7.4 we have plotted the variation of energy and pressure densities as a function of  $\rho_B/\rho_0$  for different combinations of  $g_\rho$  and  $g_\delta$ . The enlarge version of energy density in the sub-saturation region is shown in panel (c) of the figure. Similar to other parameter sets of RMF formalism, the G2+ $\delta$  set also deviates from the experimental data. It is to be recalled here that special attentions are needed to construct nucleon-nucleon interaction to fit the data at sub-saturation density. For example, the potentials of Friedman and Pandharipande [266], Baldo-Maieron [267],

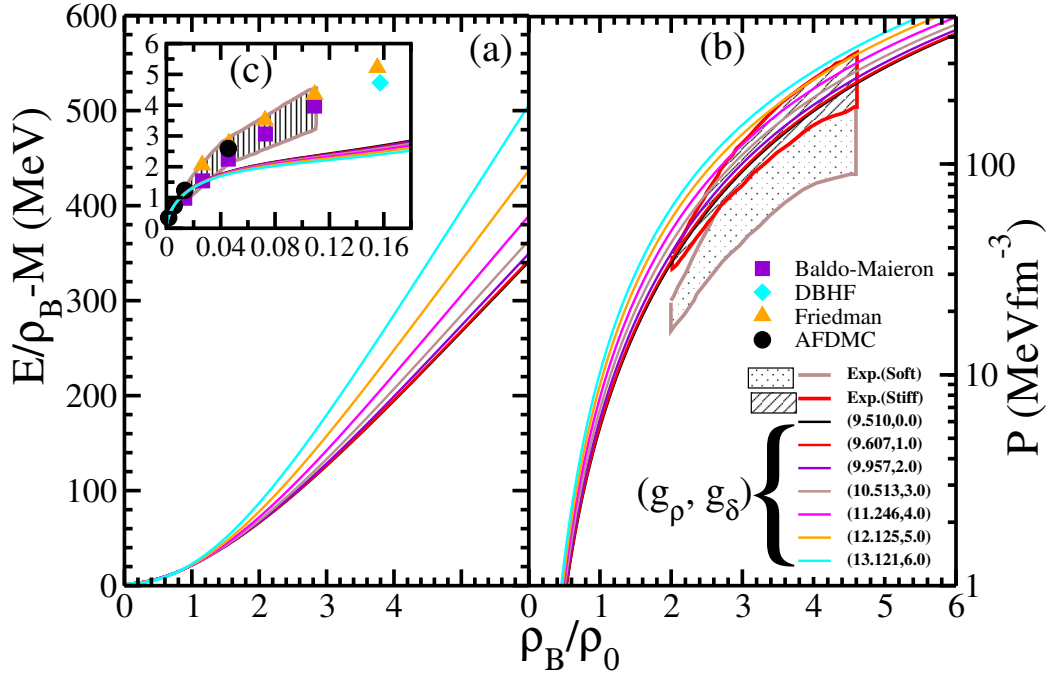


Figure 7.4: Variation of energy per particle (panel (a)) and pressure density (panel (b)) with  $\rho_B/\rho_0$  at different values of  $g_\rho$  and  $g_\delta$ . The enlarged version of energy per particle for sub-saturation region is in panel (c). The results of other theoretical models like Baldo-Maieron [267], DDHF [268], Friedman [266] and AFDMC [269] are also given for comparison.

DDHF [268] and AFDMC [269] are designed to fit the data in this region. The three-body effect also can not be ignored in this sub-saturation region of the density [270]. Although, the non-linear interactions fulfilled this demand to some extent [165, 186, 265], like Coester band problem [197], till some further modification of the couplings are needed. In this regard, the relativistic mean field calculations with density dependent meson-nucleon coupling [271] and constraining the RMF models of the nuclear matter equation of state at low densities [272] are some of the attempts. The mean field approximation is also a major limitation in the region of sub-saturation density. This is because, the assumption of classical meson field is not a proper approximation in this region to reproduce precisely the data. In higher density region, most of the RMF forces reproduces the experimental data quite well and the predictive power of these forces for finite nuclei is in excellent agreement both for  $\beta$ -stable and  $\beta$ -unstable nuclei. The energy and pressure densities with G2 set reproduce the experimental data satisfactorily [273]. The variation of pressure density as a function of  $\rho_B$  is shown in panel (b) of Fig. 4, which passes inside the stiff flow data at higher density [274]. Also, the  $\delta$ -meson coupling has significant effect in supersaturation density than the sub-saturation region. All the EOS with different  $g_\rho$  and  $g_\delta$  remain inside the stiff flow data (Fig. 4, panel (b)). In the present investigation, we are more concerned for highly dense neutron and hyperon stars, which are considered to be super-saturated nuclear objects.

### 7.3.4 Stellar properties of static and rotating neutron stars

The  $\beta$ -equilibrium and charge neutrality are two important conditions to justify the structural composition of the neutron/hyperon stars. Both these conditions force the stars to have  $\sim 90\%$  of neutron and  $\sim 10\%$  proton. With the inclusion of baryons, the  $\beta$ -equilibrium conditions between chemical potentials for different particles:

$$\begin{aligned}
\mu_p &= \mu_{\Sigma^+} = \mu_n - \mu_e, \\
\mu_n &= \mu_{\Sigma^0} = \mu_{\Xi^0} = \mu_n, \\
\mu_{\Sigma^-} &= \mu_{\Xi^-} = \mu_n + \mu_e, \\
\mu_\mu &= \mu_e,
\end{aligned}
\tag{7.15}$$

and the charge neutrality condition is satisfied by

$$n_p + n_{\Sigma^+} = n_e + n_{\mu^-} + n_{\Sigma^-} + n_{\Xi^-}. \quad (7.16)$$

To calculate the mass and radius profile of the static (non-rotating) and spherical neutron star, we solve the general relativity Tolmann-Oppenheimer-Volkov (TOV) [275] equations which are written as:

$$\frac{dP(r)}{dr} = -\frac{G [\mathcal{E}(r) + P(r)] [M(r) + \frac{4\pi r^3 P(r)}{c^2}]}{c^2 r^2 (1 - \frac{2GM(r)}{c^2 r})} \quad (7.17)$$

and

$$\frac{dM(r)}{dr} = \frac{4\pi r^2 \mathcal{E}(r)}{c^2}, \quad (7.18)$$

with  $G$  as the gravitational constant,  $\mathcal{E}(r)$  as the energy density,  $P(r)$  as the pressure density and  $M(r)$  as the gravitational mass inside radius  $r$ . We have used  $c=1$ . For a given EOS, these equations can be integrated from the origin as an initial value problem for a given choice of the central density  $\mathcal{E}_c(r)$ . The value of  $r$  ( $= R$ ) at which the pressure vanish defines the surface of the star. In order to understand the effect of  $\delta$ -meson coupling on neutron star structure, we must also look, what happens to massive objects as they rotate and how this affects the space-time around them. For this, we use the code written by Stergioulas [276] based on Komastu, Eriguchi, and Hachisu (KEH) method (fast rotation) [277, 278] to construct mass-radius of the uniform rotating star. One should note that the maximum mass of a static star is less than the rotating stars. Because, when the massive objects rotate they flatten at their poles. The forces of rotation, namely the effective centrifugal force, pulls the mass farthest from the center further out, creating the equatorial bulge. This pull away from the center will, in part, counteract gravity, allowing the star to be able to support more mass than its non-rotating star.

We know that the core of neutron stars contain hyperons at very high density ( $\sim 7-8 \rho_0$ ) matter. As it is mentioned before, with the presence of baryons, the EOS becomes softer and stellar properties will change. The maximum mass of hyperon star decreases about 10-20% depending on the choice of the meson-hyperon coupling constants. The hyperon couplings are expressed as the ratio between the meson-hyperon and meson-nucleon couplings as:

$$\chi_\sigma = \frac{g_{Y\sigma}}{g_{N\sigma}}, \chi_\omega = \frac{g_{Y\omega}}{g_{N\omega}}, \chi_\rho = \frac{g_{Y\rho}}{g_{N\rho}}, \chi_\delta = \frac{g_{Y\delta}}{g_{N\delta}}. \quad (7.19)$$

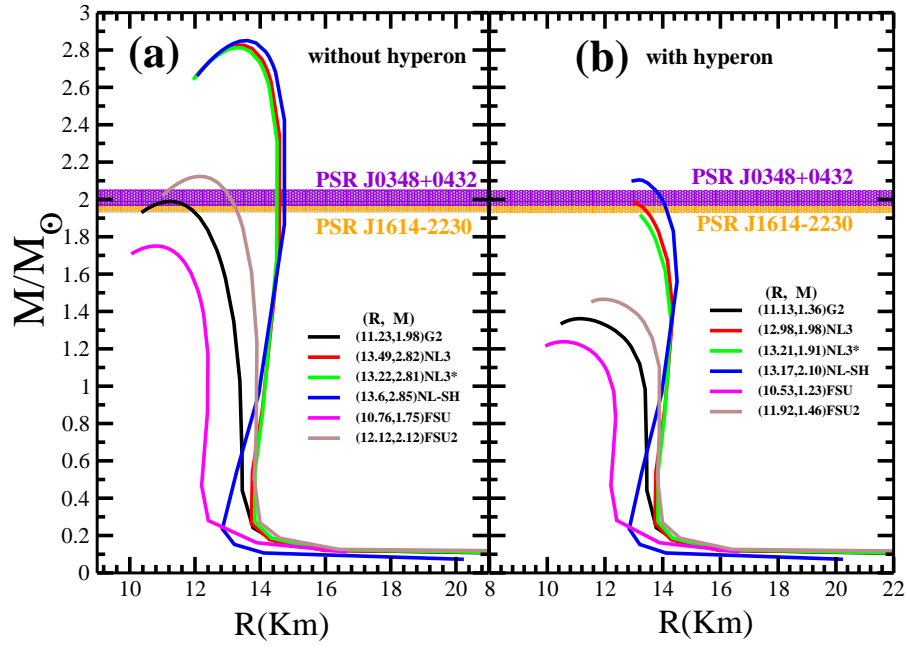


Figure 7.5: (Color online) The mass-radius profile for static star with different parametrization like G2 [251], NL3 [49], NL3\* [93], NL-SH [241], FSU [90] and FSU2 [279]. (a) is for proton-neutron star and (b) is for the hyperon star. The maximum mass  $M$  and the corresponding radius obtained by various parameter sets are given in the parenthesis.

In the present calculations, we have taken  $\chi_\sigma = \chi_\rho = \chi_\delta = 0.6104$  and  $\chi_\omega = 0.6666$  [280]. One can find similar calculations for stellar mass in Refs. [281–283]. Now we present the star properties like mass and radius in Figs. 7.5 and 7.6. In Fig. 7.5 we have plotted the mass-radius profile for the proton-neutron star as well as for the hyperon star using a wide variation of parameter sets starting from the old parameter like NL-SH [241] to the new set of FSU2 [279]. The mass-radius profile varies to a great extent over the choice of the parameter. For example, in FSU parameter set [90], the maximum possible mass of the proton-neutron star is  $\sim 1.75 M_\odot$ , while the maximum possible mass for the NL3 set [49] is  $\sim 2.8 M_\odot$ . These results are shown in the left panel of the Fig. 7.5, while right panel shows the same things for the hyperon star (the maximum mass and the corresponding radius for different forces are given in the parenthesis).

### 7.3.5 Effects of $\delta$ -meson on static and rotating stars

The main aim of this paper is to understand the effects of  $\delta$ -meson on neutron stars both with and without hyperons. Fig. 7.6 represent the mass-radius profiles for non-rotating and rotating stars taking into account the presence of with and without hyperons. These profiles are shown for various combinations of  $g_\rho$  and  $g_\delta$  (see Table 7.1), which we have obtained by fitting the symmetry energy  $E_{sym}$  of pure nuclear matter. Analyzing the graphs, we notice a slight change in the maximum mass with  $g_\delta$  value. That means, the mass of the star goes on decreasing with an increase value of the  $\delta$ -meson coupling in hyperon star. A further inspection of the results reveals that, although the  $\delta$ -meson coupling has a nominal effects on the maximum mass of the proto-neutron stars, we get an asymptotic increase in the mass. This asymptotic nature of the curves is more prominent in presence of hyperons inside the stars. Similar phenomena are also observed in case of rotating stars.

The empirical formula for the relation between maximum frequency  $f_{max}$  with mass of the neutron star for a given EOS is given as [284, 285]

$$f_{max} \approx 1.22 KHz \sqrt{M_{max}^{static}/M_\odot} (R_{max}^{static}/10Km)^{-3/2}, \quad (7.20)$$

where  $M_{max}^{static}$ =maximum static mass and  $R_{max}^{static}$ =maximum allowed radius for a neutron star. In actual, the neutron stars have a wide range of frequencies due to the

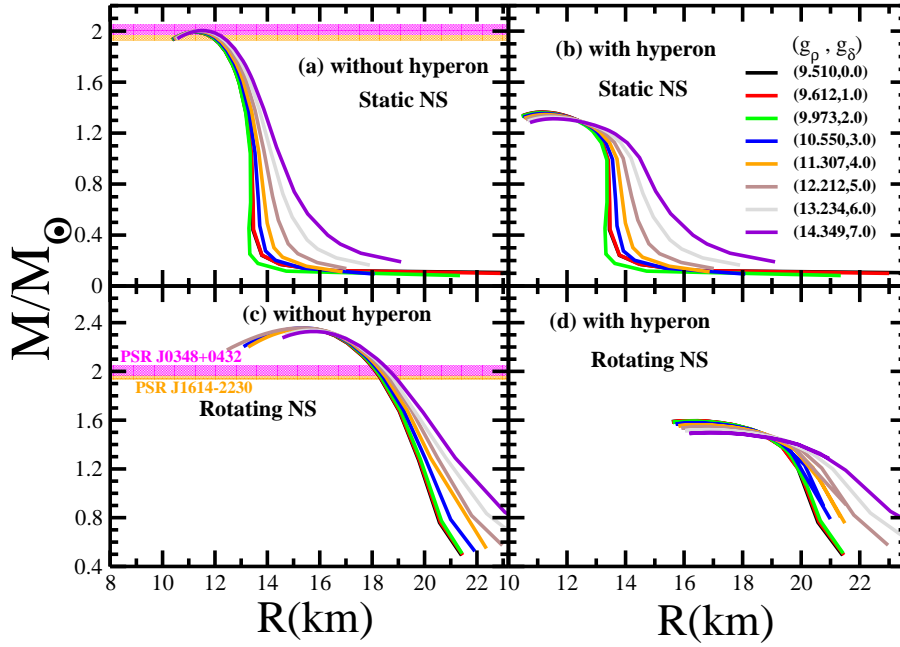


Figure 7.6: (Color online) The mass-radius profile of the static and rotating proton-neutron and hyperon stars with various combination of  $g_\delta$  and  $g_\rho$  in  $G2+\delta$ . (a,c) is for proton-neutron star and (b,d) is for the hyperon star. (a,b) for static and (c,d) for rotating cases.

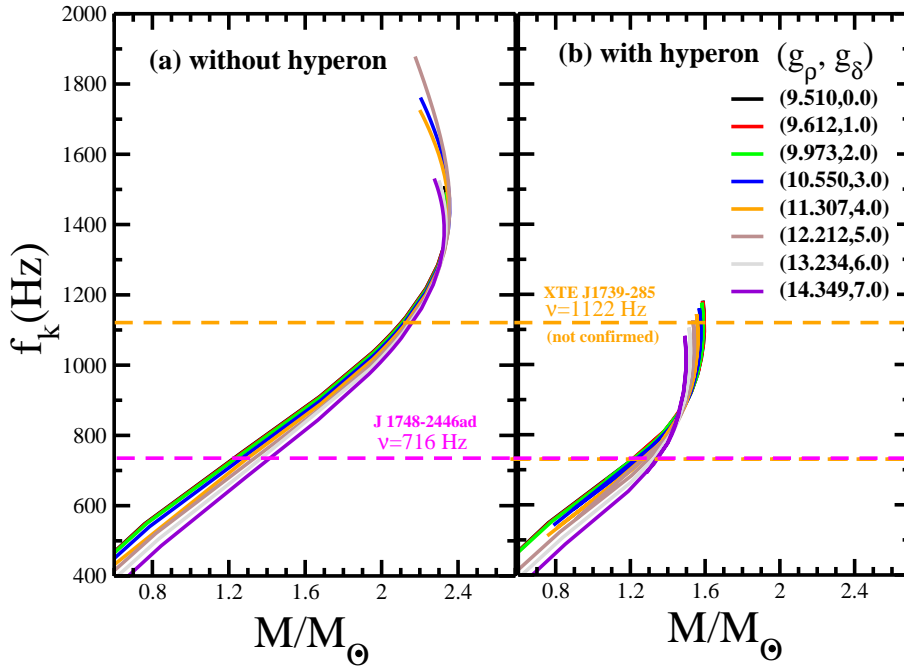


Figure 7.7: (Color online) Keplerian frequency of the rotating proton-neutron and hyperon stars with various combination of  $g_\delta$  and  $g_\rho$  in  $G2+\delta$ . (a) is for proton-neutron star and (b) is for the hyperon star. The results are obtained from RNS code [276].



fluid of the stars oscillate in various modes [286]. Among them, the most important modes are the first pressure mode ( $p_I$ -mode) and the fundamental mode of the fluid oscillation (f-mode). The empirical formula for the frequencies of these two modes are  $f_f = (0.79 \pm 0.09) + (33 \pm 2)\sqrt{M/R^3}$  and  $f_p = 1/M(-1.5 \pm 0.8) + (79 \pm 4)M/R$ , respectively, where  $M$  and  $f$  in Km and KHz. The above two relations are obtained by using a wide sample of EOSs [286].

In the present calculations, we assume the frequency of the rotating neutron star is within the Keplerian frequency limit. At this limit the spin frequency of the neutron star is equal to the orbital frequency  $f_{or}$  (along a circular path on the equator of the NS) [284]. If the orbital frequency  $f_{or} > f_K$  (Kepler frequency), then the hydrostatic equilibrium of the NS does not hold good. To make it clear, the Kepler frequency as a function of NS mass is shown in Fig. 7 with and without considering hyperon into account. The results of Fig. 7 is obtained from the RNS code and the expression for the Keplerian frequency, i.e. the maximum frequency obtained from the general theory of relativity can be found in Refs. [276, 287]. In this figure, the variation of  $f_K$  is shown as a function of  $M/M_\odot$  with various combinations of  $g_\rho$  and  $g_\delta$  which we have already fixed (see Table 1). We noticed a finite effect of  $g_\rho$  and  $g_\delta$  variation on the mass and Keplerian frequency of the pure neutron and hyperon stars.

For a quite some time pulsar B1937+21 with frequency 642 Hz was considered as the fastest spinning NS. However, Hessels et. al. [288] found even more faster spinning NS pulsar J1748-2446ad at frequency 716.356 Hz. This NS has a mass of  $0.14M_\odot$  companion. It is difficult to obtain  $0.14M_\odot$  from the equation of state at supra-nuclear densities. Our calculations suggest that if pulsar has a mass less than  $1.4M_\odot$  than the larger density slope of the symmetry energy at saturation would be excluded. If we consider the neutron star mass to be greater than  $2.0M_\odot$  and hyperons are present in it, then the star mass will be  $1.6M_\odot$ , within the pulsar XTE J1739285 NS [289].

Here, we analyzed the effects of  $\delta$ -meson coupling on neutron and hyperon stars. We observed that, the mass of the star decreases when hyperons are included in the calculations, as a result, the maximum mass of the star with G2+ $\delta$  set become much less than  $2M_\odot$ , the latest observation of a massive neutron star. In summary, the following possibilities are in order:

(i) Since the mass obtained without hyperon for static case is  $\sim 2M_\odot$ , in this situation one do not need to reduce the mass any more by adding hyperons into it. This can be justify by assuming that in massive neutron star, there is no hyperon. The absence of hyperons in massive neutron star may not be a convincing explanation, because of the highly dense matter in the core of the NS, which favor the production of hyperon. (ii) The rotation of a NS increases the maximum allowed mass. On the other hand, the inclusion of hyperon deceases the mass. In the present case, even if consider the rotation of the star, it is not sufficient to get the maximum mass  $\sim 2M_\odot$  (see Fig. 6(d)). (iii) The 3<sup>rd</sup> possibility is the effect of  $\delta$ -meson coupling, which may increase the mass of the hyperon star after its insertion into the model. Although, its effect is finite, it is not sufficient to increase the hyperon mass to two solar unit. Thus, the addition of  $\delta$ -meson may not be sufficient to explain the heavier mass of the NS. (iv) Probably, the fourth possibility may be the most acceptable explanation in which we suggest for the modification of the EOS, such that after the addition of hyperon, the mass of the static neutron-hyperon star will be  $\sim 2M_\odot$ . In particular, the hyperon-meson coupling should be re-investigated to get a proper coupling constants, which allowed the maximum mass  $\sim 2M_\odot$  with hyperon. Work in this direction is in progress [290].

### 7.3.6 Effects of $\delta$ -meson on baryon production

Finally, we want to see the effects of  $\delta$ -meson coupling on the particle production for the whole baryonic family at various densities in nuclear matter system. The Fermi energy of both proton and neutron increases with density for their Fermionic nature. After a certain density, the Fermi energy of the nucleon exceeded the rest mass energy of the nucleon ( $\sim 1000$  MeV), and strange particles ( $\Sigma, \Lambda, \Xi$ ) are produced. As a result, the equations of state of the star becomes soft and gives a smaller star mass compare to the neutron star containing only protons, neutrons and electrons. The decrease in star mass in the presence of whole baryon octet can be understood from the analysis of Fig. 7.8. From the figure, it is clear that  $\delta$ -meson has a great impact on the production of hyperons. The inclusion of  $\delta$ -meson accelerate the strange particle production. For example, the evolution of  $\Sigma^-$  takes place at density  $\rho_B = 1.75\rho_0$  in absence of  $\delta$ -meson. However, it produces at  $\rho_B = 1.67\rho_0$  when  $\delta$ -meson is

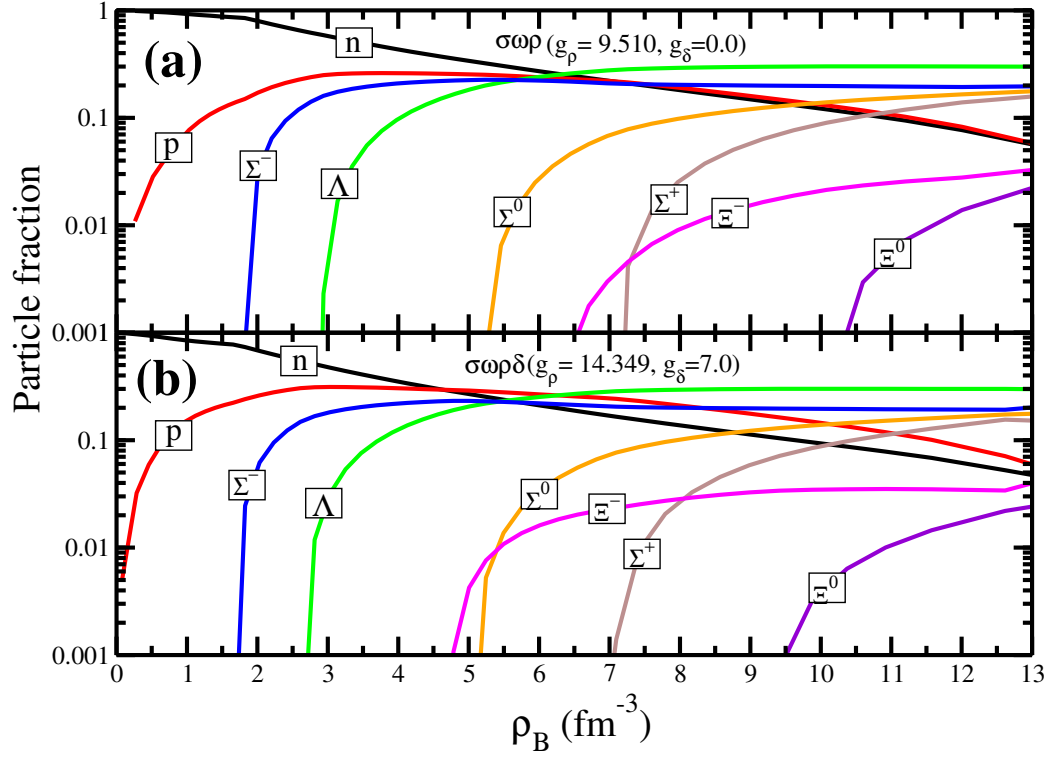


Figure 7.8: (Color online) Yield of strange particles as a function of density. The upper panel (a) is with G2 parameter set (without taking  $\delta$ -meson coupling) and the lower panel (b) is with  $\delta$ -meson coupling.

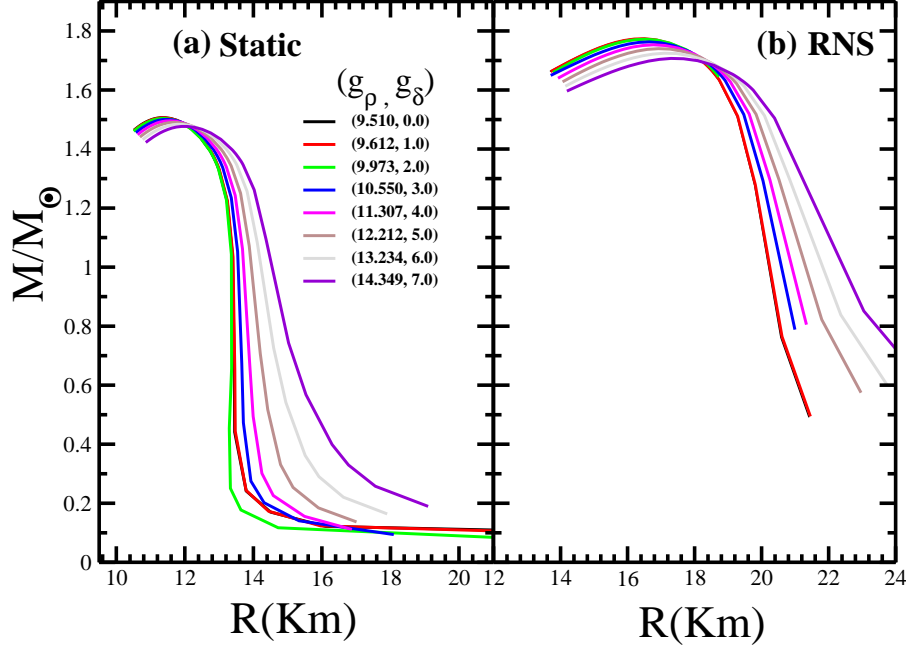


Figure 7.9: (Color online) Mass and radius profile of hyperon star with G2+ $\delta$  parameter set, but with different meson-hyperon coupling of Ref. [281].

there in the system. Similarly, analyzing the evolution of other baryons, we notice that although the early production of baryons in the presence of  $\delta$ -meson is not in a definite proportion to each other, in each case the yield is faster. A significant shifting towards lower density is maximum for heaviest hyperon ( $\Xi^0$ ) and minimum for nucleon (see Fig. 7.8). For example,  $\Xi^-$  evolves at  $\rho_B = 6.5 \rho_0$  for a non- $\delta$  system and  $\rho_B \sim 5.0 \rho_0$  for medium when  $\delta$ -meson is included. Thus, the  $\delta$ -coupling has a sizable impact on the production of hyperons like  $\Xi^-$ ,  $\Xi^0$  and  $\Sigma^+$ .

### 7.3.7 Fitting of $g_\rho$ and $g_\delta$ with fixed binding energy and charge radius

In previous sub-sections we have seen the effects of  $(g_\rho, g_\delta)$  pair with a constant symmetry energy on the maximum mass and radius of the neutron and hyperon stars. The effects of the  $(g_\rho, g_\delta)$  pairs are not prominent on the star structure in this

method. On the other hand, it affects the bulk properties, like binding energy and root mean square radius considerably for asymmetric finite nucleus. In Table 7.2, we have given the mass and charge radius for some of the selected nuclei. Although, all the combination of  $g_\rho$  and  $g_\delta$  are fixed at a constant symmetry energy, the binding of  $^{208}\text{Pb}$  differ by 90 MeV in the first and last combination of  $g_\rho$  and  $g_\delta$ . In this sub-section, we would like to change the strategy to select the  $(g_\rho, g_\delta)$  pairs. Here, we have followed the second procedure as we have discussed in the previous sub-section, i.e., we find the values of  $g_\rho$  and  $g_\delta$  by adjusting the binding energy and charge radius of  $^{208}\text{Pb}$ . Once we get the  $(g_\rho, g_\delta)$ , we used the pair for the calculations of other nuclei of Table 7.2. Surprisingly, the outcome of binding energy and charge radius matches pretty well with the original calculations. The  $g_\rho$  and  $g_\delta$  combination along with the corresponding mass and radius of a neutron star is given in the Table 7.3. From the table it is clear that these combinations are also not affecting much to the maximum mass and radius of the neutron star. However, the  $E_{sym}$ ,  $L_{sym}$  and  $K_{sym}$  calculated from the corresponding  $(g_\rho, g_\delta)$  combinations for nuclear matter changes a lot (See Table 7.3). We used the hyperon-meson coupling constants of Ref. [281] to evaluate the hyperon star structure. The calculated results for static and rotating hyperon star are plotted in Fig. 7.9. The maximum mass increases and the radius decreases slightly with the addition of  $\delta$ -meson to the star system.

## 7.4 Summary and Conclusions

In summary, using the effective field theory approach, we discussed the effects of isovector scalar meson on hyperon star. The inclusion of  $\delta$ -meson with G2 parameter set, we have investigated the static and rotating stellar properties of neutron star with hyperons. We fitted the parameters and see the variation of  $g_\rho$  and  $g_\delta$  at a constant symmetry energy for both the nuclear and neutron matter. We also used these  $(g_\rho, g_\delta)$  pairs to finite nuclei and find a large change in binding energy for asymmetric nuclei. Then we re-fitted the  $(g_\rho, g_\delta)$  pairs keeping binding energy and charge radius fixed for  $^{208}\text{Pb}$  and tested the effects for some selected nuclei and able to reproduced the data similar to the original G2 set. With the help of G2+ $\delta$  model, for static and rotating stars without hyperon core, we get the maximum mass of

$\sim 2M_\odot$  and  $\sim 2.4M_\odot$ , respectively. This prediction of masses is in agreement with the recent observation of  $M \sim 2M_\odot$  of the stars. However, with hyperon core the maximum mass obtained are  $\sim 1.4M_\odot$  and  $\sim 1.6M_\odot$  for static and rotating hyperon stars, respectively. In addition, we have also calculated the production of whole baryon octet with variation in density. We find that the particle fraction changes a lot in the presence of  $\delta$ -meson coupling. When there is  $\delta$ -meson in the system the evolution of baryons are faster compare to a non- $\delta$  system. This effect is significant for heavier masses and minimum for lighter baryon. Hence, one can conclude that the yield of baryon/hyperons depends very much on the mesons couplings. One important information is drawn from the present calculations is that the effect of  $g_\delta$  is just opposite to the effect of  $g_\rho$ . As a consequence, many long standing anomaly, such as the comparable radii of  $^{40}\text{Ca}$  and  $^{48}\text{Ca}$  be resolved by adjusting the  $(g_\rho, g_\delta)$  pairs properly. Keeping in view the importance of  $\delta$ -meson coupling and the reverse nature of  $g_\rho$  and  $g_\delta$ , it is necessary to get a new parameter set including proper values of  $g_\delta$  and  $g_\rho$ , and the work is under progress.

# Chapter 8

## Summary and Conclusions

The relativistic mean field formalism provides a common platform to study both the finite and infinite nuclear matter systems. Its relativistic nature defined a pathway from the less dense finite nuclear system to highly dense neutron star. We studied various aspects of finite nuclear structure like magicity of proton and neutron number and collective excitation like giant resonance and the nucleon-nucleon interaction . For the infinite nuclear system, we applied RMF to study the mass and radius of the neutron star. In brief, we have applied RMF formalism to study both finite and infinite nuclear systems.

Recently the advent of radioactive ion beam (RIB) facility inspires the nuclear physicists to look forward to the structure of drip-lines and super-heavy nuclei more seriously. Nuclei away from the  $\beta$ -stability lines are far different from the nuclei on the  $\beta$ -stability line. In Ch. 2, we have calculated BE,  $S_{2n}$  energy, single particle levels, pairing gaps and chemical potential, in the isotopic chain of  $Z = 82, 114, 120$  and  $126$ . All our calculations are done in the framework of non-relativistic SEI and relativistic RMF interactions. We have compared our results with FRDM and other theoretical predictions. Overall, the discussions and analysis of all possible evidence of shell closure property with SEI interaction and RMF show that one can take  $Z = 120$  and  $N = 182$  or  $184$  as the next magic combination beyond  $Z = 82$  and  $N = 126$ , which is consistent with other theoretical models.

Not only the single particle properties, which are discussed in first part of the thesis but also the collective excitation plays an important role in nuclear structure

physics. In Ch.3, we have calculated the excitation energy of isoscalar giant monopole resonance and incompressibility for O, Ca, Ni, Sn, Pb, Z=114, and Z=120 isotopic series starting from proton to neutron drip lines. We used four successful parameter sets, NL1, NL3, NL3\*, and FSUGold, with a wide range of nuclear matter incompressibility starting from 211.7 MeV to 271.76 MeV to see the dependency of the ISGMR on  $K_\infty$ . Also, we have analyzed the predictions of ISGMR with these forces, which originate from various interactions and found that whatever may be the parameter set, the differences in excitation energy ISGMR predicted by them are found to be marginal in the super heavy region. A recently developed scaling approach in a relativistic mean field theory is used. A simple, but accurately constrained approximation is also performed to evaluate the isoscalar giant monopole excitation energy. From the scaling and constrained ISGMR excitation energies, we have evaluated the resonance width  $\Sigma$  for the whole isotopic series. This is obtained by taking the root mean square difference of  $E_x^s$  and  $E_x^c$ . The value of  $E_x^s$  is always higher than the constrained result  $E_x^c$ . In a sum rule approach, the  $E_x^s$  can be compared with the higher and  $E_x^c$  as the lower limit of the resonance width. In general, we found an increasing trend of resonance width  $\Sigma$  for both the light and super heavy regions near the proton and neutron drip lines. The magnitude of  $\Sigma$  is predicted to be minimum in the vicinity of N=Z or in the neighborhood of a double closed nucleus and it is maximum for highly asymmetric system. In the present thesis, we have also estimated the incompressibility of finite nuclei. For some specific cases, the incompressibility is compared with the nuclear matter incompressibility and found a linear variation among them. It is also concluded that the nucleus becomes less compressible with the increase of neutron or proton number in an isotopic chain. Thus neutron-rich matter, like neutron star as well as drip-line nuclei, are less compressible than normal nuclei. In the case of exotic (drip-line nuclei) system, the nucleus is incompressible, although it possesses a normal density.

The recent experiment on isoscalar monopole excitation in the isotopic chain of the Sn isotopes indicates a new problem in the medium heavy mass range ( $A \sim 100$ ). In the second part of Ch. 3, we analyzed the predictive power of various force parameters, like NL1, NL2, NL3, NI-SH and FSUG in the framework of RTF and RETF



approaches for giant monopole excitation energy of Sn-isotopes. Then the calculation is extended to some other relevant nuclei in the mass range  $A \sim 100$ . The analysis shows that relativistic Thomas-Fermi and extended relativistic Thomas-Fermi approximation give comparable results with pairing+MEM prediction. It can be exactly reproduced the experimental data for Sn isotopes, when the incompressibility of the force parameter is within 210-230 MeV, however, fails to reproduce the GMR data for other nuclei within the same accuracy. We have qualitatively analyzed the difference in GMR energies ( $\Delta E_{GMR} = \text{RETF} - \text{RTF}$ ) using RETF and RTF formalisms in various force parameters. The FSUGold parameter set shows different behavior from all other forces. Also, we extended our calculations for monopole excitation energy of Sn isotopes with a force parametrization having softer symmetry energy ( $\text{NL3} + \Lambda_V$ ). The excitation energy decreases with the increase of proton-neutron asymmetry agreeing with the experimental trend. In conclusion, after all, from these thorough analyses, it seems that the softening of Sn isotopes is an open problem in nuclear theory and more work in this direction is needed. In Ch. 4 we discussed about the new constrained calculation developed by us. This new method is based on the Taylor series expansion. Although this method is very simple, it gives reasonable results which are comparable with other microscopic calculation like RRPA. For simplicity, we applied the constrained method to Thomas-Fermi approximation. But this method can be extended to extended Thomas-Fermi approach without losing any generality.

Nucleon-Nucleon interaction has a very crucial role in the nuclear structure as well as the other branch of nuclear physics. So it is important to study more about the nucleon-nucleon interaction and its effects on various properties of the nuclear system. In Ch. 5, we extensively discussed a new approach R3Y, for the N-N interaction, which is first suggested by Patra et al. We have added a new self-interacting  $\omega$  meson contribution to this new formalism and checked its contribution to finite and infinite nuclear matter system. In Ch. 6, we used the density dependent M3Y and R3Y to study the  $p-\gamma$  reaction for the proton-rich nuclei. We have folded the M3Y and R3Y interaction with RMF densities to obtain the cross-section of  $p-\gamma$  reaction. From the cross-section of these reaction, we can study the astrophysical- S factor, which is important in the study of the r-process of nuclear synthesis.

In Ch. 7, using the effective field theory approach, we discussed the effects of isovector scalar meson on hyperon star with the inclusion of  $\delta$ -meson with G2 parameter set and then investigated the static and rotating stellar properties of neutron star with hyperons. We fitted the parameters and see the variation of  $g_\rho$  and  $g_\delta$  at a constant symmetry energy for both the nuclear and neutron matter. We also used these  $(g_\rho, g_\delta)$  pairs to finite nuclei and find a large change in binding energy for asymmetric nuclei. Then we re-fitted the  $(g_\rho, g_\delta)$  pairs keeping binding energy and charge radius fixed for  $^{208}\text{Pb}$  and tested the effects for some selected nuclei and able to reproduce the data similar to the original G2 set. With the help of the G2+ $\delta$  model, for static and rotating stars without hyperon core, we get the maximum mass of  $\sim 2M_\odot$  and  $\sim 2.4M_\odot$ , respectively. This prediction of masses is in agreement with the recent observation of  $M \sim 2M_\odot$  of the stars. However, with hyperon core the maximum masses obtained are  $\sim 1.4M_\odot$  and  $\sim 1.6M_\odot$  for static and rotating hyperon stars, respectively. In addition, we have also calculated the production of whole baryon octet with variation in density. We find that the particle fraction changes a lot in the presence of  $\delta$ -meson coupling. When there is  $\delta$ -meson in the system the evolution of baryons is faster compared to a non- $\delta$  system. This effect is significant for heavier masses and minimum for lighter baryon. Hence, one can conclude that the yield of baryon/hyperons depends very much on the mesons couplings. One important information is drawn from the present calculations is that the effect of  $g_\delta$  is just opposite to the effect of  $g_\rho$ . As a consequence, many long-standing anomalies, such as the comparable radii of  $^{40}\text{Ca}$  and  $^{48}\text{Ca}$  can be resolved by adjusting the  $(g_\rho, g_\delta)$  pairs properly. Keeping in view the importance of  $\delta$ -meson coupling and the reverse nature of  $g_\rho$  and  $g_\delta$  with each other, it is necessary to get a new parameter set including proper values of  $g_\delta$  and  $g_\rho$ , and the work is in progress.

# REFERENCES

- [1] H. Geiger and E. Marsden, Proc. Roal. Soc. **82**, 495 (1909).
- [2] H. Yukawa, Proc. Phys-Math. Soc. Japan **17**, 48 (1935).
- [3] D. M. Brink, Nuclear force (Pergammon Press, Oxford) (1965).
- [4] T. H. R. Skyrme, Phil.Mag. **1**, 1043 (1956).
- [5] T. H. R. Skyrme, Nucl. Phys. **9**, 615 (1958).
- [6] J. Dechargeè and D. Gogny, Phys. Rev. C **21**, 1568 (1980).
- [7] L. D. Miller and A. E. S. Green, Phys. Rev. C **5**, 241 (1972).
- [8] J. D. Walecka, Ann. of Phys. **83**, 491 (1974).
- [9] B.D. Soret and J. D. Walecka, Adv. Nucl. Phys. **16**, 1 (1985).
- [10] Sven Gösta Nilsson, Nucl. Phys. A **131**, 1 (1969).
- [11] Z. Patyk and A. Sobiczewski, Nucl. Phys. A **533**, 132 (1991).
- [12] P. Möller and J. R. Nix, Nucl. Phys A **549**, 84 (1992).
- [13] A. Sobiczewski, Physica. Scripta **10 A**, 47 (1974).
- [14] K. Rutz et. al., Phys. Rev. C **56**, 238 (1997).
- [15] Yu. Ts. Oganessian, Radiochim. Acta **99**, 429 (2011).
- [16] P. Danielewicz, R. Lacey, and W.G. Lynch, Science **298**, 1592 (2002).

- [17] J. M. Lattimer and M. Prakash, Science 304, 536 (2004); Phys. Rep. **442**, 109 (2007).
- [18] A. W. Steiner, M. Prakash, J. M. Lattimer and P. J. Ellis, Phys. Rep. **411**, 325 (2005).
- [19] J. P. Blaizot, Phys. Rep. **64**, 171 (1980).
- [20] Oganessian Yu Ts *et al.*, Phys. Rev. C **74**, 044602 (2006).
- [21] Oganessian YU Ts *et al.*, Phys. Rev. Lett **109**, 162501 (2012).
- [22] S. K. Patra, R. K. Gupta and W. Greiner, Mod. Phys. Lett. A **12**, 1727 (1997).
- [23] T. Sil, S. K. Patra, B. K. Sharma, M. Centelles and X. Viñas, Phys. Rev. C **69**, 054313 (2004); M. Bhuyan and S. K. Patra, Mod. Phys. Lett. A **27**, 1250173 (2012).
- [24] S. Hofmann and G. Münzenberg, Rev. Mod. Phys. **72**, 733 (2000).
- [25] G. Münzenberg *et al.*, Z. Phys. A **300**, 107 (1981).
- [26] S. Hofmann *et al.*, Z. Phys. A **350**, 277 (1995).
- [27] S. Hofmann *et al.*, Z. Phys. A **350**, 281 (1995).
- [28] S. Hofmann *et al.*, Z. Phys. A **354**, 229 (1996).
- [29] S. Hofmann *et al.*, Rep. Prog. Phys. **61**, 639 (1998); Acta Phys. Pol. B **30**, 621 (1999).
- [30] S. Hofmann *Russ. Chem. Rev.* **78**, 1123 (2009).
- [31] K. Morita *et al.*, J. Phys. Soc. Jpn. **76**, 043201 (2007); *ibid* **76** 045001 (2007).
- [32] Yu. Ts. Oganessian, Phys. Rev. Lett. **83**, 3154 (1998).
- [33] Yu. Ts. Oganessian *et al.*, Nucl. Phys. A **685**, 17c (2001).
- [34] Yu. Ts. Oganessian *et al.*, Phys. Rev. C **69**, 021601(R) (2004).

- [35] Yu. Ts. Oganessian, J. Phys. G: Nucl. Part. Phys. **34**, R165 (2007).
- [36] Yu. Ts. Oganessian *et al.*, *Phys. Rev. Lett.* **104**, 142502 (2010).
- [37] Yu. Ts. Oganessian *et al.*, *Phys. Rev. C* **83**, 954315 (2011).
- [38] B. Behera, X. Viñas, M. Bhuyan, T. R. Routray, B. K. Sharma and S. K. Patra, J. Phys. G: Nucl. Part. Phys. **40**, 095105 (2013); T. R. Routray, X. Viñas, S. K. Tripathy, M. Bhuyan, S. K. Patra and B. Behera, J. Phys.: Conf. Ser. **420**, 012114 (2013).
- [39] B. Behera, T. R. Routray and R. K. Satpathy, J. Phys. G: Nucl. Part. Phys. **24**, 2073 (1998).
- [40] B. Behera, T. R. Routray, B. Sahoo and R. K. Satpathy, Nucl. Phys. A **699**, 770 (2002).
- [41] J. F. Berger, M. Girod, D. Gogny, Nucl. Phys. A **428**, 23c (1948).
- [42] B. Behera, T. R. Routray, A. Pradhan, S. K. Patra and P. K. Sahu, Nucl. Phys. A **753**, 367 (2005).
- [43] B. Behera, T. R. Routray, A. Pradhan, S. K. Patra and P. K. Sahu, Nucl. Phys. A **794**, 132 (2007).
- [44] B. Behera, T. R. Routray and S. K. Tripathy, J. Phys. G: Nucl. Part. Phys. **36**, 125105 (2009).
- [45] B. Behera, T. R. Routray and S. K. Tripathy, J. Phys. G: Nucl. Part. Phys. **38**, 115104 (2011).
- [46] J. Boguta and A. R. Bodmer, Nucl. Phys. A **292**, 413 (1977).
- [47] B. D. Serot and J. D. Walecka, *Adv. Nucl. Phys.* **16** 1 (1986).
- [48] M. Del Estal, M. Centelles, X. Viñas and S.K. Patra, *Phys. Rev C* **63**, 024314 (2001); M. Del Estal, M. Centelles, X. Viñas X and S. K. Patra, *Phys. Rev.C* **63**, 044321 (2001).
- [49] G. A. Lalazissis, J. König, and P. Ring, *Phys. Rev.C* **55** 540, (1997).

- [50] S. K. Patra, Phys. Rev. C **48**, 1449 (1993).
- [51] W. Pannert, P. Ring, and J. Bogota, Phys. Rev. Lett. **59**, 2420 (1987).
- [52] M. A. Preston and R. K. Bhaduri *Structure of Nucleus*, Addison-Wesley Publishing Company, **Ch. 8**, page 309 (1982).
- [53] P. Möller, J. R. Nix, W. D. Wyers and W. J. Swiatecki At. Data Nucl. Data Tables **59** 185 (1995); P. Möller, J. R. Nix and K. L. Kratz, *ibid.* **66**, 131 (1997).
- [54] M. Wang, G. Audi, A. H. Wapster, F. G. Kondev, M. MacCormick, Xu X and B. Pfeiffer, Chinese Physics C (HEP&NP) **36**, 12 (2012).
- [55] Gertrude Scharff-Goldhaber, **Nucleonics** **15**, 122 (1957).
- [56] W. D. Myers and W. J. Swiatecki, Nucl. Phys. **81**, 1 (1996).
- [57] S. G. Nilsson, Mat. Fys. Medd. Dan. Vid. Selsk, **29**, 16 (1995).
- [58] B. R. Mottelson and S. G. Nilsson, Phys. Rep. **99**, 1615 (1995); 1959 Mat. Fys. Skr. Dan. Vid. Selsk **8**, 1 (1959).
- [59] G. Andersson, S. E. Larsson, G. Leander, S. G. Nilsson, I. Ragnarsson and S. Aberg, Phys. Lett. B **65**, 209 (1976).
- [60] H. W. Meldner, Ark. Fys. **36**, 593 (1978).
- [61] H. W. Meldner, in Superheavy Elements ed. M. A. K. Lodhi (Oxford: Pergamon) p. 495.
- [62] H. S. Köhler, Nucl. Phys. A **162**, 385 (1971).
- [63] V. M. Strutinsky, Nucl. Phys. A **95**, 420 (1967); **122**, 1 (1968).
- [64] P. Möller and J. R. Nix, J. Phys. G **20**, 1681 (1994).
- [65] A. Sobiczewski, Phys. Part. Nuclei **25**, 295 (1994).
- [66] A. Sobiczewski and K. Pomorski, Prog. Part. Nucl. Phys. **58**, 292 (2007).

- [67] R. Smolanczuk, J. Skalski and A. Sobiczewski, Phys. Rev. C **52**, 1871 (1995).
- [68] K. Kumar, *Superheavy Elements* (IOP Publishing Ltd. 1989); Physica Scripta, **T32**, 31 (1990).
- [69] M. Bhuyan and S. K. Patra, Mod. Phys. Lett. A **27**, 1250173 (2012).
- [70] I. Tanihata, H. Hamagaki, O. Hashimoto, Y. Shida, N. Yoshikawa, K. Sugimoto, O. Yamakawa, T. Kobayashi, and N. Takahashi, Phys. Rev. Lett. **55**, 2676 (1985); A. Ozawa, T. Kobayashi, T. Suzuki, K. Yoshida, and I. Tanihata Phys. Rev. Lett. **84**, 5493 (2000); I. Tanihata, J. Phys. G: Nucl. Part. Phys. **22**, 157 (1996).
- [71] P. G. Hansen and B. Jonson, Europhys. Lett. **4**, 409 (1989).
- [72] Yu. Ts. Oganessian et al., Phys. Rev. Lett. **104**, 142502 (2010); Yu. Ts. Oganessian et al., Phys. Rev. Lett. **83**, 3154 (1999).
- [73] P. Arumugam, B.K. Sharma, P.K. Sahu, S.K. Patra, Tapas Sil, M. Centelles and X. Viñas, Phys. Lett. B **601**, 51 (2004).
- [74] Kaan Manisa, Ulfet Atav, Sibel Sariaydin, Cent. Eur. J. Phys. **8**, 587 (2010).
- [75] D. H. Youngblood, H. L. Clark and Y. W. Lui, Phys. Rev. Lett. **82**, 691 (1999).
- [76] O. Bohigas, A. Lane and J. Martorell, Phys. Rep. **51**, 267 (1979).
- [77] K. Rutz, J.A. Maruhn, P. G. Reinhard and W. Greiner, Nucl. Phys. A **590**, 680 (1995).
- [78] P. Jachimowicz, M. Kowal and J. Skalski, Phys. Rev. C **83**, 054302 (2011); A. Sobiczewski, F. A. Gareev and B. N. Kalinkin, Phys. Lett. **22**, 500 (1966); A. Sobiczewski, Z. Patyk and S. C. Cwiok, Phys. Lett. **224**, 1 (1989); A. Sobiczewski, Acta Phy. Pol. B **41**, 157 (2010); Z. Ren, Phys. Rev. C **65**, 051304(R) (2002).

- [79] M. Bhuyan, S. K. Patra and Raj K. Gupta, Phys. Rev. C **84**, 014317 (2011);  
S. K. Patra, M. Bhuyan, M. S. Mehta and Raj K. Gupta, Phys. Rev. C **80**,  
034312 (2009); S.K. Patra, Cheng-Li Wu, C.R. Praharaaj, Raj K. Gupta, Nucl.  
Phys. A **651**, 117 (1999).
- [80] S. K. Patra, X. Viñas, M. Centelles and M. Del Estal, Nucl. Phys. A **703**, 240  
(2002); *ibid* Phys. Lett. B **523**, 67 (2001); Chaoyuan Zhu and Xi-Jun Qiu, J.  
Phys. G **17**, L11 (1991).
- [81] S. K. Patra, M. Centelles, X. Viñas and M. Del Estal, Phys. Rev. C **65**,  
044304 (2002).
- [82] P. G. Reinhard et al., Z. Phys. A **323**, 13 (1986).
- [83] W. Pannert, P. Ring and J. Boguta, Phys. Rev. Lett. **59**, 2420 (1987).
- [84] S. K. Patra and C. R. Praharaaj, Phys. Rev. C **44**, 2552 (1991).
- [85] A. R. Bodmer, Nucl. Phys. A **526**, 703 (1991); A. R. Bodmer and C. E. Price,  
Nucl. Phys. A **505**, 123 (1989); Y. K. Gambhir, P. Ring, and A. Thimet, Ann.  
Phys. (N.Y.) **198**, 132 (1990).
- [86] K. Sumiyashi, D. Hirata, H. Toki and H. Sagawa, Nucl. Phys. A **552**, 437  
(1993).
- [87] Y. Sugahara and H. Toki, Nucl. Phys. A **579**, 557 (1994); S. Gmuca, J. Phys.  
G **17**, 1115 (1991); Z. Phys. A **342**, 387 (1992); Nucl. Phys. A **547**, 447 (1992).
- [88] C. J. Batty, E. Friedman, H. J. Gils and H. Rebel, Adv. Nucl. Phys. **19**, 1  
(1989).
- [89] B. A. Brown, Phys. Rev. Lett. **85**, 5296 (2000).
- [90] B. G. Todd-Rutel and J. Piekarewicz, Phys. Rev. Lett. **95**, 122501 (2005).
- [91] F. J. Fattoyev, C. J. Horowitz, J. Piekarewicz and G. Shen, Phys. Rev. C **82**,  
055803 (2010).



- [92] X. Roca-Maza, M. Centelles, X. Viñas and M. Warda, Phys. Rev. Lett. **106**, 252501 (2011).
- [93] G. A. Lalazissis, S. Karatzikos, R. Fossion, D. Pena Arteaga, A. V. Afanasjev, P. Ring, Phys. Lett. B **671**, 36 (2009).
- [94] M. Centelles, X. Viñas, M. Barranco and P. Suhuck, Ann. Phys. (NY). **221**, 165 (1993).
- [95] M. Centeles, X. Viñas, M. Barranco, S. Marco and R. J. Lombard, Nucl. Phys. A **537**, 486 (1992).
- [96] C. Speichers, E. Engle and R. M. Dreizler, Nucl. Phys. A **562**, 569 (1998).
- [97] M. Centeles, M. Del Estal and X. Viñas, Nucl. Phys. A **635**, 193 (1998).
- [98] M. Centelles, X. Viñas, M. Barranco, N. Ohtsuka, A. Faessler, Dao T. Khoa and H. Müther, Phys. Rev. C **47**, 1091 (1993).
- [99] J. Boguta and A. R. Bodmer, Nucl. Phys. A **292**, 413 (1977).
- [100] L. I. Schiff, Phys. Rev. **86**, 856 (1952).
- [101] X. Viñas, P. Schuck and M. Farine, J. Phys. Conf. Ser. **321**, 012024 (2011).
- [102] M. Baldo, L. M. Robledo, P. Schuck and X. Viñas, Phys. Rev. C **87**, 064305 (2013).
- [103] T. Maruyama and T. Suzuki, Phys. Lett. B **219**, 43 (1989).
- [104] H. F. Boersma, R. Malfiet and O. Scholten, Phys. Lett. B **269**, 1 (1991).
- [105] M. V. Stoitsov, P. Ring and M. M. Sharma, Phys. Rev. C **50**, 1445 (1994).
- [106] M. V. Stoitsov, M. L. Cescato, P. Ring and M. M. Sharma, J. Phys. G: **20**, L49 (1994).
- [107] M. Centelles, X. Viñas, S. K. Patra, J. N. De and Tapas Sil, Phys. Rev. C **72**, 014304 (2005).

- [108] M. Wang, G. Audi, A. H. Wapstra, F. G. Kondev, M. MarCormick, X. Xu and B. Pfeiffer, Chinese Physics C **36**, 1603 (2012).
- [109] I. Angeli and K.P. Marinova, At. Data Nucl. Data Tables, **99**, 69 (2013).
- [110] H. A. Bethe, Ann. Rev. Nucl. Sci. **21**, 93 (1971).
- [111] D. H. Youngblood, Y.-W. Lui, Krishichayan, J. Button, M. R. Anders, M. L. Gorelik, M. H. Urin and S. Shlomo Phys. Rev. C **88**, 021301 (2013).
- [112] P. Moller and J. R. Nix, At. Data and Nucl. Data Tables **59**, 185 (1995).
- [113] S. Yildirim, T. Gaitanos, M. Di Toro, and V. Greco, Phys. Rev. C **72**, 064317 (2005).
- [114] F. E. Bertrand, Ann. Rev. Nucl. Part. Sc. **26**, 456 (1976); J. Speth, A. V. Woude, Rep. Prog. Phys. **44**, 719 (1981); K. Goeke, J. Speth, Ann. Rev. Nucl. Part. Sc. **32**, 65 (1982).
- [115] D. H. Youngblood, Y.-W. Lui, and H. L. Clark, Phys. Rev. C **63**, 067301 (2001).
- [116] Y. W. Lui, H. L. Clark, and D. H. Youngblood, Phys. Rev. C **64**, 064308 (2001).
- [117] Wei-Chia Chen, J. Piekarewicz, and M. Centelles Phys. Rev. C **88**, 024319 (2013).
- [118] E. Khan, Phys. Rev. C **80**, 057302 (2009).
- [119] D. Patel et al, arXiv:1307.4487v2 [nucl-ex].
- [120] L. Satpathy and S. K. Patra, J. Phys. G: Nucl. Part. Phys. **30**, 771 (2004); S. K. Patra, R. K. Choudhury and L. Satpathy, J. Phys. G: Nucl. Part. Phys. **37**, 085103 (2010).
- [121] D. Vretenar, A. Wandelf and P. Ring, Phys. Lett. B **487**, 334 (2002).
- [122] J. Piekarewicz, Phys. Rev. C **66**, 034305 (2002).

- [123] G. Colo et al., Nucl. Phys. **73**, 15 (2004).
- [124] B. K. Agrawal, S. Shlomo and V. Kim Au, Phys. Rev. C **86**, 031304 (2005).
- [125] T. Li et al., Phys Rev. Lett. **99**, 162503 (2007).
- [126] U. Garg et al., Nucl. Phys. A **788**, 36c (2007).
- [127] J. Piekarewicz, Phys. Rev. C **76**, 031301 (2007).
- [128] O. Citaverese et al., Phys. Rev. C **43**, 2622 (1991).
- [129] Li-Gang Cao, H. Sagawa and G. Colo, Phys. Rev. C **86**, 054313 (2012).
- [130] Jun Li, G. Col, and J. Meng, Phys. Rev. C **78**, 064304 (2008).
- [131] E. Khan, Phys. Rev. C **80**, 011307(R) (2009).
- [132] E. Khan, J. Margueron, G. Colo, K. Hagino, and H. Sagawa, Phys. Rev. C **82**, 024322 (2002).
- [133] Wei-Chia Chen, J. Piekarewicz, and A. Volya, Phys. Rev. C **89**, 014321 (2014).
- [134] P. Vesely, J. Toivanen, B. G. Carlsson, J. Dobaczewski, N. Michel, and A. Pastore4, Phys. Rev. C **86**, 054313 (2012).
- [135] M. Centelles, X. Viña, M. Barranco and P. Schuck, Ann. Phys., NY **221**, 165 (1993).
- [136] M. Centelles, X. Viñas, M. Barranco, S. Marcos and R. J. Lombard, Nucl. Phys. A **537**, 486 (1992).
- [137] C. Speicher, E. Engel and R.M Dreizler, Nucl. Phys. A **562**, 569 (1993).
- [138] M. Centelles, M. Del Estal and X. Viñas, Nucl. Phys. A **635**, 193 (1998).
- [139] M. Centelles et al, Phys. Rev. C **47**, 1091 (1993).
- [140] V. Tselayaev, J. Speth, S. Krewald, E. Livinova, S. Kamerdzhiev, and N. Lyutorovich, Phy. Rev. C **79**, 034309 (2009).
- [141] A. R. Bodmer, Nucl. Phys. A **526**, 703 (1991).

- [142] C. J. Horowitz and J. Piekarewicz, Phys. Rev. Lett. **86**, 5647 (2001).
- [143] M. Centelles, S. K. Patra, X. Roca-Maza, P. D. Stevenson and X. Viñas, J. Phys. G: **37**, 075107 (2009).
- [144] M. Centelles, X. Roca-Maza, X. Viñas and M. Warda, Phys. Rev. Lett. **102**, 122502 (2009).
- [145] S. K. Singh, M. Bhuyan, P. K. Panda and S. K. Patra, J. Phys. G: **40**, 085104 (2013).
- [146] Giant Resonances Fundamental High-Frequency Modes of Nuclear Excitation by M. N. Harakeh and A. Van der woude (2001).
- [147] J. R. Stone, N. J. Stone and S. A. Moszkowski, Phys. Rev. C **89**, 044316 (2014).
- [148] G. C. Baldwin and G. S. Klaiber, Phys. Rev **71**, 3 (1947).
- [149] M. Goldhaber and E. Teller, Phys. Rev. **74**, 1046 (1949).
- [150] H. Steinwedel, J. H. D. Jensen, Z. Naturforsch. Teil A **5**, 413 (1950).
- [151] X Roca-Maza, M Brenna, G Colo, M Centelles, X Vias, B. K. Agrawal, Nils Paar, Dario Vretenar, J Piekarewicz, Phys. Rev . C **88**, 024361 (2013).
- [152] X. Roca-Maza, X. Viñas, M. Centelles, B. K. Agrawal, G. Col, N. Paar, J. Piekarewicz, D. Vretenar, Phys. Rev. C **92**, 604304 (2015).
- [153] B. K. Jennings and A.D. Jackson, Phys. Reports **66**, 141 (1980).
- [154] J. Treiner, H. Krivine, O. Bohigas and J. Martorell, Nucl. Phys. A **371**, 253 (1981)
- [155] J. P. Blaizot , J.E Berger, J. Decharg, M. Girod, Nuclear Physics A **591**, 435 (1995).
- [156] C. J. Horowitz, J. Piekarewicz, Nucl. Phys. A **511**, 461 (1990).
- [157] J. Piekarewicz, Phys. Rev. C **76**, 031301(R) (2007)

- [158] Z. Y. Ma, N. V. Giai, A. Wandelt, D. Vretenar, and P. Ring, Nucl. Phys. A **686**, 173 (2001).
- [159] D. Vretenar, H. Berghammer and P. Ring, Nucl. Phys. A **581**, 679 (1995).
- [160] D. Vretenar, G. A. Lalazissis, R. Behnsch, W. poschl and P. Ring, Nucl. Phys. A **621**, 853 (1997).
- [161] M. Centelles, X. viñas, M. Barranco and P. Schuck Nucl. Phys. A **519**, 73 (1990).
- [162] M. Centelles, X. Viñas, M. Barranco and P. Schuck, Annals of Physics., NY **221**, 165 (1993).
- [163] M. Bender, Paul-Henri Heenen, and Paul-Gerhard Reinhard, Rev. of Mod. Phys. **75**, 121 (2003).
- [164] M. Centelles, S. K. Patra, X Roca-Maza, B. K. Sharma, P. D. Stevenson and X. Viñas, J. Phys. G: **37**, 075107 (2010).
- [165] J. Fujita and Hironari Miyazawa, Prog. Theor. Phys. **17**, 360 (1957).
- [166] Steven C. Pieper, V. R. Pandharipande, R. B. Wiringa and J. Carlson, Phys. Rev. C **64**, 014001 (2001).
- [167] L. I. Schiff, Phys. Rev. **80** 137 (1950); *obid* **83**, 239 (1951); **84**, 1 (1950).
- [168] K. T. R. Davies, H. Flocard, S. Krieger and M. S. Weiss Nucl. Phys. A **342**, 111 (1980).
- [169] S. Levit, Phys. Lett. B **139**, 147 (1984).
- [170] D. Dalili, J. Nemeth and C. Ngo, Z. Phys. A **321**, 335 (1985).
- [171] D. H. Youngblood, Y. W. Lui, H. L. Clark, B. John, Y. Tokomoto, X. Chen, Phys. Rev. C **69**, 034315 (2001).
- [172] D. H. Youngblood, Y.-W. Lui, B. John, Y. Tokomoto, H. L. Clark, X. Chen, Phys. Rev. C **69**, 054312 (2001).

- [173] Li-Gang Cao and Xhong-Yu Ma, Chin. Phys. Lett. **20**, 1459 (2003).
- [174] B. L. Berman et. al., Rev. Mod. Phys. **47**, 713 (1975).
- [175] A. V. Varlamov, V. V. Varlamov, D. S. Rudenko, M. E. Stepanov, IAEA INDC(NDS)-394 (1999).
- [176] D. Vretenar, T. Niksic, P. Ring, Phys. Rev. C **68**, 024310 (2003).
- [177] J. Meyer, P. Quentin, B.K. Jennings, Nucl. Phys. A **385**, 269 (1982).
- [178] Li Guo-Qiang, Xu Gong-Ou, Phys. Rev. C **42**, 290 (1990).
- [179] P. Gleissl, M. Brack, J. Meyer, P. Quentin, Ann. Phys. (NY) **197**, 205 (1990).
- [180] B.G. Todd and J. Piekarewicz, Phys. Rev. C **67**, 044317 (2003).
- [181] Y. Fujiwara and K. T. Hecht, Nucl. Phys. A **451**, 625 (1986).
- [182] Y. Fujiwara and K. T. Hecht, Phys. Lett. B **171**, 17 (1986).
- [183] F. Gross, T. D. Cohen, E. Epelbaum and R. Machleidt, *Conference discussion of the nuclear force*, Few-Body Syst **50**, 31 [*arXiv:1110.3761 [nucl-th]*](2011).
- [184] R. Machleidt, Q. MacPherson, E. Marji, R. Winzer, Ch. Zeoli and D. R. Entem, *Recent progress in the theory of nuclear forces*, [*arXiv:1210.0992 [nucl-th]*].
- [185] BirBikram Singh, M. Bhuyan, S. K. Patra, and Raj K. Gupta, J. Phys. G: Nucl. Part. Phys **39**, 025101 (2012).
- [186] B. B. Sahu, S. K. Singh, M. Bhuyan, S. K. Biswal and S. K. Patra, Phys. Rev. C **89**, 034614 (2014)
- [187] W. G. Love and G. R. Satchler, Nucl. Phys. A **159**, 1 (1970).
- [188] W. G. Love and L. J. Parish, Nucl. Phys. A **157**, 625 (1970) ; W. G. Love, Nucl. Phys. A **192**, 49 (1972).
- [189] C. J. Horowitz and B. D. Serot, Nucl. Phys. A **368**, 503 (1981).

- [190] B. D. Serot and J. D. Walecka, Adv. Nucl. Phys **16**, 1 (1986).
- [191] R. Brockmann, Phys. Rev. C **18**, 1510 (1978).
- [192] S. Gmuca, Nucl. Phys. A **547**, 447 (1992).
- [193] Y. Sugahara, H. Toki, Nucl. Phys. A **579**, 557 (1994).
- [194] L. I. Schiff, Phys. Rev **84**, 1 (1950).
- [195] L. I. Schiff, Phys. Rev **80**, 137 (1950); Phys. Rev **83**, 239 (1951).
- [196] R. Brockmann and R. Machleidt, Phys. Rev. C **42**, 1965 (1990).
- [197] F. Coester, S. Cohen, B. D. Day and C. M. Vincent, Phys. Rev. C **1**, 769 (1970).
- [198] C. J. Horowitz and J. Piekarewicz, Phys. Rev. Lett **86**, 5747 (2001).
- [199] R. J. Furnstahl, C. E. Price and G. E. Walker, Phys. Rev. C **36**, 2590 (1987).
- [200] R. J. Furnstahl and C. E. Price, Phys. Rev. C **40**, 1398 (1989).
- [201] P. B. Demorest, T. Pennucci, S. M. Ransom, M. S. E. Roberts, and J. W. T. Hessels, Nature (London) **467**, 1081 (2010).
- [202] S K Singh, M Bhuyan, P K Panda and S K Patra, J. Phys. G: Nucl. Part. Phys **40**, 085104 (2013).
- [203] H. De Vries, C. W. De Jager, and C. De Vries, At. Data. Nucl. Data. Tables **36**, 495 (1987).
- [204] C. Illiadis, *Nuclear Physics of the Stars* (Wiley-VCH Verlag GmbH, Weinheim, 2007).
- [205] M. Arnould and S. Goriely, Phys. Rep. **384**, 1 (2003).
- [206] T. Rauscher and F.K. Thielemann, At. Data. Nucl. Data. Tables **75**, 1 (2000); **79**, 47 (2000).
- [207] G. Gangopadhyay, Phys. Rev. C **82**, 027603 (2010).

- [208] C. Lahiri and G. Gangopadhyay, Eur. Phys. J. A **47**, 87 (2011).
- [209] C. Lahiri and G. Gangopadhyay, Phys. Rev. C **84**, 057601 (2011).
- [210] C. Lahiri and G. Gangopadhyay, Phys. Rev. C **86**, 047601 (2012).
- [211] S. Datta, D. Chakraborty, G. Gangopadhyay, and A. Bhattacharyya, Phys. Rev. C **91**, 025804 (2015).
- [212] P. G. Reinhard, Z. Phys. A - Atomic Nuclei **329**, 257 (1988).
- [213] P. Ring, Prog. Part. Nucl. **37**, 193 (1996).
- [214] B. D. Serot and J. D. Walecka, Adv. Nucl. Phys **16**, 1 (1986).
- [215] P. G. Reinhard and M. Bender, *Extended Density Functionals in Nuclear Structure Physics Lecture Notes in Physics* **641**, 249 (2004).
- [216] Bir Bikram Sing, M. Bhuyan, S. K. Patra and Raj K Gupta, J. Phys. G: Nucl. Part. Phys. **39**, 069501 (2012).
- [217] G. Bertsch, J. Borysowicz, H. McManus, and W.G. Love, NP **284**, (1977) 399 ; W.D. Myers, Nucl. Phys. A **204**, 465 (1973); D.N. Basu, J. Phys. G: Nucl. Part. Phys. **30**, B7 (2004).
- [218] R. R. Scheerbaum, Nucl. Phys. **257**, 77 (1976).
- [219] M. Wang, G. Audi, A.H. Wapstra, F. G. Kondev, M. MacCormick, X. Xu, and B. Pfeiffer, Chinese Phys. C **36**, 1603 (2014).
- [220] I. Angeli, K.P. Marinova, At. Data. Nucl. Data. Tables **99**, 69 (2013).
- [221] A.J. Koning *et al.*, *Proc. Int. Conf. Nucl. Data Science Tech., April 22-27, 2007, Nice, France, EDP Sciences*, p. 211 (2008).
- [222] S. K. Patra, R. N. Panda, P. Arumugam, and R. K. Gupta, Phys. Rev. C **80**, 064602 (2009).
- [223] G. W. Greenlees, C. H. Poppe, J. A. Sievers, and D. L. Watson, Phys. Rev. C **3**, 1231 (1971).



- [224] S. Goriely, S. Hilaire and A. J. Koning, Phys. Rev. C **78**, 064307 (2008).
- [225] S. Goriely, F. Tondeur, J. M. Pearson, At. Data. Nucl. Data. Tables **77**, 311 (2001).
- [226] N. Özkan et. al., Nucl. Phys. A **710**, 469 (2002).
- [227] I. Dillmann et. al., Phys. Rev. C **84**, 015802 (2011).
- [228] Gy. Gyürky et.al, J. Phys. G: Nucl. Part. Phys. **34**, 817 (2007).
- [229] F. R. Chloupek et.al, Nucl. Phys. A **652**, 391 (1999).
- [230] R. T. Güray et.al, Phys. Rev. C **80**, 035804 (2009).
- [231] D. G. Yakovlev, M. Beard, L. R. Gasques and M. Wiescher, Phys. Rev. C **82**, 044609 (2010).
- [232] J. M. Lattimer and M. Prakash, Science **304**, 536 (2004).
- [233] J. M. Lattimer and M. Prakash, Phys. Rep. **442**, 109 (2007).
- [234] N. K. Glendenning, Astrophys J. **293**, 470 (1985).
- [235] P. G. Reinhard, Rep. Prog. Phys. **52**, 439 (1989).
- [236] P. Ring, Prog. Part. Nucl. Phys. **37**, 193 (1996).
- [237] B. K. Sharma, P. K. Panda and S. K. Patra, Phys. Rev. C **75**, 035808 (2007).
- [238] P. G. Reinhard, M. Rufa, J. Maruhn, W. Greiner, and J. Friedrich, Z. Phys. A **323**, 13 (1986).
- [239] Y. K. Gambhir, P. Ring, and A. Thimet, Ann. Phys. (N.Y.) **198**, 132 (1990).
- [240] P. G. Reinhard, Z. Phys. A **329**, 257 (1988).
- [241] M. M. Sharma, G. A. Lalazissis, and P. Ring, Phys. Lett. B **312**, 377 (1993).
- [242] R. Machleidt, K. Holinde and Ch. Elster, Phys. Rep. **149**, 1 (1987).
- [243] L. D. Miller and A. E. S. Green, Phys. Rev. C **5**, 241 (1971).

- [244] S. K. Singh, S. K. Biswal, M. Bhuyan, and S. K. Patra, Phys. Rev. C **89**, 044001 (2014) .
- [245] S. K. Singh, S. K. Biswal, M. Bhuyan and S. K. Patra, J. Phys. G **41**, 055201 (2014).
- [246] S. Kubis and M. Kutschera, Phys. Lett. B **399**, 191 (1997).
- [247] J. Kotulič Bunta and Štefan Gmuca, Phys. Rev. C **70**, 054309 (2004).
- [248] M. Oertel, C. Providncia, F. Gulminelli and Ad. R. Raduta, J. Phys. G:Nucl. Part. Phys. **42**, 075202 (2015).
- [249] X. Roca-Maza, X. Viñas, M. Centelles, P. Ring and P. Schuck **84**, 054309 (2011).
- [250] J. Antoniadis et al., Science **340**, 6131 (2013).
- [251] R. J. Furnstahl, B. D. Serot , Hua-Bin Tang c, Nucl. Phys. A **615**, 441 (1997).
- [252] F. Hofmann, C. M. Keil, and H. Lenske, Phys. Rev. C **64**, 034314 (2001).
- [253] B. Liu, V. Greco, V. Baran, M. Colonna and M. Di Toro, Phys. Rev. C **65**, 045201 (2002).
- [254] D. P. Menezes and C. Providência, Phys. Rev. C **70**, 058801 (2004).
- [255] A. Sulaksono, P. T. P. Hutaauruk, and T. Mart, Phys. Rev. C **72**, 065801 (2005).
- [256] S. K. Singh, M. Bhuyan, P. K. Panda and S. K. Patra, J. Phys. G **40**, 085104 (2013).
- [257] R. J. Furnstahl, B. D. Serot and H. B. Tang, Nucl. Phys. A **598**, 539 (1996).
- [258] H. Müller and B. D. Serot, Nucl. Phys. A **606** 508 (1996).
- [259] R. J. Furnstahl and B. D. Serot, Nucl. Phys. A **671**, 447 (2000).
- [260] R. Machleidt and D. R. Entem, Phys. Rep. **503**, 1 (2011).

- [261] L. W. Chen, C. M. Ko and Bao-An Li, Phys. Rev. C **76**, 054316 (2007).
- [262] M. Dutra, O. Lourenco, J. S. Sa Martins, A. Delfino. J. R. Stone and P. D. Stevenson, Phys. Rev. C **85**, 035201 (2012).
- [263] <http://www.nndc.bnl.gov/>
- [264] R. Brockmann and R. Machleidt, Phys. Rev. C **42**, 1965 (1990).
- [265] S. K. Biswal, S. K. Singh, M. Bhuyan and S. K. Patra, Brazilian Journal of Physics, **45**, 347 (2015).
- [266] B. Friedman and V. R. Pandharipande, Nucl. Phys. A **361**, 502 (1981).
- [267] M. Baldo and C. Maieron, Phys. Rev. C **77**, 015801 (2008).
- [268] J. Margueron, H. Sagawa, and K. Hagino, Phys. Rev. C **77**, 054309 (2008).
- [269] S. Gandolfi, A. Yu. Illarionov, S. Fantoni, F. Pederiva, and K. E. Schmidt, Phys. Rev. Lett. **101**, 132501 (2008).
- [270] Steven C. Pieper, V. R. Pandharipande, R. B. Wiringa, and J. Carlson, Phys. Rev. C **64**, 014001 (2001).
- [271] S. Typel and H. H. Wolter, Nucl. Phys. A **656**, 331 (1991).
- [272] M. D. Voskresenskaya, S. Typel, Nucl. Phys. A **887**, 42 (2012).
- [273] P. Arumugam, B. K. Sharma, P. K. Sahu, S. K. Patra, T. Sil, M. Centelles and X. Viñas, Phys. Lett. B **601**, 51 (2004).
- [274] P. Danielewicz, R. Lacey, W. G. Lynch, Science **208**, 1592 (2002).
- [275] J. R. Oppenheimer and G. M. Volkoff, Phys. Rev. **55**, 374 (1937); R. C. Tolman, Phys. Rev. **55**, 364 (1939).
- [276] N. Stergioulas and J. L. Friedman, Astrophys. J. **444**, 306 (1995).
- [277] H. Komatsu, Y. Eriguchi, and I. Hachisu, Mon. Not. R. Astron. Soc. **237**, 355 (1989) .

- [278] H. Komatsu, Y. Eriguchi, and I. Hachisu, Mon. Not. R. Astron. Soc. **239**, 153 (1989).
- [279] W. C. Chen and J. Piekarewicz, Phys. Rev. C **90**, 044305 (2014).
- [280] N. K. Glendenning, S. A. Moszkowski, Phys. Rev. Lett. **67**, 2414 (1991).
- [281] N. K. Glendenning, *Compact Stars*, Springer, New York -Second Edition (2000).
- [282] S. Weissenborn, D. Chatterjee, J. Schaffner-Bielich, Nucl. Phys. A **881**, (2012) 62 ; S. Weissenborn, D. Chatterjee, J. Schaffner-Bielich, Phys. Rev. C **85**, 065802 (2012).
- [283] L. L. Lopes and D. P. Menezes, Phys. Rev. C **89**, 025805 (2014).
- [284] P. Haensel, M. Bejger, M. Fortin and L. Zdunik, axXiv:1601.05368v2 [astro-ph.HE] 29 Mar 2016.
- [285] P. Haensel, A. Y. Potekhin, D. G. Yakovlev, *Neutron stars 1, Equation of state and structure* (Springer, New York 2007).
- [286] O. Benhar, V. Ferreri and L. Gualtieri, Phys. Rev. D **70** 124015 (2004); C. H. Lenzi, M. Malheiro, R. M. Marinho, C. Providencia and G. F. Marranghello, arXiv: 0810.4848v4 [gr-qc].
- [287] N. K. Glendenning and F. Weber, Phys. Rev. D **50**, 3836 (1994).
- [288] J. W. Hessels, S. M. Ransom, I. H. Stairs, P. C. C. Freire, V. M. Kaspi and F. Camilo, Science **311**, 1901 (2006).
- [289] P. Kaaret, Z. Prieskorn, J. t Zand, S. Brandt, N. Lund et al. , Astrophys. J. **657**, L97 (2007).
- [290] S. K. Patra, Bharat Kumar and S. K. Singh (in preparation).